Alberto P. Guimarães

Principles of Nanomagnetism

Springer

NanoScience and Technology

NanoScience and Technology

The series NanoScience and Technology is focused on the fascinating nano-world, meso-scopic physics, analysis with atomic resolution, nano and quantum-effect devices, nano-mechanics and atomic-scale processes. All the basic aspects and technology-oriented de-velopments in this emerging discipline are covered by comprehensive and timely books. The series constitutes a survey of the relevant special topics, which are presented by lea-ding experts in the field. These books will appeal to researchers, engineers, and advanced students.

Alberto P. Guimarães

Principles of Nanomagnetism

With 117 Figures

Springer

Professor Alberto P. Guimarães
Centro Brasileiro de Pesquisas Físicas (CBPF)
Rua Dr. Xavier Sigaud 150, 22290-180 Rio de Janeiro - RJ, Brasil/Brazil
E-mail: apguima@cbpf.br

For Juliana, Felipe, Luisa and Paulo

Preface

The field of Nanomagnetism is a young branch of the study of magnetic phenomena, phenomena that have been a source of amazement and stimulus for speculation for more than 3,000 years [1].

Nanomagnetism, despite being a young area, has already affected every sphere of human activity, through its fundamental contribution to make the computer an ubiquitous instrument for communication, control of industrial processes, medical diagnosis, scientific investigation, or leisure. The studies of particulate and thin film magnetic media and other related questions led to improvements that have multiplied, in five decades, the amount of data that can be encoded into a unitary area by some 50 million times.

The 2007 Nobel Prize in Physics, awarded to Albert Fert and Peter Grünberg, is an important recognition of the extraordinary achievements of the research in Nanomagnetism. The unfolding revolution brought about by Spintronics is intimately connected, and enhances the relevance of these developments.

Nanomagnetism already encompasses a very wide range of remarkable properties and phenomena, as illustrated in the case of thin films, for example, by the volumes of the series on *Ultrathin Magnetic Structures* [2].

In the present book I have attempted to organize, out of the myriads of publications, those results that might be more revealing of the principles that every student, material scientist, or physicist have to be familiar with. The fast pace of evolution of Nanomagnetism adds to the difficulty of this project, but this fascinating subject turns this into a very pleasant and stimulating challenge to be taken up.

I have also made an effort to facilitate the conversion of the expressions that describe the magnetic properties of nanoobjects from CGS to SI units, and viceversa, since the question of units is a recurrent obstacle in the path of the student of Magnetism.

I specially thank C.M. Chaves, H. Micklitz, D.H. Mosca, N.A. Oliveira and B.R. Pujada for reading the complete text and for their comments. Suggestions from W. Baltensperger, D.E. Ellis, D. Fiorani, E.R. Granhen, F.P. Missell, I.S. Oliveira, E.C. Passamani, H.R. Rechenberg, M.C. Santos, R.A. Silva, X.A. da Silva, A. Troper and I. Zutic are also acknowledged. I am grateful to L. Baltar, A.M. Souza,

R.S. Sarthour, M. Paranhos, S. Mendes, E. Novais, M. Reis, P.H.V. Linhares and H.S. de Mello for the figures. And last, but not least, I thank Silvia for her patience in enduring the gestation of this book.

For comments and corrections related to this volume see www.cbpf.br/nanomagnetism.

Rio de Janeiro, June 2009   *Alberto P. Guimarães*

References

1. A.P. Guimarães, *From Lodestone to Supermagnets: Understanding Magnetic Phenomena* (Wiley, Berlin, 2005)
2. J.A.C. Bland, B. Heinrich (eds.), *Ultrathin Magnetic Structures*, vols I–IV (Springer, Berlin, 2005)

Contents

1

The Basis of Nanomagnetism

Summary. What is the origin of the observed differences in magnetic behavior between a sample with nanometric dimensions and a macroscopic sample of the same material? These differences are shown to arise from broken translation symmetry in nanometric samples, from the higher proportion of atoms on the surface, or interface, from the fact that the sizes of nanoscopic objects are comparable to some fundamental or characteristic lengths of the constituent material, and other effects. The exchange length and the magnetic domain wall width are some of the characteristic lengths that are more relevant to the magnetic properties. The shape of the density of electronic states curve is also dependent on the dimensionality of the samples.

1.1 Introduction: The Importance of Nanomagnetism

The objects of study of Nanoscience are the phenomena involving objects of dimensions usually in the range from 1 ($1\,\mathrm{nm} = 10^{-9}\,\mathrm{m}$) to 100 nm. This is the range of sizes of many molecules and viruses, and is also the characteristic length scale of many physical processes. The lateral dimensions of present-day integrated circuit components, as well as the dimensions of grains in magnetic-recording film media, are contained in this range.

Nanomagnetism is the area of research in physics, which deals with the magnetic properties of objects that have at least one dimension in the nanoscopic range. Nanomagnetism includes in its scope the study of properties and applications of the magnetism of isolated nanoparticles, nanodots, nanowires, thin films and multilayers, and also macroscopic samples that contain nanoscopic particles. Materials that contain particles, films, and other structures in the nanometric scale are often described as nanostructured materials.

Objects with dimensions from 100 to 1,000 nm are usually described as mesoscopic; although our focus in the present work is on magnetic properties of objects of nanoscopic dimension, we will also consider the behavior of objects of mesoscopic size.

Nanomagnetism has many practical applications, from geology to magnetic recording, from ferrofluids [20] used in loudspeakers to small particles used in

medicine, that can be directed to specific organs and tissues, either for drug delivery [1] or for the application of the technique of magnetic hyperthermia [14].

Magnetic nanoparticles are present in many rocks and soils. The alignment of their magnetic moments under the influence of the geomagnetic field allows the study of the evolution of Earth's magnetism and the determination of the their age; this alignment can also inform on past anthropic activities [7].

Nanoparticles of magnetic materials, usually of magnetite, also occur in living beings; perhaps the best studied example is that of magnetotatic bacteria, which, through magnetic grains of nanometric dimension, align themselves in the Earth's magnetic field. These grains are synthesized by the bacteria, in a process called biomineralization. Nanomagnets have also been found in insects, birds, and other creatures [26]. Figure 1.1 illustrates this with the cross section of the beak of a pigeon, where the presence of clusters of magnetite nanoparticles with diameters of 2–4 nm was observed [8].

Finally, the most successful application of nanomagnetism has been to magnetic recording, which has taken this technology through a swift evolution in the last 5 decades. This is measured by the evolution of the areal bit density in magnetic hard disks, which has increased by a factor of many tens of millions since the introduction in the market of this technology (Fig. 1.2) (e.g., [25]). The rapid increase in the density of electronic circuits made on individual silicon chips, which has doubled every 18 months, is a tendency known as Moore's Law, a name arising from a 1965 paper by Moore that discussed the subject. Alongside this evolution, the density of magnetic storage in hard disks, measured by the data areal density, has progressed even faster, doubling every 2 months.

To reach higher and higher storage densities, a great effort was necessary in the study of the properties of small magnetic particles, and also of the magnetic thin films that are a constitutive part of hard disk platters and magnetic read heads.
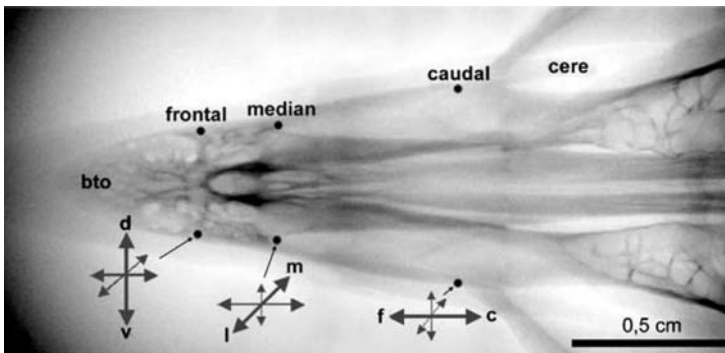
Fig. 1.1. X-ray of a homing pigeon beak showing the six regions were there are found clusters of magnetite nanoparticles, of 2–4 nm diameter. Also shown the orientation of the nerve bundles where these clusters are located. Strings of maghemite particles are also present, and both systems participate in the magnetoreception [8] (With kind permission from Springer Science + Business Media [8], Fig. 3a)
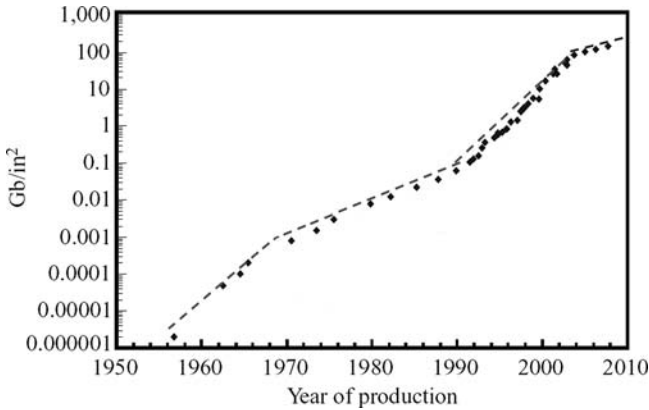
Fig. 1.2. Evolution of magnetic recording: hard disk areal density in gigabits per square inch as a function of the year in which the products became available in the market [10]. (Reprinted from [8] with permission from IBM Technical Journals)

The application to devices, particularly spintronic devices, has represented another frontier in rapid expansion (e.g., [9]). This application is based on the interaction of the spin degree-of-freedom of an electric current with the magnetic materials, and also uses films and other structures with nanometric dimensions.

1.2 The Origin of Nanomagnetic Behavior

The emergence of the new phenomena that are the object of nanomagnetism has its origin in the fact that the magnetism of samples of nanoscopic or mesoscopic sizes presents important differences compared to the magnetism of macroscopic samples. One could describe these differences, in a simplified way, as arising from the fact that the magnetic systems of nanoscopic or mesoscopic scales present: (1) dimensions comparable to characteristic lengths, such as the limiting size of magnetic domains; (2) broken translation symmetry, which results in sites with reduced coordination number, with broken exchange bonds and frustration. Also, nanoscopic or mesoscopic objects exhibit a higher proportion of surface (or interface) atoms.

Another factor that modifies the magnetic properties of the nanoobjects is that they are in general in close contact with other physical systems, for example, with a substrate or a capping layer, in the case of most thin films and multilayers. In the case of nanoparticles, these objects may be immersed in solid matrices, or compacted in a container: in both cases, each particle may feel a strong interaction with its immediate neighborhood.

Also, in general, as systems such as ensembles of nanoparticles are prepared with smaller dimensions, the presence of imperfections and defects becomes more relevant, making the obtention of identical sets of nanoobjects more difficult. Often the properties of the nanoscopic objects have to be derived from samples formed of ensembles of such objects.

The spin wave spectra of samples of nanoscopic dimensions are also modified (e.g., [17]). The dispersion relation for spin waves for wavelengths longer than the lattice spacing is $\hbar\omega = Dk^2$, where D is the stiffness constant, and k is the magnitude of the spin wavevector. For a spin wave energy comparable to the thermal energy, one has $k \approx (k_{\mathrm{B}}T/D)^{1/2}$, where k_{B} is the Boltzmann constant. For Fe, $D(4.2\,K) \approx 3\,\mathrm{meV\,nm^2}$ and the corresponding length $L = 1/k \approx 3\,\mathrm{nm}$ at liquid helium temperature, which implies that spin wave spectra of nanoscopic objects are significantly modified, if compared to those of bulk samples.

The dynamic behavior of magnetic objects of nanometric size also differs from the behavior of macroscopic samples of the same constituents. The main cause for this difference is the enhanced importance of thermal fluctuations under the usual experimental conditions. The phenomenon of superparamagnetism is observed in magnetic nanoparticles if the thermal energy $k_{\mathrm{B}}T$ is of the same order-of-magnitude of the anisotropy energy of the particles, leading to an effectively zero measured magnetic moment. The superparamagnetism of nanoparticles is discussed in Sect. 3.3 (p. 68).

1.2.1 Sample Dimensions and Characteristic Lengths

The simplest example of the effect of the characteristic lengths on the magnetic properties is the case of magnetic particles that have dimensions smaller than the critical magnetic single-domain diameter. These particles therefore have the single domain as their lowest energy configuration.

Some of these characteristic lengths, which include the exchange interaction length, the domain wall width and the spin diffusion length, are given in Table 1.1, together with their typical values. From this table, it is evident that nanoobjects have dimensions in the range of many of these characteristic lengths. The derivation of the expressions for some of these lengths, in terms of the magnetic parameters of the constituent materials, will be discussed in Chap. 2.

Table 1.1. Some characteristic lengths in magnetism and their typical magnitudes

Symbol	Length	Typical magnitude (nm)
d_{a}	Interatomic distance (Fe)	2.5×10^{-1}
d_{ex}	Range of exchange interaction	$\sim 10^{-1} - \sim 1$
d_{RKKY}	Range of RKKY interaction	$\sim 10^{-1} - \sim 10$
d_{c}	Domain size	$10 - 10^4$
$D_{\mathrm{cr}}^{\mathrm{spm}}$	Superparamagnetic critical diameter	$\sim 1 - \sim 10^2$
D_{cr}	Critical single-domain size	$\sim 10 - \sim 10^3$
δ_0	Domain wall width	$\sim 1 - \sim 10^2$
l_{ex}	Exchange length	$\sim 1 - \sim 10^2$
l_{sd}	Spin diffusion length	$\sim 10 - 10^2$
λ_{mfp}	Electron mean free path	$\sim 1 - 10^2$
ζ	Superconducting coherence length	$\sim 1 - 10^3$
λ_{F}	Fermi wavelength/metal	$\sim 10^{-1}$
λ_{F}	Fermi wavelength/semiconductor	$\sim 10^2$

The critical size for magnetic domains D_{cr}, which is the largest size that a ferromagnetic particle may have, beyond which it will be energetically more favorable to divide itself into two or more domains, varies from material to material. This size varies from about 10 nm to some thousands of nanometers (or microns); some values of this dimension for spherical particles for different materials are shown in Table 2.9, on p. 38. This critical diameter is given by the following expression, to be demonstrated in Chap. 2 (p. 49):

$$D_{\mathrm{cr}} = \frac{72\sqrt{AK}}{\mu_0 M_{\mathrm{s}}^2}.$$ (1.1)

In this expression, A is the exchange stiffness constant, or parameter, K is the uniaxial anisotropy constant (assumed >0) and M_{s} is the saturation magnetization; μ_0 is the vacuum magnetic permeability (or magnetic constant), equal to $4\pi \times 10^{-7}\,\mathrm{H\,m^{-1}}$ in the SI.

The characteristic lengths that are more relevant in defining the magnetic properties of nanoobjects are the exchange length and the domain wall width parameter. The exchange length is given by:

$$l_{\mathrm{ex}} = \sqrt{\frac{2A}{\mu_0 M_{\mathrm{s}}^2}}.$$ (1.2)

Table 1.2 illustrates the magnitude of the exchange length l_{ex} with some examples from the 3d metals.

The domain wall width parameter Δ characterizes the width of the transition region between two magnetic domains, as will be discussed in Chap. 2. It is given, as a function of the exchange stiffness constant A and the uniaxial anisotropy constant K, by

$$\Delta = \sqrt{\frac{A}{K}}.$$ (1.3)

And the domain wall width δ_0 is given by

$$\delta_0 = \pi\,\Delta.$$ (1.4)

The domain wall energy is also related to the same parameters A and K. In the simple case of a 180° wall of a cubic crystal, the energy per unit area of the wall is

$$\gamma = 4\sqrt{AK}.$$ (1.5)

Table 1.2. Exchange lengths for 3d metals (From Table 2.8, Chap. 2)

Element	l_{ex} (nm)
Fe	3.28
Co	4.70
Ni	7.64

In Chap. 2, where the properties of magnetic domains are studied, Table 2.9 (p. 38) presents values of critical domain diameters and domain wall energies for some materials.

1.2.2 Broken Translation Symmetry

Every finite crystal has frontiers, where the translational symmetry is lost or broken. In solids of nanometric size a significant proportion of the atoms are on or near these frontiers. The absence of translation symmetry brings about several important consequences to the physical properties of these systems.

Three aspects of the problem of symmetry breaking will be discussed: (1) the relation of the physical properties of the samples to their dimensionality (samples with quasi-zero dimension (0D), unidimensional (1D), bidimensional (2D) or tridimensional (3D)); (2) the change in coordination of the atoms at the interface, and (3) the effect of the increase in the proportion of surface (or interface) atoms in nanoscopic samples.

1.2.2.1 Dimensionality and Density of Electronic States

The electronic band structure of a solid depends on its dimensionality. This can be exemplified in the simplest description of a conducting solid, the free electron model, in which the electrons are treated as a gas (called a Fermi gas) only subject to the infinite potentials at the walls of the container. An electron gas in a limited spatial region will show an availability of electronic states (measured by its density of states $D(E)$) that depends on the dimensionality of this region: if it is in one dimension or two dimensions, $D(E)$ will differ from the three-dimensional case. The effects of the difference in dimensionality may be shown through the differences in $D(E)$, and are summarized in Fig. 1.3.

Let us examine initially a Fermi gas in three dimensions; we wish to obtain the form of the density of states $D(E)$. The electrons are supposed to be in a container with three dimensions and infinitely high walls; there are no interactions between the electrons.

Let us consider that the potential $V(x, y, z)$ inside the box of side L is $V_0 =$ const for $0 \leq x \leq L$, $0 \leq y \leq L$, and $0 \leq z \leq L$; $V = \infty$ otherwise.

The time-independent Schrödinger equation will be

$$-\frac{\hbar^2}{2m}\nabla^2\psi(r) + V(r)\psi(r) = E'\psi(r).$$ (1.6)

Using $E = E' - V_0(r)$ one obtains

$$-\frac{\hbar^2}{2m}\nabla^2\psi(r) = E\psi(r).$$ (1.7)

Since the infinite potential at the walls forbids the presence of the electrons outside them, the boundary conditions for $\psi(r)$ will be: $\psi = 0$ for $x = 0$ and $x = L$, $y = 0$ and $y = L$ and $z = 0$ and $z = L$.

Bulk (3D)

Quantum film (2D)

Quantum wire (1D)

Quantum dot (0D)
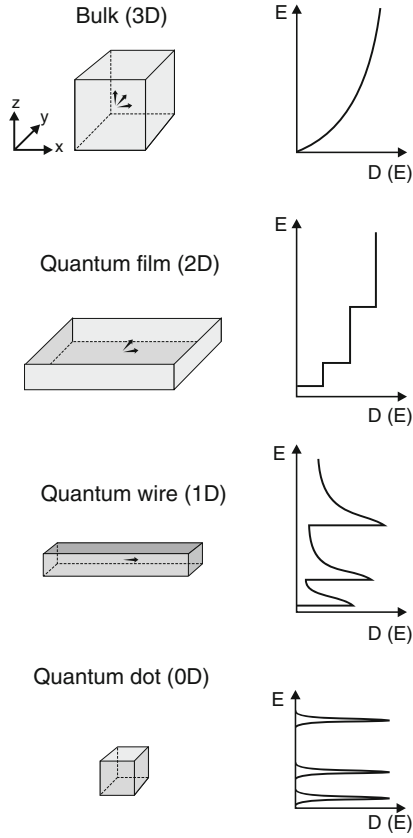
Fig. 1.3. Density of electronic states $D(E)$ as a function of energy for electrons, from *bottom to top*, in zero dimension, in one dimension, two dimensions, and three dimensions (Based on [4])

The solution of Schrödinger's equation, using these boundary conditions, will be:

$$\psi(r) = \left(\frac{2}{L}\right)^{3/2} \sin k_x x \sin k_y y \sin k_z z. \tag{1.8}$$

The corresponding energies are obtained by substituting $\psi(x)$ from (1.8) into (1.7):

$$E = \frac{\hbar^2}{2m}(k_x^2 + k_y^2 + k_z^2), \tag{1.9}$$

where m is the electron mass and k_i are the components of its wavevector.

From the boundary conditions, one obtains

$$k_x = \pm\frac{2\pi}{L}n_x, \quad k_y = \pm\frac{2\pi}{L}n_y, \quad k_z = \pm\frac{2\pi}{L}n_z, \tag{1.10}$$

where n_x, n_y, and n_z take values 1, 2, 3,....

Fig. 1.4. Graph of E/E_0 (*dotted lines*) for the lower three energy levels and wavefunctions vs. *x* (*continuous lines*) for a free electron gas confined to a one-dimensional box

The wave functions for a free electron in a one-dimensional box, for the first three values of *n*, and the corresponding energies E are illustrated in Fig. 1.4. This figure shows the form of the first three lowest energy wave functions, as well as the corresponding energies E/E_0, where E_0 is the energy for the level with $n = 1$.

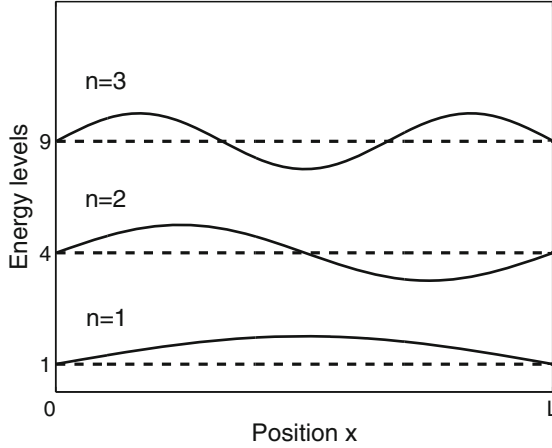According to the Pauli exclusion principle, two electrons (spin up and spin down) occupy one state defined by (n_x, n_y, n_z). But how many states are there to be occupied? To count the number of states, one has to count the number of values of k.

At $T = 0$ K, all states are occupied up to k_F, the Fermi wavevector, in a volume $V_k = \frac{4}{3}\pi k_F^3$. Since each triplet (k_x, k_y, k_z) occupies a volume of $v = (2\pi/L)^3$ in k-space, the number of states N will be

$$2 \cdot \frac{V_k}{v} = 2 \cdot \frac{\frac{4}{3}\pi k_F^3}{(2\pi/L)^3} = \frac{V}{3\pi^2} k_F^3 = N, \tag{1.11}$$

where V is the volume occupied by the electrons in real space.

From this equation one derives k_F, and substituting into the expression of the energy (1.9), one obtains the Fermi energy E_F:

$$E_F = \frac{\hbar^2}{2m} \left(\frac{3\pi^2 N}{V} \right)^{2/3}. \tag{1.12}$$

This allows writing N as a function of E_F. The derivative of the expression obtained for N is the density of electron states at the Fermi level $D(E_F)$:

$$D(E_F) \equiv \frac{dN}{dE_F} = \frac{V}{2\pi^2} \left(\frac{2m}{\hbar^2} \right)^{3/2} E_F^{1/2}. \tag{1.13}$$

This result is the density of electron states at the Fermi level for the free electron gas contained in a three-dimensional "box." The two-dimensional and the one-dimensional densities of states may be derived, using in (1.11) the corresponding expressions for the volume of the box, total volume in k-space V_k and volume per point in k-space in two and one dimensions. In two dimensions, $V_k = \pi k^2$, the volume per point is $(2\pi/L)^2$ and the volume of the box is L^2.

In one dimension, the total volume in k-space is $V_k = 2k$, the volume per point is $(2\pi/L)$ and the volume of the box is L. Consequently, the general expression for the density of states is

$$D(E) = \left(\frac{2m}{\hbar^2}\right) \frac{V_k}{v} \frac{p}{k^2}, \tag{1.14}$$

where $p = 1, 2, 3$ are the corresponding dimensionalities, as can be easily verified. Substituting, one obtains the densities of states $D(E)$, for the different dimensionalities.

In three dimensions:

$$D(E) = V \frac{1}{2\pi^2} \left(\frac{2m}{\hbar^2}\right)^{3/2} E^{1/2}. \tag{1.15}$$

In two dimensions,

$$D(E) = V \frac{1}{2\pi} \left(\frac{2m}{\hbar^2}\right). \tag{1.16}$$

Note that in this case the density of states $D(E)$ does not depend on the energy, it is a constant.

And finally, in one dimension,

$$D(E) = V \frac{1}{\pi} \left(\frac{2m}{\hbar^2}\right)^{1/2} E^{-1/2}. \tag{1.17}$$

These expressions for the densities of states of the free electron gas for different dimensions (1, 2, and 3) are represented in the graphs of Fig. 1.5.
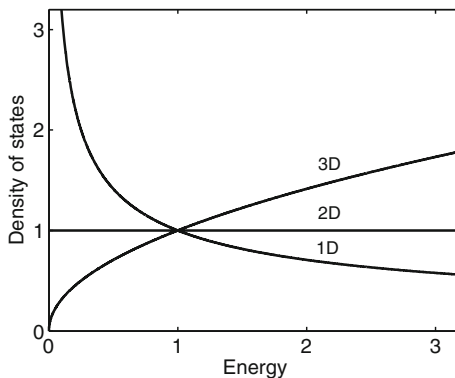

Fig. 1.5. Normalized densities of electronic states $D(E)/C_p$ (where C_p is a constant factor for each dimensionality p) as a function of energy, for different dimensionalities

We will now discuss what happens if the object that contains the electrons is a solid of nanometric dimensions. There will be quantum confinement in any case where one or more dimensions of the volume that contains the electron gas are comparable to the Fermi wavelength $\lambda_F = 2\pi/k_F$ of the electron. In objects with dimensions comparable to this wavelength the wave character of the electrons will be dominant, and their energies will be quantized.

To obtain the densities of states in the confined systems, one has to take into consideration the boundary conditions. The electrons may be confined in the three dimensions, i.e., they may be contained in an object that is nanometric in the three dimensions – this is the case of a quantum dot. If the electrons are confined in two dimensions, i.e., if the third dimension is macroscopic, one has a quantum wire, or a nanowire. If the electrons are confined in one dimension, one has a quantum well, or a quantum film. If the electrons are not confined in any dimension, one has a macroscopic object.

1. Object confined in three dimensions (quantum dot):

The allowed values for the energy of the electrons are given by (1.9). The energies of the different levels depend on k_x, k_y, and k_z. The condition of infinite potential at the walls implies $k_x = n_x\pi/L_x$, $k_y = n_y\pi/L_y$ and $k_z = n_z\pi/L_z$, where L_x, L_y and L_z are the dimensions of the box where the electrons are contained.

$$E = \frac{\hbar^2\pi^2}{2m}\left(\frac{n_x^2}{L_x^2} + \frac{n_y^2}{L_y^2} + \frac{n_z^2}{L_z^2}\right). \tag{1.18}$$

The separation between the energy levels is given by dE_k. One assumes to simplify $L_x = L_y = L_z = L$, and also $n_x = n_y = n_z = n$. For a nanoscopic solid with $L = 1$ nm, the energy levels are separated by $dE = 3\hbar^2\pi^2/mL^2 \sim 1$ eV. Therefore, the energy spectrum is formed of discrete levels, similar to the atomic levels, with energies given by

$$E_n = \frac{3\hbar^2\pi^2}{2mL^2}n^2. \tag{1.19}$$

The density of states curve $D(E)$ is formed of a series of delta functions at the energies E_n.

2. Object confined in two dimensions, and free in one dimension (quantum wire or nanowire):

One may assume that the object is macroscopic in the z direction, and the dimensions $L_x = L_y$ are nanoscopic.

From (1.18), taking $L_z = L$ and $n_z = n$ one obtains

$$E = \frac{\hbar^2\pi^2}{2m}\left(\frac{n_x^2}{L_x^2} + \frac{n_y^2}{L_y^2} + \frac{n^2}{L^2}\right). \tag{1.20}$$

In this case the separation between the energy levels labelled by n_x and n_y remains large, of the order of eV. The separation of the levels corresponding to n is much smaller, since L is a number typically $10^7 - 10^9$ times larger than the x and y dimensions. One may consider these levels as occupying a practically continuous range of values. $E(k)$ is then given by parabolas displaced by $\hbar^2\pi^2/2mL^2$.

The density of states curve $D(E)$ is formed of a series of peaks at the values of E_n; above each peak there exists a region with a continuous dependence with E.

3. Object confined in one dimension and free in two dimensions (quantum film or quantum well):

If the confinement is limited to the x axis, the electrons are free to move in the directions of the plane (y and z axes) and the energy levels are given (for $L_y=L_z=L$) by

$$E = \frac{\hbar^2\pi^2}{2m}\left(\frac{n_x^2}{L_x^2} + 2\frac{n^2}{L^2}\right). \tag{1.21}$$

In the same way as in the preceding case, the energies of the levels, labelled by n_x, exhibit a large difference. E vs. k_x and k_y is given by parabolic surfaces displaced of $\hbar^2\pi^2/2mL^2$. The density of states curve $D(E)$ is formed of a series of steps, within a parabolic envelope.

4. Object without confinement, electrons free to move in the three directions (macroscopic object):

Taking the frontiers defined by $L_x = L_y = L_z = L$ as macroscopic lengths, the energies are given by

$$E = \frac{\hbar^2\pi^2}{2m}\left(3\frac{n^2}{L^2}\right). \tag{1.22}$$

The energy levels are now distributed over a continuum of states, as shown in Fig. 1.5. The graph of E_k is represented by a parabolic surface and the density of states curve $D(E)$ is the familiar parabola shown in Fig. 1.5.

The density of state curves shown in Fig. 1.3 differ from those that appear in Fig. 1.5, since there are obvious steps or discontinuities in Fig. 1.3. These steps arise, for example, in the case of a $D2$ solid (quantum film, or quantum well), from the electron confinement in the dimension perpendicular to the plane. This confinement induces the appearance of discrete levels in the density of states; the dependence $D(E) = $ constant is observed at the energies corresponding to these levels.

A simple visual examination of the density of states curves $D(E)$ shown in Fig. 1.3 reveals important differences in this function. The appearance of $D(E)$ for the 0D sample is similar to the same function for atoms: $D(E)$ has narrow peaks, corresponding to well-defined values of the kinetic energy of the conduction electrons. For this reason, quantum dots are often referred to as "artificial atoms."

The curve $D(E)$ for quantum wires (one-dimensional) also has narrow peaks, but in this case there are electronic states that may be occupied for intermediate values of

the energy E. The curve for a two-dimensional nanosystem shows some well-defined steps, and again there exists a quasi-continuum of states that may be occupied in the whole range of energies. The result of $D(E)$ for a macroscopic system in the free electron approximation is the well-known parabola, applicable in the simplest description of the metals.

Many physical properties of a solid may be directly related to the electronic density of states $D(E)$, such as the Pauli susceptibility, the conduction electron contribution to the specific heat, and so on. The Pauli susceptibility, that measures the response of the free electron gas to an applied magnetic field, is given by

$$\chi_P = \mu_0 \mu_B^2 D(E_F), \tag{1.23}$$

where $D(E_F)$ is the density of states at the Fermi level.

The importance of the effect of low dimensionality on the properties of the conduction electrons can be estimated from the size of the nanoobject relative to the Fermi wavelength. This wavelength can be computed from the expression relating N to k_F (1.11).

$$k_F = \left(\frac{3\pi^2 N}{V} \right)^{1/3}. \tag{1.24}$$

Using the electronic density $n = N/V$, the Fermi wavelength becomes

$$\lambda_F = 2\pi \left(\frac{1}{3\pi^2 n} \right)^{1/3}. \tag{1.25}$$

Therefore, the Fermi wavelength is inversely proportional to $n^{1/3}$, and consequently this wavelength is much larger in semiconductors ($\sim$100 nm) than in the metals ($\sim$0.1 nm). For example, in Fe, the Fermi wavelength is $\lambda_F = 0.37$ nm.

The magnetic moments of the transition element atoms also depend on the dimensionality of the structures where they are found. This dependence is evident in the computed magnetic moments of Ni and Fe for different dimensionalities, given in Table 1.3. The iron magnetic moment, for example, varies from $2.27\,\mu_B$, for a three-dimensional solid, to $4.0\,\mu_B$ for 0D (free atom).

The charge and spin densities near surfaces and interfaces are modified, as is illustrated in Fig. 1.6, where there are shown the computed charge density in the Fe(001) surface of a thin film [21] and the spin density on a Fe(110) surface [12]. It is apparent that the charge and spin densities of the surface atoms are significantly different from the corresponding densities at the inner rows of atoms.

Table 1.3. Computed magnetic moments (in μ_B) and dimensionality for Ni and Fe samples [23]

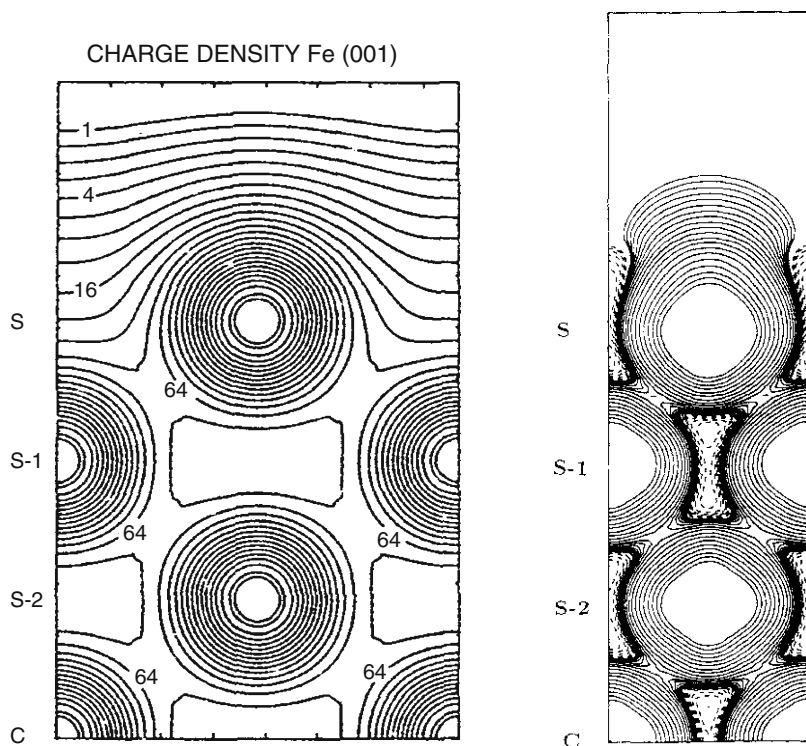| Element	Zero (0D)	One (1D)	Two (2D)	Three (3D)
Ni	2.0	1.1	0.68	0.56
Fe	4.0	3.3	2.96	2.27

CHARGE DENSITY Fe (001)

Fig. 1.6. *Left*: representation of the computed conduction electron charge density at the surface of a seven-layer Fe(001) film; from each line to the next the density varies by a factor of $\sqrt{2}$ [21]. (Reprinted figure with permission from [21]. Copyright (1983) by the American Physical Society); *Right*: total spin density for Fe(110) surface. *Solid* and *dashed lines* indicate positive and negative spin density, respectively [12]. (Reprinted figure with permission from [12]. Copyright (1992) by the American Physical Society)

An additional circumstance that modifies the magnetic properties of nanoscopic systems is the relevance of their immediate neighborhood, or physical systems in close contact. This is the case of magnetic thin films that are deposited on substrates or are covered with protective capping layers. For example, films of Co deposited on Cu(001) have Curie temperatures that vary a few degrees, in an oscillatory way, with the thickness of a Cu capping layer [24].

1.2.2.2 Dimensionality and Reduced Coordination Number

An effect related to the broken translation symmetry at surfaces is that, atoms in these regions have a reduced number of neighbors, as compared to atoms in the bulk of the sample. Let us take as an example of the interface between two regions, one formed of atoms *A* and the other of atoms *B*. The *A* atoms at the interface may have
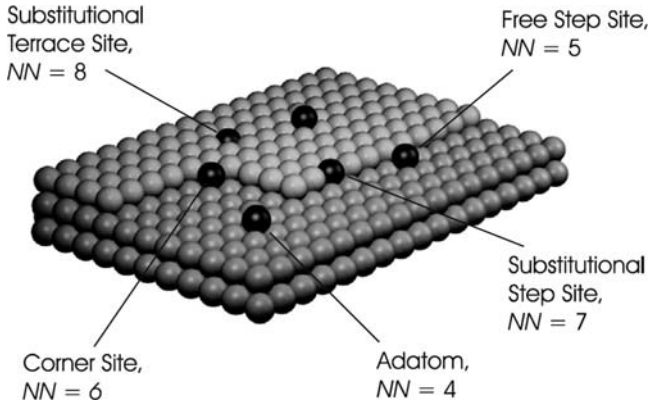
Fig. 1.7. Atomic sites on a thin film showing the different coordination numbers. The number *NN* of nearest neighbors of the atoms on the surface (adatom, *NN* = 4), atom near a step (*NN* = 5), atom in the step (*NN* = 7) and finally, a substitutional atom at the surface (*NN* = 8). (Reprinted with permission from [22])

the same number of nearest neighbors as in the macroscopic sample, but there, of course, they will have a different neighborhood, formed of atoms *A* and *B*.

The atoms at the boundary of the sample, e.g., at the interface sample–vacuum are surrounded by a smaller number of neighbors: they may have one neighbor less, two less, and so on. These surface atoms may be at a plane surface, at the corner of a step, or inside a step. An illustration of these different surroundings is given in Fig. 1.7. The figure shows atoms on different locations of the same surface, atoms with 4, 5, 6, 7, and 8 near neighbor atoms.

In general, the electronic structure of the atoms with a smaller coordination number is different from that of the atoms in the bulk. The density of states shows that the reduction in the coordination number results in a narrowing of the electronic bands (e.g., [5]). This effect is illustrated in Fig. 1.8, with densities of states of bulk metals compared to those of atoms on a (100) surface. For Fe, Co, and Ni, the (100) surface atoms exhibit narrower density of states curves, compared to those of bulk samples of the same materials.

The increasing orbital contribution to the magnetic moment with decreasing dimensionality is made evident from measurements made on Co in Pt, as illustrated on Table 1.4; the increase in anisotropy energy is also apparent.

The atoms located on the interfaces also have the point symmetry at their sites reduced, an effect that leads to level splitting and modification of the magnitude of the atomic magnetic moments. In Fe thin films in contact with Cu, Pd, and Ag, for example, the Fe atoms exhibit enhanced magnetic moments (e.g., [24]).

The magnetic properties of atoms in interfaces are also affected by the presence of defects and impurities, such as adsorbates; strain may also change these properties, and modify the lattice parameters.
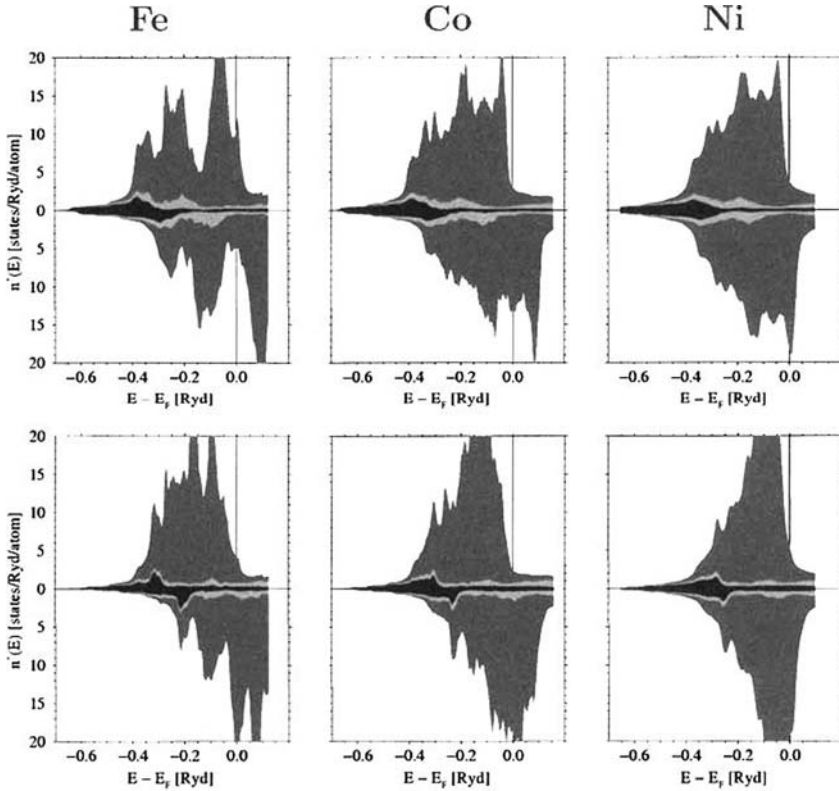
Fig. 1.8. Density of states for Fe, Co, and Ni in bulk metals (*above*) and on a (100) surface (*below*), showing the narrowing of the electronic bands in the latter case. The darkest areas represent the contribution of s electrons, the lightest p, and the intermediate d electrons. (Reprinted with permission from [19])

Table 1.4. Magnetic orbital moment and magnetic anisotropy energy of Co in Pt with different dimensionalities [11]

	Bulk	Monolayer	Diatomic wire	Monoatomic wire	Two atoms	Single atom
Orbital moment (μ_B/atom)	0.14	0.31	0.37	0.68	0.78	1.13
Anisotropy energy (meV/atom)	0.04	0.14	0.34	2.0	3.4	9.2

Also, materials in the form of small particles may present a crystal structure that is different from that observed in bulk samples. This is the case, for example, of metallic cobalt that changes from hcp (hexagonal close packed) to fcc (face centered cubic) for particle diameters below approximately 30 nm.

Table 1.5. Proportion of number of surface atoms in cubic nanoscopic clusters [15]

Number of atoms on each side	Number of surface atoms	Total number of atoms	Ratio of surface atoms to total number
5	98	125	78.5
10	488	1,000	48.8
100	58,800	1×10^6	5.9
1,000	6×10^6	1×10^9	0.6

1.2.2.3 Nanoscopic Samples and Proportion of Surface Atoms

The role of surface atoms is widely utilized in catalysis. Catalysts are usually prepared in the form of finely divided powders, or porous matrices, since their activity relies on the contact of the substances that participate in the chemical reaction with atoms at their surface.

In the study of nanoscopic samples the contribution of the surface atoms to the physical properties increases with decreasing sample sizes. This is obvious, since the area of the surface of the samples varies typically as $\sim r^2$, while the volume of the samples varies as $\sim r^3$. As a consequence, the ratio of surface to volume varies roughly speaking as r^{-1}, therefore increasing with decreasing sample size. This is illustrated with the ratio of surface atoms to total number of atoms in cubic clusters, in Table 1.5. For example, a cube with 10 atoms of side has about half of the atoms on its surface.

The area per unit mass, or specific surface area can be very large: for typical 2 nm spherical particles this may be in the range of hundreds of square meters per gram.

In some limiting cases, as for example, in a thin film formed of only one or two atomic layers, every atom of the sample is a surface atom.

1.2.3 Nanoscopic Samples and Magnetization Reversal

The dynamic behavior of the magnetization of nanomagnets may also be very different from that of macroscopic objects. This arises because, under the usual experimental conditions, thermal fluctuations play in this case a more important role. For example, in nanoscopic magnetic particles it is observed the phenomenon of superparamagnetism: in such particles the magnetization inverts spontaneously, since the thermal energy $k_B T$ is comparable to their anisotropy energy (see Sect. 3.3, p. 68). A single-domain magnetic particle may spontaneously invert its magnetization, i.e., its direction may change from $+z$ to $-z$, if its temperature T is above a certain blocking temperature T_B. This effect has important implications, since if the magnetization of such particle were to be used for information storage, at $T = T_B$ the information would be lost. Therefore, in magnetic storage, with the reduction in physical size of the recorded bit, its thermal stability becomes more and more an important issue.

This phenomenon will be discussed in Chap. 3, which is devoted to magnetic nanoparticles.

1.3 Dimensionality and Critical Behavior

The change in magnetic behavior of the physical systems as a function of dimensionality is also reflected in the critical exponents that appear in the description of the divergences in the neighborhood of their critical temperatures.

Measurements of physical quatities in ferromagnetic samples at temperatures close to the transition temperature T_C – the Curie temperature – exhibit a power law dependence. From this dependence there may be defined critical exponents, or critical indices. We therefore, have for the specific heat C, for the saturation magnetization M_s, for the magnetic susceptibility χ and for the magnetic induction B:

$$
\begin{aligned}
C &\sim |T - T_C|^{-\alpha} \\
M_s &\sim |T_C - T|^{\beta} \quad (T < T_C) \\
\chi &\sim |T - T_C|^{-\gamma} \\
B &\sim M^{\delta} \qquad (T = T_C)
\end{aligned}
$$

The experimentally measured values of the critical exponents for different magnetic systems are $\alpha \sim 0$, $\beta \sim 0.3$, and $\gamma \sim 1 - 2$.

In the Weiss model (mean field) description of ferromagnetism, the magnetization M can be written, in the case of magnetic ions with angular momentum $J = 1/2$, as

$$
M = M_0 B_{1/2}(x) = M_0 \tanh\left(\frac{\mu_B B + \lambda_m M}{k_B T}\right), \qquad (1.26)
$$

where $B_{1/2}(x)$ is the Brillouin function, given by (2.6), on p. 25. This equation can be re-written as

$$
\tanh^{-1}\left(\frac{M}{M_0}\right) = \frac{\mu_B B}{k_B T} + \frac{\lambda_m}{k_B T}M, \qquad (1.27)
$$

where λ_m is the molecular field parameter.

For temperatures close to the critical temperature T_C, the magnetization will be small and we can expand the Brillouin function. From this expansion, one can determine (e.g., [2]) the critical exponents in the case of the mean field model. The exponents in this case are given at Table 1.6, together with values calculated numerically using a high temperature expansion for dimensionality $D = 3$. In general the agreement between the mean field critical exponents and the calculated values increases with increasing dimensionality.

Table 1.6. Critical exponents in the mean field model, and values calculated numerically using a high temperature expansion for three dimensions ($D = 3$) [2]

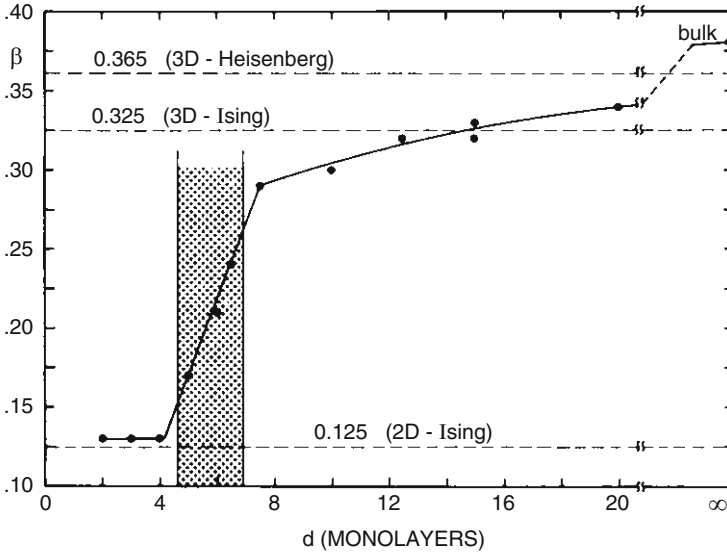| Magnitude	Exponent	Mean field	High T expansion ($D = 3$)
Specific heat	α	0	0.110 ± 0.005
Magnetization	β	$\frac{1}{2}$	0.312 ± 0.003
Susceptibility	γ	1	1.238 ± 0.002
Induction B	δ	3	5.0 ± 0.05

Fig. 1.9. Critical exponent β as a function of thickness, measured in number of monolayers, in thin films of Ni(111) on W(110), showing the transition from a bidimensional to a tridimensional behavior [18]. (Reprinted figure with permission from [18]. Copyright (1992) by the American Physical Society)

Magnetization measurements as a function of temperature in mesoscopic and nanoscopic systems have been used to obtain critical exponents, and from these, verify the change in dimensionality as a function of their diameter, length, thickness and so on. For example, in thin films the transition from bidimensional to tridimensional behavior was observed (Fig. 1.9). For the thinnest samples of Ni films, the observed critical exponent is near 0.325, the value predicted for bidimensional systems (in the Ising model); as the thickness increases, the exponent changes, at about six monolayers, to a value close to that expected for tridimensional physical systems (0.365), in the same model [18]. The same effect was observed in Ni on Cu(111) and Ni on Cu(100) [16].

It is not easy to identify experimentally the effects of change in dimensionality on the magnetic properties of low-dimensional samples. For example, the variation of magnetic ordering temperature T_C of thin films as a function of thickness may be related to the morphology of the films. Clusters may be formed in the process of film growth [24]; percolation of these clusters produces magnetic transitions, and at finite temperatures, smaller islands will exhibit superparamagnetic behavior.

If one atomic magnetic moment changes its direction, it will affect the direction of the moments of the neighbor atoms within a radius r. The correlation length ξ in magnetism can be understood in simple terms as associated to this radius. Another critical exponent relevant to the study of magnetic systems is the exponent ν that enters the expression of the temperature dependence of the correlation length ξ:

$$\xi \sim |T - T_C|^{-\nu}. \tag{1.28}$$

This exponent is related to the shift exponent λ, that appears in the Curie temperature shift in geometrically confined samples. In this case the relation between the Curie temperatures T_C of the low-dimensional system $(T_C(d))$ and T_C of the material in bulk form $(T_C(\infty))$ is:

$$\frac{(T_C(\infty) - T_C(d))}{T_C(\infty)} = \left(\frac{\xi}{d}\right)^{\lambda}. \tag{1.29}$$

In the above equation, d is the thickness of a thin film or the diameter of a particle, and $\lambda = 1/\nu$ is the displacement, or shift exponent, a number between 1.0 and 2.0. In mean field theory $\lambda = 1$, and an estimate in the three-dimensional Heisenberg model obtained $\lambda = 1.419 \pm 0.006$ [6]. An experimental study of maghemite nanoparticles resulted in a value of $\lambda = 1.1 \pm 0.2$ [13].

Further Reading

S.D. Bader, Rev. Mod. Phys. **78**, 1–15 (2006)

X. Batlle, A. Labarta, J. Phys. D: Appl. Phys. **35**, R15–R42 (2002)

J.A.C. Bland, B. Heinrich, (eds.), *Ultrathin Magnetic Structures*, vols I–IV (Springer, Berlin, 2005)

J.F. Bobo, L. Gabillet, M. Bibes, J. Phys. Condens. Matter. **16**, S471–S496 (2004)

C. Chappert, A. Barthelémy, in *Nanomagnetism and Spin Electronics*, ed. by C. Dupas, P. Houdy, M. Lahmany. Nanoscience (Springer, Berlin, 2007), pp. 503–582

C.L. Dennis, R.P. Borges, L.D. Buda, U. Ebels, J.F. Gregg, M. Hehn, E. Jouguelet, K. Ounadjela, I. Petej, I.L. Prejbeanu, M.J. Thornton, J. Phys. Condens. Matter **14**, R1175–R1262 (2002)

A. Enders, P. Gambardella, K. Kern, in *Magnetism of Low-Dimensional Metallic Structures*, ed. by H. Kronmüller, S. Parkin. Handbook of Magnetism and Advanced Magnetic Materials, vol 1 (Wiley, Chichester, 2007), pp. 577–639

M.R. Fitzsimmons, S.D. Bader, J.A. Borchers, G.P. Felcher, J.K. Furdyna, A. Hoffmann, J.B. Kortright, I.K. Schuller, T.C. Schulthess, S.K. Sinha, M.F. Toney, D. Weller, S. Wolf, J. Magn. Magn. Mat. **271**, 103–146 (2004)

O. Fruchart, A. Thiaville, Compt. Rend. Phys. **6**, 921–933 (2005)

C.P. Poole Jr., F.J. Owens, *Introduction to Nanotechnology* (Wiley, Hoboken, 2003)

R. Skomski, J. Phys. Condens. Matter. **15**, R841–R896 (2003)

C.A.F. Vaz, J.A.C. Bland, G. Lauhoff, Rep. Prog. Phys. **71**, 056501–056578 (2008)

References

1. C. Alexiou, R. Jurgons, in *Magnetic Drug Targeting*, ed. by W. Andrä, H. Nowak. Magnetism in Medicine: A Handbook, 2nd edn. (Wiley, Weinheim, 2007), pp. 596–605
2. M. Le Bellac, *Quantum and Statistical Field Theory* (Oxford University Press, Oxford, 1991)
3. J.A.C. Bland, B. Heinrich, *Ultrathin Magnetic Structures* (Springer, Berlin, 2005)
4. V.E. Borisenko, S. Ossicini, *What is What in the Nanoworld* (Wiley, Weinheim, 2004)

5. K.H.J. Buschow (ed.), *Concise Encyclopedia of Magnetic and Superconducting Materials*, 2nd edn. (Elsevier, Amsterdam, 2005)
6. K. Chen, A.M. Ferrenberg, D.P. Landau, Phys. Rev. B **48**, 3249–3256 (1993)
7. M.E. Evans, F. Heller, *Environmental Magnetism* (Academic Press, San Diego, 2003)
8. G. Fleissner, B. Stahl, P. Thalau, G. Falkenberg, G. Fleissner, Naturwissenschaften **94**, 631–642 (2007)
9. P.P. Freitas, H. Ferreira, S. Cardoso, S. van Dijken, J. Gregg, in *Nanostructures for Spin Electronics*, ed. by D. Sellmyer, R. Skomski. Advanced Magnetic Nanostructures (Springer, New York, 2006), pp. 403–460
10. R.F. Freitas, W.W. Wilcke, IBM J. Res. Dev. **52**, 439–447 (2008)
11. O. Fruchart, A. Thiaville, Compt. Rend. Phys. **6**, 921–933 (2005)
12. R. Wu, A.J. Freeman, Phys. Rev. Lett. **69**, 2867–2870 (1992)
13. L. He, C. Chen, N. Wang, W. Zhou, L. Guo, J. Appl. Phys. **102**, 103911–103914 (2007)
14. R. Hergt, W. Andrä, in *Magnetic Hyperthermia and Thermoablation*, ed. by W. Andrä, H. Nowak. Magnetism in Medicine: A Handbook, 2nd edn. (Wiley, Weinheim, 2007), pp. 550–570
15. M. Hosokawa, K. Nogi, M. Naito, T. Yokoyama, *Nanoparticle Technology Handbook* (Elsevier, Amsterdam, 2007)
16. F. Huang, M.T. Kief, G.J. Mankey, R.F. Willis, Phys. Rev. B **49**, 3962–3971 (1994)
17. J. Jorzick, C. Kramer, S.O. Demokritov, B. Hillebrands, B. Bartenlian, C. Chappert, D. Decanini, F. Rousseaux, E. Cambril, E. Sondergard, M. Bailleul, C. Fermon, A.N. Slavin, J. Appl. Phys. **89**, 7091–7095 (2001)
18. Y. Li, K. Baberschke, Phys. Rev. Lett. **68**, 1208–1211 (1992)
19. I. Mertig, in *Thin Film Magnetism: Band Calculations*, ed. by K.H.J. Buschow. Concise Encyclopedia of Magnetic and Superconducting Materials, 2nd edn. (Elsevier, Amsterdam, 2005)
20. S. Odenbach, in *Ferrofluids*, ed. by K.H.J. Buschow. Handbook of Magnetic Materials, vol 16 (Elsevier, Amsterdam, 2006), pp. 127–208
21. S. Ohnishi, A.J. Freeman, M. Weinert, Phys. Rev. B **28**, 6741–6748 (1983)
22. M.J. Prandolini, Rep. Prog. Phys. **69**, 1235–1324 (2006)
23. S.N. Song, J. Ketterson, in *Ultrathin Films and Superlattices*, ed. by R.W. Cahn, P. Haasen, E.J. Kramer. Electronic and Magnetic Properties of Metals and Ceramics, vol 3A (Wiley, New York, 1991)
24. C.A.F. Vaz, J.A.C. Bland, G. Lauhoff, Rep. Prog. Phys. **71**, 056501–056578 (2008)
25. D. Weller, T. McDaniel, in *Media for Extremely High Density Recording*, ed. by D. Sellmyer, R. Skomski. Advanced Magnetic Nanostructures (Springer, New York, 2006), pp. 295–324
26. R. Wiltschko, W. Wiltschko, *Magnetic Orientation in Animals* (Springer, Berlin, 1995)

2

Magnetic Domains

Summary. The existence of magnetic domains arises from the effect of several interactions present in magnetic materials, mainly exchange, anisotropy and dipolar. This chapter deals with some properties of magnetic domains and magnetic domain walls, including the motion of these walls under an applied magnetic field. A short introduction to micromagnetism, an approach to the study of magnetic materials that considers these materials as a continuum, is also given, as well as the origin of some of the characteristic lengths in magnetism.

2.1 Introduction

Magnetic order, observed for example in the parallelism of atomic magnetic moments in a ferromagnetic material, arises essentially from the action of the exchange interaction. The presence of other interactions (anisotropy, dipolar, magnetoelastic) leads to the formation of magnetic domains, regions of the sample where one can consider as a first approximation the moments perfectly ordered. Under an applied magnetic field, the boundaries between these domains – the domain walls – are displaced, changing in consequence the magnetization of the ferromagnet.

The magnetic properties of a magnetic body of nanometric dimensions, as discussed in Chap. 1, are strongly affected by the fact that these dimensions may be comparable to some fundamental lengths, such as the exchange length l_{ex}. Many samples of interest, for example, magnetic nanoparticles, may have dimensions such that a magnetic configuration with one single domain is energetically more favorable. As the diameter of such particles increases above a certain critical value D_{cr}, the lowest energy configuration shifts to an arrangement with more than one magnetic domain, with significant changes in magnetic behavior of the particles; this will be discussed in Chap. 3.

It is important to note that magnetic samples are usually found with domain structures that do not correspond to the state of minimum energy; they are often in metastable states. Also, different domain structures of a sample may correspond to the same value of the magnetization; this is found, for example, in the two branches of the hysteresis curve (see below).

These very brief remarks suggest how important is the study of magnetic domains: their form, the interactions that shape them, their behavior under applied magnetic fields, and so on.

The field of magnetism encompasses the study of the magnetic properties of matter in general, as well as its interaction with magnetic fields. The most interesting materials from the magnetism point of view are those, where atomic magnetic moments μ are present. Systems where these moments exist, although are not ordered, are known as paramagnets, and usually contain atoms of d transition elements (3d, 4d, 5d), lanthanides (4f), and actinides (5f).

The materials where these moments may have a regular orientation, the magnetically ordered materials, or shortly, magnetic materials, present a variety of magnetic structures; in these materials the atomic magnetic moments arrange themselves following a certain spatial order. The main classes of magnetic materials are the ferromagnets, antiferromagnets, and ferrimagnets, defined in terms of the relative orientation and magnitude of the atomic or molecular magnetic moments.

The most important parameters that characterize the magnetic behavior of the materials in an elementary way, are:

1. The magnetization $\mathbf{M}$, defined as the sum of magnetic moments divided by the volume (V):

$$\mathbf{M} = \frac{\sum \mu}{V}. \tag{2.1}$$

The magnetization is measured in the SI in A m^{-1} (amperes per meter).

2. The magnetic susceptibility χ, defined as the magnetization divided by the intensity of the magnetic field:

$$\chi = \frac{|\mathbf{M}|}{|\mathbf{H}|}. \tag{2.2}$$

The magnetic susceptibility is dimensionless.

3. In the case of materials that present spontaneous magnetic order, the ordering temperatures are the highest temperatures for which this order is still found. These are the Curie temperature T_C of the ferromagnets and the Néel temperature T_N for the antiferromagnets and ferrimagnets

4. The magnetic permeability μ, defined as

$$\mu = \frac{|\mathbf{M}|}{|\mathbf{B}|}, \tag{2.3}$$

where $\mathbf{B}$ is the magnetic induction or magnetic flux density or simply $\mathbf{B}$ field; μ is measured in henry per meter (SI). The magnetic induction in matter depends on the magnetic field intensity $\mathbf{H}$ and the magnetization $\mathbf{M}$, and is given by

$$\mathbf{B} = \mu_0(\mathbf{H} + \mathbf{M}), \tag{2.4}$$

where $\mu_0 = 4\pi \times 10^{-7}\,\mathrm{H\,m^{-1}}$ (henry per meter) is the vacuum permeability, or magnetic constant. In vacuum, the expression is reduced to $\mathbf{B} = \mu_0\mathbf{H}$.

The unit of magnetic induction $\mathbf{B}$ is the tesla (T); the quantity $\mathbf{J} = \mu_0\mathbf{M}$, the magnetic polarization is also measured in teslas.

Table 2.1. Magnetic quantities and units. To obtain the values of the quantities in the SI, the corresponding CGS values should be multiplied by the conversion factors

Quantity	Symbol	CGS	SI	Conversion factor
Magnetic induction	**B**	G	T	10^{-4}
Magnetic field intensity	**H**	Oe	$A\,m^{-1}$	$10^3/4\pi$
Magnetization	**M**	$erg\,G^{-1}\,cm^{-3}$ or emu cm^{-3}	$A\,m^{-1}$	10^3
Magnetic polarization	**J**	–	T	–
Magnetic moment	m	erg/G ($\equiv$ emu)	$J\,T^{-1}$ ($\equiv A\,m^2$)	10^{-3}
Susceptibility (volume)	χ	–	–	4π
Magnetic permeability	μ	G/Oe	$H\,m^{-1}$	$4\pi \times 10^{-7}$
Relative permeability	μ_r	–	–	1
Magnetic constant (vacuum permeability)	μ_0	G/Oe	$H\,m^{-1}$	$4\pi \times 10^{-7}$

Table 2.2. Micromagnetic parameters of some materials at room temperature, computed using $\alpha = 0.472$ (see Sect. 2.4.1). They are: the exchange length l_{ex}, the domain wall width δ_0, the critical single-domain diameter D_{cr}, and the domain wall energy density γ [13]

Material	l_{ex} (nm)	δ_0 (nm)	D_{cr} ($10^{-3}\,J\,m^{-2}$)	γ ($10^3\,J\,m^{-2}$)
$Nd_2Fe_{14}B$	2.8	3.82	210	24
$SmCo_5$	5.3	2.64	1,170	57
Sm_2Co_{17}	4.6	5.74	420	31
$BaFe_{12}O_{19}$	8.3	1.94	62	6.3

In the centimeter-gram-second (CGS) system of units, magnetic induction **B** is given by $\mathbf{B} = \mathbf{H} + 4\pi\mathbf{M}$. The unit of **B** is gauss (G) and **H** is oersted (Oe), and the magnetization **M** is measured in erg G^{-1} cm^{-3} (or emu cm^{-3}). The units of magnetism, with the conversion factors, are presented in Appendix A, and the magnetic constants are presented in Appendix B; a short list of units and conversion factors are also given in Table 2.1.

Micromagnetic parameters of some magnetic materials are given in Table 2.2.

The main classes of materials, including diamagnets, paramagnets, ferromagnets, antiferromagnets, and ferrimagnets, can be characterized through the dependence of the magnetization and inverse of the susceptibility as a function of temperature. The behavior of the magnetization and susceptibility of these materials is shown schematically in Fig. 2.1. The values of the Curie temperature and magnetization at $T = 0\,K$ of some materials are presented in Table 2.3.

A simple description of the magnetization of a sample containing paramagnetic ions with total atomic angular momentum J in a magnetic field is given by

$$|\mathbf{M}| = M_0 B_J(x), \tag{2.5}$$

a χ

Pauli paramagnetism
$\chi_{pauli} = \mu_B^2 \, N(E_F)$

Diamagnetism
$\chi_{dia} = \chi_{D,ion} + \chi_{D,band}$

b χ^{-1}

Ideal paramagnetism
$\chi = \dfrac{C}{T}; \; M_s = 0$

$C = \dfrac{N\mu_B^2 g_J^2 \, J(J+1)}{3k_B}$

c χ^{-1}, M

Ferromagnetism
$\chi = \dfrac{C}{T - \Theta_p}; \; \Theta_p = T_C > 0$

$M_s = Ng_J \, J\mu_B \; (T \to 0)$

$\Theta_p = T_C$

d χ^{-1}, M

Antiferromagnetism
$\chi = \dfrac{C}{T - \Theta_p}; \; \Theta_p < 0$

$M_s = 0$

T_N

e χ^{-1}, M

Ferrimagnetism
$\chi^{-1} = \dfrac{T}{C} - \chi_0^{-1} \; (T \gg T_c)$

$M_s = \left| (Ng_J J)_A - (Ng_J J)_B \right| \mu_B (T \to 0)$

$C = C_A + C_B$

T_C

$\chi_0^{-1} = \dfrac{1}{C^2} \left(C_A^2 N_{AA} + C_B^2 N_{BB} + 2C_A C_B N_{AB} \right)$
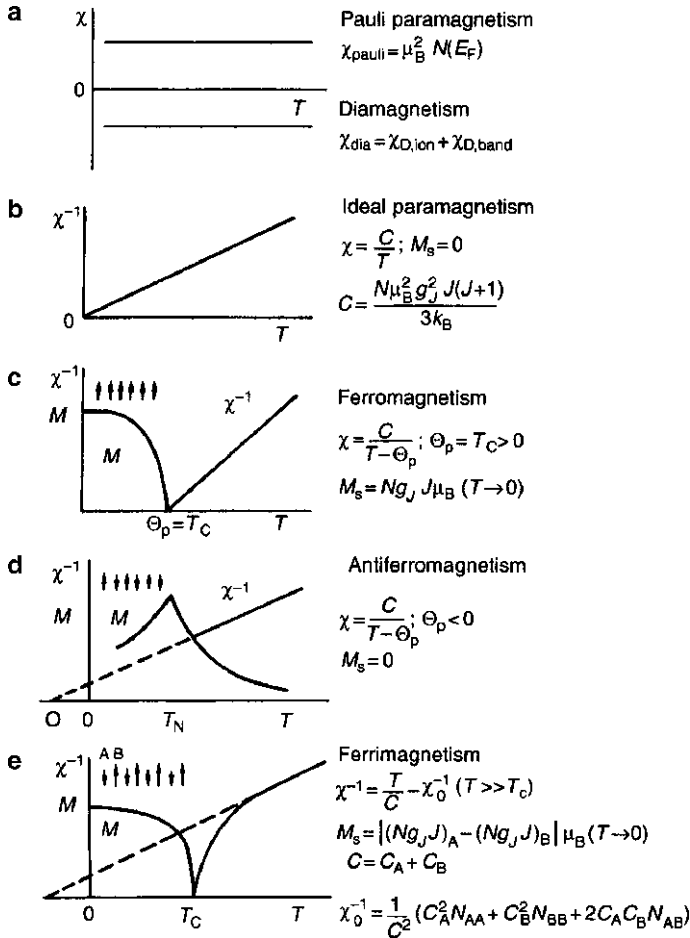
Fig. 2.1. Schematic behavior of the main types of magnetic materials. Temperature dependence of (**a**) susceptibility of a Pauli paramagnet, (**b**) inverse susceptibility of a paramagnet; temperature dependence of magnetization and inverse susceptibility of (**c**) ferromagnet, (**d**) antiferromagnet, (**e**) ferrimagnet [6]. (With kind permission of Springer Science and Business Media [6])

Table 2.3. Magnetic parameters for some elements: Curie temperature T_C and magnetization at low temperature [16]

Material	T_C (K)	M_0 (10^3 Am^{-1})
Fe	1,044	1,766
Co	1,398	1,475
Ni	627	528

where M_0 is the magnetization at $T = 0$ K and $B_J(x)$ is the Brillouin function, derived by assuming the quantization of the total atomic angular momentum J and defined by

$$B_J(x) = \left(1 + \frac{1}{2J}\right)\left[\coth\left(1 + \frac{1}{2J}\right)x\right] - \frac{1}{2J}\coth\left(\frac{x}{2J}\right).\qquad(2.6)$$

The variable x is the ratio of magnetic to thermal energy, given by

$$x = \frac{g\mu_0\mu_B JH}{k_B T},\qquad(2.7)$$

with g the g-factor, $\mu_B = e\hbar/2m_e$ is the Bohr magneton, and H the magnetic field; k_B is Boltzmann constant and T is the absolute temperature.

The Brillouin function also describes, in the limit of high temperature or small x, the behavior of the magnetic susceptibility of paramagnets. In this case, the magnetic susceptibility is given by

$$\chi = \frac{\mu_0 n g^2 \mu_B^2 J(J+1)}{3k_B T} = \frac{C}{T},\qquad(2.8)$$

an expression known as Curie Law, that is represented in Fig. 2.1b. The constant C is the Curie constant, given by

$$C = \frac{\mu_0 n g^2 \mu_B^2 J(J+1)}{3k_B},\qquad(2.9)$$

where n is the number of ions per unit volume.

The atomic magnetic moment is given by

$$\mu_J = -g\mu_B J;\qquad(2.10)$$

note that the atomic magnetic moment is opposite to the angular momentum J.

In the Weiss molecular field model, ferromagnetism arises from the interaction of each atomic magnetic moment with a molecular field that is proportional to the magnetization: $\mathbf{B}_m = \lambda_m \mathbf{M}$, where λ_m is the molecular field constant. Within this model, the ferromagnetic critical temperature, the Curie temperature T_C, is given by

$$T_C = \frac{g^2 \mu_B^2 n \lambda_m J(J+1)}{3k_B}.\qquad(2.11)$$

Above T_C, the susceptibility is given by an expression known as the Curie–Weiss law:

$$\chi = \frac{C}{T - C\lambda_m/\mu_0} = \frac{C}{T - \theta_P},\qquad(2.12)$$

where θ_P is the paramagnetic Curie temperature, also given by the same equation as T_C (2.11) in the Weiss model.

The magnetism of metals is simply described in terms of the itinerant electron model; in the simplest hypothesis, the electrons are regarded as constituting a free

electron gas. The solution of the Schrödinger equation leads to an electronic density of states $D(E)$ for three-dimensional solids (1.15) given by

$$D(E) = \frac{1}{2\pi^2} \left(\frac{2m}{\hbar^2} \right)^{3/2} E^{1/2}. \tag{2.13}$$

The electrons occupy states up to a level known as the Fermi level, of energy E_F, the Fermi energy.

If a magnetic field is applied to this electron gas, the electrons with spin-up and spin-down will have different energies, the sub-bands will have different populations, and as a consequence there will appear a spin magnetic moment per unit volume given by

$$\mu_s = \mu_B (n_\uparrow - n_\downarrow), \tag{2.14}$$

where $n_\uparrow$ and $n_\downarrow$ are, respectively, the number of electrons with spin-up and spin-down. This phenomenon is known as Pauli paramagnetism, and the corresponding magnetic susceptibility is called Pauli susceptibility. This susceptibility is practically temperature-independent, as shown schematically in Fig. 2.1a. The scheme of the electron conduction band split by the applied magnetic field, with different spin-up and spin-down populations, is shown in Fig. 2.2. The sub-band of lower energy has a magnetic moment parallel to the applied field; since this sub-band has more electrons than the other sub-band, it is called the majority spin sub-band. It should be noted that the magnetic moment of the electron is antiparallel to its spin angular momentum:

$$\mu_s = -g\mu_B s, \tag{2.15}$$

where s is the spin angular momentum, μ_B is the Bohr magneton and $g = 2.0023$ is the electron g-factor.

The susceptibility of the free electron gas for $k_B T \ll E_F$ (where E_F is the Fermi energy), i.e., the Pauli magnetic susceptibility χ_P, is proportional to the electron density of states at the Fermi energy, and is given by
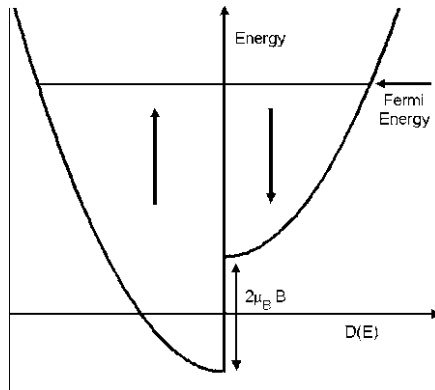
Fig. 2.2. Density of states of a gas of free electrons in three dimensions in a magnetic field B_0. The gas has a magnetization $\mu = \mu_B (n_\uparrow - n_\downarrow)$, where $n_\uparrow$ and $n_\downarrow$ are the number of electrons with spin-up and spin-down per unit volume
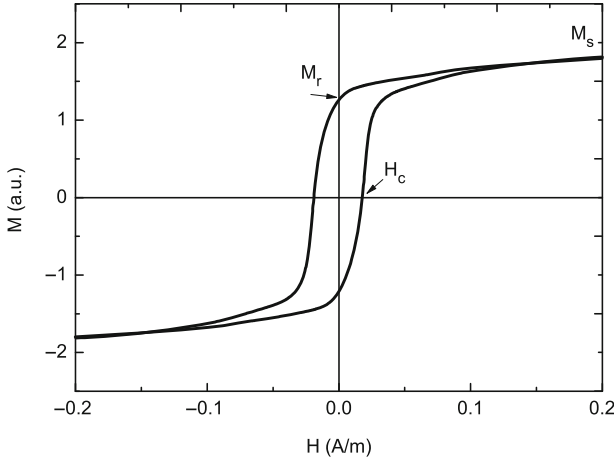
Fig. 2.3. Example of hysteresis curve of a ferromagnetic material, showing some of the parameters that are derived from this curve: the coercive field, or coercivity H_c, the remanent magnetization M_r, and the saturation magnetization M_s

$$\chi_P = \mu_0 \mu_B^2 D(E_F). \tag{2.16}$$

The curve of magnetization vs. magnetic field, drawn by varying the field from H_{max}, a field that saturates a ferromagnetic sample, to $-H_{max}$ and back to H_{max}, is a closed curve, known as hysteresis loop, or hysteresis curve (Fig. 2.3). As the magnetic field is reduced from H_{max} to zero, the magnetization varies from M_s, the saturation magnetization, to a value M_r, the magnetic remanence (or retentivity). The measurement of magnetization with $H = 0$, starting from magnetic saturation, is referred to as measurement at remanence.

The hysteresis curve is used to characterize a ferromagnetic material, and a common curve shape is shown in Fig. 2.3, with the parameters that are normally obtained from it. These parameters are the saturation magnetization M_s, the magnetic coercivity H_c (or coercive field) and the retentivity M_r. To trace the curve starting from the maximum magnetic field $H_{max} > 0$ and reducing it to obtain the negative magnetic field for which $M = 0$ ($H = -H_c$), one finds that the value of this field (H_c) depends on the intensity of the field H_{max}. To distinguish between different situations, H_c is called coercive field or coercivity when H_{max} saturates magnetically the sample, and coercive force when it does not; the same difference is made between the retentivity (from saturation), and the remanence.

The value of the coercive field H_c is a measure of a property known as the magnetic hardness of a material; one can divide the materials into magnetically soft, encompassing broadly materials that have $H_c < 10^3 \, \mathrm{A\,m^{-1}}$, and magnetically hard, for $H_c > 10^4 \, \mathrm{A\,m^{-1}}$. This is the classification of magnetic materials that is more relevant for their applications: soft materials are used as magnetic shields, transformer cores and sensors, and hard magnetic materials are used to make permanent magnets. Examples of soft magnetic materials are permalloy (a magnetic alloy of

typical composition $Ni_{0.8}Fe_{0.2}$), FeSi alloys and soft ferrites; hard magnetic materials include NdFeB, Sm_2Co_{17}, and $SmCo_5$.

The form of the hysteresis curve, specifically the measure of how near to rectangular is its shape, is given by the squareness ratio (or remanence squareness) S, defined as the ratio of the remanence to the saturation magnetization:

$$S = \frac{M_r}{M_s}. \tag{2.17}$$

Another measure of the squareness is the coercive squareness S^*, related to the slope of the magnetization curve at $H = H_c$ and defined through the relation

$$\left(\frac{dM}{dH}\right)_{M=0} = \frac{M_r}{H_c(1 - S^*)}. \tag{2.18}$$

2.2 Interactions in Magnetic Materials

The Gibbs free energy of a ferromagnet is given by

$$\phi = \int_V (U - T \cdot S - \sigma \cdot \varepsilon - \mu_0 \mathbf{M} \cdot \mathbf{H}_{ext}) dV. \tag{2.19}$$

where U is the internal energy, T the temperature, S the entropy, and σ and ε are the strain and stress tensors. The last term describes the interaction of the magnetization with an applied external magnetic field $\mathbf{H}_{ext}$. In the internal energy U are included the energy terms related to the exchange interaction, to the anisotropy, to the dipolar or magnetostatic interaction, and the elastic terms.

The interactions that contribute to the internal energy may be local or non-local, in the sense that they may at a given point depend only on the values of the local magnetization, or else depend on the magnetization at every point of the sample. The exchange energy, the anisotropy energy, the interaction with an external magnetic field, and the magnetoelastic contribution that arises from nonmagnetic effects are all local terms. Nonlocal contributions are the dipolar, or stray field contribution and the magnetostrictive term due to differences in direction of magnetization of different regions of a sample.

2.2.1 Exchange Interaction

The exchange interaction is the interaction responsible for the establishment of magnetic order in magnetic materials. This interaction arises from a quantum effect with no classical analogue, due to the indistinguishability of the electrons. The exchange interaction between two contiguous spins, S_i and S_j, can be described by the hamiltonian

$$\mathcal{H} = -2 \mathcal{J} \mathbf{S}_i \cdot \mathbf{S}_j, \tag{2.20}$$

where $\mathscr{J}$ is the exchange constant, which is a measure of the intensity of the inter-action. This is known as the Heisenberg hamiltonian, and it is widely used for the description of many magnetic properties of materials, particularly insulators.

In the classical description the energy of a pair of spins is

$$E_{\text{ex}}^{\text{pair}} = -2\,\mathscr{J}\,\mathbf{S}_i \cdot \mathbf{S}_j. \tag{2.21}$$

Or, writing the angle between the two spins i and j as $\theta(i,j) = \Delta\theta$,

$$E_{\text{ex}}^{\text{pair}} = -2\,\mathscr{J}\,S^2 \cos\Delta\theta \approx \mathscr{J}\,S^2(\Delta\theta)^2, \tag{2.22}$$

where we have used the approximation $\cos\Delta\theta \approx 1 - (\Delta\theta)^2/2!$, and neglected a term that does not depend on the angle θ.

The interaction energy can also be written as

$$E_{\text{ex}}^{\text{pair}} = -2\,\mathscr{J}\,S_i \cdot S_j = -2\,\mathscr{J}\,S^2 \mathbf{m}_i \cdot \mathbf{m}_j, \tag{2.23}$$

where we have used the reduced magnetization

$$\mathbf{m} = \frac{\mathbf{M}}{M_s}, \tag{2.24}$$

using M_s for the saturation magnetization.

Assuming that the vector $\mathbf{M}$ retains its saturation value, only changing its direction, one has that $|\mathbf{m}| = 1$.

For small $\Delta\theta_{ij}$, $|\Delta\theta_{ij}| = |\mathbf{m}_j - \mathbf{m}_i|$. Assuming that one can introduce a continuous function $\mathbf{m}$, such that $\mathbf{m}$ is expanded around $\mathbf{r}_j$, the position vector of the lattice site j, as:

$$\mathbf{m}_j - \mathbf{m}_i = (\mathbf{r}_j \cdot \nabla)\mathbf{m}, \tag{2.25}$$

where ∇ is the gradient operator, and

$$\mathbf{r}_j = x_j\mathbf{i} + y_j\mathbf{j} + z_j\mathbf{k}, \tag{2.26}$$

it follows, from (2.22),

$$E_{\text{ex}}^{\text{pair}} = \mathscr{J}\,S^2((\mathbf{r}_j \cdot \nabla)\mathbf{m})^2 =$$
$$= \mathscr{J}\,S^2[(\mathbf{r}_j \cdot \nabla m_x)^2 + (\mathbf{r}_j \cdot \nabla m_y)^2 + (\mathbf{r}_j \cdot \nabla m_z)^2]. \tag{2.27}$$

This is the exchange energy of a pair; to get the total energy, one must sum over j and divide by two to avoid counting twice the contribution of the pairs. In cubic symmetry, the sums of the products of the coordinates of $\mathbf{r}$ (i.e., $\sum_j x_i y_j$) is zero, and $\sum_j x_j^2 = \frac{1}{3}\sum_j r_j^2$.

The exchange energy per unit volume is found by dividing by $V = a^3$, in the simple cubic case. In this case $\sum_j r_j^2 = 6a^2$, and we have:

$$\frac{E_{\text{ex}}}{V} = \frac{\mathscr{J}\,S^2}{a}[(\nabla m_x)^2 + (\nabla m_y)^2 + (\nabla m_z)^2]. \tag{2.28}$$

The coefficient in E_{ex} is the exchange stiffness constant A, proportional to the exchange constant $\mathscr{J}$ and measured in J m^{-1} (or erg cm^{-1}, in the CGS); it gives the strength of the magnetic coupling, and therefore measures how difficult it is for a given spin to deviate from the direction of the exchange field. For a cubic lattice with one nonequivalent atom,

$$A = \frac{n \mathscr{J} S^2}{a}. \tag{2.29}$$

The number n is equal to 1 for the simple cubic lattice, 2 for the bcc lattice, and 4 for the fcc lattice.

In the most general case, where the material is not cubic and isotropic, A is a tensor and the exchange energy is

$$E_{\text{ex}} = \int \sum_{i,k,l} A_{kl} \frac{\partial m_i}{\partial x_k} \frac{\partial m_i}{\partial x_l} \mathrm{d}V. \tag{2.30}$$

Another form for the exchange energy is:

$$\frac{E_{\text{ex}}}{V} = A(\nabla\, \mathbf{m})^2 = -A\, \mathbf{m} \cdot \Delta \mathbf{m}, \tag{2.31}$$

where $\Delta \mathbf{m} = \mathbf{div\ grad\ m} = \nabla^2 m_x \mathbf{i} + \nabla^2 m_y \mathbf{j} + \nabla^2 m_z \mathbf{k}$ is the Laplacian[1] of $\mathbf{m}$. This can be derived by applying the gradient operator (∇) twice to the expression $\mathbf{m}^2 = 1$ [12].

One can see from the earlier expression (2.31) that the exchange energy is proportional to the gradient of the magnetization, which means that the exchange term measures the nonuniformity of the magnetization. If the magnetization is uniform, the exchange energy contribution is minimum, and from (2.31) equal to zero.

2.2.2 Magnetostatic Energy

The magnetostatic energy or stray field energy or dipolar energy, is measured by the magnetic energy of a sample in its own magnetic field. This field is the demagnetization or demagnetizing field $\mathbf{H}_{\text{d}}$, the magnetic field arising from the divergence of the magnetization. It is given, using Maxwell's equation $\mathbf{div\ B} = \mathbf{div}\ \mu_0(\mathbf{H} + \mathbf{M}) = 0$ by

$$\mathbf{div\ H_d} = -\mathbf{div\ M}. \tag{2.32}$$

The magnetostatic energy E_{ms}, given by the energy of the magnetization in the demagnetizing field is:

$$E_{\text{ms}} = -\frac{1}{2}\mu_0 \int_V \mathbf{H}_{\text{d}} \cdot \mathbf{M} \mathrm{d}V, \tag{2.33}$$

where the integral is performed over V, the volume of the sample. The factor $\frac{1}{2}$ accounts for the fact that this energy term, also called magnetic self-energy, arises from the interaction of the magnetization with the magnetic field that it creates.

---

[1] $(\nabla M)^2 = \sum_{ik}(\partial M_i/\partial x_k)^2$

Using $\int \mathbf{B} \cdot \mathbf{H}_d dV \equiv 0$, where the integral is over the whole space, an identity valid in the absence of conduction currents, and the expression of $\mathbf{B}$, one obtains:

$$E_{ms} = \frac{1}{2}\mu_0 \int_{\text{all space}} \mathbf{H}_d^2 dV. \tag{2.34}$$

Therefore, there are two equivalent expressions – (2.33) and (2.34) – that can be used to compute the magnetostatic energy.

The magnetostatic energy of samples of ellipsoidal shape is simple to calculate since the magnetic field is the same at every point of the sample. This is also approximately true for sample shapes that are limiting cases of an ellipsoid, such as a thin film or a wire. With no applied external field, this field is the demagnetizing field $\mathbf{H}_d$, given by

$$\mathbf{H}_d = -N_d \mathbf{M}, \tag{2.35}$$

where N_d is the demagnetizing factor that depends on the sample shape (and direction of the magnetization). Some values of the demagnetizing factor for simple shapes are given in Table 2.4. One should bear in mind that in samples with nonellipsoidal shapes the demagnetizing field is not constant throughout the volume.

The magnetostatic energy of an ellipsoid is given, from (2.33), in terms of the demagnetizing factors N_i and the components of the magnetization M_i along the axes a, b, and c by

$$E_{ms} = -\frac{1}{2}\mu_0 V (N_a M_a^2 + N_b M_b^2 + N_c M_c^2). \tag{2.36}$$

This can be simplified in the case of an ellipsoid of rotational symmetry; using the fact that the demagnetizing tensor has trace 1 (in the SI), it follows that $N_\parallel + 2N_\perp = 1$, and one has, using the saturation magnetization M_s:

$$E_{ms} = \frac{1}{2}\mu_0 M_s^2 V (N_\perp \sin^2 \theta + N_\parallel \cos^2 \theta), \tag{2.37}$$

with θ the angle between the direction of magnetization and the rotational symmetry axis of the ellipsoid. This expression is equivalent to

$$E_{ms} = \frac{1}{2}\mu_0 N_\parallel M_s^2 V + \frac{1}{4}\mu_0 M_s^2 V (1 - 3N_\parallel) \sin^2 \theta. \tag{2.38}$$

Table 2.4. Demagnetizing factors N_d (SI); to obtain the values in the CGS system, one has to multiply by 4π

Shape	Direction	N_d
Plane	$\perp$	1
Plane	$\parallel$	0
Cylinder ($l/d = 1$)	$\parallel$	0.27
Cylinder ($l/d = 5$)	$\parallel$	0.04
Long cylinder	$\parallel$	0
Sphere	–	1/3

The general expression of the demagnetizing factors N_a, N_b, and N_c for an ellipsoid, along the semi-axes (a, b, c), is given by integrals of the form

$$N_a = \frac{1}{2}abc \int_0^\infty [(a^2 + \eta)\sqrt{(a^2 + \eta)(b^2 + \eta)(c^2 + \eta)}]^{-1} d\eta, \qquad (2.39)$$

and analogous expressions for the other axes. The sum is $N_a + N_b + N_c = 1$ in the SI system of units, or 4π in the CGS.

For an ellipsoid with rotation symmetry, there are explicit expressions for the demagnetizing factors. For prolate, or cigar-shaped, ellipsoids, with $c > b = a$, with aspect ratio $\alpha = c/a > 1$, one has for the demagnetizing factor for the direction parallel to the long axis [21]:

$$N_c = \frac{1}{\alpha^2 - 1} \times \left[\frac{\alpha}{2(\alpha^2 - 1)^{1/2}} \times \ln\left(\frac{\alpha + (\alpha^2 - 1)^{1/2}}{\alpha - (\alpha^2 - 1)^{1/2}} \right) - 1 \right]. \qquad (2.40)$$

The other factors are $N_a = N_b = \frac{1}{2}(1 - N_c)$; in every case, to obtain the values in the CGS system, these expressions have to be multiplied by 4π.

For an oblate, or disc-shaped, ellipsoid, with $c = b > a$, the demagnetizing factor along the small axis N_a is given by

$$N_a = \frac{\alpha^2}{\alpha^2 - 1} \left[1 - \frac{1}{(\alpha^2 - 1)^{1/2}} \times \arcsin\frac{(\alpha^2 - 1)^{1/2}}{\alpha} \right]. \qquad (2.41)$$

In this case, $N_b = N_c = \frac{1}{2}(1 - N_a)$.

2.2.3 Magnetic Anisotropy

The energy of a magnetically ordered sample depends on the relative direction of the magnetization and the structural axes; in the simplest case, the solid has an axis along which the energy is at a minimum. The magnetic anisotropy may originate from several causes: it may be of crystalline origin, or due to the shape of the sample, or to stress in the material, or atomic segregation, etc.

The anisotropy energy E_A is written as a function of the direction cosines α_1, α_2, and α_3, defined in relation to the axes of the crystal. Since the energy is only a function of the angle with the easy axis, e.g., in the case of uniaxial anisotropy (and does not depend on the direction along this axis), it is invariant when we change the signal of these cosines, and therefore, odd powers of the cosines cannot appear in its expression. Also, the permutations among the cosines must leave the energy E_A invariant.

2.2.3.1 Uniaxial Anisotropy

In some samples one can make the approximation that the anisotropy depends only on the angle θ between the magnetization and a given axis. This typically applies to hexagonal systems, such as crystals of rare-earth metals. The anisotropy energy per unit volume then takes the form

$$\frac{E_A}{V} = K_1 \sin^2 \theta + K_2 \sin^4 \theta, \qquad (2.42)$$

where θ is the angle of the magnetization with the single axis. Depending on the magnitude of the anisotropy constants K_1 and K_2 the sample has an easy axis (for large $|K_1|$, $K_1 > 0$), easy plane (for large $|K_1|$, $K_1 < 0$), and conical in the case of intermediate values of the constants. The anisotropy constants have dimension of energy per volume, and are measured in the SI in J m^{-1} (see Table 2.6).

2.2.3.2 Cubic Crystals

For a cubic crystal, the most general form that the energy may have in terms of the powers of the components of the reduced magnetization m_i (which are equal to the direction cosines) is

$$\frac{E_A}{V} = K_{c0} + K_{c1}(m_1^2 m_2^2 + m_2^2 m_3^2 + m_3^2 m_1^2) + K_{c2}(m_1 m_2 m_3)^2 + \cdots. \qquad (2.43)$$

Substituting into E_A the direction cosines for the directions [100], [110], and [111], symmetry directions in the cubic system, we obtain the expression of the energy for these three cases:

$$\frac{E_{100}}{V} = K_{c0}, \qquad (2.44)$$

$$\frac{E_{110}}{V} = K_{c0} + K_{c1}/4, \qquad (2.45)$$

$$\frac{E_{111}}{V} = K_{c0} + K_{c1}/3 + K_{c2}/27. \qquad (2.46)$$

Since the anisotropy energy for each direction is given by the area between the magnetization curve and the M axis, the anisotropy constants K_{c0}, K_{c1}, and K_{c2} may then be derived from the areas of the curves obtained for each direction.

2.2.3.3 Other Symmetries and Contributions

The anisotropy energy in orthorhombic symmetry is written [11],

$$\frac{E_A}{V} = K_1 m_1^2 + K_2 m_2^2 + K_3 m_3^2. \qquad (2.47)$$

In this expression, m_i are the components of the magnetization along the major axes of the anisotropy tensor K.

There is another contribution to the anisotropy observed in thin films, due to the broken translation symmetry at a surface or an interface, referred to as the surface or interface magnetic anisotropy [20], discussed in Chap. 4.

2.2.4 Magnetoelastic Energy and Magnetostriction

The elastic energy of a magnetic solid has a contribution arising from the interaction between the magnetization and the strains ε_{ij}. The magnetoelastic energy is the

increase in anisotropy energy of a magnetic solid submitted to a stress. Its expression for a cubic crystal is given by [12] as

$$\frac{E_{me}}{V} = B_1(\alpha_1^2\varepsilon_{xx} + \alpha_2^2\varepsilon_{yy} + \alpha_3^2\varepsilon_{zz}) + B_2(\alpha_1\alpha_2\varepsilon_{xy} + \alpha_2\alpha_3\varepsilon_{yz} + \alpha_3\alpha_1\varepsilon_{zx}). \quad (2.48)$$

The B-factors are the magnetoelastic coupling constants and the α_i are the direction cosines.

Magnetostriction is the effect of change of dimensions of a solid as its magnetic state is changed. It is measured by the relative linear deformation λ:

$$\lambda = \frac{\delta l}{l_0}, \quad (2.49)$$

where $\delta l = l - l_0$ is the variation in linear dimension of the solid.

The saturation magnetostriction λ_s, corresponding to a solid magnetized to saturation, is related to the magnetoelastic energy E_{me} in the case of a cubic crystal submitted to a stress σ by

$$\frac{E_{me}}{V} = \frac{3}{2}\lambda_s\sigma\,\sin^2\theta, \quad (2.50)$$

where θ is the angle between the direction of magnetization and the direction along which the magnetostriction is measured.

Different interactions in a magnetic material effectively contribute to its total anisotropy. The total anisotropy energy density can in simple cases be written in terms of an anisotropy constant K_{eff}, as

$$\frac{E_A}{V} = K_{eff}\,\sin^2\theta. \quad (2.51)$$

The terms that contribute to K_{eff}, and the different underlying physical mechanisms are shown in Table 2.5. To illustrate the relative magnitudes of the main energy contributions in magnetic materials, the range of values of these terms is given in Table 2.6.

Table 2.5. Examples of axial anisotropy constants and anisotropy mechanisms [9]

Anisotropy	Mechanism	Uniaxial constant
Crystalline	Crystal field	$K_u = K_1$
Shape	Magnetostatic	$K_u = K_s = \frac{1}{2}\mu_0(N_a - N_c)M_s^2$
Stress	Magnetoelastic	$K_u = K_\sigma = \frac{3}{2}\lambda_s\sigma$
Néel	Surface	$K_u = K_s$

Table 2.6. Magnitude of the main energy terms in magnetic materials, measured by the corresponding parameters or expressions

Energy	Expression	Range	Unit (SI)
Exchange energy	A	$10^{-12} - 10^{-11}$	$J\,m^{-1}$
Anisotropy energy	K_u	$\pm(10^2 - 10^7)$	$J\,m^{-3}$
Magnetostatic energy	$\frac{1}{2}\mu_0 M_s^2$	$0 - 10^6$	$J\,m^{-3}$

2.3 Elements of Micromagnetism

The microscopic description of magnetic materials employs the atomic spins as the relevant physical entities, with interactions that give rise to their measurable macroscopic properties. Another approach, known as Micromagnetism, describes the magnetic medium as a continuum and is centered on the evolution of $\mathbf{M}(\mathbf{r})$ (or the magnetic polarization $J(\mathbf{r}) = \mu_0 \mathbf{M}(\mathbf{r})$), the magnetization of a volume element larger than the atomic dimensions, but much smaller than the sample. It is assumed that each volume element reaches thermodynamic equilibrium in a short time, much shorter than it takes for the whole sample to reach equilibrium.

This is the appropriate treatment to describe magnetized media in a more realistic way, with the static magnetization departing from the idealized homogenous approximation, and the dynamic behavior that deviates from the coherent limit, as described by the Stoner–Wohlfarth model (see Sect. 3.5, p. 79). This approach was developed by Landau and Lifshitz [15], Brown [3, 4], and Kittel [12]. It can be found in an early review by Brown [5] and it is the basis of many computer programs that simulate numerically the static and dynamic properties of magnets in the mesoscopic and nanoscopic scales.

The stationary local magnetization $\mathbf{M}(\mathbf{r})$ at every point of the sample is obtained from the minimization of the total energy functional that contains the exchange energy, the anisotropy energy, and the dipolar energy.

To these terms one must add the Zeeman energy, or the energy of the total magnetic moment in the external magnetic field E_{ext}, given by:

$$\frac{E_{\text{ext}}}{V} = -\mu_0 \mathbf{M} \cdot \mathbf{H}. \tag{2.52}$$

The total energy is then:

$$E_{\text{tot}} = E_{\text{ex}} + E_{\text{A}} + E_{\text{ms}} + E_{\text{ext}}. \tag{2.53}$$

The total energy is given, using (2.31) and writing, for an axial anisotropy energy, $E_{\text{A}}/V = K_1 e_{\text{A}}(\theta)$, by the volume integral

$$E = \int_V \left\{ A \left[\nabla \left(\frac{\mathbf{M}}{M_{\text{s}}} \right) \right]^2 + K_1 e_{\text{A}}(\theta) - \frac{\mu_0}{2} \mathbf{M} \cdot \mathbf{H}_{\text{d}}(M) - \mu_0 \mathbf{M} \cdot \mathbf{H} \right\} dV. \tag{2.54}$$

In terms of $\mathbf{m}$, the reduced magnetization, the energy is written:

$$E = \int_V \left\{ A(\nabla \mathbf{m})^2 + K_1 e_{\text{A}}(\theta) - \frac{\mu_0}{2} M_{\text{s}} \mathbf{m} \cdot \mathbf{H}_{\text{d}}(M) - \mu_0 M_{\text{s}} \mathbf{m} \cdot \mathbf{H} \right\} dV. \tag{2.55}$$

The minimization of the energy functional leads to the condition that $\mathbf{M}(\mathbf{r})$ has to be parallel to the effective magnetic field acting at the point $\mathbf{r}$, a field whose interaction with $\mathbf{M}(\mathbf{r})$ is equivalent to the exchange, anisotropy and magnetostatic

interactions, and to the effect of the external magnetic field. This amounts to the condition that the torque exerted by this effective field acting on the magnetization at each point is zero:

$$\mu_0 \mathbf{m} \times \mathbf{H}_{\text{eff}} = 0. \tag{2.56}$$

The effective field $\mathbf{H}_{\text{eff}}$ acting on $\mathbf{M}(\mathbf{r})$ is obtained by derivation of the energy with respect of the magnetization vector [1], and is given by

$$\mathbf{H}_{\text{eff}} = \frac{2}{\mu_0 M_{\text{s}}} \nabla \cdot (A \nabla \mathbf{m}) - \frac{1}{\mu_0 M_{\text{s}}} \frac{\partial E_A}{\partial \mathbf{m}} + \mathbf{H}_{\text{ms}} + \mathbf{H}_{\text{ext}}, \tag{2.57}$$

with contributions from the exchange interaction, anisotropy, magnetostatic field, and external applied field. E_A is the anisotropy energy density.

Since the component of $\mathbf{H}_{\text{eff}}$ parallel to the magnetization does not contribute to the vector product in (2.56), this equation is equivalent to

$$\mathbf{H}_{\text{eff}}^{\perp} = 0. \tag{2.58}$$

It is assumed in this approach that the saturation magnetization M_{s} is not affected by the parallel component of $\mathbf{H}_{\text{eff}}$.

The energy minimization requires the boundary condition:

$$\mathbf{m} \times \frac{\partial \mathbf{m}}{\partial n} = 0, \tag{2.59}$$

where $\partial/\partial n$ is the derivative in the direction normal to the surface of the sample. Since the modulus of $\mathbf{m}$ is fixed, the above equation is equivalent to

$$\frac{\partial \mathbf{m}}{\partial n} = 0, \tag{2.60}$$

a condition that cannot be fulfilled if there is surface anisotropy.

Equations (2.56) and (2.59) are known as Brown's equations.

The equilibrium condition can be obtained from the variational calculation of $\delta E = 0$, where E is given by (2.54); one then obtains:

$$H_{\text{c}} = \frac{2K_1}{\mu_0 M_{\text{s}}} - N_{\text{eff}} M_{\text{s}} \quad \text{with} \quad N_{\text{eff}} = N_{\|} - N_{\perp}. \tag{2.61}$$

In this equation, N_{eff} is the effective demagnetizing factor. It is assumed here that $K_1 > 0$; otherwise one would express these quantities in terms of $|K_1|$.

The first term in the expression of H_{c} is the anisotropy field H_A:

$$H_A = \frac{2K_1}{\mu_0 M_{\text{s}}}. \tag{2.62}$$

Some magnetic quantities of interest arise from the expression of the total magnetic energy density (2.55). Dividing and multiplying all the terms by $2/(\mu_0 M_{\text{s}}^2)$ one obtains:

$$E = \frac{\mu_0 M_s^2}{2} \int_V \left\{ \frac{2A}{\mu_0 M_s^2} (\nabla \mathbf{m})^2 + \frac{2K_1}{\mu_0 M_s^2} e_A(\theta) - \frac{1}{M_s} m \cdot H_d(M) - \frac{2}{M_s} m \cdot H \right\} dV.$$

(2.63)

The coefficient of the first term is equated to l_{ex}^2, and thus used to define the exchange length l_{ex} (1.2). This is a length characteristic of the magnetic material, and represents the spatial scale below which exchange dominates magnetostatic effects. It is given by

$$l_{ex} = \sqrt{\frac{2A}{\mu_0 M_s^2}}.$$

(2.64)

From the coefficient of the second term of (2.63), one can define the parameter κ. This is called the hardness parameter (or quality parameter (Q)), and it measures the relative importance of anisotropy compared to magnetostatic effects. It is given by

$$\kappa = \frac{2K_1}{\mu_0 M_s^2}.$$

(2.65)

From the expression of the magnetostatic energy (2.34), and the definition of demagnetizing field (2.35) one can see that the magnetic field responsible for the magnetostatic contribution is proportional to M_s. The parameter κ is then the ratio of the uniaxial anisotropy energy (K_1) (2.42) to the magnetostatic energy (($1/2)\mu_0 M_s^2$) (2.37).

The quantities l_{ex} and κ are related through another length, the domain wall width parameter Δ (1.3), given by

$$\Delta = \sqrt{\frac{A}{K_1}} = \frac{l_{ex}}{\sqrt{\kappa}}.$$

(2.66)

The domain wall width parameter is related to the domain wall width δ_0, which will be derived below, and is given by

$$\delta_0 = \pi \sqrt{\frac{A}{K_1}} = \pi \Delta.$$

(2.67)

Another related length is the single-domain critical diameter D_{cr}, the diameter above which the multidomain configuration is energetically more favorable for a magnetic sample:

$$D_{cr} = \frac{72\sqrt{AK}}{\mu_0 M_s^2}.$$

(2.68)

This expression will be derived in Sect. 2.4.1. A summary of the definitions of these characteristic lengths and their values for α-Fe and NdFeB, a soft and a hard magnetic material, are given in Table 2.7.

Tables 2.8 and 2.9 give some values of the single-domain critical diameter D_{cr} for different magnetic materials; in these tables D_{cr} varies from about 5 nm for a soft magnetic material to over 1,000 nm for a hard one.

Table 2.8 gives the saturation magnetization at room temperature, the anisotropy constant, and the exchange stiffness constant A for some 3d metals and for permalloy. Some micromagnetic parameters are also given: the exchange length l_{ex} (from

Table 2.7. Definition of some characteristic lengths (SI), with values, in nanometers, for Fe (Table 2.8) and NdFeB [13]

Length	SI	Material	
		Fe	NdFeB
Exchange length	$l_{\mathrm{ex}} = \sqrt{\frac{2A}{\mu_0 M_s^2}}$	3.28	2.8
Domain wall width parameter	$\Delta = \sqrt{\frac{A}{K_1}}$	20.3	1.22
Domain wall width	$\delta_0 = \pi\sqrt{\frac{A}{K_1}}$	63.7	3.82
Single-domain critical diameter	$D_{\mathrm{cr}} = \frac{72\sqrt{AK}}{\mu_0 M_s^2}$	19.0	210

Table 2.8. Room temperature saturation magnetization $M_s(RT)$, anisotropy constant K and exchange stiffness constant A of some 3d metals and permalloy, from [23], and some micromagnetic parameters. The parameters were computed using (2.64), (2.65), (2.67), (2.68), and (2.97)

Material	$M_s(RT)$ $(10^3 \mathrm{Am}^{-1})$	K $(10^5 \mathrm{Jm}^{-3})$	A $(10^{-11} \mathrm{Jm}^{-1})$	l_{ex} (nm)	δ_0 (nm)	κ	D_{cr} (nm)	γ $(10^{-3} \mathrm{Jm}^{-2})$
Fe	1,714	0.481	1.98	3.28	63.7	0.0261	19.0	3.90
Co	1,422	4.12	2.81	4.70	25.9	0.324	96.4	13.6
Ni	484.1	−0.056	0.86	7.64	123	0.038	53.6	0.878
Ni$_{0.8}$Fe$_{0.2}$	813	0.0027	1.07	5.08	625	0.0007	4.66	0.215

Table 2.9. Critical single-domain diameter D_{cr} for spherical particles, and domain wall energy per unit area γ for different materials [13]

Material	$\mu_0 M_s^2$ $(10^6 \mathrm{Jm}^{-3})$	D_{cr} (nm)	Domain wall energy γ $(10^{-3} \mathrm{J\,m}^{-2})$
Fe$_3$O$_4$	0.29	12.4	2.0
CrO$_2$	0.20	180	2.0
MnBi	0.45	480	12
Nd$_2$Fe$_{14}$B	2.06	210	24
SmCo$_5$	0.88	1,170	57
Sm$_2$Fe$_{17}$	1.33	420	31
FePt	1.44	340	32
BaFe$_{12}$O$_{19}$	0.183	62	6.3

(2.64)), the domain wall width δ_0 (2.67), the hardness parameter κ (2.65), the critical single-domain diameter D_{cr} (2.68) and the Bloch domain wall energy γ (2.97). One should note that the values of the micromagnetic parameters that appear in the literature present a wide dispersion, reflecting the experimental uncertainty of some magnetic quantities, for example, in the estimate of the exchange stiffness constant A. The values of A given in Table 2.8 are obtained from inelastic neutron scattering data,

Table 2.10. Expressions of some magnetic quantities in the SI and CGS. Note that $N_d^{CGS} = 4\pi N_d$. The domain wall energy is $\gamma = 4\sqrt{AK}$ in either system

Length	SI	CGS
Exchange length	$l_{ex} = \sqrt{\dfrac{2A}{\mu_0 M_s^2}}$	$l_{ex} = \sqrt{\dfrac{2A}{4\pi M_s^2}}$
Single-domain critical diameter	$D_{cr} = \dfrac{72\sqrt{AK}}{\mu_0 M_s^2}$	$D_{cr} = \dfrac{72\sqrt{AK}}{4\pi M_s^2}$
Magnetostatic energy	$E_{ms} = \frac{1}{2}\mu_0 N_d M_s^2$	$E_{ms} = \frac{1}{2}N_d^{CGS} M_s^2$
Anisotropy field	$H_A = \dfrac{2K}{\mu_0 M_s}$	$H_A = \dfrac{2K}{4\pi M_s}$
Hardness parameter	$\kappa = \dfrac{2K}{\mu_0 M_s^2}$	$\kappa = \dfrac{2K}{4\pi M_s^2}$

Table 2.11. Units used for some micromagnetic quantities, and conversion factors between the SI and CGS systems of units

	Symbol	Unit	Equivalence
Saturation magnetization	M_s	$A\,m^{-1}$	($1\,A\,m^{-1} = 10^{-3}$ emu cm^{-3})
Anisotropy constant	K	$J\,m^{-3}$	($1\,J\,m^{-3} = 10$ erg cm^{-3})
Exchange stiffness	A	$J\,m^{-1}$	($1\,J\,m^{-1} = 10^5$ erg cm^{-1})
Domain wall energy	γ	$J\,m^{-2}$	($1\,J\,m^{-2} = 10^3$ erg cm^{-2})

regarded as more reliable than those obtained from other techniques, for example, from the measurement of the Curie temperatures.

The relative values of the characteristic lengths change as a function of the degree of magnetic hardness of the materials. For soft magnetic materials, one has

$$D_{cr} \sim l_{ex} \ll \Delta, \tag{2.69}$$

and for hard magnetic materials,

$$D_{cr} \gg l_{ex} \gtrsim \Delta. \tag{2.70}$$

Table 2.10 gives the expressions of some micromagnetic quantities in both systems of units, SI and CGS. The units used to express these quantities, and the conversion factors between the two systems of units, are given in Table 2.11.

For other conversion factors, see Table A, on p. 187, part of Appendix A.

2.3.1 Equation of Motion

The equation of motion of the magnetization **M** in an applied magnetic field is determined by the fact that the electrons, responsible for the magnetism of atoms and molecules, also have angular momentum, collinear with their magnetic moments. Therefore, the magnetization **M** precesses in an applied magnetic field, and the torque exerted by this field is $-\gamma_e \mathbf{M} \times \mu_0 \mathbf{H}$, where γ_e is the electron gyromagnetic

ratio and μ_0 is the magnetic constant, or vacuum permeability. Thus, the equation of motion for the magnetization, in the absence of damping or relaxation, is given by

$$\frac{d\mathbf{M}}{dt} = -\gamma_e \mathbf{M} \times \mu_0 \mathbf{H} = -\gamma_G \mathbf{M} \times \mathbf{H}. \tag{2.71}$$

The constant γ_G is the Gilbert gyromagnetic ratio, a positive number, proportional to the electron gyromagnetic ratio γ_e. The latter is given, in the SI system of units by $\gamma_e = \frac{2\mu_e}{\hbar} = 1.760859 \times 10^{11} \, \mathrm{s}^{-1} \, \mathrm{T}^{-1}$ [18]. The Gilbert gyromagnetic ratio is therefore:

$$\gamma_G = \mu_0 \gamma_e = 2.2127606 \times 10^5 \, \mathrm{m \, A}^{-1} \mathrm{s}^{-1}. \tag{2.72}$$

Equation 2.71 describes a motion of precession of $\mathbf{M}$ around the direction of $\mathbf{H}$; this field cannot vary the component of the magnetization parallel to it. This description is applicable to isolated magnetic moments, i.e., magnetic moments that do not interact, or interchange energy with another sub-system, that would act as a thermal reservoir. This assembly of magnetic moments will only change its magnetization, reaching another equilibrium configuration, if there is a mechanism for this interchange. In this case, the corresponding mathematical description would include damping, or magnetic relaxation. A phenomenological description that contains such damping, is the Gilbert equation:

$$\frac{d\mathbf{M}}{dt} = -\gamma_G \mathbf{M} \times \mathbf{H} + \frac{\alpha_G}{M_s} \mathbf{M} \times \frac{d\mathbf{M}}{dt}, \tag{2.73}$$

where α_G is the Gilbert damping constant, a dimensionless parameter, and γ_G is the Gilbert gyromagnetic ratio.

Another description of the motion of the magnetization $\mathbf{M}$ that does not have the inconvenience of containing $d\mathbf{M}/dt$ in both sides of the equation is the Landau–Lifshitz–Gilbert equation, that is mathematically equivalent, but has a relaxation term with a different form. This equation can be derived from the above, and is written:

$$\frac{d\mathbf{M}}{dt} = -\gamma \, \mathbf{M} \times \mathbf{H}_{\mathrm{eff}} + \frac{\alpha}{M_s} \, \mathbf{M} \times (\mathbf{M} \times \mathbf{H}_{\mathrm{eff}}). \tag{2.74}$$

The phenomenological damping constants (the α terms) and the gyromagnetic ratios used in the two equations are related through:

$$\gamma = \frac{\gamma_G}{1 + \alpha_G^2}. \tag{2.75}$$

$$\alpha = \frac{\alpha_G \gamma_G}{1 + \alpha_G^2}. \tag{2.76}$$

sometimes written as γ_L and α_L.

The Landau–Lifshitz–Gilbert (LLG) equation allows one to describe how the magnetization evolves with time. The time evolution of the magnetization of a sample is given by solving a set of coupled Landau–Lifshitz–Gilbert equations, each one corresponding to an element of volume into which the sample is divided. The solution of the LLG equations is usually done numerically.

In the description of the magnetization dynamics in a metal, eddy currents are important. Their effect can be approximately accounted for by adding to $\mathbf{H}_{\text{eff}}$ a term $\mathbf{H}_{\text{eddy}}$, that is proportional to $\partial\mathbf{m}/\partial t$.

2.4 Magnetic Domains

Why every sample of magnetic material is not necessarily a magnet? The explanation, of course, is that macroscopic samples of magnetic materials are formed of magnetic domains, regions where the atomic magnetic moments point approximately in the same direction. The presence of domains with different directions may lead to an approximate cancellation of the total magnetic moment, or to an average magnetization close to zero.

The division of the volume of a sample into magnetic domains arises from the balance of the contributions of the different energy terms.

As the number of domains is increased, the magnetostatic energy is reduced. This cannot continue indefinitely, since the presence of the transition region between the domains, the domain walls, also brings about an increase in exchange and anisotropy energy. The magnetostatic energy can also be reduced through the formation of closure domains, where the magnetization has a direction approximately parallel to the surface of the sample. This result is one of the consequences of the principle known as pole avoidance. It expresses the fact that the reduction of the number of free magnetic poles leads to lower magnetostatic, or stray energy.

Single domains deviate from the ideal image of a region where the magnetization is exactly the same at every point. This arises since the demagnetizing field H_{d} varies from point to point in every sample that has a nonellipsoidal shape, and as a consequence the equilibrium configuration of the magnetic moments in such samples also deviates from homogeneity. These samples are still described as single-domain samples, and this denomination is extended to every magnetic object that does not have clearly defined domain walls. For example, single domains may exhibit some distinctive spin arrangements, which include the "flower," "leaf," and "C" configurations, shown schematically in Fig. 2.4.

The form of the magnetic domains can be given in an approximate way making use of the van den Berg construction. This consists of the following set of rules
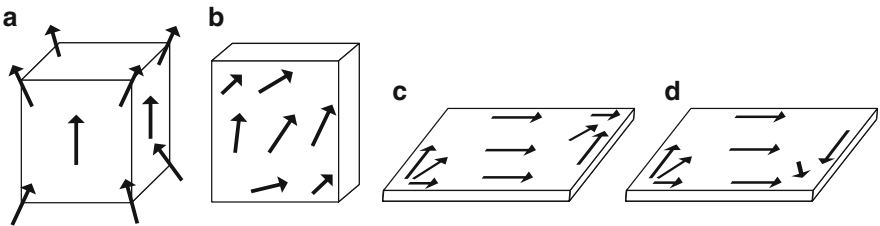
Fig. 2.4. Schematic representation of the types of spin arrangement in single domains: (**a**) flower, (**b**) leaf, (**c**) S, and (**d**) C (Adapted from [7])
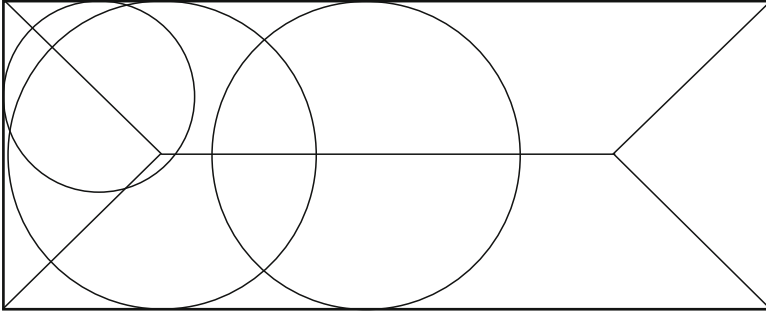
Fig. 2.5. Example of van den Berg construction of magnetic domains for a bidimensional soft magnet of rectangular shape. The *straight lines* represent the magnetic domain walls

applied here to a two-dimensional sample [11]: (1) draw circles that are contained in the sample and are tangential at two or more points of the edge. The locus of the centers of the circles forms the domain walls; (2) the magnetization in each circle is perpendicular to the radius that touches the edge; (3) if a circle has more than two points of contact with the edge, its center forms a junction of walls; (4) if the tangential points are neighbors, the wall ends at the center of the circle; and (5) if the sample has an acute edge, the wall passes through this point. The application of these rules and the resulting structure of domains for a bidimensional magnetic sample of rectangular shape, is shown in Fig. 2.5.

The van den Berg construction incorporates a tendency observed in magnetic samples, of the appearance of domain structures that minimize stray fields, or produce flux closures, leading to a reduction in magnetostatic energy or magnetic dipole energy.

The van den Berg construction does not take into account the scale or size of the sample; also, the domain walls are simple lines. In real samples, however, the domain wall has a finite width that becomes relatively more important the smaller their sizes. Also, a flux closure structure known as a vortex or swirl, a static circular arrangement of magnetic moments, results as this construction is applied to samples of circular or near circular shapes.

Domain walls can have many different forms; there are, however, two main types known as Bloch walls and Néel walls. They are distinguished from one another in the way the atomic magnetic moments in the wall turn: perpendicularly to the plane of the moments in contiguous domains, in the case of Bloch domain walls, or parallel to this plane (Néel wall). These two arrangements are illustrated in the case of a 180° magnetic domain wall in Fig. 2.6.

2.4.1 Domain Wall Width

The magnetic domain wall width can be computed in an approximate way taking into account only the exchange and anisotropy interactions. Two adjoining domains, with the corresponding magnetizations forming 180°, will be separated by a transition region – a 180° domain wall. Inside the wall the atomic moments will make

a

b
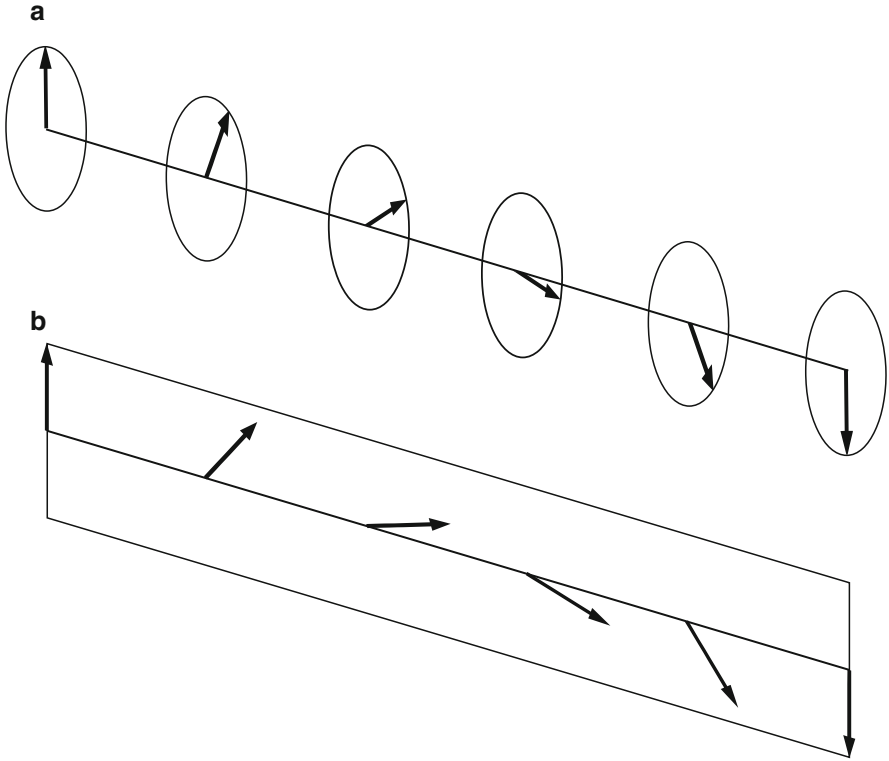
Fig. 2.6. Two main types of magnetic domain walls, exemplified for a $180°$ wall: (**a**) Bloch wall, where the magnetic moments turn in a plane perpendicular to the line connecting the two domains, and (**b**) Néel wall, where the moments in the wall are confined to the same plane of the moments in the domain

intermediate angles with the initial axis; let us assume that the first domain has its moment pointing in the $+z$ direction and the second, in the $-z$ direction. The closer to parallelism the neighbor magnetic moments in the wall are, the lower the exchange energy; this favors a broad domain wall. On the other hand, the smaller the number of atoms in the wall, the smaller the anisotropy energy, since each magnetic moment pointing away from the z axis will pay a price in anisotropy energy. Consequently, to minimize the anisotropy energy, it is preferable to have a narrow domain wall. These conflicting demands lead to a balance of energy contributions from exchange and anisotropy that defines the wall configuration with lowest energy.

Let us consider a $180°$ Bloch domain wall of a simple cubic material; the $N+1$ magnetic moments in the wall are represented in Fig. 2.7. The average value of the angle ϕ between two neighbor moments inside the wall is π/N. The exchange interaction energy of one pair of atoms, from (2.22) and (2.29), is $E_{\text{ex}}^{\text{pair}} = \mathscr{J} S^2 (\pi/N)^2 = aA(\pi/N)^2$, in the simple cubic lattice. $\mathscr{J}$ is the exchange integral, A is the exchange stiffness constant, and a is the lattice parameter, or atomic separation.
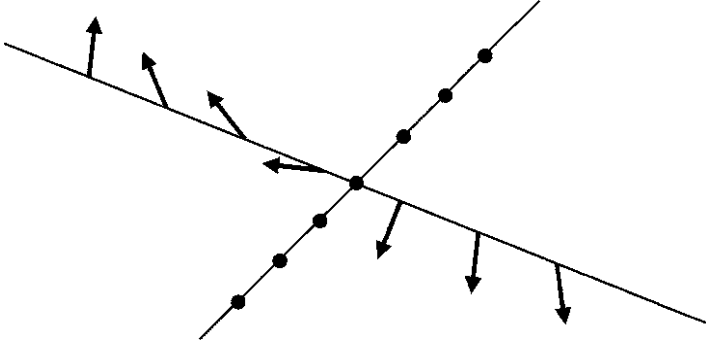
Fig. 2.7. Magnetic moments inside a 180° Bloch magnetic domain wall perpendicular to a line with $N+1$ atoms

A line of $N+1$ neighbor atoms, perpendicular to the plane of this wall, has an exchange energy given by

$$E_{ex} = NE_{ex}^{pair} = \frac{\pi^2 aA}{N}. \tag{2.77}$$

From this expression, one verifies that the condition for minimum exchange energy E_{ex} is that N grows indefinitely; however, in this case the anisotropy energy increases, since the number of spins not aligned with the easy direction also increases. If the separation between the atoms is a, a unit length of the wall is crossed by $1/a$ lines of atoms; one unit area of wall is crossed by $1/a^2$ lines. The exchange energy per unit area is therefore

$$e_{ex} = \frac{\pi^2 A}{aN}. \tag{2.78}$$

The anisotropy energy per unit volume in a uniaxial crystal is $E_A/V = K_1 \sin^2 \theta$ (taking only the first term of the uniaxial anisotropy energy expression given by (2.42)). Since a domain wall of unit area has a volume Na, the anisotropy energy per unit area is

$$e_A = K_1 \overline{\sin^2 \theta} Na \approx K_1 Na. \tag{2.79}$$

The total energy per unit area is $e = e_{ex} + e_{K_1}$ (exchange plus anisotropy), and the condition that minimizes e is

$$\frac{\partial e}{\partial N} = -\frac{\pi^2 A}{aN^2} + K_1 a = 0, \tag{2.80}$$

and the number N of atomic spacings in the domain wall that satisfies this condition is

$$N = \frac{\pi}{a}\sqrt{A/K_1}. \tag{2.81}$$

Therefore, the domain wall thickness is

$$\delta_0 = Na = \pi\sqrt{\frac{A}{K_1}}. \tag{2.82}$$

In conclusion, the domain wall thickness is directly proportional to the square root of the exchange stiffness constant, and inversely proportional to $\sqrt{K_1}$.

Since $|\mathbf{m}|=1$, then $dm^2=d\theta^2 + (\sin\theta d\phi)^2$, and the exchange energy term becomes:

$$e_{\text{ex}} = A(\nabla\mathbf{m})^2 = A\left[\left(\frac{\partial\mathbf{m}}{\partial y}\right)^2\right] = A\left[\left(\frac{\partial\theta}{\partial y}\right)^2 + \left(\sin\theta\frac{\partial\phi}{\partial y}\right)^2\right]. \tag{2.83}$$

The total energy density, containing contributions of exchange, anisotropy, magnetostatic energy arising from magnetic charges on the domain wall plane (plane xz) and Zeeman interaction is $e = e_{\text{ex}} + e_{\text{A}} + e_{\text{ms}} + e_{\text{ext}}$,

$$e = e_{\text{ex}} + \left(K + \frac{\mu_0}{2}M^2\sin^2\phi\right)\sin^2\theta - \mu_0 MH\cos\theta. \tag{2.84}$$

The condition for equilibrium is that, the combined torque from exchange and anisotropy is zero. This is mathematically equivalent to the condition that $\int e\,dy$ is stationary with respect to variations of $\theta(y)$ and $\phi(y)$, which is given by the Euler–Lagrange equations, expressed through the variational or functional derivatives $\delta e/\delta X$ [17]:

$$\frac{\delta e}{\delta\theta} = \frac{\partial e}{\partial\theta} - \frac{\mathrm{d}}{\mathrm{d}y}\frac{\partial e}{\partial\theta'} = 0 \tag{2.85}$$

and

$$\frac{\delta e}{\delta\phi} = \frac{\partial e}{\partial\phi} - \frac{\mathrm{d}}{\mathrm{d}y}\frac{\partial e}{\partial\phi'} = 0. \tag{2.86}$$

This leads to the following equations, ignoring the magnetostatic and the Zeeman terms:

$$2A\left(\frac{\partial^2\theta}{\partial y^2}\right) - \left[K + A\left(\frac{\partial\phi}{\partial y}\right)^2\right]\sin 2\theta = 0. \tag{2.87}$$

$$\left(\frac{\partial^2\phi}{\partial y^2}\right)\sin^2\theta + \left(\frac{\partial\phi}{\partial y}\right)\left(\frac{\partial\theta}{\partial y}\right)\sin 2\theta = 0. \tag{2.88}$$

A solution is

$$\phi(y) = const., \tag{2.89}$$

which leads to

$$2A\left(\frac{\partial^2\theta}{\partial y^2}\right) - K\sin 2\theta = 0. \tag{2.90}$$

Multiplying by $\partial\theta/\partial y$ and using the condition that for $x\to\infty$, $\theta = 0$ or π, the integration gives

$$\theta(y) = \pm 2\arctan e^{(y/\Delta)}. \tag{2.91}$$

With

$$\Delta = \sqrt{\frac{A}{K}}, \tag{2.92}$$

the domain wall width parameter.

The occurrence of a positive and a negative sign in (2.91) means that there are Bloch walls that turn in clockwise or counterclockwise directions. When lines of

opposite direction of rotation occur side by side in a three-dimensional sample, their boundary is a Bloch line. The existence of such a line has as consequence a reduction in stray field energy.

Deriving (2.91), one obtains:

$$\Delta \frac{\partial \theta}{\partial y} = \pm \sin \theta. \tag{2.93}$$

The square of this expressions gives

$$A \left(\frac{\partial \theta}{\partial y} \right)^2 = K \sin^2 \theta. \tag{2.94}$$

The above equation expresses the fact that at each point inside the domain wall the exchange and anisotropy energies have the same magnitude.

Defining the domain wall width as the width of the region around $x = 0$, where the magnetization would turn π if the dependence of $\theta(x)$ were linear, with the same slope of $\theta(x)$ for $x = 0$ (Fig. 2.8), one finds

$$\delta_0 = \pi \sqrt{\frac{A}{K_1}}. \tag{2.95}$$

Another expression sometimes used for the domain wall width is $\delta_0 = 2\sqrt{A/K_1}$.

Figure 2.8 shows the dependence of θ with x around the center of the domain wall. Substituting the result of (2.94) into the expression of the energy functional, and using dy from the square root of this equation, one obtains the energy density inside the domain wall:

$$e(y)dy = 2K_1 \sin^2 \theta dy = 2\sqrt{AK_1} \sin \theta d\theta. \tag{2.96}$$
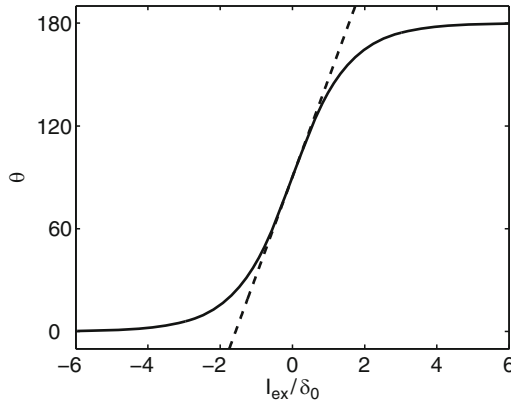
Fig. 2.8. Variation of the angle θ around the center of a Bloch domain wall, showing the linear extrapolation that leads to the value of the domain wall width δ_0

The total domain wall energy density γ is twice the integral of $e(y)\mathrm{d}y$ from $\theta = 0$ to $\theta = \pi/2$; the expression for the domain wall energy density (energy per unit area) is therefore,

$$\gamma = 4\sqrt{AK_1}. \tag{2.97}$$

The wall energy density therefore increases with the increase of both exchange energy and anisotropy energy. Domain wall energy densities vary from about 0.1 $\times 10^{-3}\,\mathrm{Jm^{-2}}$ for magnetically soft materials to some tens of $10^{-3}\,\mathrm{Jm^{-2}}$ for hard magnets. Transition metals of the d group exhibit wall energy densities of the order of $10^{-3}\,\mathrm{Jm^{-2}}$.

In a Bloch wall, the angle ϕ between the plane containing the magnetization and the plane defined by the magnetizations of the domains M_1 and M_2 (the plane xz) is constant, equal to $\pi/2$ (Fig. 2.9). In a Néel domain wall, $\phi = 0°$, and the magnetic moments inside the wall are contained in the plane xz. In this type of wall, the magnetostatic energy contribution is more relevant, since the uncompensated magnetic charges in the domain wall all add up along the axis of the domain, the x direction in Fig. 2.9. This energy term can be derived from div $\mathbf{B} = 0$; it then follows

$$\frac{\mathrm{d}H_x}{\mathrm{d}x} = -\frac{\mathrm{d}M_z}{\mathrm{d}x} = -M_s\frac{\mathrm{d}(\cos\theta)}{\mathrm{d}x}. \tag{2.98}$$

The integration gives $H_x = -M_s(\cos\theta - \cos\theta_0)$, where θ_0 is half the total angle variation across the domain wall. The magnetostatic energy is therefore

$$e_{ms} = -\frac{1}{2}\mu_0 M_s^2 \cos\theta. \tag{2.99}$$
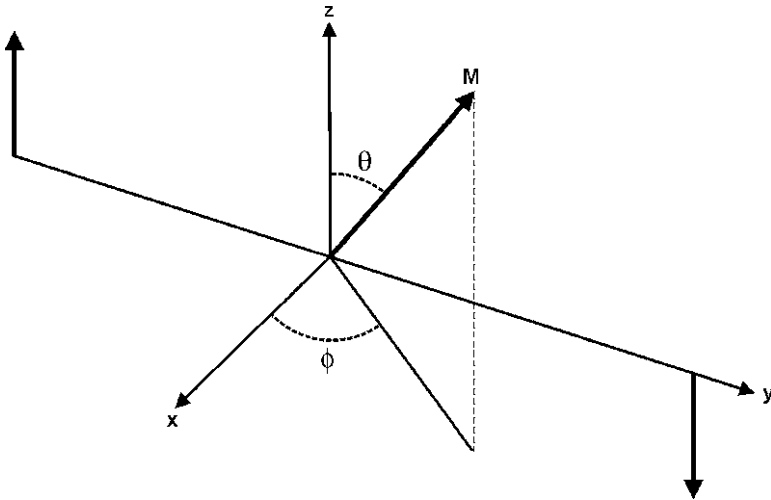
Fig. 2.9. Angles characterizing the direction of the magnetization $\mathbf{M}$ inside a 180° domain wall. The two adjacent magnetic domains have magnetizations in the $+z$ and $-z$ directions, and the plane of the domain wall is the plane xz

The energy minimization allows the derivation of the parameters that characterize the Néel domain walls [14]. The Néel domain wall width is given by

$$\delta_0^{N\acute{e}} = \pi \sqrt{\frac{A}{K_1 + \frac{1}{2}\mu_0 M_s^2}}. \tag{2.100}$$

The Néel domain wall energy density is

$$\gamma^{N\acute{e}} = 4\sqrt{A\left(K_1 + \frac{1}{2}\mu_0 M_s^2\right)}. \tag{2.101}$$

Both expressions exhibit the importance of the magnetostatic contribution to the properties of the Néel domain wall; these results contrast with the corresponding expressions for the Bloch walls, given by (2.95) and (2.97), that do not depend on the saturation magnetization M_s.

In inhomogeneous solids, where, for example, the anisotropy constant K_1 may change from point to point, the domain wall energy density will also vary. As a consequence, the mobility of the domain wall will be affected, since the inhomogeneities will become pinning centers for the walls. The domain walls will prefer to reside in the lower anisotropy regions, where the energies will be lower, and, conversely, they will require higher magnetic fields to move across regions of higher anisotropy.

The single-domain critical diameter D_{cr}, the cross-over diameter below which a single-domain configuration is energetically more favorable, can be derived from the analysis of the free energy of different spin configurations. This can be done, for instance, in the case of a sample in the form of an ellipsoid. Let us consider two magnetization configurations for an ellipsoidal sample (Fig. 2.10): (1) single domain and (2) two domains separated by a domain wall. In both cases the magnetizations
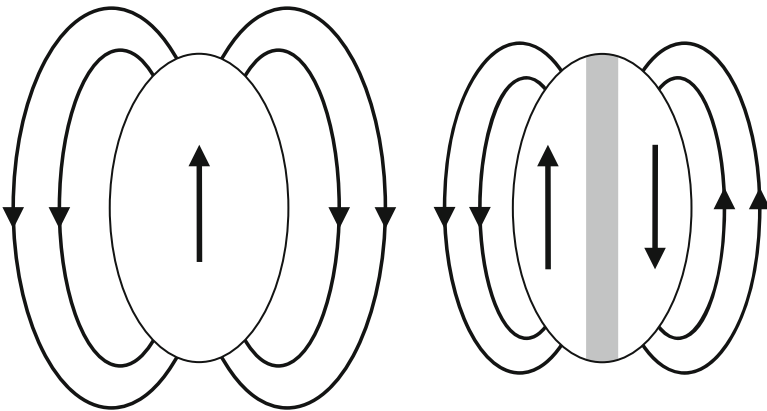
Fig. 2.10. Single-domain and two-domain configurations of a magnetically ordered ellipsoid, showing the magnetic moments of the domains, the lines of field, and in the second case, the domain wall

of the domains are aligned along the major axis of the ellipsoid. The question is to find out for which diameter (the critical diameter) these two configurations will have the same free energy.

This problem will be revisited in Chap. 3 (Sect. 3.1), where another spin arrangement – a vortex – will be considered as another possible structure leading to an energy minimum.

The terms contributing to the total energy of the magnetic ellipsoid will be exchange, anisotropy and magnetostatic. The magnetoelastic contribution will not be taken into account in this simple derivation. As mentioned earlier, the magnetostatic energy can be expressed in two forms, either as an integral over the whole space or as an integral limited to the volume of the magnetized body (2.34) and (2.33). Since the first form is an integral in the whole space, it has contributions away from the sample that for large distances are essentially those of a magnetic dipole field. These contributions can be neglected in the case of the arrangement with two domains, since the sample has in this case zero total magnetic moment. We assume then that the total magnetostatic energy in this case is reduced, multiplied by a factor $\alpha < 1$.

The magnetostatic term of a sample with the shape of an ellipsoid with rotational symmetry, with short semi-axis a, long semi-axis b, in the single-domain configuration, will be

$$E(1) = E_{\mathrm{ms}}(1) = -\frac{1}{2}\mu_0 \mathbf{H_d} \cdot \mathbf{M} V = \frac{1}{2}\mu_0 N_\| M_{\mathrm{s}}^2 \frac{4}{3}\pi a^2 b, \qquad (2.102)$$

where $N_\|$ is the demagnetizing factor along the major axis of the ellipsoid.

In the two-domain configuration, a domain wall energy term has to be added to the magnetostatic term. The wall term is given by the surface energy density γ multiplied by the cross section area πab:

$$E(2) = E_{\mathrm{ms}}(2) + E_{wall} = \alpha \frac{1}{2}\mu_0 N_\| M_{\mathrm{s}}^2 \frac{4}{3}\pi a^2 b + \pi ab\gamma. \qquad (2.103)$$

Equating the two expressions, one obtains the critical single-domain diameter $D_{\mathrm{cr}} = 2a$ for an ellipsoid:

$$D_{\mathrm{cr}} = \frac{3\gamma}{(1-\alpha)N_\| \mu_0 M_{\mathrm{s}}^2}. \qquad (2.104)$$

Substituting the expression for the domain wall energy ($\gamma = 4\sqrt{AK}$, (2.97)), and assuming $\alpha = 0.5$, one obtains for a sphere, which has a demagnetizing factor $N = 1/3$, the critical diameter:

$$D_{\mathrm{cr}} = \frac{72\sqrt{AK}}{\mu_0 M_{\mathrm{s}}^2}. \qquad (2.105)$$

The critical single-domain diameters obtained from this equation, for example, for Fe, Co and Ni, are in the range of tens of nanometers. See Tables 2.8 and 2.9 for domain wall energies and critical single-domain diameters for different materials.

From the above expression, one infers that for the same saturation magnetization M_{s}, the critical single-domain diameter is proportional to the domain wall energy.
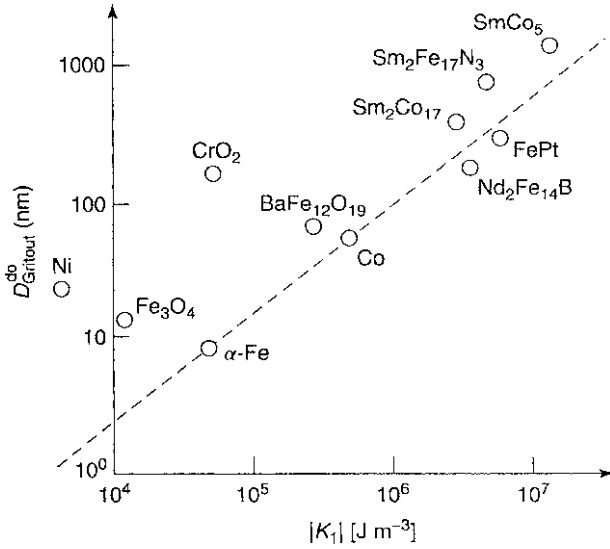
Fig. 2.11. Critical single-domain diameters versus modulus of the anisotropy constant for several magnetic materials, showing the correlation between these two quantities. It is evident that the critical diameters increase with increasing $|K|$ [13]. (Reproduced from [13] with permission from Wiley)

Therefore, as expected, if the domain wall energy increases, the critical single-domain diameter will also increase. In other words, if the price paid for the creation of a domain wall increases, the single-domain configuration will remain energetically more favorable up to larger diameters.

A more accurate value for the parameter α, which gives an estimate for the reduction in magnetostatic energy in the case of a spherical particle is $\alpha = 0.472$ [8]. Values of critical single-domain diameters computed using this value of α are given in Table 2.9. These critical diameters depend, from (2.105), on the value (the absolute value) of the anisotropy constant K_1, and this dependence is shown, for several materials, in Fig. 2.11.

2.4.2 Domain Wall Motion

A magnetic field applied to a multidomain sample will, in principle, induce a displacement of the magnetic domain walls. Consider, for example, the 180° domain wall between two magnetic domains shown in Fig. 2.9. A magnetic field applied in the z direction will create a torque on the magnetic moments inside the wall; this will generate a magnetization component perpendicular to the plane of the wall (the yz plane). This component, in its turn, creates a demagnetizing field also perpendicular to the wall, with a consequent torque that rotates the moments of the wall in such a way as to increase the size of the domain with magnetization in the $+z$ direction. This is the mechanism that induces domain wall motion under an applied magnetic field.

Let us assume that there are impurities and defects that hinder the motion of the domain wall, acting as pinning centers. For low applied magnetic fields, the domain wall motion is thermally excited, and the position of the wall changes as the successive pinning potentials are overcome. This regime is characterized by the condition $\partial\phi/\partial x = 0$, i.e., the angle between the plane defined by the local magnetization and the anisotropy axis, and the plane of the magnetic domain moments is constant; see the definition of the angles in Fig. 2.9.

The most important characteristic of this regime is that the domain wall velocity is proportional to the applied magnetic field, as will be shown later.

Above a certain intensity of the field H, called the Walker field, or Walker breakdown field, another regime is entered, where the domain wall motion is erratic. The average wall propagation velocity is still proportional to the intensity of the magnetic field, but with a different proportionality constant. The velocity of transition is referred to as the Walker velocity, and the phenomenon as the Walker breakdown.

The quantitative derivation of the limiting velocity is obtained from the computation of the free energy in the case of a $180°$ wall. A polar coordinate system is chosen, with the easy axis (z) as the polar axis, the magnetic field H is applied along this axis and the domain wall moves along the x axis (Fig. 2.9). From the expression of the free energy (2.54), one can derive how the velocity of the domain wall varies with the applied magnetic field.

Taking into account the magnetostatic and the Zeeman contributions, one notes that for $K_1 + \mu_0/2M_s^2 > \mu_0 MH$, and consequently, to first order in H, the variation of the angle θ in the domain wall satisfies an equation of the form of $\theta(y)$ given by (2.91), with the domain width parameter Δ replaced by Δ_H, the width parameter under an applied magnetic field, a quantity to be determined [17].

Deriving $\theta(y)$ (2.91), expressed in terms of Δ_H, instead of Δ, one obtains:

$$\Delta_H \frac{\partial\theta}{\partial y} = \sin\theta. \tag{2.106}$$

Using (2.106) and the expression of the total energy (2.84), one obtains the integrated domain wall energy:

$$\gamma = \int_{-\infty}^{+\infty} w\,dy = \int_0^\pi \frac{w}{(\partial\theta/\partial y)}\,d\theta =$$

$$\gamma = \frac{2A}{\Delta_H} + 2K_t\Delta_H. \tag{2.107}$$

The total anisotropy K_t is written

$$K_t = K_1 + \frac{\mu_0}{2}M^2\sin^2\phi. \tag{2.108}$$

The energy minimum is obtained by minimizing (2.107) with respect to Δ_H; it then follows for the wall energy:

$$\gamma = 4\sqrt{AK_t}, \tag{2.109}$$

which is analogous to the expression for the energy of the static domain wall (2.97), where instead of K, one has K_t.

The expression of Δ_H is therefore

$$\Delta_H = \sqrt{\frac{A}{K_t}} = 4\frac{A}{\gamma}. \tag{2.110}$$

From the expansion of γ for small applied magnetic field H_{ext}, two relations can be derived between the rate of change of the position of the domain wall $\dot{q}$ and the change of the angle ϕ, $\dot{\phi}$ [17]:

$$\dot{\phi} = \gamma_G H - \frac{\alpha_G}{\Delta_H}\dot{q} . \tag{2.111}$$

$$\dot{q} = \gamma_G \Delta_H \mu_0 M_s \sin\phi \cos\phi + \alpha_G \Delta_H \dot{\phi} . \tag{2.112}$$

In the condition of dynamic equilibrium, $\dot{\phi} = 0$ and $\dot{q} = \text{const.}$, it follows from (2.111) that the velocity v of the wall is given by

$$\dot{q} = v = \frac{\gamma_G \Delta}{\alpha_G}H . \tag{2.113}$$

Therefore, in this limit, the domain wall velocity is proportional to the applied magnetic field H.

In the expression of $\dot{q}$ (2.112), the maximum in the term with ϕ occurs for $\sin 2\phi = 1$, i.e., $\phi = \pi/4$, and one has for the maximum, or peak velocity:

$$\dot{q}_p = v_p = \frac{1}{2}\gamma_G \Delta \mu_0 M_s . \tag{2.114}$$

This is the maximum velocity for the constant-angle regime. Beyond v_p, this regime is not observed anymore, and ϕ varies, as the moments perform a precessional motion.

The applied magnetic field that leads to this maximum domain wall velocity v_p is the peak field H_p, or Walker breakdown field [22], whose expression is obtained from (2.111)

$$H_p = 2\alpha\frac{K}{\mu_0 M_s}. \tag{2.115}$$

The instantaneous domain wall velocity above the maximum domain wall velocity v_p can be either positive or negative, only the average velocity remains positive. Immediately beyond the peak velocity, for a range of values of H, the average velocity decreases with increasing H, as shown in Fig. 2.12, for an experiment with permalloy nanowires. The rate of change of the velocity with H, called mobility (μ), is therefore negative in this interval.

The existence of a limit to the domain wall velocity in the constant velocity regime has important implications, since information may be encoded by controlling the motion of domain walls, and the faster the domain wall motion the faster would be the response of a device using this principle (see Chap. 7 for a discussion of magnetic recording).
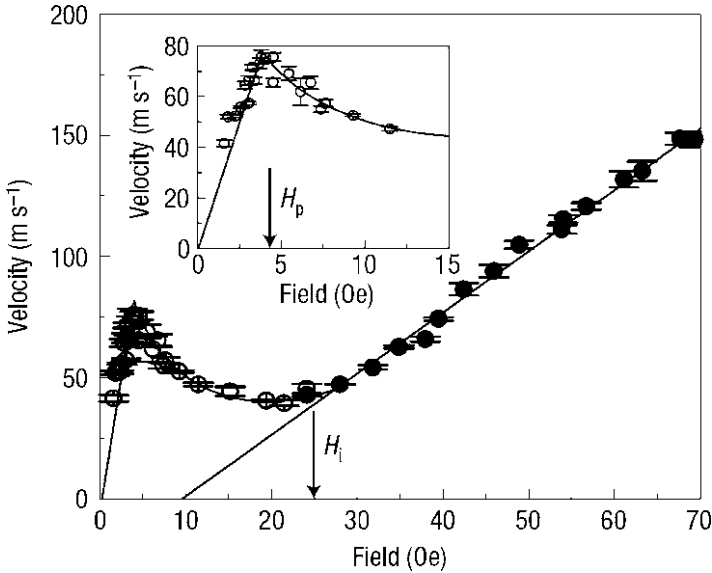
Fig. 2.12. Average domain wall velocity vs. applied H for permalloy nanowires, exhibiting the change in regime at the Walker breakdown. The *insert* shows the region of the graph around this change, at the peak field $H_p \sim 4$ Oe [2]. (Reprinted by permission from Macmillan Publishers Ltd. [2], copyright (2005))

This behavior is exemplified in measurements made with a 600 nm-wide permalloy wire of rectangular cross section, or stripe, where the critical field was reached for $H_p = 4$ Oe (Fig. 2.12), corresponding to a velocity of approximately 75 m s^{-1}; the decrease in velocity above v_p and the change in slope above this region are also apparent [2].

The dependence of domain wall velocity with applied magnetic field has been studied, both experimentally and through numerical simulations in other nanostructures, mostly in nanowires. In many of these studies the domain wall motion is also affected by the application of polarized electric currents (see Sect. 6.4, on nanowires, p. 160).

It has been demonstrated by numerical simulation that the limiting velocity, or Walker velocity, can be overcome in nanowires with rough sides [19].

2.5 Random Anisotropy

An important class of materials with nanomagnetic properties is the family of soft nanocrystalline alloys, alloys containing precipitated grains of nanometric dimensions. Their magnetic behavior is determined by the averaging out of the magnetocrystalline anisotropy due to a distribution of directions of the anisotropy axes in the spatial scale of the grain size. This description of the soft magnetic properties of these alloys is known as the random anisotropy model (see [10]). This model

has been applied to explain the magnetic properties of the Fe-based nanocrystalline alloys, formed of ultrafine crystalline particles of Fe or FeSi embedded in an amorphous matrix. Both regions, particles and matrix, are ferromagnetic.

The first member of this family to be studied was the $Fe_{73.5}Cu_1Nb_3Si_{13.5}B_9$ alloy known as Finemet [24]. The nanocrystalline material is obtained by partial devitrification induced by thermal treatment of an amorphous precursor alloy, usually produced by the technique of melt-spinning.

The averaging out of the crystalline anisotropy occurs for particle sizes D that are smaller than the exchange length, given by (1.2):

$$l_{ex} = \sqrt{\kappa}\,\Delta = \sqrt{\kappa}\sqrt{\frac{A}{K_1}}, \tag{2.116}$$

where κ, given by (2.65), is of the order of 0.1 for soft magnets, A is the exchange stiffness constant and $K_1 > 0$ is the local anisotropy parameter, usually taken as of crystalline origin.

The reduction of the effective anisotropy due to the averaging of K_1 occurs in Fe systems where $l_{ex} \approx 20 - -40$ nm for amorphous alloys ($D \approx$ atomic spacing), or for nanocrystalline alloys ($D \approx 5 - -20$ nm). This leads to an average anisotropy $\langle K \rangle$ given by [10]:

$$\langle K_1 \rangle = |K_1|\,x^2 \left(\frac{D}{l_{ex}}\right)^6, \tag{2.117}$$

where x is the crystalline volume fraction, i.e., the proportion of the sample volume occupied by the nanocrystals. This effect produces a reduction of several orders-of-magnitude in the effective anisotropy constant, as a function of the particle diameter.
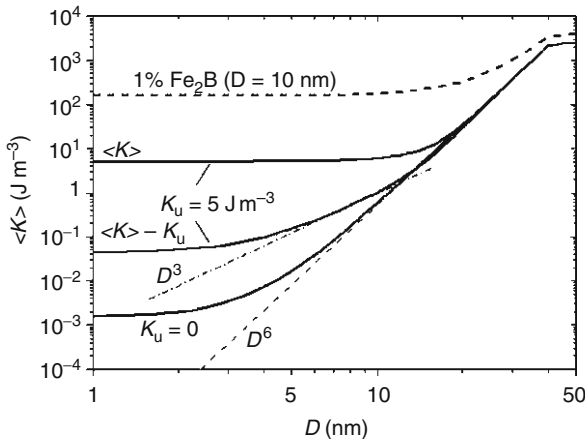
Fig. 2.13. Computed average anisotropy $\langle K \rangle$ of FeSi versus particle diameter in an amorphous matrix, using $K_1 = 5$ J m^{-3} (and $K_1 = 0$ J m^{-3}) and volume fraction $x = 0.75$ [10]. (With permission from Elsevier Science and Technology. The contribution of the random anisotropy $\delta K = \langle K \rangle - K_u$ varies from a dependence on D^3–D^6, with increasing D)
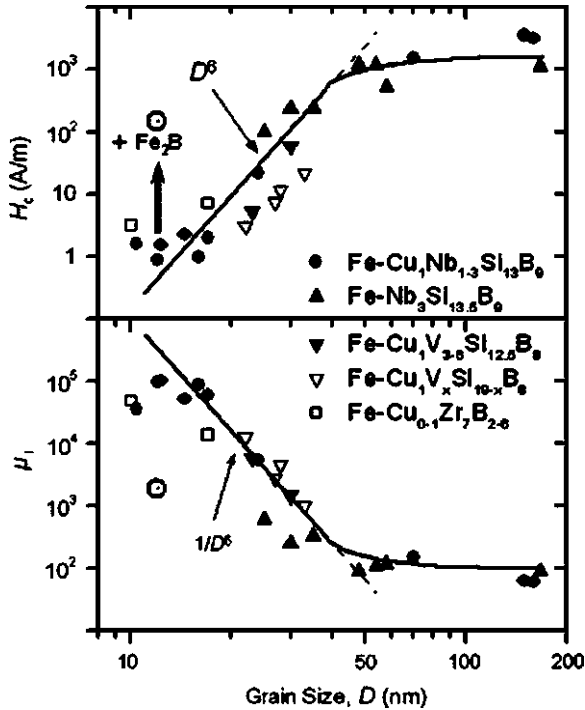
Fig. 2.14. Variation of the coercivity and magnetic permeability of Fe alloys versus particle diameter, showing the dependence of the coercivity ($H_c \propto D^6$) and magnetic permeability ($\mu \propto 1/D^6$) with particle diameter [10]. (Reproduced from [10] with permission from Elsevier Science and Technology Journals)

A graph of $\langle K_1 \rangle$ computed with the earlier equation (2.117), vs. diameter, is given in Fig. 2.13 for FeSi particles.

A reduction of the effective anisotropy of the alloys implies a reduction of the coercivity ($H_c \propto \langle K_1 \rangle$) and an increase of the magnetic permeability ($\mu \propto 1/\langle K_1 \rangle$). This behavior is observed experimentally for Fe-based nanocrystalline alloys, as shown in the graph of coercivity and magnetic permeability vs. particle diameter (Fig. 2.14). The curves show the trend of $H_c \propto D^6$ and the magnetic permeability $\mu \propto 1/D^6$ for some Fe alloys.

Further Reading

A. Aharoni, *Introduction to the Theory of Ferromagnetism*, 2nd edn. (Oxford University Press, Oxford, 2000)

G. Bertotti, *Hysteresis in Magnetism* (Academic Press, San Diego, 1998)

A.P. Guimarães, *Magnetism and Magnetic Resonance in Solids* (Wiley, New York, 1998)

G. Herzer, J. Magn. Magn. Mater. **294**, 99–106 (2005)

A. Hubert, R. Schäfer, *Magnetic Domains. The Analysis of Magnetic Microstructures* (Springer, Berlin, 1999)

H. Kronmüller, M. Fähnle, *Micromagnetism and the Microstructure of Ferromagnetic Solids* (Cambridge University Press, Cambridge, 2003)

H. Kronmüller, in *General Micromagnetic Theory*, ed. by H. Kronmüller, S. Parkin. Handbook of Magnetism and Advanced Magnetic Materials, vol 2 (Wiley, Chichester, 2007), pp. 703–741

A.P. Malozemoff, J.C. Slonczewski, *Magnetic Domain Walls in Bubble Materials* (Academic Press, New York, 1979)

R.C. O'Handley. *Modern Magnetic Materials* (Wiley, New York, 2000)

R. Skomski, J.M.D. Coey, *Permanent Magnetism* (Institute of Physics, Bristol, 1999)

R. Skomski, J. Zhou, in *Nanomagnetic Models*, ed. by D. Sellmyer, R. Skomski. Advanced Magnetic Nanostructures (Springer, New York, 2006)

References

1. A. Aharoni, *Introduction to the Theory of Ferromagnetism*, 2 edn. (Oxford University Press, Oxford, 2000)
2. G.S.D. Beach, C. Nistor, C. Knutson, M. Tsoi, J.L. Erskine, Nat. Mater. **4**, 741–744 (2005)
3. W.F. Brown, Phys. Rev. **58**, 736–743 (1940)
4. W.F. Brown, Phys. Rev. **60**, 139–147 (1941)
5. W.F. Brown Jr., *Magnetostatic Principles in Ferromagnetism* (North-Holland, Amsterdam, 1962)
6. K.H.J. Buschow, F.R. de Boer, *Physics of Magnetism and Magnetic Materials* (Kluwer, New York, 2003)
7. O. Fruchart, A. Thiaville, Compt. Rend. Phys. **6**, 921–933 (2005)
8. D. Goll, A.E. Berkowitz, H.N. Bertram, Phys. Rev. B **70**, 184432 (2004)
9. A.P. Guimarães, *Magnetism and Magnetic Resonance in Solids* (Wiley, New York, 1998)
10. G. Herzer, J. Magn. Magn. Mater. **294**, 99–106 (2005)
11. A. Hubert, R. Schäfer, *Magnetic Domains. The Analysis of Magnetic Microstructures* (Springer, Berlin, 1999)
12. C. Kittel, Rev. Mod. Phys. **21**, 541–583 (1949)
13. H. Kronmüller, in *General Micromagnetic Theory*, ed. by H. Kronmüller, S. Parkin. Handbook of Magnetism and Advanced Magnetic Materials, vol 2 (Wiley, Chichester, 2007), pp. 703–741
14. H. Kronmüller, M. Fähnle, *Micromagnetism and the Microstructure of Ferromagnetic Solids* (Cambridge University Press, Cambridge, 2003)
15. L.D. Landau, E. Lifshitz, Phys. Z. Sowjetunion **8**, 153–169 (1935)
16. Landolt-Börnstein, *Tables of Magnetic Properties of 3d Elements*, New Series, vol 3 (Springer, Berlin, 1986)
17. A.P. Malozemoff, J.C. Slonczewski, *Magnetic Domain Walls in Bubble Materials* (Academic Press, New York, 1979)
18. P.J. Mohr, B.N. Taylor, D.B. Newell, Rev. Mod. Phys. **80**, 633–730 (2008)
19. Y. Nakatani, A. Thiaville, J. Miltat, Nat. Mater. **2**, 521–523 (2003)
20. L. Néel, J. Phys. Rad. **15**, 225–239 (1954)
21. J.A. Osborn, Phys. Rev. **67**, 351–357 (1945)
22. N.L. Schryer and L.R. Walker, J. Appl. Phys. **45**, 5406–5420 (1974)
23. C.A.F. Vaz, J.A.C. Bland, G. Lauhoff, Rep. Prog. Phys. **71**, 056501–056578 (2008)
24. Y. Yoshizawa, S. Oguma, K. Yamauchi, J. Appl. Phys. **64**, 6044–6046 (1988)

3

Magnetism of Small Particles

Summary. Magnetic nanoparticles are important physical systems, relevant for many applications, and in many cases the starting point of fundamental developments in Nanomagnetism. The Stoner–Wohlfarth theory, discussed in this chapter, represents a milestone in the process of understanding nanoparticle magnetism. This theory describes the magnetic properties of ellipsoidal magnetic particles, including the conditions for the homogeneous reversal of their magnetization under applied magnetic field. Magnetic nanoparticles present spin arrangements that may be single-domain, vortex state, or multidomain, with their magnetic behavior depending on the spin configuration. The critical diameters for these configurations can be derived in an approximate form. Nanoparticles in the smaller range of diameters do not behave as stable magnets, exhibiting the phenomenon of Superparamagnetism.

3.1 Introduction

Many magnetic systems of interest are formed of particles with dimensions in the nanoscopic or mesoscopic ranges. Nanoscopic and mesoscopic particles may be constituents of magnetic recording media, Magnetic Resonance Imaging (MRI) contrast reagents, drug carriers, and also may form ferrofluids when held in suspension, employed to dissipate heat in hyperthermia applications or used for biomagnetic separation. In all these examples, the magnetic properties of the particles are determinant to the application, and are tailored or controlled to optimize it. Figure 3.1 shows a high-resolution image of a nanoscopic particle of iron oxide obtained with a transmission electron microscope, where the crystal lattice is clearly visible.

   The magnetic behavior of nanoparticles is, in general, strongly dependent on their dimensions. For example, the smaller magnetically ordered particles will tend to be single-domain, and the larger ones, above a certain critical diameter D_{cr}, will be multidomain, or else exhibit a vortex configuration, an arrangement where the local magnetizations are aligned tangentially to circles. Magnetic nanoparticles also have other properties that depend on their sizes (see Chap. 1). For example, the magnetic
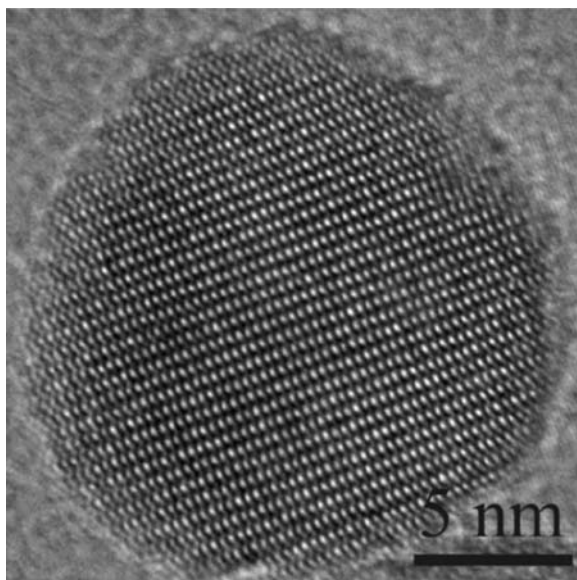
Fig. 3.1. High resolution transmission electron microscope (HRTEM) image of a $\sim$18 nm-diameter Fe_3O_4 particle, showing its crystalline structure [40]
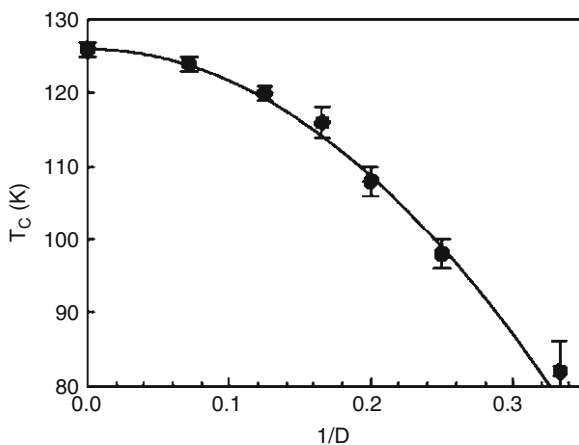
Fig. 3.2. Curie temperature of spherical maghemite (γ-Fe_2O_3) particles obtained by Monte Carlo simulation, vs. inverse diameter. The *continuous line* is given by the equation $(T_C(d) - T_C(\infty))/(T_C(\infty)) = \pm(D/D_0)^{-1/\nu}$, where D_0 is a characteristic length [25]. (Reprinted figure with permission from [25]. Copyright (2001) by the American Physical Society)

ordering temperature of nanoparticles depends in a regular fashion on their diameter. This may be seen in the gradual reduction of the Curie temperature of ferromagnetic nanoparticles of maghemite (γ-Fe_2O_3) vs. inverse diameter (Fig. 3.2). These values of T_C were obtained by Monte Carlo simulation.

In this chapter, we will discuss the magnetic properties of nanoparticles, specifically the form of the curve of magnetization vs. magnetic field and the process of inversion of the magnetization under the action of applied magnetic fields, either static or pulsed. The case of a static field in the direction opposite to the magnetization will be treated first.

Let us consider a small ellipsoidal single-domain magnetic particle with uniaxial anisotropy, under the influence of a magnetic field, applied antiparallel to the initial direction of magnetization. The magnetization originally points along the anisotropy axis, parallel to the z axis ($\theta = 0$) and in this case the anisotropy energy is at a minimum. There is another minimum in the anisotropy energy in the configuration in which the magnetization points in the opposite direction ($\theta = \pi$); these two minima are separated by an energy barrier, that has to be surmounted to invert the magnetization. In the absence of an applied magnetic field ($H = 0$), the height of the barrier is $E_B = KV$, where K is the effective uniaxial anisotropy constant and V is the volume of the particle. Figure 3.3 shows the energy of a single-domain magnetic particle as a function of the angle θ between the anisotropy axis and the magnetic field direction, for three different intensities of the applied magnetic field H. One sees that as the magnetic-field intensity is increased, the shape of the $E(\theta)$ curve is changed, from symmetric with two minima to asymmetric with one single minimum for $\theta = \pi$.
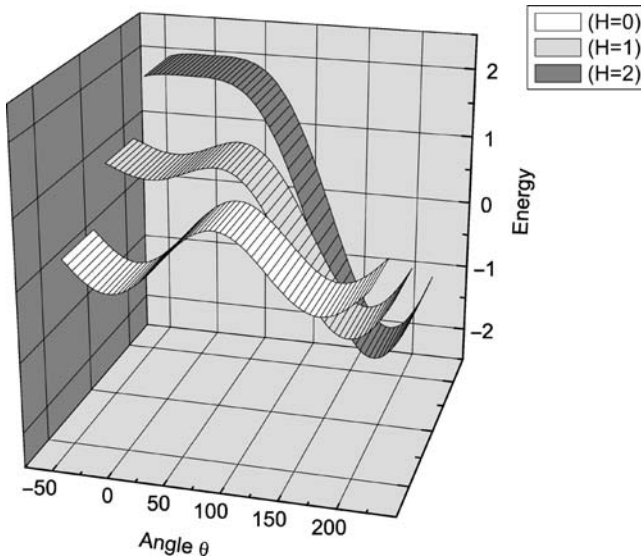
Fig. 3.3. Energy of a single-domain magnetic particle with uniaxial anisotropy, in the presence of an applied magnetic field H, as a function of the angle θ of the field with the anisotropy axis, for three different values of the magnetic field intensity. Note the change in the form of the curve as a function of the intensity of H, from a curve with two equal minima, for $H = 0$, to an asymmetric curve, with increasing H

If single-domain magnetic particles have a volume equal to a certain critical volume V_{cr}^{spm}, the thermal energy ($k_B T$) will be comparable to the height of the potential barrier E_B. In this condition the particles will behave as superparamagnets, a name that arises from the fact that such particles have magnetic moments that are much larger than individual atomic (paramagnetic) moments. These particles will jump between two possible orientations, and their average magnetic moments will be zero. Their magnetic behavior will then be described by the Langevin function, the classical limit of the Brillouin function, as discussed in Sect. 3.3.1.

Particles with volumes larger than V_{cr}^{spm} (but still single-domain) will have a stable, or stationary, direction of magnetization, and their magnetization curve will be described by the Stoner–Wohlfarth model (Sect. 3.5). In the Stoner–Wohlfarth regime, the individual atomic moments turn in a homogeneous or coherent fashion, through the action of the magnetic field, whereby the magnetizations of the elements of volume of the particle remain parallel throughout the process. This normal rotation of the magnetization, or rotation in unison, is called Néel rotation. On the other hand, in small particles that are free to rotate as a whole, for example, particles in suspension in a fluid, one may observe bodily rotation, often referred to as Brown rotation.

As the particle size increases, typically to sizes above the exchange length l_{ex}, the inversion of its magnetization cannot be considered homogeneous, and the magnetization evolves through processes known as curling and buckling. Each one of these processes shows a characteristic configuration of the individual spins, or of the local magnetization $\mathbf{M}(\mathbf{r})$ throughout the particle. Another rotation mechanism is a collective behavior involving several homogeneously magnetized particles, called fanning. These magnetization processes will be discussed in Sect. 3.5.1.

The largest particles, on their turn, are multidomain, and change their magnetization by re-arranging the magnetic domain structure, in other words, the magnetization varies through the motion of magnetic domain walls, or changes in the shape of the domains. Depending on the balance of magnetic anisotropy and exchange energy, the configuration of lowest energy for a nanoparticle of diameter above the critical single-domain diameter is not a multidomain, but a swirl, or vortex, a circular arrangement of magnetic moments. Figure 3.4 illustrates these two spin arrangements observed in 200 nm Co (001) nanodisks, with two micromagnetic simulations (Fig. 3.4c, d); magnetic force microscopy (MFM) images of an array of four such disks exhibiting these two configurations are also shown.

In considering these different magnetic moment configurations one should bear in mind that magnetic systems are often in metastable states, i.e., they are found in configurations that do not necessarily correspond to their lowest energy states. One may therefore discuss which spin arrangement corresponds to the lowest free energy of the system, but the actual spin configuration will depend on the magnetic history of the sample, specifically, on the time evolution of conditions such as temperature and applied magnetic field.
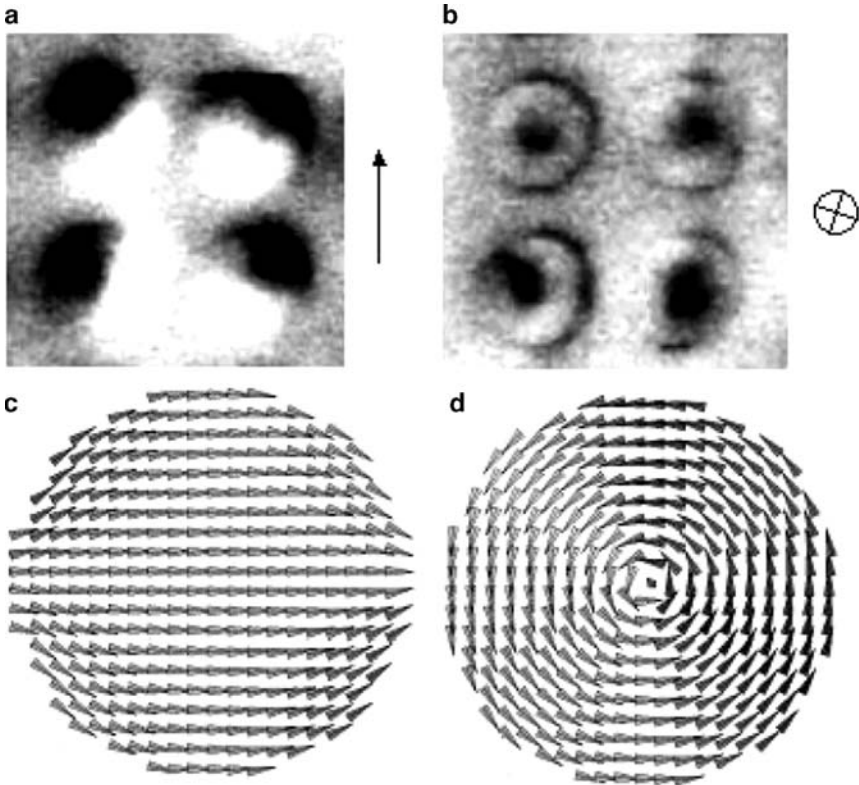
Fig. 3.4. MFM image of four 200 nm diameter Co (001) disks, (**a**) as single-domains, and (**b**) as vortices. The distribution of local magnetizations obtained for a single disk from three-dimensional micromagnetic modeling shows (**c**) a single-domain structure and (**d**) a vortex structure. (Reproduced with permission from [12])

3.2 Particle Size and Magnetic Behavior

To illustrate the significance of the particle size to its magnetic behavior one can make use of the coercive field H_c, a relevant property of magnetic samples, and which is dependent on the size of the particle to characterize the different magnetic regimes. This is shown schematically in Fig. 3.5, where H_c is plotted against particle diameter.

Four regions can be identified in the graph: (1) for very small diameters, typically a few nanometers, the magnetic moment is not stable, and therefore $H_c = 0$ below D_{cr}^{spm}, (2) for an intermediate diameter (typically $20\,nm < D < 100\,nm$ for a soft magnetic material), the moment is stable, the particle is single-domain and the coercivity grows with D. Depending on the magnetic hardness, (3) there may be a region where coercivity falls due to vortex magnetic order, and finally, (4) for larger diameters, typically above several μm, the multidomain regime sets in, and the coercivity falls with increasing diameter D.
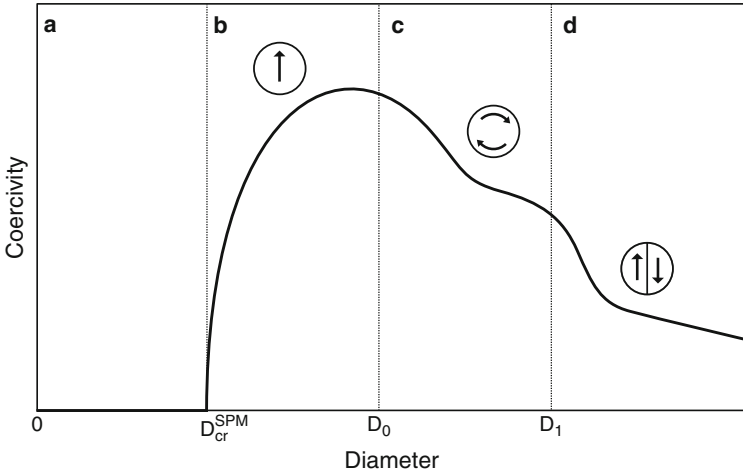
Fig. 3.5. Curve of coercivity vs. size of magnetic particle, showing four regimes: (**a**) super-paramagnetic $0 < D < D_{cr}^{spm}$, (**b**) ferromagnetic single-domain, for $D_{cr}^{spm} < D < D_0$, (**c**) vortex state, for $D_0 < D < D_1$ (for soft magnetic samples) and (**d**) multidomain, for $D > D_1 = D_{cr}$
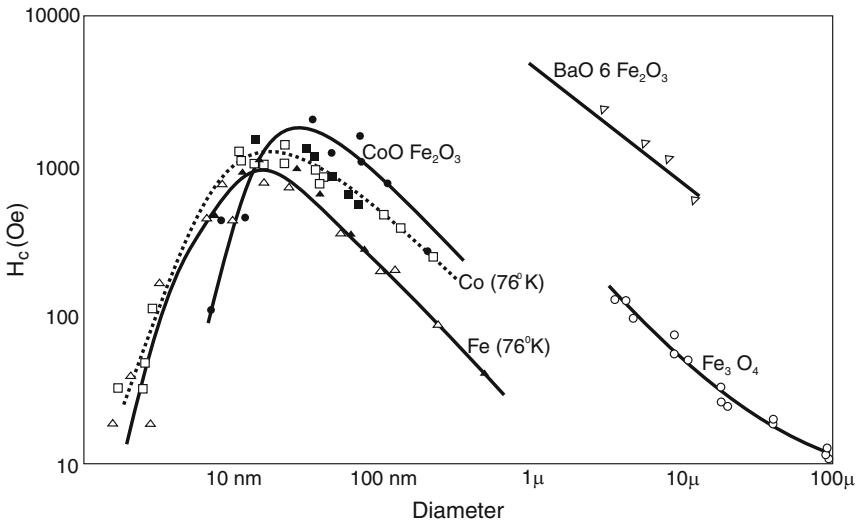
Fig. 3.6. Dependence of the magnetic coercivity with size of different magnetic small particles. (Reprinted (re-drawn) with permission from [37]. Copyright (1961), American Institute of Physics)

An example of the dependence of the coercive field on size is given by the magnetic behavior of particles of Fe, Co, and CoFe$_2$O$_3$, from an early study, shown in Fig. 3.6 [37]. This figure shows, for example, that the coercive field of Fe and Co particles is maximum for diameters of ≈ 20 nm at liquid nitrogen temperature.

To study the evolution of the magnetism of a nanoparticle, one may initially apply a magnetic field H that is sufficient to saturate it magnetically. If now one starts to reduce the amplitude of this field, crossing zero and continuing in the opposite direction, there will be a point at which the magnetization jumps to another value that does not correspond to a state of magnetic saturation. The magnetic field at this point is the nucleation field H_N; the name is not very appropriate, since there is not necessarily a nucleation process occurring for this value of field (see the comment in [2], p. 184).

There are three characteristic values of magnetic fields that are given specific names in the discussion of the properties of magnetic materials, and which are the object of different definitions by different authors: they are the nucleation field H_N (defined earlier), the coercive field H_c and the switching field H_{sw}. The coercive field (or coercivity) is usually defined as the magnetic field applied in the direction opposite to the direction of the original magnetization for which $M = 0$. The switching field is the value of magnetic field that corresponds to a sudden variation of the magnetization, or to a maximum in $|dM/dH|$. The nucleation field and the switching field are more precisely defined for a single particle; for an ensemble of particles it is more meaningful to determine the coercive field.

Another related field is the inversion field, the magnetic field that saturates the magnetization in the negative direction.

A nanoparticle with a diameter larger than that corresponding to the superparamagnetic regime, has as its lowest energy configuration a single-domain structure, as shown in Fig. 3.5. As the particle diameter increases, two different situations are observed: for the hard magnetic materials, increasing the particle diameter produces a transition to the multidomain regime. In the case of particles of soft magnetic materials, however, a curling or vortex arrangement of magnetic moments is favored above the diameter for the single-domain regime. Samples of larger sizes will develop a multidomain structure.

One can employ the magnetic hardness parameter $\kappa = H_A/M_s$ ((2.65), p. 37) to set the different materials into classes defined in terms of the relative importance of the anisotropy energy term. Two main cases are apparent: magnetically soft samples, characterized by a hardness parameter $\kappa \ll 1$, and magnetically hard samples, with larger values of κ, exemplified here with the value $\kappa = 1$. This is broadly equivalent to the classification of hard and soft magnetic materials based on the value of H_c (Sect. 2.1, p. 27).

One can consider, a priori, that the possible lower free energy spin configurations for a spherical magnetic particle will be a single-domain, a two-domain structure and a vortex structure (Fig. 3.7). The energies corresponding to these arrangements can be estimated in an approximate way, as will be shown next [8].

For the single-domain structure, since all the magnetic moments are aligned along the anisotropy axis, the free energy contribution from exchange and anisotropy are both zero. Therefore, it is reasonable to assume that the only relevant energy term
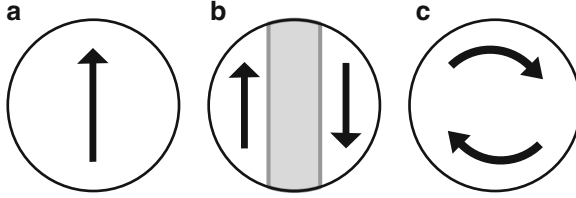
Fig. 3.7. Three possible spin configurations for the lowest energy state of a spherical magnetic particle: (**a**) single-domain, (**b**) two-domain structure and (**c**) vortex

is the magnetostatic energy. The magnetostatic energy for a single-domain sphere is given, using (2.102), p. 49:

$$E_a = -\frac{1}{2}\mu_0 \mathbf{H}_d \cdot \mathbf{M} V = \frac{1}{6}\mu_0 M_s^2 \frac{4}{3}\pi R^3. \tag{3.1}$$

A dimensionless quantity can be obtained from E_a, dividing by $\mu_0 M_s^2 V$, where V is the volume of the particle: the result, $g_a = 1/6$, does not depend on the radius of the particle.

For the configuration with two domains, on the other hand, the magnetic field at a distance from the particle will be reduced, since it will represent a field due to two opposing dipoles. One can therefore, to a first approximation, ignore the magnetostatic term. In the domain wall, the region separating the two domains, there will be contributions from exchange and anisotropy. Inside the two domains, these terms are again zero, since the magnetic moments are aligned along the anisotropy axis. Assuming that the magnetic moments in the wall turn outside the plane, two components of **m** (which is a vector of unitary length) vary of the order of 1 in a distance of the order of $\Delta/2$, where Δ is the domain wall width parameter. Therefore, $(\nabla\mathbf{m})^2 \approx (\Delta\mathbf{m}/\Delta x)^2 \sim 2(2/\Delta)^2$. Considering that the domain wall occupies a fraction of the order of Δ/R of the volume of the sphere, the exchange energy, from ((2.54), p. 35), is $E_{ex} \approx (8A/\Delta^2)(\Delta/R)$. The anisotropy energy of the moments inside the volume V_d of the domain wall, $K_1 \sin^2\theta \cdot V_d = K_1(1/2)(\Delta/R)V$, where we have used the average $\overline{\sin^2\theta} = 1/2$.

Therefore, the energy corresponding to the arrangement with two domains is

$$E_b \approx \frac{1}{R}\left(\frac{8A}{\Delta} + \frac{K_1\Delta}{2}\right)V. \tag{3.2}$$

The variable Δ can be eliminated by minimizing the energy, i.e., solving $dE/d\Delta = 0$. The solution is

$$\Delta_s = 4\sqrt{\frac{A}{K_1}} = 4\,\Delta, \tag{3.3}$$

where Δ is the domain wall width parameter, $\Delta = \sqrt{A/K_1}$. Substituting Δ_s into the expression of the energy, it follows:

$$E_b = \left(\frac{4K_1}{R} \sqrt{\frac{A}{K_1}} \right) V = \frac{4K_1}{R} \Delta V. \tag{3.4}$$

Dividing the energy by $\mu_0 M_s^2 V$, to obtain a dimensionless expression:

$$g_b = \frac{4K_1}{\mu_0 M_s^2 R} \sqrt{\frac{A}{K_1}} = \frac{2}{R} l_{ex} \sqrt{\kappa}, \tag{3.5}$$

where $l_{ex} = \sqrt{2A/\mu_0 M_s^2}$ (2.64) and $\kappa = 2K_1/\mu_0 M_s^2$ (2.65).

The energy corresponding to the vortex configuration can be roughly estimated by assuming that the sample in this case is equivalent to a domain wall with $\Delta = 2R$. Substituting into (3.2):

$$E_c \approx \left(\frac{4A}{R^2} + K_1 \right) V. \tag{3.6}$$

Dividing this energy by $\mu_0 M_s^2 V$, again to express this result in a dimensionless form:

$$g_c \approx \frac{2l_{ex}^2}{R^2} + \frac{\kappa}{2}. \tag{3.7}$$

If one plots the normalized energies corresponding to the three spin arrangements of a spherical particle, g_a, g_b, and g_c, vs. normalized radius (R/l_{ex}), the graphs obtained in the cases of magnetically soft and hard samples are shown in Figs. 3.8 and 3.9 [8].
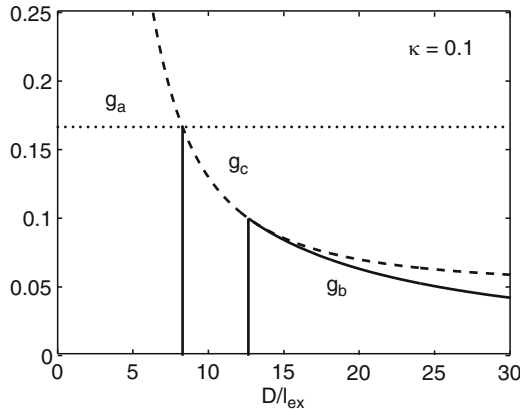
Fig. 3.8. Computed energy vs. particle diameter (in units of the exchange length l_{ex}) for $\kappa = 0.1$ (magnetically soft material), showing: (**a**) for diameter up to 8 l_{ex} the lowest energy configuration is a single domain, (**b**) for an intermediate range of diameters the vortex state is favored, and (**c**) for diameters above about 13 l_{ex} the lowest energy corresponds to a multidomain configuration. (Adapted from [8])
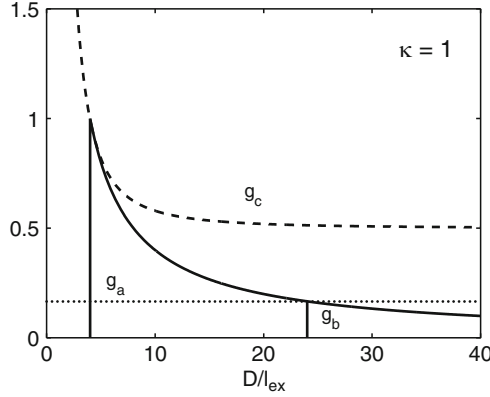
Fig. 3.9. Computed energy vs. particle diameter (in units of the exchange length l_{ex}) for $\kappa = 1$ (hard material). Up to about $D = 4\ l_{ex}$, the lowest energy state is single-domain; above this diameter, it has more than one domain. (Adapted from [8])

In the case of a magnetically soft material, with $\kappa = 0.1$, it is shown in Fig. 3.8 that for particle diameter between zero and about four times the exchange length l_{ex}, the minimum energy configuration is a single-domain. For an intermediate diameter, from about four times the exchange length l_{ex} to six times the exchange length, the lowest energy configuration is a vortex state. The minimum free energy state for particles with diameters above about $6\ l_{ex}$ is a multidomain spin structure.

For particles of hard magnetic material (e.g., with $\kappa = 1$), as represented in Fig. 3.9, the vortex state is not clearly favored for any range of diameters. The states that minimize the total energy are the single-domain arrangement, up to about $D = 2\ l_{ex}$, and bi-domain, above about $13\ l_{ex}$.

Taking into account only two possible spin arrangements, single-domain and two domains separated by a domain wall, we have obtained in Sect. 2.4.1, in a simple way, the single-domain critical diameter for a spherical magnetic particle. The expression obtained for D_{cr}, in terms of the parameters A, K and M_s, was ((2.105), p. 49):

$$D_{cr} = \frac{72\sqrt{AK}}{\mu_0 M_s^2}. \tag{3.8}$$

As we have seen earlier ((3.1)–(3.7)), if no restrictions are made on the magnetic hardness of the sample, one has to consider, besides the single-domain and bi-domain spin structures, another magnetization distribution for small particles, an arrangement in which the atomic magnetic moments are not aligned, but instead form a vortex, as in the case of the Co disk shown in Fig. 3.4.

Brown [9, 10] derived analytically, within the micromagnetic approximation, expressions for the critical diameters of spherical particles of both hard and soft magnetic materials. He considered the three spin configurations: single-domain, vortex, and two-domain, and assumed uniaxial anisotropy. The vortex arrangement was described in cylindrical coordinates (z, ρ, ϕ) by the relations $M_z = M_s(1 - \rho^2/r^2)$,

$M_\rho = 0$, $M_\phi = (M_s^2 - M_z^2)^{1/2}$. He considered that the crossover from soft to hard materials occurred for a value of the hardness parameter given by $\kappa = 2K_1/\mu_0 M_s^2 = 0.35360$.

This analysis led to a critical diameter D_0, which is the upper limit for the diameter of the single-domain configuration to remain the minimum energy arrangement, given by:

$$D_0 = 7.211\sqrt{\frac{2A}{\mu_0 M_s^2}} = 7.211\, l_{ex}, \tag{3.9}$$

where l_{ex} is the exchange length.

The critical diameter for a transition from vortex to multidomain configuration, for a soft magnetic material is

$$D_1 = \frac{9.0584\sqrt{\frac{2A}{\mu_0 M_s^2}}}{\left(1 - 2.8075\frac{2K_1}{\mu_0 M_s^2}\right)} = \frac{9.0584}{1 - 2.8075\,\kappa}\, l_{ex}, \tag{3.10}$$

where κ is the hardness parameter.

Substituting the parameters corresponding to α-Fe, one obtains for the critical diameter of the sphere for vortex formation $D_0 \sim 20$ nm, and the diameter for the division into domains, $D_1 \sim 30$ nm.

For hard magnetic materials, the critical diameter for the transition from single-domain to multidomain is given by:

$$D_2 = \frac{9\pi\sqrt{2A(K_1 + 2\sigma\mu_0 M_s^2)}}{\mu_0 M_s^2 (3\sigma - 2)} = \frac{9\pi\sqrt{\kappa + 4\sigma}}{\sqrt{2}(3\sigma - 2)}\, l_{ex}, \tag{3.11}$$

with $\sigma = 0.785398$.

The lower limiting diameter for a nonuniform configuration to be an energy minimum is the smallest of the two earlier expressions ((3.10) and (3.11)). In other words, particles with diameters greater than the smallest of these two expressions will not have the single-domain configuration as their lowest energy state.

The critical diameters for some soft magnetic materials computed using these expressions are shown in Table 3.1. Micromagnetic simulations performed with spherical samples and using the parameters for the soft materials Fe, $Fe_{80}Si_{20}$ and

Table 3.1. Critical diameters calculated for spheres of some materials using Brown's formulas. D_0 is the maximum diameter for a single-domain arrangement and D_1 is the maximum diameter for a vortex structure. D_{single} and D_{vortex} are the corresponding values obtained from micromagnetic simulation [31]

Material	D_0 (nm)	D_1 (nm)	D_{single} (nm)	D_{vortex} (nm)
Fe	24.3	31.7	25	40
$Fe_{80}Si_{20}$	35.4	45.4	35	50
Permalloy	36.8	45.2	35	50

permalloy, gave for the three different spin arrangements (single-domain, vortex, and two-domain), values of the critical diameters (also shown in Table 3.1) in reasonable agreement with Brown's expressions [31]. The agreement is not better, according to the authors, probably due to surface effects, including surface anisotropy, and also to the fact that the shape used in the simulation was not perfectly spherical.

Note that the values of D_0 differ significantly from those obtained from the approximate expression D_{cr}, derived in Chap. 2, that appears on p. 37.

3.3 Superparamagnetism

As we have seen in the introduction, a magnetic particle with anisotropy energy KV has two energy minima, separated by a barrier of height $E_B = KV$. The transition from one minimum to the other can be thermally activated for $T \neq 0$ K, the transition probability being very large if the thermal energy $k_B T$ is comparable to or larger than KV.

If one takes an ensemble of magnetized particles at $T \neq 0$ K and sets $H = 0$ at the instant $t = 0$, the magnetization will evolve with time, since there will be thermally activated transitions between the two minima. The magnetization will vary with time with a dependence of exponential form:

$$\frac{\mathrm{d}M}{\mathrm{d}t} = -\frac{1}{\tau_0} M \mathrm{e}^{-\frac{KV}{k_B T}} = -\frac{M}{\tau}, \tag{3.12}$$

where τ is the relaxation time, or inverse of the switching frequency. The prefactor τ_0, the inverse of the attempt frequency, is usually in the range 10^{-12}–10^{-9} s. The fact described by this equation, in simple terms, is that under the influence of thermal energy, the system makes $1/\tau_0$ attempts per second to surmount the energy barrier.

The relaxation time is therefore given by an equation of the form

$$\tau = \tau_0 \mathrm{e}^{\frac{E_B}{k_B T}}, \tag{3.13}$$

known as Néel–Arrhenius Law, describing the exponential dependence of τ on the ratio $E_B/k_B T$ of the height of the energy barrier to the thermal energy. In the present case the energy E_B is the anisotropy energy $E_B = KV$.

Note that τ depends exponentially both on V and T. The frequency of jumps, or inversions, is given by

$$\nu = \tau_0^{-1} e^{-\frac{KV}{k_B T}}. \tag{3.14}$$

The observed magnetic behavior of a magnetic particle depends on the time scale, or time window, of the measurement. For macroscopic techniques such as the direct measurement of the magnetization M, the measuring time is usually taken as $t_m = 100$ s. For a microscopic measurement, e.g., using Mössbauer spectroscopy or nuclear magnetic resonance (NMR), the time window is much shorter, in the range 10^{-9}–10^{-7} s. If the relaxation time τ is shorter than t_m, the spontaneous magnetization is zero, and the particle is said to be in the superparamagnetic regime. If the

opposite occurs (i.e., $\tau > t_m$) the particle is in the blocked regime, and a nonzero magnetization is observed.

Therefore, depending on the relation between relaxation time τ and measurement time t_m, one has:

$$\begin{cases} \text{For } \tau < t_m \rightarrow \text{superparamagnetic regime} \\ \text{For } \tau > t_m \rightarrow \text{blocked regime (ferromagnet)} \end{cases}$$

As the volume V of the magnetic particle varies, $E_B = KV$ will vary, and for a given temperature, the particle may change from one regime to the other. Since, from (3.13),

$$ln\ \tau = ln\ \tau_0 + \frac{KV}{k_B T}, \tag{3.15}$$

one can obtain the critical volume of a magnetic particle for a temperature T, using $t_m = 100$ s and $\tau_0 = 10^{-9}$ s:

$$V_{cr}^{spm} \approx \frac{25 k_B T}{K}. \tag{3.16}$$

Or the superparamagnetic critical diameter for a spherical particle:

$$D_{cr}^{spm} = \left(\frac{6}{\pi} V_{cr}^{spm} \right)^{1/3}. \tag{3.17}$$

Values for this critical diameter at room temperature, computed using (3.16) and (3.17) are given in Table 3.2; they vary from a few nanometers to some tens of nanometers.

The critical volume V_{cr} is the maximum volume below which, at a given temperature, an experiment detects the sample in the superparamagnetic regime. For example, a Fe_3O_4 nanoparticle exhibits superparamagnetic behavior below a diameter of ≈ 17 nm in a magnetic susceptibility measurement, or ≈ 9 nm in an experiment with Mössbauer spectroscopy [14].

Conversely, for a given volume V, the temperature below which ferromagnetic behavior is observed is the blocking temperature T_B, given by

$$T_B \approx \frac{KV}{25k}. \tag{3.18}$$

In Fig. 3.10, it is shown a graph of the relaxation time τ vs. blocking temperature T_B for Fe_3O_4 nanoparticles, showing a linear increase of $ln(\tau)$ with inverse blocking temperature [22].

Table 3.2. Superparamagnetic critical diameters D_{cr}^{spm} calculated for spheres of some materials at room temperature, using (3.16) and (3.17)

Material	α-Fe	Co	Ni	Fe_3O_4	$SmCo_5$
D_{cr}^{spm} (nm)	16	8	35	4	2
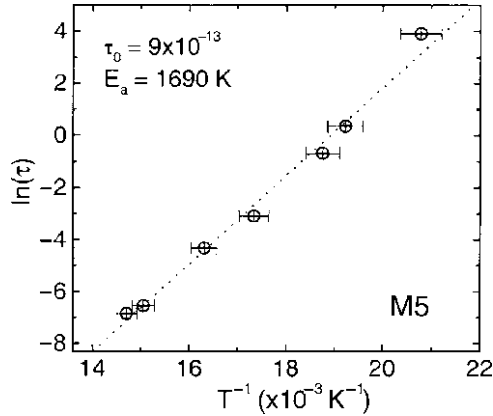
Fig. 3.10. Relaxation time vs. inverse of the blocking temperature for Fe_3O_4 nanoparticles of mean diameter 5 nm. (Reprinted with permission from [22]. Copyright (2003), American Institute of Physics)

It should be pointed out that the blocking temperature is not uniquely defined, since it depends on the time scale of the technique of measurement; for example, the expression of T_B (3.18) was derived assuming a measuring time $t_m = 100$ s.

Using (3.15), and noting that $KV = E_B$ is the barrier height, one obtains:

$$E_B(t,T) = k_B T \, ln \, \frac{t}{\tau_0}. \tag{3.19}$$

From this equation, it follows that the inversions of the magnetization that occur with barriers of energy around $E_B(t,T)$ may be effected by sweeping either the temperature or the time. Therefore, a measurement of the relaxation at a given temperature is equivalent to an experiment performed at a different temperature T, with the time window displaced according to the earlier relation. This may be illustrated by plotting the magnetization measured at different temperatures as a function of the variable $T ln (t/\tau_0)$, in this case with $\tau_0 = 3.5 \times 10^{-11}$ s (Fig. 3.11).

At very low temperatures the probability of reversion of the magnetization departs from the dependence described by (3.12). This effect arises from the fact that there is a finite probability of tunneling, or macroscopic quantum tunneling (MQT). When this occurs, the particle jumps from one spin configuration to the opposite one in a process that does not require thermal excitation.

The rate or frequency of inversion through tunneling is [12]

$$v = A(T)e^{-\frac{E_B}{k_B T_{esc}(T)}}, \tag{3.20}$$

where E_B is the barrier height and $T_{esc}(T)$ is the escape temperature. At high temperatures $T_{esc}(T) = T$ and one reverts to the classical thermal activation described by (3.14).
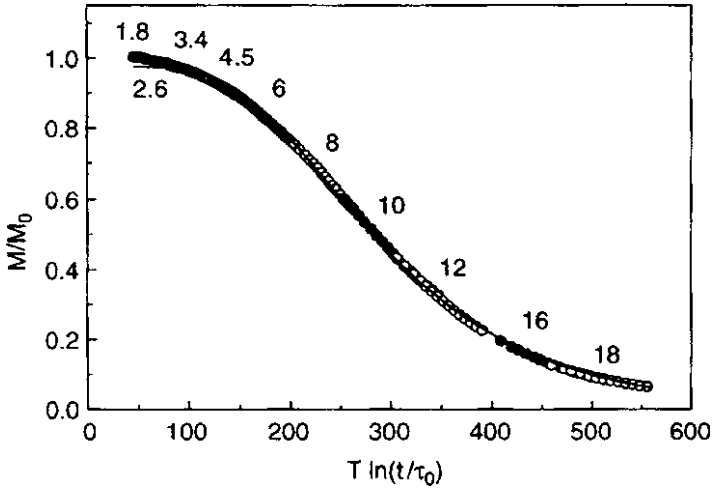
Fig. 3.11. Scaling of the magnetization for FeC particles vs. $T ln(t/\tau_0)$ [35]. (Reprinted figure with permission from [35]. Copyright (1993) by the American Physical Society)

As the temperature of an ensemble of magnetic nanoparticles is raised from $T \approx 0\,\mathrm{K}$, it will eventually reach a temperature $T = T'$ at which the two mechanisms of inversion, thermal activation and tunneling, are equally probable.

In polydisperse samples, i.e., samples formed of particles with a distribution of sizes, there may exist, at a given temperature, particles that are blocked and particles that are in the superparamagnetic regime. One distribution of particle sizes (or particle volumes V) that occurs frequently is the log-normal distribution, a distribution that has the logarithm of a variable normally distributed. It is defined by

$$f(V) = \frac{1}{\sigma V \sqrt{2\pi}} e^{\frac{[-\ln(V) - \ln(V_0)]^2}{2\sigma^2}}, \tag{3.21}$$

where σ is the standard deviation of $\ln V$ and $\ln(V_0)$ is its average. The log-normal distribution of particle volumes is displayed in Fig. 3.12, for two values of the standard deviation σ.

If one takes an ensemble of particles magnetized to saturation and applies a magnetic field in the opposite direction, the fraction of particles that remain without inverting the magnetization after a time t, or the probability $P(t)$ that a given particle has not inverted the magnetization, is

$$P(t) = e^{-\frac{t}{\tau}}. \tag{3.22}$$

This probability is measured experimentally by increasing the applied magnetic field to a value near the inverting or switching field H_{sw} and determining the time required for the particle to invert its magnetization. This procedure is repeated many times, to obtain a histogram of the waiting times; the integral of this histogram gives
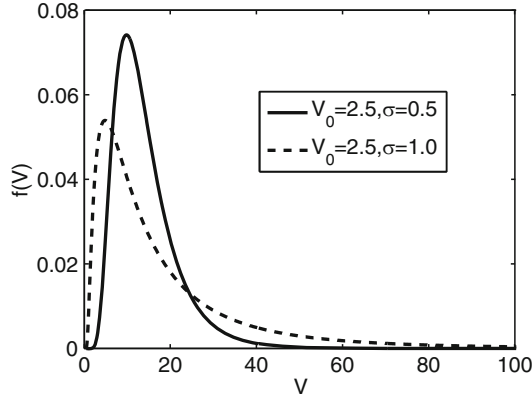
Fig. 3.12. Log-normal distribution $f(V)$ of particle volumes vs. volume, for two values of the average volume V_0 and standard deviation σ
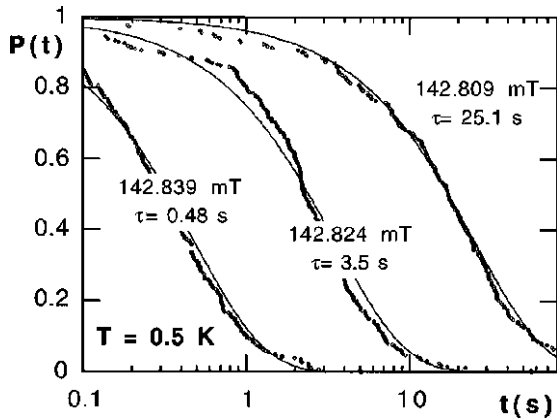
Fig. 3.13. Probability that a particle of Co of 20 nm diameter at 0.5 K has not inverted its magnetization M after a time t, vs. t. The lines are best fits to the function $P(t)$ (3.22), at different fields, for different values of the relaxation time τ. Note the large variation in τ for minute changes in magnetic field B. (Reprinted with permission from [56]. Copyright (1997), American Institute of Physics)

the probability of commutation. In the example shown in Fig. 3.13, $P(t)$ for a 20 nm diameter Co particle was measured by observing the particle switching its magnetization at three very close values of magnetic induction B, around 142 mT. The computer fits to the function of (3.22) result in three values of the relaxation time τ: 0.485, 3.5, and 25.1 s.

If the energy barriers of the ensemble of particles do not have the same height, the relaxation of the magnetization out of equilibrium in this case can be characterized by a dependence of the relaxation time τ with the energy:

$$\tau = \tau(E). \tag{3.23}$$

The relaxation of the total magnetization for such an inhomogeneous sample is given by a sum of magnetization relaxation terms arising from regions of the sample with relaxation times $\tau(E_i)$, where E_i are the energy barrier heights:

$$M(t) = M_1(0)e^{\frac{1}{\tau(E_1)}} + M_2(0)e^{\frac{1}{\tau(E_2)}} + \cdots$$
$$= \sum M_i(0)e^{\frac{1}{\tau(E_i)}} = M(0)\sum f(E_i)e^{\frac{1}{\tau(E_i)}}, \tag{3.24}$$

where $f(E_i)$ is the fraction of the magnetization of initial value $M_i(0)$ that, to rotate, has to surmount a barrier with energy E_i:

$$f(E_i) = \frac{M_i(0)}{M(0)}. \tag{3.25}$$

In the continuous limit,

$$M(t) = M(0) \int_0^\infty f(E)e^{\frac{1}{\tau(E)}} \, dE. \tag{3.26}$$

The above integral can be approximated by

$$M(t) \approx M(0) \left[1 - k_\mathrm{B} T f(\overline{E_\mathrm{B}}) \ln\left(\frac{t}{\tau_0}\right) \right], \tag{3.27}$$

where $\overline{E_\mathrm{B}}$ is the average barrier energy relevant for the experimental time window.

The phenomenon of magnetic viscosity consists in the variation of the magnetization with time, due to thermally excited jumps over the energy barriers. This effect is maximum when the sample is under an applied magnetic field with intensity close to the value of the coercive field. This effect has important practical consequences, meaning, for example, that a permanent magnet will gradually lose some of its magnetization with time, and also that magnetically recorded data may be lost after some period.

The quantity S, the magnetic viscosity, is defined as

$$S = -\frac{1}{M(0)} \frac{\partial M}{\partial(\ln t)}, \tag{3.28}$$

where $M(0)$ is the magnetization at the time $t = 0$. It should be noted that the above expression is not valid for $t \to \infty$.

The magnetic viscosity is usually measured by magnetizing the system under study, maintaining a constant magnetic field, and observing the variation of the magnetization as a function of time t; the decrease of the remanent magnetization is illustrated in Fig. 3.14 for FePt nanoparticles. The figure shows that the remanent magnetization of the FePt particles exhibit a linear dependence vs. $\ln t$, with approximately the same slope in the temperature range from 3 to 12 K.

The magnetic viscosity may be related to a volume element called activation volume V^*, through (e.g., [19]):

$$S = \frac{k_\mathrm{B} T}{\mu_0 V^* M_\mathrm{s}}. \tag{3.29}$$
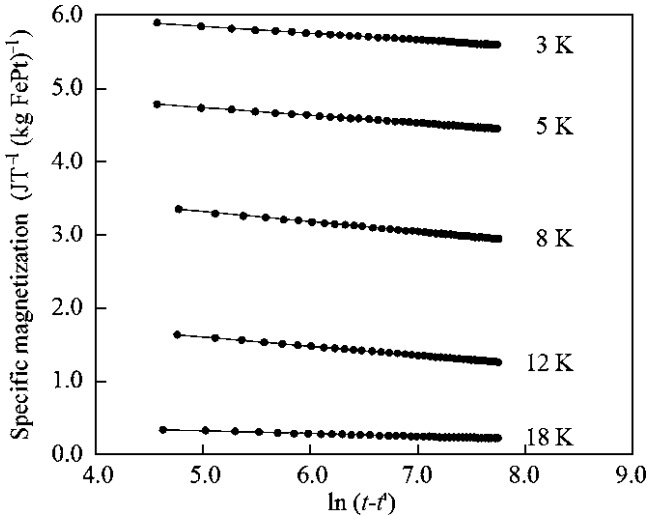
Fig. 3.14. Decay of the remanent magnetization of FePt nanoparticles as a function of $ln\ (t-t')$, for different temperatures, exhibiting a linear behavior; t' is a fitting parameter [21]. (With permission from Elsevier Science and Technology)

From the definition of S and the approximate expression for $M(t)$ (3.27), one obtains

$$S = -\frac{1}{M(0)}\frac{\partial M}{\partial(\ln t)} = f(\overline{E_B})k_B T. \tag{3.30}$$

One can read the above equation as a description of the fact that as the average energy barrier height $\overline{E_B}$ varies, the measurement of the viscosity maps the distribution of energy barriers. This is so because at a given temperature, the smaller barriers are the first to be overcome; the higher barriers have a smaller probability of being surmounted, and therefore the corresponding magnetizations contribute to the signal mostly for longer measurement times. If the system is now observed at a higher temperature, the time scale is contracted: the lower barriers will now be overcome in an even shorter time, and the reversals associated to the higher barriers will also occur at times shorter than those at the previous temperature.

An illustration of the magnetic viscosity measurement reflecting the distribution of energy barrier heights is given in Fig. 3.15 for the case of FePt nanoparticles [21]. In this case, from the appearance of two peaks in the curve, there seem to be two components in the distribution of barriers.

3.3.1 Superparamagnetism: The Langevin Function

The temperature dependence of the magnetization of an assembly of particles in the superparamagnetic regime is described by the Langevin function. Its derivation follows the same steps used to obtain the expression of the magnetization of an
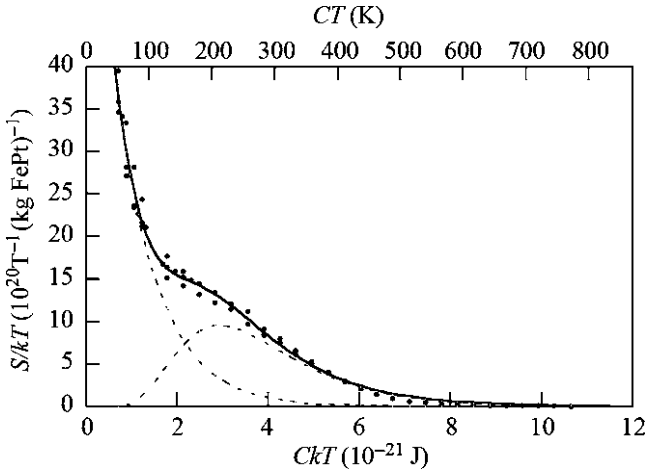
Fig. 3.15. Graph of $S/k_B T$ vs. $k_B T$ giving the apparent distribution of energy barriers of FePt particles weighted by their magnetizations. The *curve* indicates the existence of two components in this distribution [21]. (With permission from Elsevier Science and Technology)

ensemble of paramagnetic atoms (e.g., [23]). At variance with the case of atoms, in which the quantization of the angular momentum has to be taken into account, here this quantity is not quantized, since the angular momentum of a particle is a sum of contributions from a large number of atoms; hence the name superparamagnetic. If, differently from the quantum case, the angular momenta are allowed to vary continuously, every value between $-\mu_J$ and μ_J of the projection μ^z along the z axis will be allowed. The total magnetic moments will form any angle with the direction of the external magnetic field **B**, in this classical limit.

The projection of the magnetic moment μ along the z direction in the classical case is given by

$$\mu^z = \mu \cdot \mathbf{k} = \mu \cos \theta, \tag{3.31}$$

where the angle θ may take any value between 0 and π.

Making the average over θ, one arrives, after some algebra, at the expression for the z projection of the magnetic moment:

$$\langle \mu^z \rangle_T = \mu \, L(x), \tag{3.32}$$

where x is the ratio of the magnetic energy to the thermal energy ($x = \mu B / k_B T$) and $L(x)$ is the Langevin function, given by

$$L(x) = \coth x - \frac{1}{x}. \tag{3.33}$$

The Langevin function $L(x)$ is therefore the classical analogue of the Brillouin function ((2.6), p. 25), which describes paramagnetism. The Langevin function describes well the magnetization of small particles formed of clusters of atoms, which
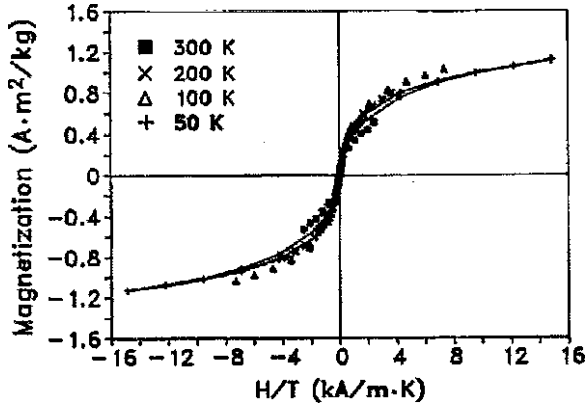
Fig. 3.16. Hysteresis curves of $\gamma-Fe_2O_3$ nanoparticles at temperatures above 50 K, showing the superposition of the curves obtained at different temperatures, when plotted vs. H/T. (Reprinted with permission from [53]. Copyright [1993], American Institute of Physics)

constitute superparamagnetic systems. This is shown in Fig. 3.16, where the magnetization of superparamagnetic $\gamma-Fe_2O_3$ nanoparticles is represented vs. the ratio H/T. Since the Langevin function depends only on the quantity x, experimental results obtained for different temperatures fall on the same curve when drawn vs. H/T.

3.4 Surface Effects

The breaking of translation symmetry observed at the surface of small magnetic particles or clusters modifies the anisotropy of the atoms. Usually, this effect at the surface amounts to the appearance of an extra term in the anisotropy acting on the spins in this region, of the form

$$\mathscr{H} = K_s S_\perp^2,\tag{3.34}$$

where $S_\perp$ is the perpendicular component of the spin and K_s is the surface anisotropy, given in units of energy per unit area. The surface anisotropy constant K_s can be positive or negative: if this term is locally dominant, as it often happens, the surface in the first case becomes an easy plane, in the second, its normal becomes an easy direction; these two situations are represented in Fig. 3.17.

The corresponding anisotropy energy term has the form

$$e_s = K_s[1 - (\mathbf{m}\cdot\mathbf{n})^2],\tag{3.35}$$

where $\mathbf{m}$ is the magnetization and $\mathbf{n}$ is the normal to the surface. For example, the surface anisotropy constant for Co films on different substrates have values in the range 0.1–0.9 J m^{-2}.
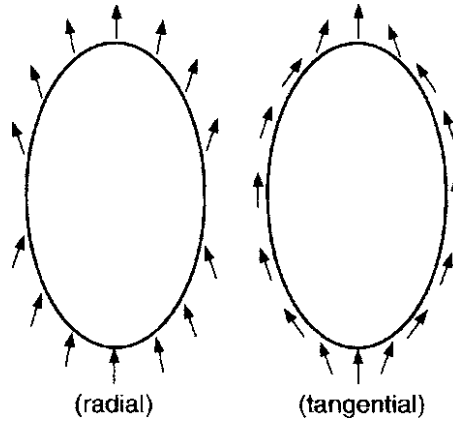
(radial)   (tangential)

Fig. 3.17. The effective anisotropy at the surface of a particle of the form S_z^2 in two cases: (**a**) K < 0 (radial) and (**b**) K > 0 (tangential). (Reproduced with permission from [4])

Due to the importance of the surface contribution for small particles, the effective anisotropy for spherical particles usually exhibits the following empirical dependence with the diameter d (e.g., [6]):

$$K_{\text{eff}} = K_{\text{vol}} + 6\,\frac{K_{\text{s}}}{d}, \tag{3.36}$$

where K_{vol} is the anisotropy constant of a macroscopic sample, and K_{s}, the surface anisotropy constant.

The effective anisotropy of a small particle is enhanced as its diameter is reduced, as described by the $1/d$ dependence of the surface anisotropy term. An example of this behavior of increasing K_{eff} with decreasing diameter is shown in Fig. 3.18 for nanometric Co grains in a copper matrix, derived from FMR measurements [41]. This increase in anisotropy is also evident from measurement of the relaxation times of individual Fe_3O_4 nanoparticles using Lorentz microscopy, a variant of transmission electron microscopy (TEM) [38].

The surface contribution to the anisotropy may lead to a complex distribution of directions of the individual spins near the surface. The picture of the surface of the particles that emerges from many studies is that of a region with spin disorder, similar to a spin glass, with the surface spins magnetically coupled to the ordered core of the particle. The disorder at the surface is related to the occurrence of irreversible behavior, as well as time dependent phenomena, and an increased magnetic hardness. These effects have been observed, for example, with $NiFe_2O_4$ particles [32]. The disordered spin configuration of a 4 nm diameter $NiFe_2O_4$ particle, computed using a Monte Carlo simulation, illustrates this point (Fig. 3.19).

Many types of nanoparticles have their magnetism described in terms of a core-shell spin structure (Fig. 3.20). In the core-shell description, the particle is divided into two regions that are magnetically coupled, one usually with ferromagnetic spin ordering (the core), surrounded by a shell, either of antiferromagnetic (AFM), or
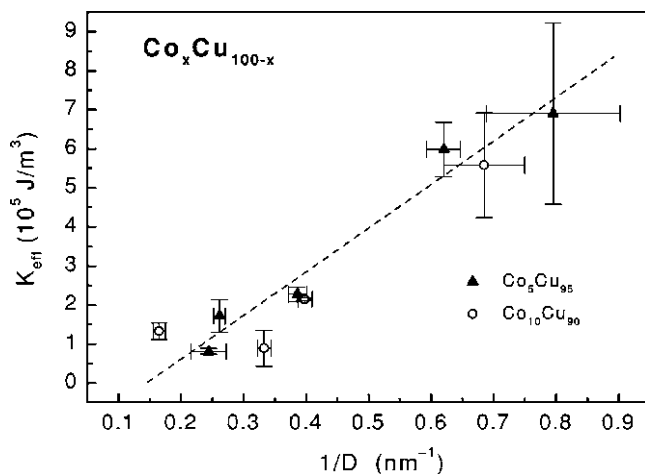
Fig. 3.18. Effective anisotropy parameter vs. diameter of Co grains in CoCu alloys measured with ferromagnetic resonance (FMR). (Reprinted figure with permission from [41]. Copyright (2003) by the American Physical Society [41])
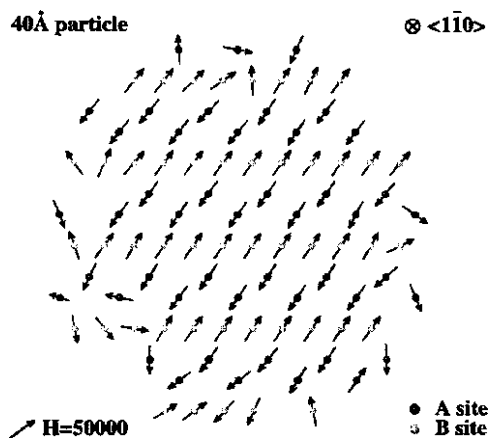
Fig. 3.19. Computed spin configuration of a nanoparticle of 4 nm of $NiFe_2O_4$, showing the spin disorder at the surface of the particles [32]. (Reprinted figure with permission from [32]. Copyright (1999) by the American Physical Society)

of disordered spin-glass-like spin structure. These two regions may have the same chemical composition, or may be formed of different materials, e.g., Co and CoO.

Nanoparticles prepared from 3d metals are chemically reactive, and tend to develop a layer of metal oxide. For example, Fe nanoparticles with diameters in the range 5–20 nm, with an outer layer of iron oxides, exhibit a core-shell structure, as inferred from magnetic measurements and TEM images [17]. The shell is magnetically
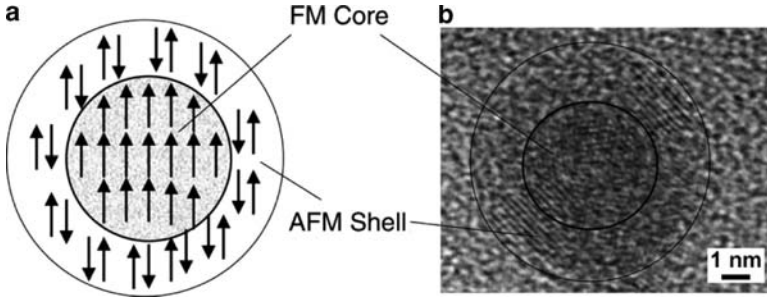
Fig. 3.20. (a) Core-shell structure **(b)** and TEM image of a magnetic nanoparticle of oxidized Co [39]. (With permission from Elsevier Science and Technology)

coupled to the core, and exhibits superparamagnetic behavior. The experimental results also show for the smaller particles a higher coercivity, that depends strongly on temperature.

Particles with core-shell structure, with FM cores surrounded by AFM shells are also known to present the exchange bias phenomenon [26] (see Sect. 4.4, on exchange bias, p. 117).

3.5 The Stoner–Wohlfarth Model

The first model that was proposed to describe the magnetism of small particles was developed by Stoner and Wohlfarth in 1948 [46] and is still used today. This treatment considers the magnetic particles homogeneous single-domains with the shape of elongated ellipsoids.

In the equation used in Chap. 2 to describe the free energy of the magnetic material ((2.54), p. 35), the first term is the contribution arising from the exchange interaction. If the magnetization is homogeneous, $\nabla \mathbf{M} = 0$ and the exchange contribution is zero. The Stoner–Wohlfarth treatment therefore corresponds to the simplest micromagnetic approach, one that neglects the exchange term in the total free energy function. This treatment, that assumes coherent reversal of the ensemble of individual atomic magnetic moments, behaving as a single moment, is sometimes referred to as the macrospin model.

Let us consider a single-domain particle in the shape of an elongated rotationally symmetric ellipsoid, with homogeneous magnetization and easy axis of magnetization along the z direction, the direction of its long axis. The magnetostatic energy terms along the major axis ($E_{ms}^{\parallel}$) and perpendicular to this axis ($E_{ms}^{\perp}$) will be (from (2.34), p. 31):

$$E_{ms}^{\parallel} = -\frac{1}{2} N_{\parallel} \mu_0 M_s^2 V \cos^2 \theta, \tag{3.37}$$

and

$$E_{ms}^{\perp} = -\frac{1}{2} N_{\perp} \mu_0 M_s^2 V \sin^2 \theta. \tag{3.38}$$
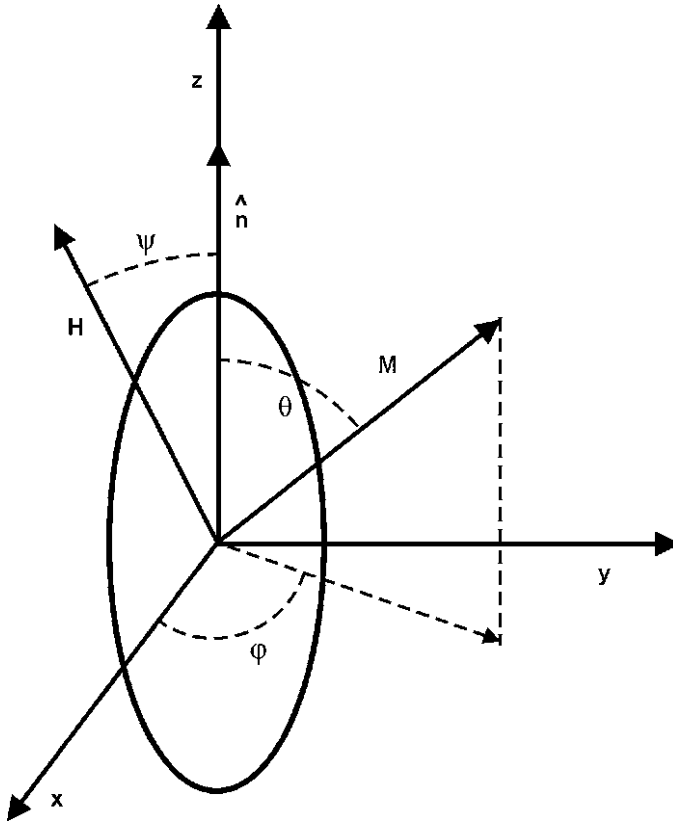
Fig. 3.21. Single-domain ellipsoidal particle in a magnetic field **H**, showing the relevant angles between this field, the anisotropy axis z and the magnetization M

The angle θ is the angle between the magnetization and the anisotropy axis (Fig. 3.21), and $N_\perp$ and $N_\parallel$ are the demagnetization or demagnetizing factors in the perpendicular and parallel directions. Figure 3.21 represents this ellipsoid, with the long axis pointing along the z axis, the same direction of the effective uniaxial anisotropy.

The total energy of the ellipsoid in the presence of an external magnetic field H that forms an angle ψ with its direction of easy magnetization, and whose magnetization forms an angle θ with this direction (with **H** on the xz plane and **M** not in the same plane, Fig. 3.21) is given by

$$\frac{E}{V} = K_1 \sin^2 \theta + K_2 \sin^4 \theta - \frac{1}{2}\mu_0 N_\perp M_s^2 \sin^2 \theta - \frac{1}{2}\mu_0 N_\parallel M_s^2 \cos^2 \theta - \mu_0 M_s H$$
$$\times (\cos \theta \cos \psi + \sin \theta \sin \psi \cos \varphi), \tag{3.39}$$

where K_1 and K_2 are the first and second uniaxial anisotropy constants, V is the volume of the particle, and M_s is the saturation magnetization. The anisotropy axis here coincides with the long axis of the ellipsoid. The physical origin of this anisotropy can be the shape anisotropy or a sum of crystal and shape effects, both along the same axis. φ is the angle that the projection of $\mathbf{M}$ makes with the x axis.

With $H = 0$, the magnetization points along the anisotropy axis; with a nonzero magnetic field, the magnetization rotates and the problem is reduced to a planar configuration ($\varphi = 0$). Ignoring the second order anisotropy term, one has:

$$\begin{aligned} \frac{E}{V} &= K_1 \sin^2 \theta - \frac{1}{2}\mu_0 M_s^2 (N_\perp \sin^2 \theta + N_\parallel \cos^2 \theta) \\ &\quad - \mu_0 M_s H(\cos \theta \cos \psi + \sin \theta \sin \psi) \\ &= K_1 \sin^2 \theta - \frac{1}{2}\mu_0 M_s^2 (N_\perp \sin^2 \theta N_\parallel \cos^2 \theta) - \mu_0 M_s H(\cos (\psi - \theta)). \end{aligned} \quad (3.40)$$

In the simplest case, the magnetic field $\mathbf{H}$ is applied along the anisotropy axis, and therefore $\psi = 0$. To obtain the angle θ between the anisotropy axis and the magnetization, one needs to minimize the energy, computing $\partial E(\theta)/\partial \theta = 0$:

$$2K_1 \sin \theta \cos \theta - \mu_0 M_s^2 \sin \theta \cos \theta (N_\perp - N_\parallel) - \mu_0 M_s H \sin (\psi - \theta) = 0. \quad (3.41)$$

Computing the second derivative to define a minimum, one obtains the expression for the nucleation field H_N:

$$H_N = \frac{2K_1}{\mu_0 M_s} - M_s(N_\perp - N_\parallel). \quad (3.42)$$

A magnetic field that has precisely this magnitude is sufficient to rotate the magnetization, and is therefore equal to the coercive field. It should be pointed out that this result does not depend on the size of the particle, only on its shape. In the limiting cases of a sphere and a bidimensional sample, or plate, one has

$$H_N^{\text{sph}} = \frac{2K_1}{\mu_0 M_s}. \quad (3.43)$$

and

$$H_N^{\text{pla}} = \frac{2K_1}{\mu_0 M_s} + M_s. \quad (3.44)$$

The term $N_\perp - N_\parallel = N_{\text{eff}}$ is the effective demagnetizing factor of the particle in the direction of $\mathbf{M}$. Since $N_\parallel + 2N_\perp = 1$, N_{eff} is also given, using $N = N_\parallel$, by

$$N_{\text{eff}} = \frac{1}{2}(1 - 3N). \quad (3.45)$$

The value of the nucleation field given by (3.42) is not observed experimentally. In real systems, the nucleation field or the coercive field are always smaller than $2K_1/(\mu_0 M_s) - M_s(N_\perp - N_\parallel)$. This disagreement is usually referred to as Brown's paradox, and arises from the fact that there are always imperfections that favor the

nucleation of magnetic domains with opposite magnetization, reducing in consequence the nucleation or coercive fields.

The height of the barrier separating the two anisotropy energy minima can be computed by solving $\partial E(\theta)/\partial\theta = 0$. For $\psi = 0$, there are three solutions, given by the following values of the angle: $\theta = 0$, $\theta = \arccos(-\mu_0 M_s H/(2K_1))$ and $\theta = \pi$. The second solution corresponds to the position of the maximum of the barrier, with energy E_{max}. Since $\cos(\mu_0 M_s H/(2K_1)) \leq 1$, this expression gives the minimum field that allows (at $T = 0$ K) the inversion of the magnetization, which is H_A, the anisotropy field in the absence of the demagnetizing field:

$$H_A = \frac{2K_1}{\mu_0 M_s}. \tag{3.46}$$

From the position of the minima, one can derive the height of the barrier, corresponding to $\Delta E = E_{max} - E(\theta = 0)$. Doing some algebra, one arrives at:

$$\Delta E = K_1 V \left(1 - \frac{H}{H_A}\right)^2. \tag{3.47}$$

Therefore, the barrier height is proportional to $K_1 V$ and disappears for $H = H_A$.

The inclusion of the second term in the uniaxial anisotropy energy ($K_2 \sin^4\theta$) leads to a more complicated result, with a change in magnetic behavior under the external field, with the appearance of two nucleation fields, if $K_1 < 4K_2$ (with $K_1 > 0$).

This description is applicable to ferromagnetic particles at $T = 0$ K. At $T \neq 0$ K, when the applied magnetic field reaches a value that makes the barrier height comparable to $25k_B T$, thermal activation induces the transition into the superparamagnetic regime. Equating $\Delta E = 25k_B T$, one can obtain the value of the magnetic field that reverses the magnetization, the nucleation field at finite temperature [27]:

$$H_N = \frac{2K_1}{\mu_0 M_s}\left[1 - 5\left(\frac{k_B T}{K_1 V}\right)^{1/2}\right]. \tag{3.48}$$

This formula, for $T = 0$ K, gives the Stoner–Wohlfarth expression (3.46); it is valid from $T = 0$ K to $T = K_1 V/25k_B$, at which temperature the expression of the nucleation field is zero. Above this temperature, the sample behaves as a superparamagnet, and the coercive field H_c is zero.

Expressing the volume of the particle as $V = \alpha D^3$, where α is a geometrical factor that takes into account the shape of the particle, the critical superparamagnetic diameter is written $D_{cr}^{spm} = (25k_B T/\alpha K_1)^3$; the expression for D_{cr}^{spm} given previously in (3.17), for a sphere, had $\alpha = \pi/6$. Using D_{cr}^{spm}, one obtains an alternative expression for the nucleation field H_N, where the factor α cancels out:

$$H_N = \frac{2K_1}{\mu_0 M_s}\left[1 - \left(\frac{D_{cr}^{spm}}{D}\right)^{3/2}\right]. \tag{3.49}$$
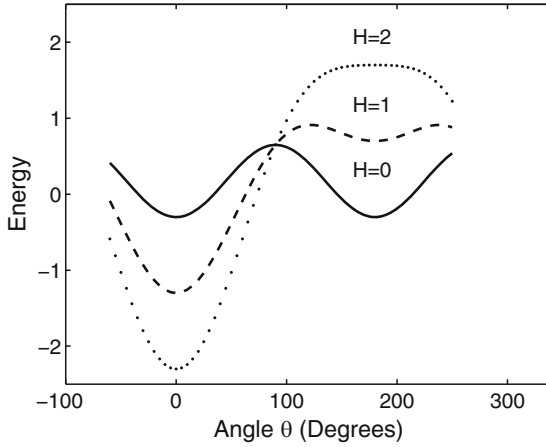
Fig. 3.22. Dependence of the energy with the angle between the magnetization and the anisotropy axis $E(\theta)$ in the Stoner–Wohlfarth model, for different values of H, for H parallel to the anisotropy axis (i.e., $\psi = 0$)
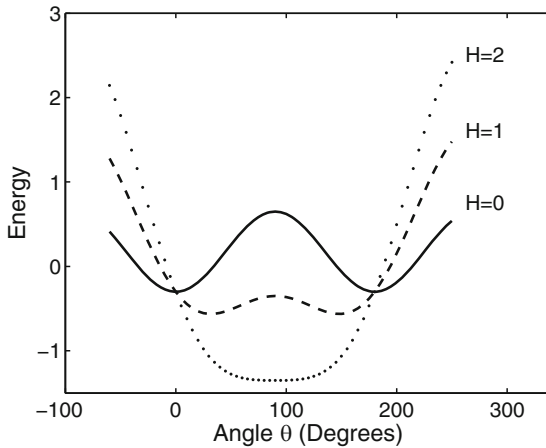
Fig. 3.23. Dependence of the energy with the angle between the magnetization and the anisotropy axis $E(\theta)$ in the Stoner–Wohlfarth model, for different values of H, for H perpendicular to the anisotropy axis (i.e., $\psi = \pi/2$)

The nucleation field given by this equation is the magnetic field that starts the inversion in the direction of magnetization of the particle. When a field of intensity given by (3.46) is applied in the direction opposite to the magnetization (still along the anisotropy axis) **M** turns, and in this case the nucleation field H_N is equal to the anisotropy field H_A.

The curves of the energy $E(\theta)$ for different values of applied magnetic field H, applied parallel or perpendicular to the ellipsoid long axis are plotted, respectively, in Figs. 3.22 and 3.23.

The anisotropy of the particle can be characterized through its curve of switching field (the magnetic field for maximum $|dM/dH|$) vs. the angle ψ between **H** and the anisotropy axis.

From (3.41), neglecting the magnetostatic term, it follows:

$$\sin 2\theta = -\frac{\mu_0 M_s H}{K_1} \sin (\theta - \psi).$$ (3.50)

The angle θ for stable equilibrium condition is obtained by computing $\partial^2 (E/V)/\partial \theta^2$ (where E/V is given by (3.40)) and equating to zero:

$$2K_1 \cos 2\theta + \mu_0 M_s H (\cos (\psi - \theta)) = 0,$$ (3.51)

and

$$\cos 2\theta = -\frac{\mu_0 M_s H}{2K_1} \cos (\theta - \psi).$$ (3.52)

Dividing (3.50) by (3.52) one obtains:

$$\tan 2\theta = 2 \tan (\theta - \psi),$$ (3.53)

which leads to

$$\tan \theta = - \tan^{1/3} \psi.$$ (3.54)

Summing the squares of (3.50) and (3.52), one obtains, after doing some algebra, the magnetic field H_{sw}, the field that satisfies the condition of switching the magnetization. It is described by the function

$$\frac{H_{sw}}{H_A} = \frac{1}{(\sin^{2/3} \psi + \cos^{2/3} \psi)^{3/2}},$$ (3.55)

where

$$H_A = \frac{2K_1}{\mu_0 M_s}$$ (3.56)

is the anisotropy field.

From the angles defined in Fig. 3.21, one can express the components of the switching field H_{sw} parallel and perpendicular to the anisotropy axis as:

$$H_{para} = H_{sw} \cos \psi$$ (3.57)

and

$$H_{perp} = H_{sw} \sin \psi.$$ (3.58)

Dividing H_{para} and H_{perp} by the anisotropy field H_A one obtains the reduced fields h_{para} and h_{perp}. Substituting $\sin \psi$ and $\cos \psi$ into (3.55), it follows

$$1 = \frac{1}{(h_{perp}^{2/3} + h_{para}^{2/3})^{3/2}}.$$ (3.59)
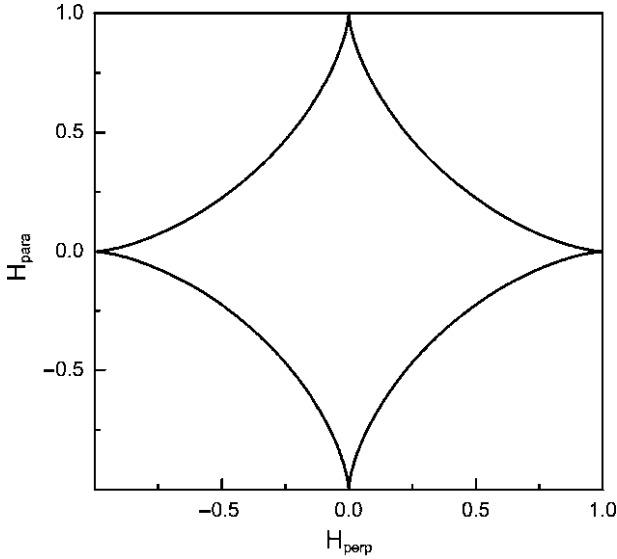
Fig. 3.24. Astroid curve, obtained by drawing the component of the switching field (divided by H_A) parallel to the anisotropy axis h_{para} vs. the perpendicular component h_{perp}, with the dependence given by (3.59)

The curve given by (3.55) or (3.59), is known as an astroid; it is the curve drawn by a point on the perimeter of a circle of radius $1/4$ rolling inside a circle of radius 1. The astroid curve is shown in Fig. 3.24.

The angular dependence of the switching field given by the equation of the astroid (3.55) differs from that predicted in an early work of Kondorsky (1937) [33], $H(\theta) = H_0/\cos\theta$.

If one includes the second-order contribution to the magnetic anisotropy, the term containing K_2, (3.55) is modified, becoming [34]:

$$H_{sw} = \frac{2(K_1 + K_d)}{\mu_0 M_s} \frac{1}{(\sin^{2/3}\psi + \cos^{2/3}\psi)^{3/2}}$$
$$\times \left[1 + \frac{2K_2}{K_1 + K_d} \frac{\sin^{2/3}\psi}{(\sin^{2/3}\psi + \cos^{2/3}\psi)}\right]. \qquad (3.60)$$

In the above equation, we have included the shape anisotropy energy K_d; this anisotropy term and the crystal anisotropy are assumed to be minimum along the same axis:

$$K_d = \frac{1}{2}\mu_0 M_s^2 (N_\perp - N_\parallel). \qquad (3.61)$$

The curve of H_{sw}/H_A, drawn as ψ varies from 0 to 2π is obtained by measuring the switching field as a function of angle, for a single particle. Measurements of switching fields performed on individual single-domain magnetic particles using

micro-SQUIDs give the form of dependence predicted by the Stoner–Wohlfarth model (3.55), as shown in Fig. 3.25.

In Fig. 3.26 it is displayed the dependence of the switching field with the angle in the Stoner–Wohlfarth model. Also the angular dependence of the coercive field H_c is shown. This graph shows how, in the Stoner–Wohlfarth model, for angles beyond
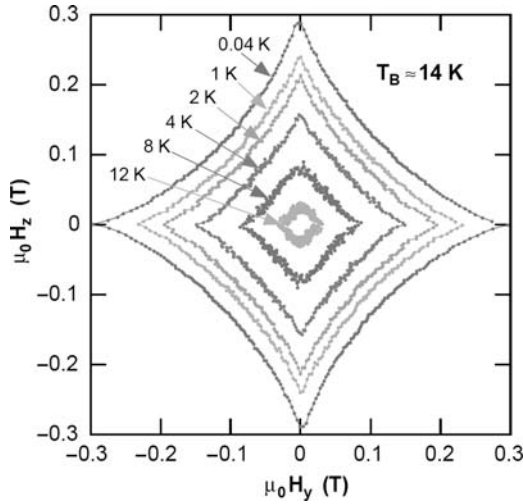
Fig. 3.25. Switching field vs. angle curves (astroid curves), for a Co nanoparticle at different temperatures [52]. (With permission from Elsevier Science and Technology)
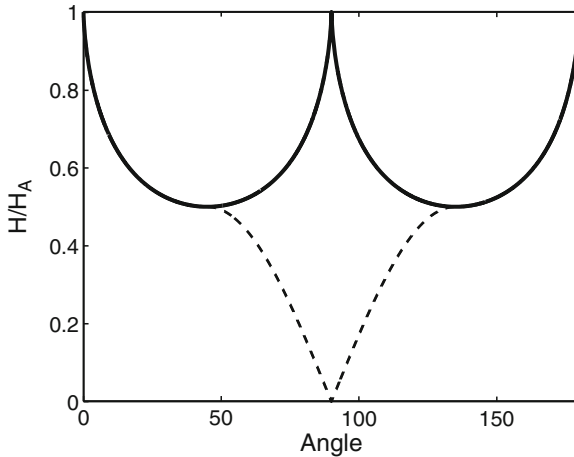
Fig. 3.26. Angular dependence of the switching field H_{sw} (*continuous line*) in the Stoner–Wohlfarth model. The graph shows that H_{sw}/H_A is maximum for $\theta = 0$ and $\theta = \pi/2$, and minimum for $\theta = \pi/4$. The graph also shows H_c/H_A, that has the same dependence, except around $\theta = \pi/2$ (*dotted lines*)
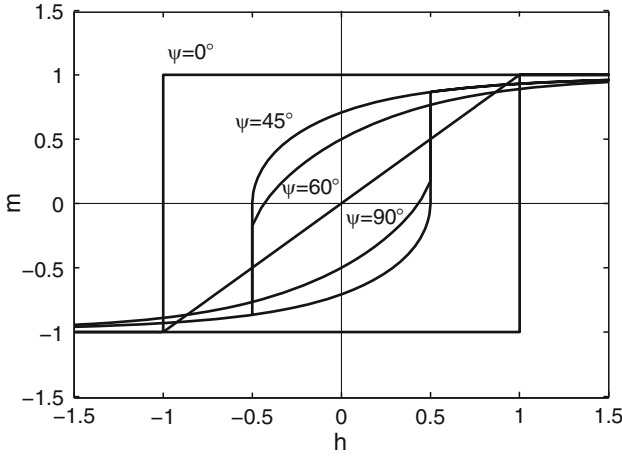
Fig. 3.27. Hysteresis loops of reduced magnetization m of homogeneously magnetized ellipsoids, vs. reduced magnetic field $h = H/H_A$, for different angles θ, in the Stoner–Wohlfarth model

45°, the magnetic fields for which $M = 0$ (usual definition of coercive fields) differ from the fields of maximum $|dM/dH|$ (switching fields), as can be noted in the graph of the hysteresis curves (Fig. 3.27).

A magnetic field smaller than the switching field predicted by the Stoner–Wohlfarth model may produce a magnetization reversal under some special circumstances, e.g., when the applied magnetic field direction is made to vary in a specified way with time during the switching process [47].

From the minimization of the energy of the magnetic particle as a function of θ, one obtains the magnetization as a function of H, for each value of the angle θ. This is obtained by solving the equation (derived from (3.41) and (3.42)):

$$H_N \sin(2\theta) - H\sin(\psi - \theta) = 0. \tag{3.62}$$

The solution, in terms of $m = (M/M_s)\cos(\theta - \psi)$, the reduced magnetization in the direction of the applied magnetic field, is represented in Fig. 3.27, as a function of H, showing the corresponding hysteresis loops, for some values of θ.

Stoner and Wohlfarth also considered the hysteresis curve of an assembly of magnetic particles, with every value of the angle θ; summing the magnetization curves of these particles, one obtains a hysteresis curve that has (at $T = 0$ K) a magnetic remanence of $\frac{1}{2}M_s$ and a reduced coercivity $H_c/H = 0.48\ h$, where h is the reduced magnetic field $h = H/H_A = \mu_0 HM_s/2K_1$ (Fig. 3.28).

The Stoner–Wohlfarth model describes the magnetization of magnetic particles at $T = 0$ K. At $T = 0$ K the particles invert their magnetizations when, under the action of the field H, the energy barriers that separate the two configurations (up or down along the anisotropy axis) tend to zero.

The Stoner–Wohlfarth model does not take into account the possibility of thermal excitation to surmount the energy barrier between the two magnetization directions,
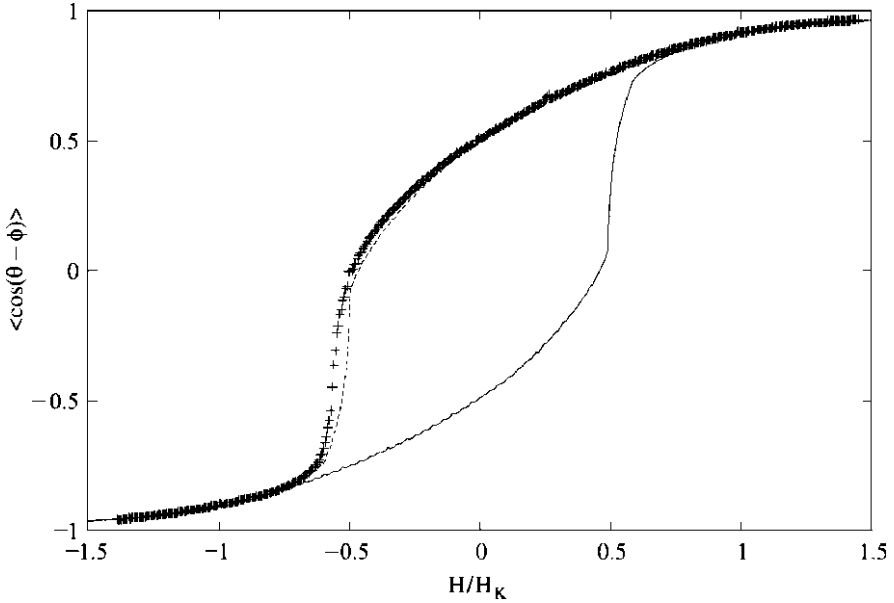
Fig. 3.28. Stoner–Wohlfarth hysteresis curve for an assembly of particles with every possible value of θ (*points*, only the upper branch of the graph). The *continuous line* was calculated from a three-dimensional simulation [48]

in other words, the model is valid only for $T = 0$ K, but the theory may be generalized for any temperature. In order to do this it is only necessary to include the thermal excitations for $T \neq 0$ K. In this case there will occur jumps over the barrier, and the particles will invert their magnetization before the variation of magnetic field H makes the barrier height reach zero.

For the same value of the magnetic field H, the height of the barrier for switching the magnetization shows a dependence with angle θ that is different for different values of the angle ψ between H and the direction of the axis of each particle. This is shown in Fig. 3.29.

The coercivity is a property that can be derived from the hysteresis curve of a sample. The fastest the rate of change of the magnetic field sweep used to obtain the hysteresis loop, the higher the measured coercivity. This sweep rate dependence of the coercivity is related to the magnetic viscosity phenomenon and results from the fact that the coercivity is a dynamic property.

The rate dependence of the coercivity can be shown in a simple way by inserting the expression of the energy barrier height as a function of the anisotropy field (3.47),

$$\Delta E = K_1 V \left(1 - \frac{H}{H_A} \right)^2, \tag{3.63}$$

into the Néel–Arrhenius Law (3.13), that describes the relaxation time, or inverse of the switching frequency: $\tau = \tau_0 \, \exp(E_B/k_B T)$.
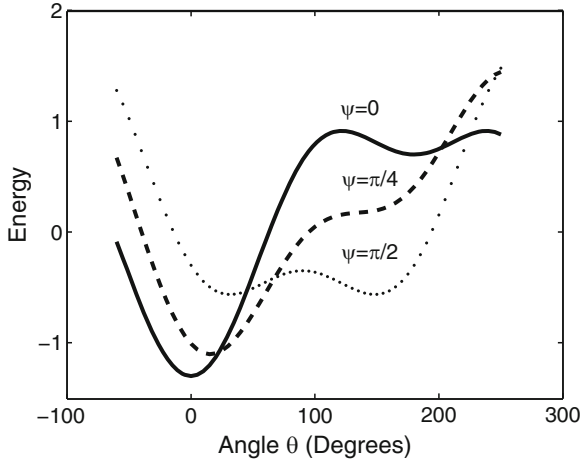
Fig. 3.29. Energy as a function of the angle θ, for different values of the angle ψ between H and the direction of the axis of the particle, for the same value of H, showing the variation in barrier height for inversion of the magnetization in the Stoner–Wohlfarth model

Identifying the magnetic field H as the coercive field of the sample, one obtains for H_c:

$$H_c = H_A \left[1 - \left(\frac{k_B T}{KV} ln \frac{\tau}{\tau_0} \right)^{1/2} \right]. \tag{3.64}$$

Writing this expression in terms of the magnetic field sweep rate $\eta = dH/dt \sim 1/\tau$ and generalizing for an exponent $1/m$, using generalized parameters K_0 and V_0, which make the result applicable to other magnetization reversal processes besides that of the aligned Stoner–Wohlfarth particle, it follows [44]:

$$H_c = H_A \left[1 - \left(\frac{k_B T}{K_0 V_0} ln \frac{\eta}{\eta_0} \right)^{1/m} \right]. \tag{3.65}$$

This equation shows an explicit dependence of the coercive field with the sweep rate η.

The magnetization of a polydisperse ensemble of particles (i.e., with a distribution of volumes $f(V)$), is given by the sum of the contributions of their magnetizations. In this case there may be a coexistence of different magnetic regimes: at $T \neq 0$, there will be three contributions to the magnetization: (1) the contribution of the particles with volume below the critical blocking volume V_{cr}^{spm}, that therefore exhibit superparamagnetic behavior, (2) the contribution of the particles with the axes in a direction such that the thermal excitation inverts the magnetization ($V_{cr} > V > V_{cr}^{spm}$, where $V_{cr} = V_{cr}(H, \psi)$ is the critical volume for this effect) and finally, (3) the ferromagnetic contribution of the particles with $V > V_{cr}$.

Consequently the magnetization of the ensemble of particles is described as a sum of the three volume integrals:

$$M = \int_0^{V_b} L(V,H)f(V)dV + \int_{V_b}^{V_{cr}} M(V,H,\psi)f(V)dV + \int_{V_{cr}}^{\infty} M(V,H,\psi)f(V)dV, \tag{3.66}$$

where $L(V,H)$ is the Langevin function.

Introducing θ_1 and θ_2, the angles between the anisotropy axis and the equilibrium magnetization before and after the inversion due to the magnetic field, the above equation becomes [11]:

$$M = \int_0^{V_b} L(V,H)f(V)dV$$
$$+ \int_0^{\pi/2} \left(\int_{V_{cr}}^{\infty} \cos(\theta_1) \sin \psi f(V)dV - \int_{V_b}^{V_{cr}} \cos(\theta_2) \sin \psi f(V)dV \right) d\psi. \tag{3.67}$$

In this equation, the first integral represents the contribution to the magnetization due to the superparamagnetic particles; the second and the third integrals account for, respectively, the contribution of the particles that have inverted the magnetization and that due to those particles whose magnetizations have not been inverted.

The Stoner–Wohlfarth model is strictly applicable to the case of particles with uniaxial anisotropy; in the case of cubic anisotropy, for example, the problem of magnetization switching is more complex, and requires for its description a three-dimensional model [51].

3.5.1 Inhomogeneous Magnetization Reversal

The magnetization reversal of small particles, as described by the Stoner–Wohlfarth model, is a coherent process, in the sense that the magnetic moments remain strictly in parallel throughout the reversal process. This ideal situation is approximately realized in homogenous nanoparticles.

In the inhomogeneous or incoherent reversal of the magnetization, the local magnetization vectors do not remain parallel to one another as the applied magnetic field forces the reversal of the magnetization. The main form of incoherent reversal of the magnetization is the curling process; another form, the buckling process, is less common. They are both illustrated in the case of a cylinder, in Fig. 3.30. In the curling mode the magnetization is tangential to cylindrical surfaces that have as axes the common longitudinal axis. The buckling mode describes an arrangement where the deviation of the local magnetization is a periodic function of the position along a longitudinal axis.

Also shown in Fig. 3.30 is the process known as fanning, where the reversal arises from the interaction between particles in a chain.

The appearance of uncompensated magnetic charges during the process of magnetization reversal increases the magnetostatic energy. In a cylinder that reverses the magnetization through the curling mode, these charges appear only on the flat
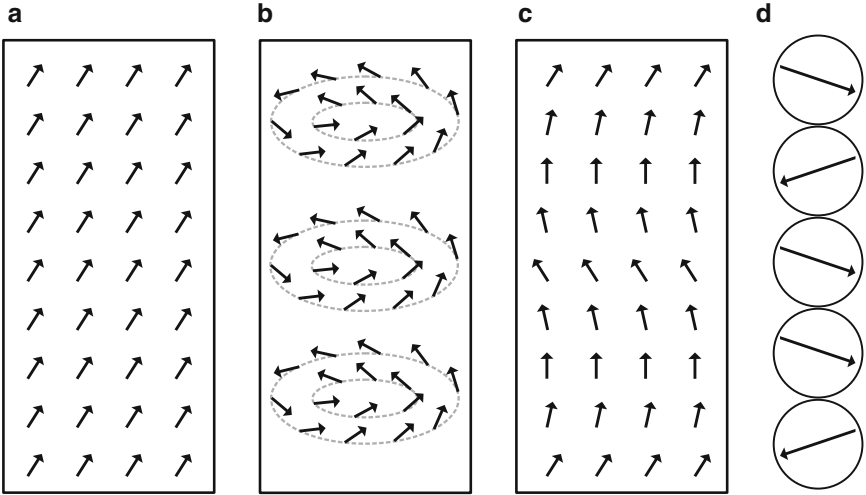
Fig. 3.30. Magnetization reversal modes for a cylinder, or cylinder-like sample: (**a**) coherent, (**b**) curling, (**c**) buckling and (**d**) fanning, a mechanism of reversal for a chain of magnetic spheres

surfaces (top or bottom), and therefore the magnetostatic energy remains small. The exchange term in the free energy increases, since in this case, differently from the homogeneous case, $\nabla \mathbf{m} \neq 0$.

The inhomogeneous reversal of the magnetization is a phenomenon intrinsically more complex than the homogeneous process. As a consequence, its theoretical description has been by and large limited to systems with simple shapes, in restricted physical circumstances.

The nucleation field for an ellipsoidal sample reversing the magnetization through a curling process is given by [43]:

$$H_N = \frac{2K_1}{\mu_0 M_s} - N_d M_s + \frac{cA}{\mu_0 M_s} \frac{1}{R^2}, \tag{3.68}$$

where R is either the smaller dimension of the ellipsoid or the radius of a sphere. For a sphere, $c = 8.666$ (and the demagnetizing factor $N_d = 1/3$), $c = 8.946$ for a plane ($N_d = 1$), $c = 6.780$ for an infinite cylinder or a needle-like sample ($N_d = 0$).

This equation expresses the fact that, since H_N varies as $\sim 1/R^2$, for small radii, homogeneous nucleation is dominant, since the nucleation field for homogenous reversal is smaller (3.42). For larger radii the magnetization reverses through inhomogeneous nucleation.

The critical diameter D_{cr}^{inh} for the transition from homogeneous to inhomogeneous nucleation can be found by equating the above expression to the nucleation field for homogeneous reversal (3.42). The result is:

$$D_{cr}^{inh} = 2\sqrt{\frac{2A}{\mu_0 M_s^2}} \sqrt{\frac{c}{2N_\perp}} = 2\sqrt{\frac{c}{2N_\perp}} \, l_{ex}. \tag{3.69}$$

Note that as the two expressions are equated ((3.42 and (3.68)), the anisotropy terms cancel out; this arises from the fact that the critical diameter for inhomogeneous reversal does not depend on the anisotropy, only on the exchange stiffness constant A and the saturation magnetization.

For an infinite cylinder, $c = 6.780$, $N_\perp = 1/2$, and one obtains:

$$D_{cr}^{inh} = 5.20\, l_{ex}. \tag{3.70}$$

This result predicts for long cylinders of α-Fe, Co and Ni, critical diameters for inhomogeneous nucleation of $\sim$15, $\sim$25 and $\sim$40 nm, respectively (see the table with values of l_{ex} on page **??**).

The form of the dependence of the nucleation field on the diameter of an infinite cylinder can be derived neglecting anisotropy (i.e., with $K = 0$) from (3.42) in the case of the coherent reversal and (3.68) for curling, using $c = 6.780$.

For a reversal by buckling, the condition is given, in the limit of large diameter $D = 2R$, by [16]:

$$\frac{H_N}{H_c} = \frac{278}{\rho^{2/3}} = \frac{3.78}{(D/l_{ex})^{2/3}}, \tag{3.71}$$

where $\rho = R/R_0 = R/l_{ex}\sqrt{(2/\mu_0)}$, R is the radius and D is the diameter.

This dependence of the nucleation field with diameter is illustrated in Fig. 3.31, where this effect is represented by H_N divided by the coercive field for coherent rotation $H_c = M_s/2$; the graph shows how the cylinders with smaller diameters tend to reverse the magnetization via coherent rotation, and above a certain critical diameter, the incoherent mechanisms, curling and buckling, are dominant. The coercive field in each case corresponds to the lowest switching field.
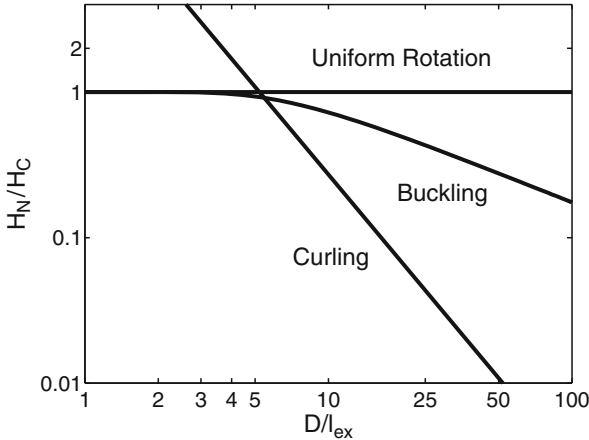
Fig. 3.31. Normalized nucleation fields vs. effective diameter of an infinite cylinder, for different processes of magnetization reversal: coherent, curling and buckling, based on [16]. The effective diameter is D/l_{ex}, where $l_{ex} = \sqrt{2A/\mu_0 M_s^2}$ is the exchange length. The graph shows that up to a certain sample diameter, coherent rotation is preferred, and above this value, one of the incoherent mechanisms is favored

If the experimental conditions are such that there is no demagnetizing field, for example, if the sample has a toroidal shape, the coercivity measured is the intrinsic coercivity H_c^i. Its expression can be obtained if one subtracts the demagnetizing field $-N_d M_s$ from the expression of (3.68). The result is:

$$H_c^i = \frac{2K_1}{\mu_0 M_s} + \frac{cA}{\mu_0 M_s R^2}. \qquad (3.72)$$

The dependence of the coercivity on the shape of the sample is still present in the second term of the intrinsic coercivity H_c^i, through the quantity c.

The angular dependence of the curling process differs from that derived for homogeneous rotation, in the Stoner–Wohlfarth model, given by (3.55). Neglecting the anisotropy contribution, the nucleation field for the curling process in a sample with the shape of a prolate (cigar-like) spheroid is given, as a function of the angle ψ, by [1]:

$$H_N = \mu_0 M_s \frac{\left(2N_c - \frac{c}{2\pi\rho^2}\right)\left(2N_a - \frac{c}{2\pi\rho^2}\right)}{\left[\left(2N_c - \frac{c}{2\pi\rho^2}\right)^2 \sin^2\psi + \left(2N_a - \frac{c}{2\pi\rho^2}\right)^2 \cos^2\psi\right]^{1/2}}. \qquad (3.73)$$

In this equation N_a and N_c are the demagnetizing factors along the short and long axes, respectively, c is the same numerical factor that depends on the sample shape, used in (3.68), and $\rho = R/R_0$, where R is the shortest semi-axis and $R_0 = \sqrt{(\mu_0/2)}l_{ex}$. This expression is also valid for a sphere, in which case $N_a = N_c$, and it results that H_N does not depend on the angle ψ. For $\rho \sim 2$ this expression also gives the coercive field, since in this case $H_c = H_N$.

3.5.2 Precessional Magnetization Reversal

The problem of magnetization reversal of a magnetic sample is very relevant for magnetic recording technology, since recording data involves changing the magnetization of a small portion of a magnetic medium, and achieving high writing speed on a magnetic disk, for example, requires the adequate understanding of this phenomenon. A single bit of information is recorded in a time much shorter than a nanosecond, and further advances in high-density magnetic recording demand forms of reducing this time even further (see Chap. 7, on magnetic recording). The increase in storage capacity of magnetic hard disks, to be of practical use, has to be accompanied by the development of faster forms of handling the recorded information.

In the Stoner–Wohlfarth model the conditions for the reversal of the magnetization are discussed from energy balance considerations: the particle switches when the applied magnetic field reduces the energy barrier to zero. The time scale of the application of the field is supposed to be much longer than the time τ_0, the inverse of the attempt frequency. For shorter time scales, the dynamics of the reversal has to be taken into account, with a description of the temporal evolution of the magnetization,

as given in approximate form by the Landau–Lifshitz–Gilbert equation (Sect. 2.3.1, beginning on page 39). This equation is:

$$\frac{d\mathbf{M}}{dt} = -\gamma\,\mathbf{M} \times \mathbf{H}_{\text{eff}} + \frac{\alpha}{M_{\text{s}}}\,\mathbf{M} \times (\mathbf{M} \times \mathbf{H}_{\text{eff}}),\tag{3.74}$$

where γ is the gyromagnetic factor, $\mathbf{H}_{\text{eff}}$ is the effective magnetic field and α is a damping factor.

The magnetization of a magnetic particle can also be reversed through the application of a pulsed magnetic field. In this case, the particle magnetization may be made to precess before switching to the opposite direction. The conditions for this precessional reversal present a great interest, due to the obvious application of this process to magnetic recording, since the inversion of the state of a recorded bit can be made this way. The parameters that allow attaining the shortest switching times are of particular relevance.

The time interval Δt required to reverse, under an applied magnetic field, the magnetization of a uniformly magnetized sphere, was computed in the early work of Kikuchi [30,59], using the Landau–Lifshitz–Gilbert equation. The expression of Δt, for a magnetic field H applied in a direction approximately opposite to that of the magnetization, is

$$\Delta t = \frac{1}{\alpha(H - H_{\text{sw}})}\,ln\left(\frac{\tan(\theta_{\text{f}}/2)}{\tan(\theta_{\text{i}}/2)}\right),\tag{3.75}$$

where α is the Landau damping constant ((2.76), p. 40), θ_{i} and θ_{f} are the initial and the final angles between the magnetization and the applied field H, and H_{sw} is the switching field. Note that if the initial angle is $\theta_{\text{i}} = 0$ the magnetization never reverses; a nonzero value of θ_{i} is therefore required for the reversal. In practice, this initial deviation of the magnetization from equilibrium may be provided by the thermal energy.

A damping factor equal to zero also implies no reversal: in this case the magnetization simply precesses around the direction of the field H, with constant angle θ. This is understandable, since in the process of magnetization reversal, magnetic energy has to be passed on to some thermal reservoir, e.g., the lattice, which means that there must be some form of damping, or magnetic relaxation. The magnetization precession for a spherical magnetic particle is illustrated in Fig. 3.32 for two values of the damping constant, $\alpha = 0$ and $\alpha = 0.1$.

A smaller damping factor α leads to a faster angular velocity, but also to a larger number of turns of the tip of the magnetic moment vector in the magnetization reversal process. A larger value of α, on the contrary, corresponds to slower precession and shorter paths. The minimum time interval for the reversal of the magnetization of a sphere is obtained for a damping factor $\alpha = \gamma/2$ or $\alpha_{\text{G}} = 1$ [30,59].

Simulations of reversal of the magnetization of ellipsoidal particles made for different magnetic field pulse lengths and shapes, and different directions of applied field, have revealed that ultrafast switching can be achieved by tailoring the pulse parameters [5]. The results are exhibited in an angular diagram in Fig. 3.33, where the radius of the diagram is proportional to the field intensity, and the angle
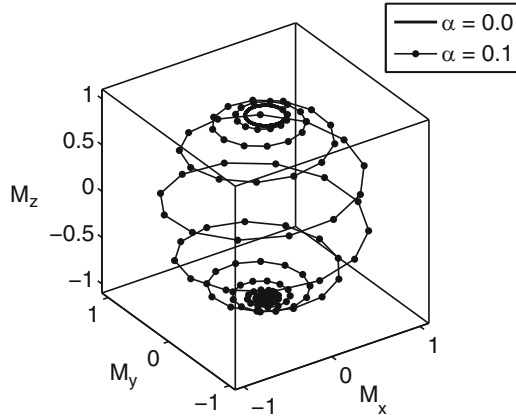
Fig. 3.32. The lines connecting the points show the magnetization trajectory for a spherical particle during homogenous reversal, with damping ($\alpha = 0.1$), computed using the Landau–Lifshitz–Gilbert equation. The *circle* drawn with the *continuous line* shows the precession with no reversal, in the case of zero damping
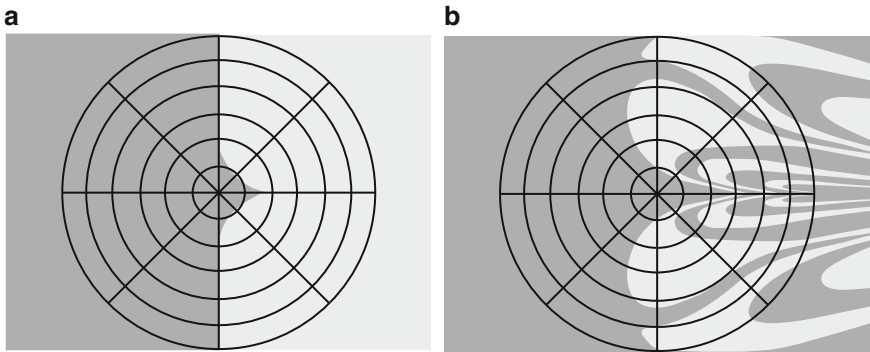
Fig. 3.33. Precessional magnetization inversion, with pulse lengths of (**a**) 2.75 ns showing in the *middle*, part of the Stoner–Wohlfarth astroid and (**b**) 0.25 ns. The diagram shows magnetization inversion (*light gray areas*) as a function of the angle of the field H and intensity (represented by the radius of the diagram) [5]. (Reprinted figure with permission from [5]. Copyright (2000) by the American Physical Society)

represents the field direction. The light gray areas correspond to the configurations (intensity and angle) that lead to magnetization reversal, and the darker ones to those that do not produce reversal. For long pulses, the same curve of magnetization reversal reproduces the Stoner–Wohlfarth astroid curve, as seen in the center of Fig. 3.33a. For short pulses a complex pattern appears in the polar graph (Fig. 3.33b). An analogous effect was also demonstrated in elliptical submicron permalloy thin film islands [58].

A related process of magnetization reversal consists in the simultaneous application of a static magnetic field and a microwave field [60]. This results in reversal of the magnetization with reduced switching fields or, in applications to magnetic recording, allows the use of higher coercivity magnetic media, see Chap. 7. In this microwave-assisted magnetic recording (MAMR) technique, the rf field is applied perpendicularly to the easy axis of the magnetic particle, and its effect for the same magnetic material coercivity is the reduction of the necessary switching field to about 1/3 of the intensity of the field in the Stoner–Wohlfarth case [60].

3.5.3 Current-Induced Magnetization Reversal

Another form of reversal, or switching of the magnetization, uses the fact that a polarized electron current, i.e., a current of unbalanced spin-up and spin-down electrons, can interact with the magnetic moment of a nanomagnet, applying a torque on it (see Chap. 6, for a discussion on nanodots, nanorings and nanowires). This is a quantum-mechanical effect that can be described in a simple way [7,45].

A simple way of accounting for the torque exerted by a current of polarized electrons is to include a spin-transfer torque (STT) term in the LLG equations. This term is a function of the volume of the nanostructure V, and is proportional to the current i [54]:

$$\Gamma = \left(\frac{d(\mathbf{M}V)}{dt}\right)_{STT} = \frac{\gamma\hbar i}{\mu_0 e}\, g\, \mathbf{m} \times (\mathbf{m}\cdot\hat{s}), \tag{3.76}$$

with the unit vector $\mathbf{m}$ of $\mathbf{M}$, and the polarization direction of the current $\hat{s}$; e is the electron charge.

The factor g depends on the current polarization; an expression of g that provides agreement with many experimental results is [45]:

$$g(P,\mathbf{m}\cdot\hat{s}) = \frac{4P^{3/2}}{(1+P)^3(3+\mathbf{m}\cdot\hat{s}) - 16P^{3/2}}, \tag{3.77}$$

where P is the degree of polarization of the current.

The LLG equation with the extra term therefore describes the temporal evolution of the magnetization of the magnetic sample, with the current-induced torque.

The effect of the torque is observed in multilayers containing a layer with fixed magnetization and another whose magnetization is free to turn. The Landau–Gilbert equation in this case describes the time evolution of the magnetization of the soft layer. The micromagnetic simulations using this modified Landau–Gilbert equation show that above a critical value of the current, the magnetization will be inverted. Using current pulses with values of i above the critical current, the torque may produce the inversion of the magnetization, depending on the duration of the pulses. This is shown in the plot of the magnetization component M_x in the case of a magnetic multilayer with a spin valve structure (see Chap. 5, on magnetotransport) submitted to a square current pulse of varying width (Fig. 3.34). The figure shows that above a certain pulse width, the magnetization component M_x of the soft layer reverses;
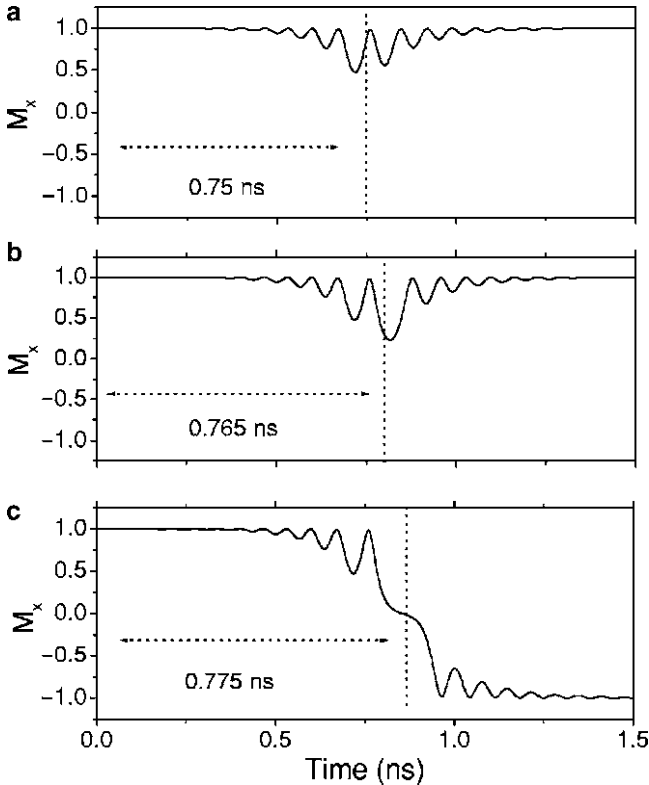
Fig. 3.34. Micromagnetic simulation of current-induced magnetization reversal. In the figure, the evolution of the x component of the magnetization as a function of time is shown for different current pulse durations. In the first figures (**a** and **b**) the pulses do not reverse the magnetization, but in (**c**), a longer pulse reverses it [36]. (Reprinted figure with permission from [36]. Copyright (2003) by the American Physical Society)

oscillations in M_x are also apparent. The simulations also show that the time interval for magnetization reversal, or switching speed, is dependent on the spin current.

An analogous effect was observed with a spin-polarized low energy electron beam that crosses a thin film of Fe, Co or Ni, turning the magnetization of the film. For a Co film, the beam turns the magnetization **M** by $19°$ per nanometer of film thickness [55].

3.6 Interaction Between Particles

An assembly of magnetic nanoparticles may interact, depending on the distance between them, through different physical mechanisms, such as the dipolar interaction, exchange interaction, superexchange, in some insulators, or through the Ruderman–Kittel–Kasuya–Yosida (RKKY) interaction, in the case of particles in a conducting

medium. These interactions modify the magnetism of the system, and, as a consequence, the description of the parameters that characterize the hysteresis curves cannot be made with models as simple as the Stoner–Wohlfarth model.

A system of magnetic particles may be demagnetized through a process that leads to a configuration in which the probability that a particle has magnetization along any direction is equal to the probability of magnetization along the opposite direction. An ensemble of non-interacting particles demagnetized in such way would have, in consequence, a curve of virgin magnetization m_{vir} drawn halfway between the upper branch of the hysteresis curve m_{sup} and the lower branch m_{inf} [49,50],

$$\Delta m = m_{\text{vir}} - \frac{1}{2}(m_{\text{sup}} - m_{\text{inf}}) = 0. \tag{3.78}$$

When there are interactions between the particles, on the other hand, the probability of alignment of the magnetization of the particles with direction is altered and an experimental displacement Δm_{exp} of the virgin magnetization curve is observed, and this displacement can be used as a measure of the intensity of these interactions:

$$\Delta m_{\text{exp}} = (m_{\text{vir}})_{\text{exp}} - \frac{1}{2}(m_{\text{sup}} - m_{\text{inf}})_{\text{exp}}. \tag{3.79}$$

Measurements of the remanent magnetization can also be used to evaluate the interaction between magnetic particles. The remanent magnetization is normally measured by reducing to zero the magnetic field applied to a saturated sample; the remanent magnetization is the magnetization for $H = 0$. There are two main remanent magnetization curves that can be used to study the magnetic properties of an ensemble of particles: the DC remanent magnetization curve $M_{\text{d}}(H)$ and the isothermal remanent magnetization, $M_{\text{r}}(H)$. The curve $M_{\text{d}}(H)$ is traced by taking initially the system to saturation; after that, the field is taken to a negative value $-H$ and the DC remanent magnetization for this field is $M_{\text{d}}(H)$. The full curve is traced by repeating this procedure with negative fields of increasing amplitude up to the field of same modulus as the initial saturation field (Fig. 3.35a). The curve of $M_{\text{r}}(H)$, on the other hand, is obtained by starting from a demagnetized sample and measuring the remanence for increasing fields up to H_{sat} (Fig. 3.35b). There are several alternative experimental procedures that can be used to take the sample to a demagnetized state; for a discussion, see [50].

Curves of DC and isothermal magnetic remanence for hexaferrite nanoparticles are shown in Fig. 3.35; note that, differently from $M_{\text{d}}(H)$, the values of $M_{\text{r}}(H)$ are all positive.

The curves of $M_{\text{d}}(H)$ and $M_{\text{r}}(H)$ are related in a simple way to the Stoner–Wohlfarth model. This relation expresses the fact that the DC remanence measurement starts with the remanence having the value $M_{\text{r}}(\infty)$. Applying a field $H < 0$ the moments corresponding to $M_{\text{r}}(H)$ will be reversed, and therefore, the positive remanent magnetization decreases by $M_{\text{r}}(H)$, and the negative increases by $M_{\text{r}}(H)$. Thus, the total variation of $M_{\text{d}}(H)$ is $-2M_{\text{r}}(H)$, or $M_{\text{d}}(H) = M_{\text{r}}(\infty) - 2M_{\text{r}}(H)$.
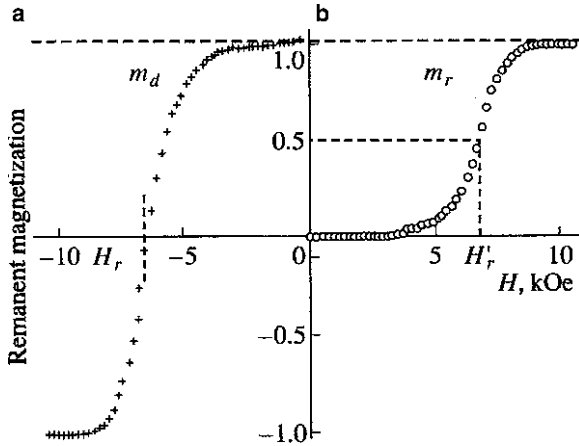
Fig. 3.35. Curves of (**a**) DC remanent magnetization $m_d(H)$ and (**b**) isothermal remanent magnetization $m_r(H)$ for hexaferrite nanoparticles [20]

This result, divided by $M_r(\infty)$, giving $m_d(H) = M_d(H)/M_r(\infty)$, is known as the Wohlfarth relation [57]:

$$m_d(H) = 1 - 2m_r(H). \qquad (3.80)$$

When every condition for the applicability of the Stoner–Wohlfarth model is satisfied, except for the presence of interactions between the magnetic particles, one can use this relation to evaluate the importance, or the magnitude, of this interaction: when the above relation is verified, the interaction can be neglected.

This result is frequently used in the form of a graph known as the Henkel plot [24], built by plotting $m_d(H)$ vs. $m_r(H)$. Any deviation from linearity given by (3.80) is indicative of the importance of the interaction between the particles. A Henkel plot drawn for uniaxial nanoparticles, in the non-interacting limit, and for two different interaction strengths, based on a Monte Carlo simulation, is exhibited in Fig. 3.36.

A modified form of this plot [29], also used for the same purpose, is the graph of $\Delta m(H)$ vs. H, where $\Delta m(H)$ is given by

$$\Delta m(H) = m_d(H) - [1 - 2m_r(H)]. \qquad (3.81)$$

In this case the quantitative measure of the effect of the interaction is evident in the graph of Δm as a function of the field H.

Another important aspect of the magnetism of a system of particles is the form of the dependence of its magnetization with the applied magnetic field $M(H)$. As we have seen in Sect. 3.3, a system formed of identical superparamagnetic particles has its magnetization vs. H curve well-described by a Langevin function $L(x)$ (3.33):

$$M = N\mu \, L\left(\frac{\mu B}{k_B T}\right). \qquad (3.82)$$

Numerical simulations show that the effect of dipolar interactions on the magnetization may be estimated maintaining the formulation of the magnetization in the
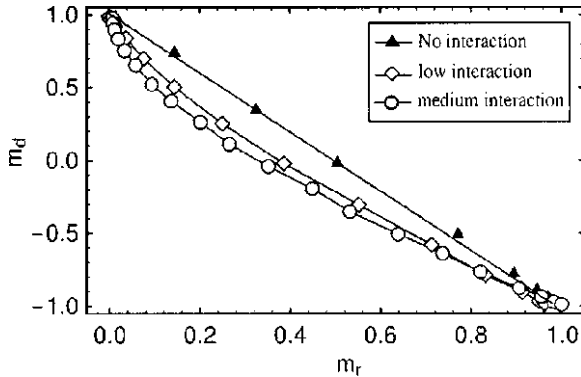
Fig. 3.36. Henkel plots computed for uniaxial magnetic particles using the Monte Carlo method. The graph with full *triangles* describes the case of non-interacting particles; the other two graphs refer to cases of particles with interactions, showing deviations from linearity. (Reprinted with permission from [18]. Copyright (2000), American Institute of Physics)

above form, but introducing an apparent temperature $T_a > T$, that substitutes T in the denominator of the argument of the Langevin function $L(x)$ [3]. This may be justified if one assumes that a random dipolar field due to the other particles, fluctuating with a high frequency ($\approx 10^9$ Hz), has the effect of reducing the order arising from the external magnetic field. The temperature T_a is related to T through the equation $T_a = T + T^*$, where $k_B T^*$ is the dipolar energy ε_d arising from the interaction between the magnetic moments μ:

$$k_B T^* = \varepsilon_d = \frac{\alpha_d \mu^2}{d^3}, \tag{3.83}$$

with d the average distance between the particles and α_d a proportionality constant that arises from the dipolar sum. Some experimental results for the quantity T^*, that measures the intensity of the interaction between the magnetic particles, are given in Table 3.3, for $Co_{90}Cu_{10}$ particles of different radii.

The relaxation processes of small magnetic particles are also affected by the interaction between them. In the presence of interactions, the picture of a single energy barrier between two configurations ($\theta = 0$, $\theta = \pi$) that we have discussed in Sect. 3.3.1 loses its validity, and the process of inversion of the magnetization now involves a complex landscape with many local minima, analogously to the case of a spin glass. The inversion of the magnetization of a single particle modifies this landscape, affecting the magnetic relaxation time.

In the simplest model that describes this phenomenon, the blocking temperature T_B and the relaxation time τ are related through a Vogel–Fulcher-type of equation [42]:

$$\tau = \tau_0 \, e^{\left(\frac{E_B}{k_B(T_B - T_0)}\right)}. \tag{3.84}$$

In the above equation, T_0 is a quantity that measures the intensity of the interaction between the particles, with dimension of temperature.

Table 3.3. Temperature $T^* = T_a - T$ that characterizes the intensity of the interaction between particles in the $Co_{90}Cu_{10}$ system, for particles of different equivalent radius $\langle R \rangle$, at $T = 300$ K. T_a is the apparent temperature [3]

$\langle R \rangle$ (nm)	T^* (300 K)
4.2	3,310
5.3	5,960
2.6	1,170
1.4	210[a]
1.5	55[b]
2.2	215
2.4	270
2.4	325

[a]$T = 251$ K; [b]$T = 244$ K
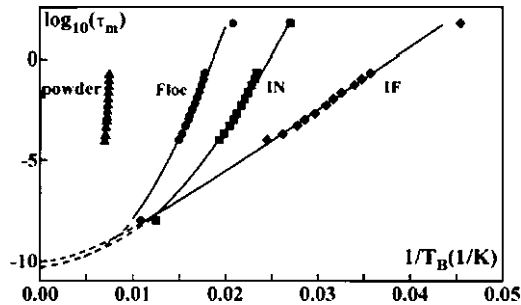
Fig. 3.37. Graph of $\log_{10}\tau$ vs. inverse blocking temperature for 4.7 nm γ–Fe_2O_3 particles. The different curves, derived from the model of [14], correspond to samples with different strength of the interaction between the particles, obtained by varying the separation between them. The plots *from left to right* correspond to the separations: $\gtrsim$4.7 nm, 6.8 nm, 7.3 nm and 21 nm [13]. (With permission from Elsevier Science and Technology)

A model for particles interacting through the dipolar field, with the magnetization described by the Langevin function, leads to a dependence of the relaxation time τ with the inverse blocking temperature $1/T_B$ that is in good agreement with the experimental results obtained with different magnetic nanoparticles [13, 14]. This may be seen in the graph of Fig. 3.37, where τ for γ−Fe_2O_3 particles was measured for different intensities of the interaction between the particles. The interaction intensity was modified by varying the average inter-particle distance; the differences in the strength of the interaction (T_0) appears in the graph as a difference in slope.

A study performed in a system composed of magnetic particles of different diameters (polydisperse) has showed that the interactions between them lead, at low temperatures, to a reduction of the coercivity and remanence [15]. In this study, made with simulations using the Monte Carlo technique, there were considered dipolar interactions and exchange interactions. Depending on their diameters, the particles

were found in the blocked or in the superparamagnetic state. The total magnetic field H_t acting on each particle of moment μ_i is given by:

$$H_t = H\hat{z} + \sum_{i \neq j} \left(\frac{3(\mu_j \cdot \mathbf{r}_{ij})\mathbf{r}_{ij}}{r_{ij}^5} - \frac{\mu_j}{r_{ij}^3} \right) + C^* \sum_{i \neq j} \mu_j. \tag{3.85}$$

In this expression, H is the applied field; the second term is the magnetic dipolar field and the third term is the exchange field. The dipolar field is taken as resulting from the interaction of particles found at a distance of up to three times the mean particle diameter, and the exchange field is due only to particles that are closer. C^* is a parameter that measures the intensity of the exchange field.

The total energy of a particle is a sum of the anisotropy energy with the energy of interaction with the magnetic field H_t:

$$E_T = KV \, \sin^2 \theta - \mu_0 \mu H_t \, \cos \beta. \tag{3.86}$$

In this expression, KV has the usual meaning, θ is the angle between μ and the anisotropy axis, and β is the angle of μ with H.

A study assuming only dipolar interactions between the particles, also performed using the Monte Carlo simulation, found a maximum in the coercivity as a function of the particle concentration, or as a function of the inverse of the distance between them [28]. This maximum is clearly observed in the case of zero magnetic anisotropy, and disappears for increased anisotropy.

Further Reading

X. Batlle, A. Labarta, J. Phys. D: Appl. Phys. **35**, R15–R42 (2002)

G. Bertotti, *Hysteresis in Magnetism* (Academic Press, San Diego, 1998)

R.W. Chantrell, K. O'Grady, in *The Magnetic Properties of Fine Particles*, ed. by R. Gerber, C.C. Wright, G. Asti Applied Magnetism (Kluwer, Dordrecht, 1994), pp. 113–164

B.D. Cullity, *Introduction to Magnetic Materials* (Addison-Wesley, Reading, 1972)

A.B. Denison, L.J. Hope-Weeks, R.W. Meulenberg, in *Quantum Dots*, ed. by M. di Ventra, S. Evoy, J.R. Heflein Jr. Introduction to Nanoscale Science and Technology (Springer, New York, 2004) p. 183

C.L. Dennis, R.P. Borges, L.D. Buda, U. Ebels, J.F. Gregg, M. Hehn, E. Jouguelet, K. Ounadjela, I. Petej, I.L. Prejbeanu, M.J. Thornton, J. Phys. Condens. Matter **14**, R1175-R1262 (2002)

J.L. Dormann, D. Fiorani, E. Tronc, Adv. Chem. Phys. **98**, 283–494 (1997)

D. Fiorani, (ed.), *Surface Effects in Magnetic Nanoparticles* (Springer, New York, 2005)

I.S. Jacobs, C.P. Bean, in *Fine Particles, Thin Films and Exchange Anisotropy (Effects of Finite Dimensions and Interfaces on the Basic Properties of Ferromagnets)*, ed. by G.T. Rado, H. Suhl, Magnetism, vol. III (Academic Press, New York, 1963) pp.271–350

S. Mørup, M.F. Hansen, in *Superparamagnetic Particles*, ed. by H. Kronmüller, S. Parkin, Handbook of Magnetism and Advanced Magnetic Materials, vol. 4, (Wiley, Chichester, 2007) pp. 2159–2176

J. Stöhr, H.C. Siegmann, *Magnetism From Fundamentals to Nanoscale Dynamics* (Springer, Berlin, 2006)

C. Tannous, J. Gieraltowski, Eur. J. Phys. **29**, 475–487 (2008)

W. Wernsdorfer, in *Magnetic Anisotropy and Magnetization Reversal Studied in Individual Particles*, ed. by D. Fiorani, Surface Effects in Magnetic Nanoparticles (Springer, New York, 2005) p. 263

E.P. Wohlfarth, in *Fine Particle Magnetism*, ed. by L. Falicov, J. Moran-Lopez. Magnetic Properties of Low-Dimensional Systems (Springer, Berlin, 1986) pp. 13–138

References

1. A. Aharoni, J. Appl. Phys. **82**, 1281–1287 (1997)
2. A. Aharoni, *Introduction to the Theory of Ferromagnetism*, 2nd edn. (Oxford University Press, Oxford, 2000)
3. P. Allia, M. Coisson, P. Tiberto, F. Vinai, M. Knobel, M.A. Novak, W.C. Nunes, Phys. Rev. B **64**, 14420 (2001)
4. X. Batlle, A. Labarta, J. Phys. D: Appl. Phys. **35**, R15–R42 (2002)
5. M. Bauer, J. Fassbender, B. Hillebrands, R.L. Stamps, Phys. Rev. B **61**, 3410–3416 (2000)
6. F. Bødker, S. Mørup, S. Linderoth, Phys. Rev. Lett. **72**, 282–285 (1994)
7. L. Berger, Phys. Rev. B **54**, 9353–9358 (1996)
8. G. Bertotti, *Hysteresis in Magnetism* (Academic Press, San Diego, 1998)
9. W.F. Brown Jr., Ann. N.Y. Acad. Sci. **147**, 463–488 (1969)
10. W.F. Brown Jr., J. Appl. Phys. **39**, 993–994 (1968)
11. R.W. Chantrell, K. O'Grady, in *The Magnetic Properties of Fine Particles*, ed. by R. Gerber, C.C. Wright, G. Asti. Applied Magnetism (Kluwer, Dordrecht, 1994), pp. 113–164
12. C.L. Dennis, R.P. Borges, L.D. Buda, U. Ebels, J.F. Gregg, M. Hehn, E. Jouguelet, K. Ounadjela, I. Petej, I.L. Prejbeanu, M.J. Thornton, J. Phys. Condens. Matter **14**, R1175–R1262 (2002)
13. J.L. Dormann, R. Cherkaoui, L. Spinu, M. Nogués, L. Lucari, F. D'Orazio, D. Fiorani, A. Garcia, E. Tronc, J.P. Olivet, J. Magn. Magn. Mater. **187**, L139–L144 (1998)
14. J.L. Dormann, D. Fiorani, E. Tronc, Adv. Chem. Phys. **98**, 283–494 (1997)
15. M. El-Hilo, R.W. Chantrell, K. O'Grady, J. Appl. Phys. **84**, 5114–5122 (1998)
16. E.H. Frei, S. Shtrikman, D. Treves, Phys. Rev. **106**, 446–455 (1957)
17. S. Gangopadhyay, G.C. Hadjipanayis, B. Dale, C.M. Sorensen, K.J. Klabunde, V. Papaefthymiou, A. Kostikas, Phys. Rev. B **45**, 9778–9787 (1992)
18. J. García-Otero, M. Porto, J. Rivas, J. Appl. Phys. **87**, 7376–7381 (2000)
19. D. Givord, M.F. Rossignol, in *Coercivity*, ed. by J.M.D. Coey. Rare-Earth Iron Permanent Magnets (Clarendon Press, Oxford, 1996)
20. Z.V. Golubenko, A.Z. Kamzin, L.P. Ol'khovik, M.M. Khvorov, Z.I. Sizova, V.P. Shabatin, Phys. Solid. State **44**, 1698–1702 (2002)
21. N.T. Gorham, R.C. Woodward, T.G.St. Pierre, B.D. Terris, S. Sun, J. Magn. Magn. Mater. **295**, 174–176 (2005)
22. G.F. Goya, T.S. Berquó, F.C. Fonseca, M.P. Moralesm, J. Appl. Phys. **94**, 3520–3528 (2003)
23. A.P. Guimarães, *Magnetism and Magnetic Resonance in Solids* (Wiley, New York, 1998)
24. O. Henkel, Phys. Stat. Solidi. **7**, 919–929 (1964)
25. O. Iglesias, A. Labarta, Phys. Rev. B **63**, 184416 (2001)
26. O. Iglesias, A. Labarta, X. Batlle, J. Phys.:Condens. Matter **19**, 406232–406237 (2007)
27. I.S. Jacobs, C.P. Bean, in *Fine Particles, Thin Films and Exchange Anisotropy (Effects of Finite Dimensions and Interfaces on the Basic Properties of Ferromagnets)*, ed. by G.T. Rado, H. Suhl. Magnetism, vol III (Academic Press, New York, 1963), p. 271–350

28. D. Kechrakos, K.N. Trohidou, J. Magn. Magn. Mater. **177**, 943–944 (1998)
29. P.E. Kelly, K. O'Grady, P.I. Mayo, R.W. Chantrell, IEEE Trans. Magn. **25**, 3881–3883 (1989)
30. R. Kikuchi, J. Appl. Phys. **27**, 1352–1357 (1956)
31. A. Kákay, L.K. Varga, J. Appl. Phys. **97**, 083901–083904 (2005)
32. R.H. Kodama, A.E. Berkowitz, Phys. Rev. B **59**, 6321–6336 (1999)
33. E. Kondorsky, J. Phys. Moscow **2**, 161 (1940)
34. H. Kronmüller, K.-D. Durst, G. Martinek, J. Magn. Magn. Mater. **69**, 149–157 (1987)
35. A. Labarta, O. Iglesias, L. Balcells, F. Badia, Phys. Rev. B **48**, 10240–10246 (1993)
36. Z. Li, S. Zhang, Phys. Rev. B **68**, 024404–024410 (2003)
37. F.E. Luborsky, J. Appl. Phys. **32**, 171S–183S (1961)
38. S.A. Majetich, Y. Jin, Science **284**, 470–473 (1999)
39. J. Nogués, J. Sort, V. Langlais, V. Skumryev, S. Suriñach, J.S. Muñoz, M.D. Baró, Phys. Repts. **422**, 65–117 (2005)
40. N. Pinna, S. Grancharov, P. Beato, P. Bonville, M. Antonietti, M. Niederberger, Chem. Mater. **17**, 3044–3049 (2005)
41. B.R. Pujada, E.H.C.P. Sinnecker, A.M. Rossi, C.A. Ramos, A.P. Guimarães, Phys. Rev. B **67**, 024402–024406 (2003)
42. S. Shtrikman, E.P. Wohlfarth, Phys. Lett. A **85**, 467 (1981)
43. R. Skomski, J.M.D. Coey, *Permanent Magnetism* (Institute of Physics Publishing, Bristol, 1999)
44. R. Skomski, J. Zhou, in *Nanomagnetic Models*, ed. by D. Sellmyer, R. Skomski. Advanced Magnetic Nanostructures (Springer, New York, 2006), pp. 41–90
45. J.C. Slonczewski, J. Magn. Magn. Mater. **159**, L1–L7 (1996)
46. E.C. Stoner, E.P. Wohlfarth, Phil. Trans. Roy. Soc. A **240**, 599–642 (1948). Reprinted in IEEE Trans. Magn. **27**, 3475–3518 (1991)
47. Z.Z. Sun, X.R. Wang, Phys. Rev. Lett. **97**, 077205-1–077205-4 (2006)
48. C. Tannous, J. Gieraltowski, Eur. J. Phys. **29**, 475–487 (2008)
49. S. Thamm, J. Hesse, J. Magn. Magn. Mater. **154**, 254–262 (1996)
50. S. Thamm, J. Hesse, J. Magn. Magn. Mater. **184**, 245–255 (1998)
51. A. Thiaville, Phys. Rev. B **61**, 12221–12232 (2000)
52. C. Thirion, W. Wernsdorfer, M. Jamet, V. Dupuis, P. Mélinon, A. Pérez, D. Mailly, J. Magn. Magn. Mater. **242–245**, 993–995 (2002)
53. J.K. Vassiliou, V. Mehrotra, M.W. Russell, E.P. Giannelis, R.D. McMichael, R.D. Shull, R.F. Ziolo, J. Appl. Phys. **73**, 5109–5116 (1993)
54. X.R. Wang, Z.Z. Sun, Phys. Rev. Lett. **98**, 077201–077204 (2007)
55. W. Weber, S. Riesen, H.C. Siegmann, Science **291**, 1015–1018 (2001)
56. W. Wernsdorfer, E.B. Orozco, B. Barbara, K. Hasselbach, A. Benoit, D. Mailly, B. Doudin, J. Meier, J.E. Wegrowe, J.P. Ansermet, N. Demoncy, H. Pascard, N. Demoncy, A. Loiseau, L. François, N. Duxin, M.P. Pileni, J. Appl. Phys. **81**, 5543–5545 (1997)
57. E.P. Wohlfarth, J. Appl. Phys. **29**, 595–596 (1958)
58. Q.F. Xiao, B.C. Choi, J. Rudge, Y.K. Hong, G. Donohoe, J. Appl. Phys. **101**, 24306 (2007)
59. J.G. Zhu, in *Magnetization Reversal Dynamics*, ed. by K.H.J. Buschow. Concise Encyclopedia of Magnetic and Superconducting Materials, 2nd edn. (Elsevier, Amsterdam, 2005), pp. 754–760
60. J.-G. Zhu, X. Zhu, Y. Tang, IEEE Trans. Magn. **44**, 125–131 (2008)

4

Magnetism of Thin Films and Multilayers

Summary. Magnetic thin films are the most extensively studied magnetic system with nanoscopic dimensions. The study of the properties of magnetic thin films has made the development of film media possible, which is used in magnetic hard disks, and the progress in reading heads. In this chapter, these properties are discussed including the anisotropy of thin films. Multilayers prepared from thin films give rise to a wealth of properties, arising in particular, from the interaction between the magnetic layers, the interlayer exchange coupling. The phenomenon of exchange bias, discovered in granular materials, has been systematically studied in thin films, and finds important applications.

4.1 Introduction

Magnetic films and multilayers are the most intensely studied systems that present nanomagnetic properties. The main application of nanomagnetism, namely magnetic recording, involves reading and writing with heads that are made with multilayers of nanometric dimensions, information stored in hard disks, and flexible media that may be coated with thin magnetic films. This is illustrated in Fig. 4.1, where the cross section of a perpendicular recording magnetic hard disk platter is shown, with the many layers required to perform its function. These include a layer of the recording medium, some 10–20 nm thick, and a layer of soft magnetic material of some 100–200 nm.

The field of Spintronics, or electronics of spin (see Chap. 5), is based on the manipulation of spin-polarized electron currents, i.e., electrical currents where the number of electrons with spin up is different from the number with spin down. Since this polarization is modified or lost beyond electron path lengths above some tens of nanometers, the spintronic devices also use components of nanometric dimensions, notably thin films.

One may distinguish two types of thin films or multilayers relevant to nanomagnetism: those that are planar, with nanometric thicknesses (Sect. 4.1.1), and those that, besides having this characteristic, also have structures that have lateral dimensions in this range (Sect. 4.1.2). These laterally structured systems may be prepared
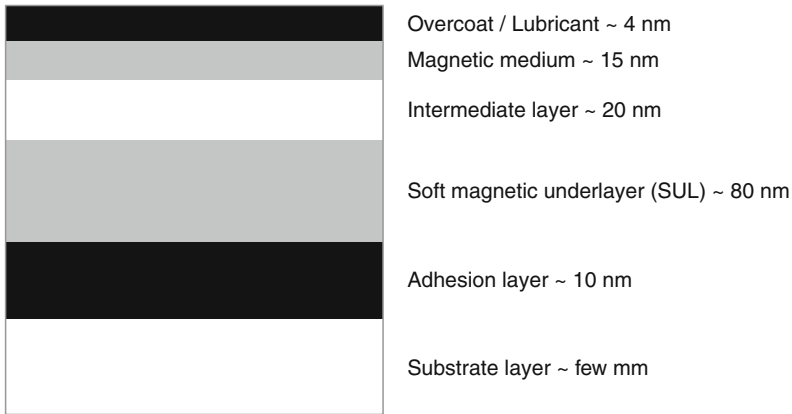
Fig. 4.1. Cross section of a typical perpendicular recording magnetic hard disk showing the different layers. Note the presence of the soft magnetic underlayer (SUL), required to close the magnetic circuit between the two poles of the write head (see Chap. 7). (Adapted from [30])

either by depositing thin films on a structured substrate or by other means, such as creating a pattern on a film with lithography. Depending on the form of the lateral structures, their magnetic properties are discussed together with the properties of nanoparticles in Chap. 3, or nanodisks, nanorings, and nanowires in Chap. 6.

Many different techniques are employed to prepare thin films, among them vapor deposition, magnetron sputtering, molecular beam epitaxy (MBE), electrodeposition, chemical deposition (see e.g., [4], and the third volume of the series [19]). Some of these techniques, such as magnetron sputtering and MBE, have been developed for the fabrication of integrated circuits, where the electronic components are made of several layers of films.

4.1.1 Thin Films: Planar Systems

The morphology of the deposit of an atom A on a substrate of element B depends on the surface free energies of A and B, as well as on the AB interface energy (see [13]). The higher the surface energy of the substrate, the stronger the tendency of the element deposited to wet the surface, in other words, to spread or form a homogeneous film.

Consequently, the favorable condition for the formation of a uniform film of a material on a substrate is given by the following relation between the surface energies per unit area γ:

$$\gamma_{\text{subs}} > \gamma_{\text{overlayer}} + \gamma_{\text{interface}}. \tag{4.1}$$

The d transition elements that are magnetic tend to have higher surface energies γ; for example, the 3d elements have surface energies from ~ 1.5 to $\sim 3\,\text{J\,m}^{-2}$, whereas semiconductors may vary from ~ 1 to $\sim 2\,\text{J\,m}^{-2}$. The free energies of some materials are shown in Table 4.1, where one sees that the d metals have surface energies that are larger than those of noble metals, semiconductors and insulators.

Table 4.1. Free energy γ of some materials, in $J\,m^{-2}$ [13]

Magnetic metal	Cr	Mn	Fe	Co	Ni	Gd				
	2.1	1.4	2.9	2.7	2.5	0.9				
Transition metal	Ti	V	Nb	Mo	Ru	Rh	Pd	Ta	W	Pt
	2.6	2.9	3.0	2.9	3.4	2.8	2.0	3.0	3.5	2.7
Simple or noble metal	Al		Cu		Ag		Au			
	1.1		1.9		1.3		1.6			
Semiconductor	Diamond		Si		Ge		GaP		GaAs	
	1.7		1.2		1.1		1.9		0.9	
Insulator	LiF		NaCl		CaF_2		MgO		Al_2O_3	
	0.34		0.3		0.45		1.2		1.4	

In the process of deposition of a thin film, once a first layer of atoms A is formed, the morphology of the second layer is defined under different energy conditions, because the new interface is now formed between two layers of A atoms. Since in general the lattice spacings of the elements A and B are different, as the thickness of the deposited element increases, the misfit strain energy also increases, an effect that works against a layer-by-layer deposition. Typically, a lattice parameter misfit of some 1–2% leads to breakdown of layer-by-layer growth beyond some ten atomic layers.

Highly miscible elements show a strong attractive force, and therefore an increased interface energy. This is the case, for example, of Fe films deposited on a Cr surface.

If the energy relationship is opposite to that of (4.1), the overlayer tends to develop three-dimensional islands from the beginning of the deposition process.

One can in general consider that there exists two regimes of film growth: the equilibrium regime, and non-equilibrium regime. In the first case, the temperature and rate of growth are such that the atoms relax to the positions corresponding to potential energy minima. The types of growth in these two regimes, depending on the relative free energies, are illustrated in Fig. 4.2. These types are: (1) growth in islands or Volmer–Weber, (2) layer by layer or Frank–van der Merwe growth, and (3) an intermediate or Stranski–Krastonov growth.

When one wishes to deposit a homogeneous film of an element that, from surface energy considerations, tends to form tridimensional islands, it is usual to appeal to deposition in the non-equilibrium regime, using low temperatures and/or high deposition rates to avoid the formation of these islands.

The structural properties of the atoms in a thin film of nanometric dimensions change, as compared to the behavior of bulk samples, and this is reflected, for example, in the lattice parameter of the surface layers. This is exemplified in Fig. 4.3, where the atomic spacing of thin films is shown to vary in comparison to the separation in thick samples. The graph shows the variation of interplanar spacing between the first two atomic layers $\Delta d(12)$, vs. the equilibrium spacing d_e in bulk samples of the same elements.

When deposited on substrates that present different coefficients of thermal expansion, thin films develop tensile or compressive stresses. The tensions also arise
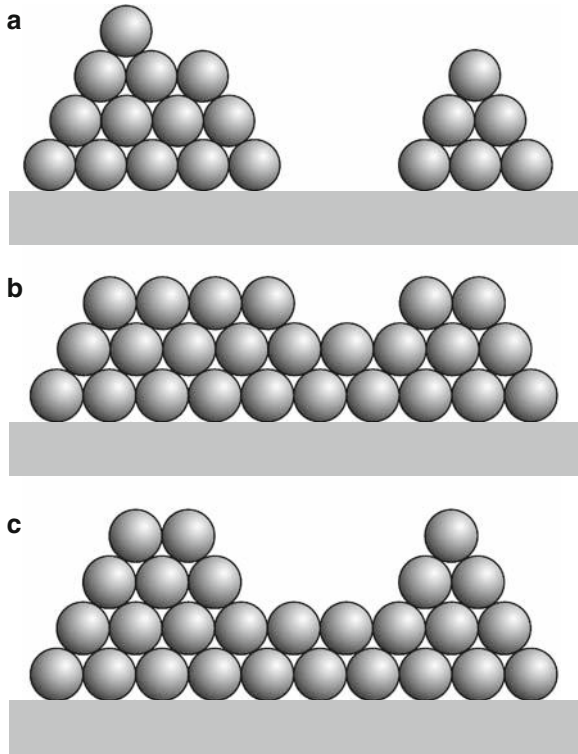
Fig. 4.2. Forms of film growth for different relative free energies, from *top to bottom*: (**a**) growth in islands or Volmer–Weber; (**b**) layer by layer or Frank–van der Merwe growth and (**c**) intermediate or Stranski–Krastonov growth. (Based on [4])
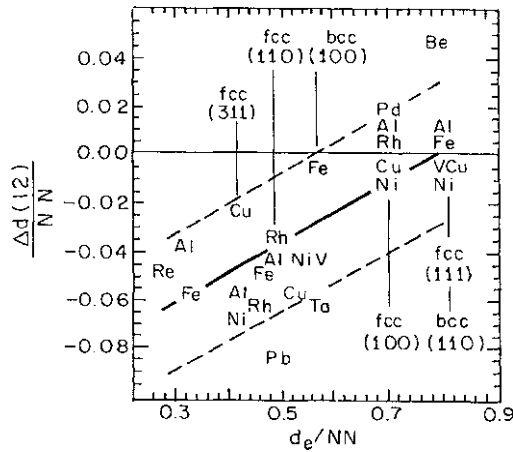
Fig. 4.3. Variation of interplanar spacing between the first two layers $\Delta d(12)$ divided by the number of nearest neighbors *NN* in films, vs. normalized equilibrium spacing d_e/NN in bulk samples [8]. (Reprinted figure with permission from [8]. Copyright (1992) by the American Physical Society)

due to lattice parameters misfit. A thinner film may accommodate this last type of tension, but as its thickness increases, it is energetically more favorable the appearance of dislocations.

The magnetic moment of surface atoms is also different from the moments of the atoms of the bulk. This is illustrated with the computed magnetic moments of Ni atoms in each one of the eight atomic layers of a thin film of Ni deposited on a Cu substrate (Fig. 4.4). One notes that the computed Ni magnetic moments near the interface with the Cu are lower than the moments in bulk samples of Ni; in the middle layers the moments are comparable to those of the bulk, and near the surface of the film they are larger than in the bulk.

The magnetic ordering temperature also differs in thin films from the values found in bulk samples. This is illustrated in Fig. 4.5, where it is evident the fall in Curie temperature for ferromagnetic thin films, as the thickness is reduced to a few atomic layers.
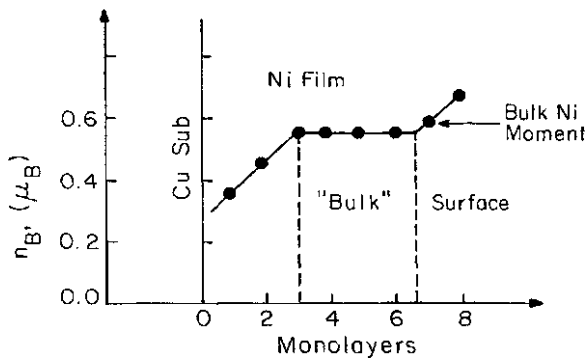
Fig. 4.4. Computed magnetic moment of Ni atoms in eight multilayers of metal deposited on Cu. The Ni moment is reduced relative to its value in bulk metal at the Cu interface (*left*) and increased at the free surface (*right*) ([29], adapted from [37]). (Reproduced from [37] with permission from Wiley)
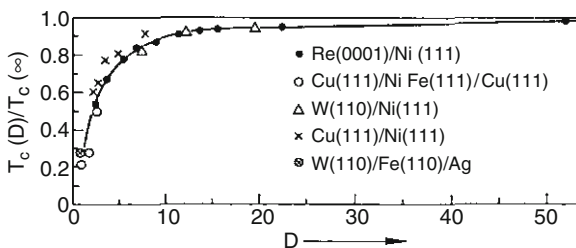
Fig. 4.5. Ratios of magnetic ordering temperature (Curie temperature T_C) of ultrathin metallic films to T_C of the corresponding bulk metals, as a function of the thickness measured in numbers of atomic monolayers [11]. (Reproduced from [11] with permission from Elsevier)

4.1.2 Thin Films: Laterally Structured Systems

Thin films with lateral structures of nanometric dimensions can be prepared in different ways, for example, by depositing the films on a structured substrate, or by film patterning using lithography techniques.
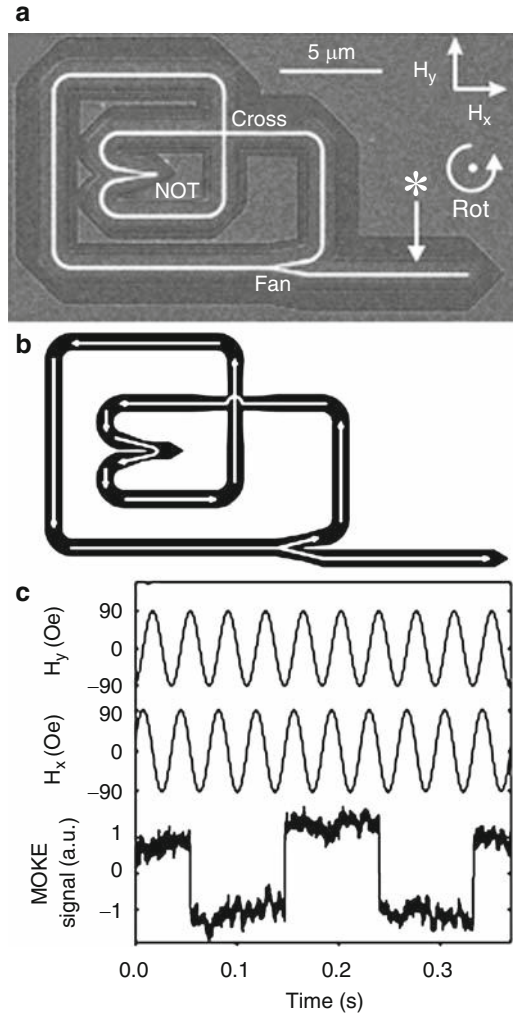
Fig. 4.6. (**a**) NOT logic gate consisting of magnetic tracks operated with the motion of magnetic domain walls, (**b**) route of the domain walls under the action of a counterclockwise rotating magnetic field, (**c**) MOKE signal obtained at the point marked with an asterisk in (**a**). From [1]. (Reprinted with permission from AAAS [1])

Magnetic nanowires, nanorods or nanostripes, for example, may be prepared by depositing magnetic elements or alloys on a stepped surface of single crystals. This has been done, for example, with Fe deposited onto a (110) surface of a tungsten single crystal.

Other techniques such as irradiation with an ion beam can be used to create, on a thin film, regions of locally modified coercivity or magnetic ordering temperature. The techniques that use this idea are the focused ion beam (FIB) technique, ionic implantation, etc. They allow the induction of changes in the magnetism of the films without affecting its topography (e.g., [10]).

Arrays of nanoscopic or sub-micron structures, can be created by lithography or by FIB, in the shape of elliptic permalloy dots [7] or checkerboard patterns [14]. Or still as magnetic trails employed to build logical devices that operate through the motion of magnetic domain walls (e.g., the NOT gate circuit made from a track of permalloy shown in Fig. 4.6 [1]).

Other logical devices were designed with single-domain nanoscopic elliptic structures of permalloy that interact through dipolar fields. A device may be built with a "majority" gate that simulates any logical gate, as shown in Fig. 4.7 [5, 15]. In these structures, through the application of external magnetic fields, logical operations can be performed with a frequency of 100 MHz and low-energy dissipation (10^{10} gates would dissipate only 0.1 W). This approach is promising, since the same technology of producing nanoscopic structures could be used to store information and to process it through the logical gates.
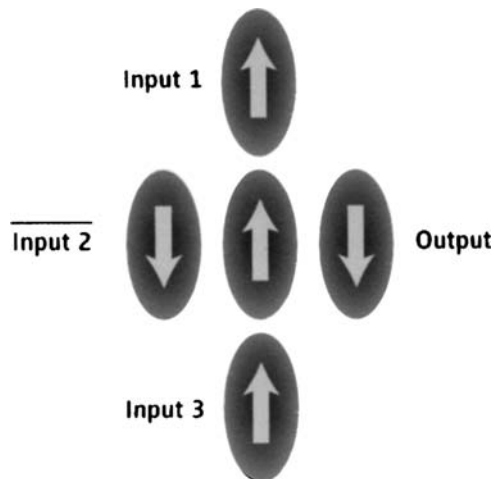
Fig. 4.7. Majority logic gate created with single-domain permalloy elliptical dots. The dot at the *center* aligns its moment through the effect of the dipolar fields, following the majority of the three inputs. The output magnetic moment orders antiparallel to this dot. From [5]. (Reprinted with permission from AAAS [5], quoting [15])

4.2 Anisotropy in Thin Films

The magnetic anisotropy energy in thin films can be expressed in general form, using the effective anisotropy constant K_{eff}

$$E = K_{\text{eff}} \sin^2 \theta, \qquad (4.2)$$

where θ is the angle between the magnetization and the normal to the surface.

The anisotropy mechanisms that give rise to the effective anisotropy may be the crystalline anisotropy, the magnetostatic contribution, the magnetoelastic term and the surface anisotropy term. The magnetostatic contribution is the shape anisotropy term. The surface term is a contribution to the anisotropy that arises from the broken translation symmetry at an interface, known as the surface, or interface, magnetic anisotropy [27]. The other terms, i.e., crystalline, magnetostatic and magnetoelastic, may be considered volume-related terms. The surface anisotropy is represented in the expression of anisotropy energy per unit area, by a term

$$\sigma = K_{\text{s}} \sin^2 \theta. \qquad (4.3)$$

This corresponds to an energy per volume

$$\frac{E_{\text{s}}}{V} = \frac{1}{d} K_{\text{s}} \sin^2 \theta. \qquad (4.4)$$

In this expression K_{s} is the out of plane surface anisotropy constant, and d is the film thickness [11]; $|K_{\text{s}}|$ is in the range $0.1–1.0 \times 10^{-3}\,\text{J}\,\text{m}^{-2}$. Values of K_{s} for some materials are given in Table 4.2. For lower symmetry surfaces, e.g., Fe (110), an in-plane anisotropy term has to be added to (4.3), of the form $K_{\text{sp}} \sin^2 \theta \cos^2 \phi$ [11].

Several terms that contribute to the energy in magnetic materials may also lead to an effective anisotropy. The terms that contribute to the effective anisotropy constant are listed in Table 2.5 (p. 34). They include volume and surface terms, such as the uniaxial anisotropy energy, the shape anisotropy term (involving the magnetostatic energy), the magnetoelastic term and the surface anisotropy term K_{s}:

Table 4.2. Values of the interface anisotropy constant K_{s} for different interfaces (/UHV stands for the free surface) [12]

Interface	K_s (mJ m^{-2})
Co/Pd	-0.92
Co/Pt	-1.15
Co/Ni	-0.42
Co/Au	-1.28
Ni/UHV	0.48
Ni/Cu	0.22
Fe/Ag	-0.79
Fe/Au	-0.54
Fe/UHV	-0.89
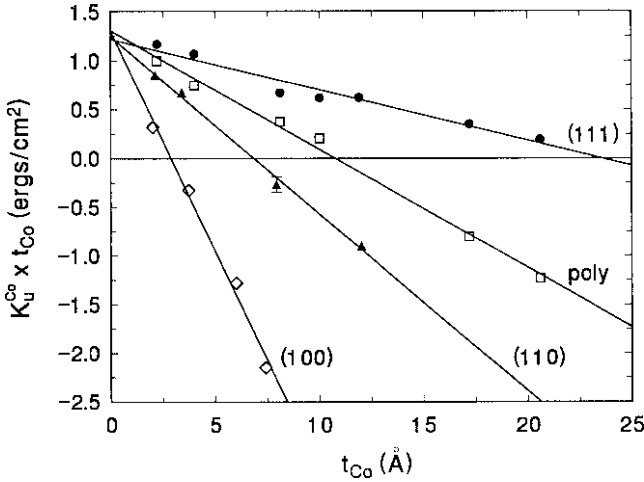
Fig. 4.8. Effective anisotropy of Co films on Si vs. thickness t_{Co} for different epitaxial films and for a polycrystalline film [9]. (Reprinted with permission from [9]. Copyright (1991) by the American Physical Society)

$$K_{\text{eff}} = K_{\text{u}} - \frac{1}{2}\mu_0 M_s^2 + K_{\text{me}} + \frac{K_s}{d}. \tag{4.5}$$

When there are two surfaces contributing to the surface anisotropy term, as in a thin film, this term should include a factor 2, becoming $(2K_s/d)$. Note that the surface anisotropy term for a nanoparticle has a factor of 6 multiplying K_s ((3.36) on p. 77, Chap. 3).

The magnetostatic term for a thin film is written in the CGS as $-(1/2)N_{\text{d}}^{\text{CGS}}M_s^2 = -2\pi M_s^2$, instead of $-(1/2)\mu_0 M_s^2$ (see Table 2.10, on p. 39, where the expressions of some magnetic quantities are given both in SI and CGS units). Figure 4.8 is an example of the thickness dependence of the anisotropy, showing this effect for Co films on Si.

The magnetoelastic anisotropy term is given by

$$K_{\text{me}} = \frac{3}{2}\lambda_s \sigma, \tag{4.6}$$

where λ_s is the saturation magnetostriction and σ is the stress acting on the film. This term can also be written in terms of the strain ε, as $K_{\text{me}} = B_{\text{me}}\varepsilon$, where B_{me} is the magnetoelastic coupling coefficient.

For $K_{\text{eff}} > 0$ the lowest energy configuration corresponds to perpendicular magnetization, an effect that has applications in magnetic recording. This is observed, for example, in thin films of Ni/Cu(001), for thickness below about 10 nm; in this system, this effect appears to be due to strain.

In general, as the thickness d of the film increases, the effects of the demagnetizing fields tend to dominate, since the corresponding anisotropy contribution of a film
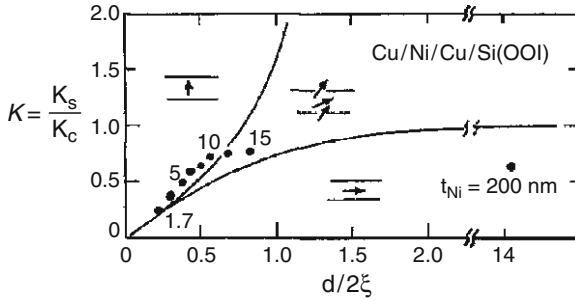
Fig. 4.9. Phase diagram of a Cu/Ni/Cu/Si film in the graph of surface anisotropy vs. Ni film thickness t_{Ni} (in units of exchange length). For small values of $d/2\xi$ and large values of κ, the magnetization is perpendicular; for large $d/2\xi$ and small κ, the magnetization is parallel. In the middle region, the magnetization points along an intermediate direction. The points correspond to measurements on Ni films of up to 200 nm thick [29]

in the demagnetizing field is $\frac{1}{2}\mu_0 M_s^2 d$, and therefore the magnetization tends to become parallel to the plane of the film. The thin film critical thickness d_{cr} for which the magnetic anisotropy changes from favoring in-plane magnetization to perpendicular magnetization is obtained from (4.5); ignoring the magnetoelastic term, it follows:

$$d_{cr} = -\frac{K_s}{K_u - \frac{1}{2}\mu_0 M_s^2}. \tag{4.7}$$

In Fig. 4.9 the normalized surface anisotropy of Cu\Ni\Si(001) is plotted vs. normalized thickness of the Ni film; one sees how, with increasing film thickness, its magnetization gradually turns to parallel to the plane of the film.

In the case of a thin film of Fe on Au, a monoatomic layer has perpendicular anisotropy, and the anisotropy also changes to in-plane for larger thicknesses. One form of increasing the perpendicular anisotropy in this case is through the creation of several Fe\Au interfaces, which is obtained by depositing a multilayer of the form $(Fe\backslash Au)_n$.

4.3 Domain Walls and Magnetization Reversal in Thin Films

The magnetic domain walls formed in thin films may be more complex than the walls formed in the same material in bulk form. Among the variety of types of magnetic domain walls found in thin films, three types are more common: (1) Bloch walls, (2) Néel walls, and (3) cross-tie walls. The cross-tie domain wall is intermediate between the other two forms, and is formed of a line of vortices and antivortices (see Sect. 6.2). These three domain wall types are shown schematically in Fig. 4.10.

As we have seen in Sect. 2.4, Néel domain walls are energetically more favorable in magnetic films below a certain thickness, as illustrated in Fig. 4.11, using expressions given by [25]; for thicker films, Bloch walls are favored.
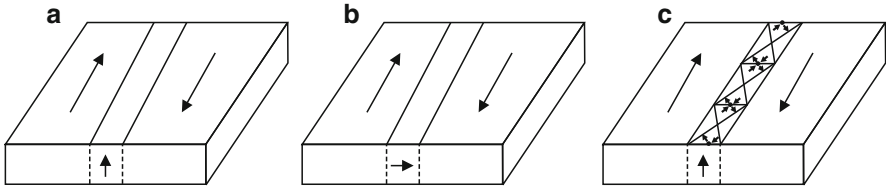
Fig. 4.10. Types of magnetic domain walls: (**a**) Bloch wall, (**b**) Néel wall, and (**c**) cross-tie wall
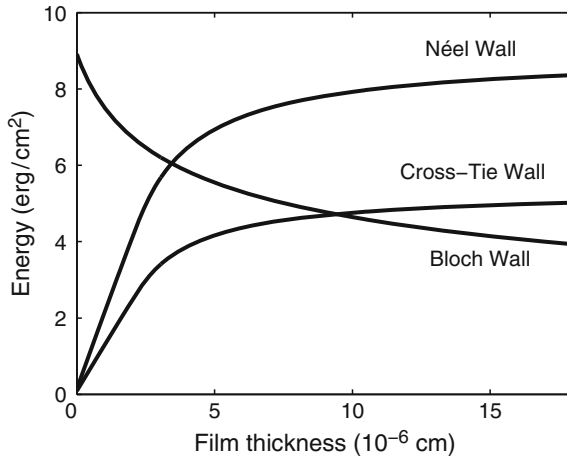
Fig. 4.11. Domain wall energy for Bloch walls, Néel walls and cross-tie walls, as a function of film thickness, computed using expressions given by [25]. The graph shows that for thinner films cross-tie walls and Néel walls correspond to the lowest energy configurations

The phenomenon of magnetization reversal in thin films, analogously to the case of magnetic nanoparticles, has attracted much interest, and is relevant both for the understanding of the magnetism of these systems, as for their applications, particularly to magnetic recording on thin film media.

The coercivity measured through the hysteresis curve is dependent on the magnetic field sweep rate $\eta = dH/dt$, and in the context where this aspect is emphasized, this coercivity (H_c^*) is called dynamic coercivity. In the case of thin films it is related to the field sweep rate as $H_c^* \sim \eta^\alpha$ where α is an exponent that for low η, varies with the film thickness.

This expression is obtained in a model that assumes that the domain wall velocity is proportional to the rate of change of the magnetic field, and that the magnetization reversal is effected through nucleation and propagation of circular domain walls [32]. The domain wall velocity $v(H)$ is zero for a magnetic field intensity $|H| < H_{dp}$, where H_{dp} is the depinning field, a magnetic field sufficiently intense to overcome the pinning forces. The velocity shows a linear variation with field: $v(H) = \mu(|H| - H_{dp})$ for $|H| \geq H_{dp}$, with μ the domain wall mobility, a phenomenological parameter.

For a straight domain wall, the change in normalized magnetization (m) with time results to be

$$\frac{dm}{dt}(t) = \pm\sqrt{\rho}\,\mu[H(t) - H_{dp}], \tag{4.8}$$

where ρ is the density of reversed domains at the depinning field H_{dp}. The "+" and "−" signs refer to positive or negative magnetic fields. A slightly more complicated expression follows if one assumes circular domain walls, a description which seems to be applicable to ultrathin Fe films [6].

The hysteresis loops computed with this model show dynamic coercivities H_c^* that depend on the magnetic field sweep rate in the same way as the experimental results. At low sweep rates a quasilinear response is observed for H_c^*, and this quantity increases more rapidly for increasing rates, with periods comparable to the magnetization reversal times. These predictions of the model agree with the experimental results of H_c^* for Fe/GaAs(001) films (Fig. 4.12).

The reversal of the magnetization of a thin film under an applied magnetic field parallel to the plane of the film was the object of an early study by Kikuchi [16] using the Landau–Lifshitz–Gilbert equation. The time Δt required to reverse the magnetization was computed. The fastest switching in the case of a film is obtained using in the description a small damping factor α, dependent on the magnetization. The motion of the magnetization is very different from that in the case of a spherical particle (Sect. 3.5.2, p. 93). For example, in the case of the film, for zero damping factor, the magnetization oscillates in a pendular-like motion. For a nonzero damping, as the magnetization begins to turn, the component of the magnetization perpendicular to the plane generates a demagnetizing field that drives the precession of the magnetization; these two behaviors, for zero and nonzero damping, are shown in Fig. 4.13.

An alternative form of reversing the magnetization of thin films uses ultra-short magnetic field pulses. They have been used to induce the reversal of the magnetization of Co films [2]. Pulses of under $200\,\mathrm{kA\,m^{-1}}$ were applied in the plane of the films, perpendicular to the Co magnetization. The demagnetizing field is important for the magnetization reversal, acting even after these pulses are over. The magnetization reversal time found in this experiment was very short, of the order of 10^{-12} s.
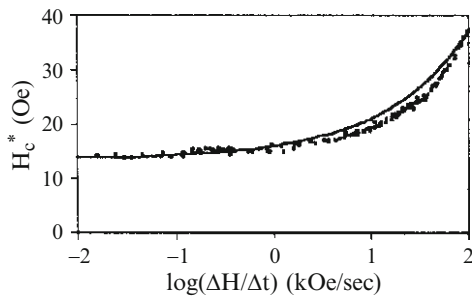
Fig. 4.12. Dynamic coercivity of thin films vs. log of magnetic sweep field rate. The *dots* are experimental points obtained with Fe/GaAs(001) films, the *continuous line* results from the model of straight domain walls [32]. (Reprinted with permission from [32]. Copyright (2002) by the American Physical Society)
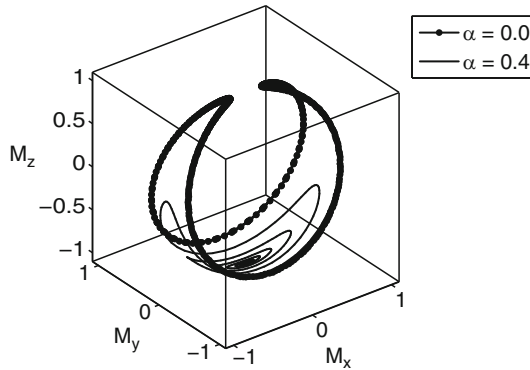
Fig. 4.13. The *points* show the magnetization trajectory for the homogenous reversal of a thin plate under an in-plane applied magnetic field, for damping factor $\alpha = 0$, computed using the Landau–Lifshitz–Gilbert equation; the *continuous line* describes the trajectory with $\alpha = 0.4$. Compare with Fig. 3.32, p. 95, the magnetization trajectory for a spherical particle

4.4 Exchange Bias

The exchange bias phenomenon arises from the interaction through the interface between a ferromagnet (FM) and an antiferromagnet (AFM) or ferrimagnet (FI); also between an AFM and a FI. In simple terms, this interaction acts as an effective field that changes the behavior of the ferromagnet under an applied magnetic field. The signature of the exchange bias phenomenon is the shift of the hysteresis loop either to lower or higher magnetic fields, shown, for example, for FeF_2 at 10 K in Fig. 4.14.

This effect was first observed in studies of field-cooled (FC) oxidized Co particles [24]. In this case the relevant interface is that between the Co grains (ferromagnetic) surrounded by a CoO layer (antiferromagnetic). The exchange bias can also be observed even when there is a nonmagnetic thin film between the antiferromagnetic and ferromagnetic layers, as shown, for example, in the hysteresis loop of the Co/Au/CoO multilayer system (Fig. 4.15) [31].

The antiferromagnetic side of the interface where this phenomenon is observed may be either compensated or uncompensated. In the compensated case, the first AFM layer contains moments pointing in both directions, in such a way that the total magnetization of this layer is zero, as shown in Fig. 4.16b. The AFM layer is uncompensated when the opposing moments are in the next layer, and the total moment of the first layer is nonzero (Fig. 4.16a).

In a magnetization measurement where the sample is cooled under an applied magnetic field, done at a temperature above the Néel temperature T_N of the antiferromagnet (but below T_C of the ferromagnet), the magnetic moments of the AFM atoms are at this point disordered. As T_N is reached, the AFM atoms at the interface align ferromagnetically to the FM moments.
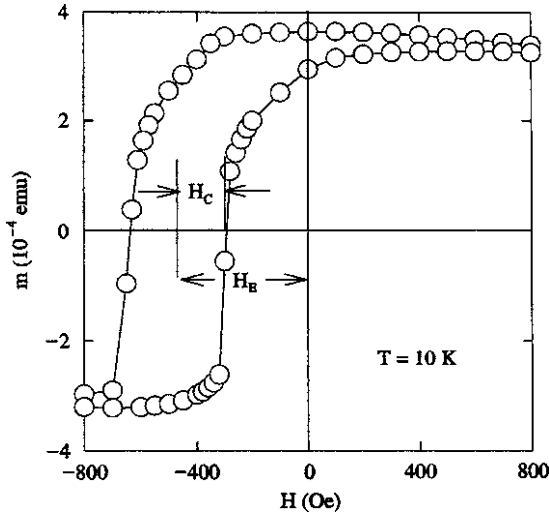
Fig. 4.14. Hysteresis curve for field-cooled FeF$_2$ at 10 K showing exchange bias. The exchange bias field H_E and the coercivity H_c are indicated in the figure. The *curve* also exhibits the lack of symmetry commonly found in these samples [28]. (With permission from Elsevier Science and Technology)
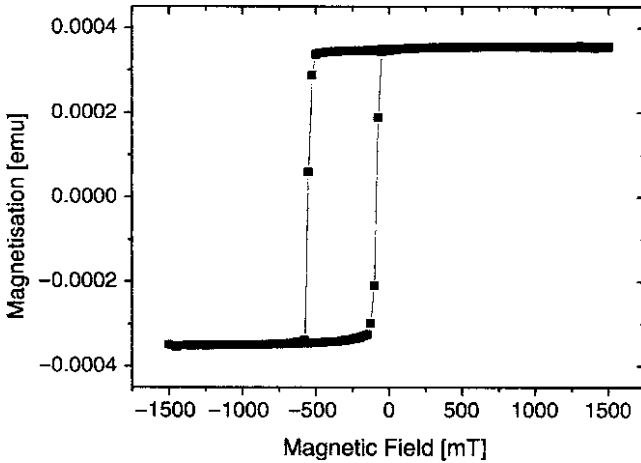
Fig. 4.15. Hysteresis curve showing exchange bias in the system Co/Au/CoO, obtained with a SQUID magnetometer. Note that in this case the exchange bias effect is still observed, even with a nonmagnetic film between the FM layer and the AFM layer. (Reproduced with permission from [31])

The hysteresis curve obtained for such sample is shown schematically in Fig. 4.17; beginning from magnetic saturation (a), as one reverses the field, the FM moments start to turn (b), but the AFM atoms exert locally a restoring force, arising from a magnetic field across the interface.
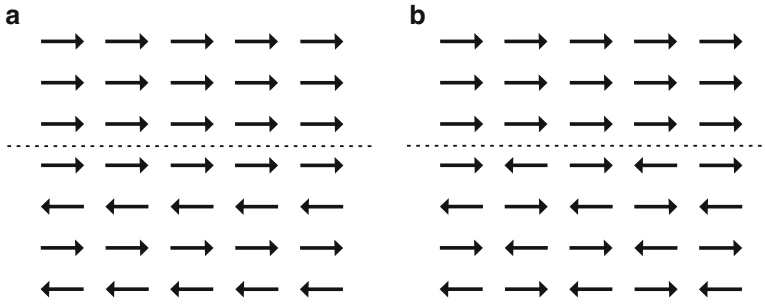
Fig. 4.16. Types of FM/AFM interfaces: (**a**) uncompensated and (**b**) compensated. In the second type of interface, the total magnetic moment of the AFM layer nearest to the interface is zero
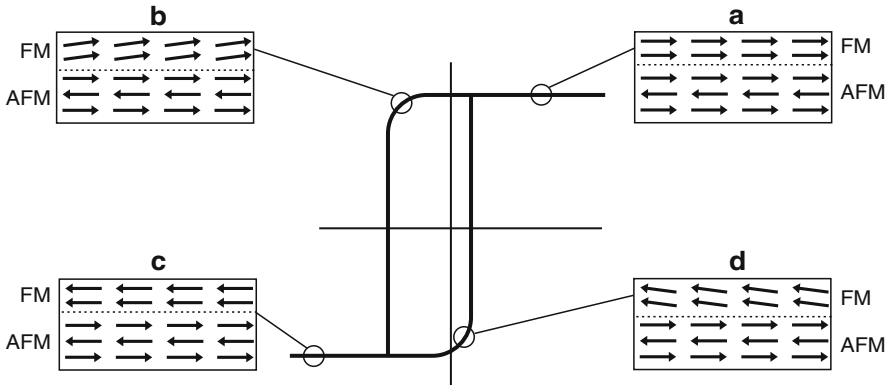
Fig. 4.17. Simplified scheme of the magnetic moments near the interface in the exchange bias phenomenon, showing (**a**) the moments at the interface with the applied field H, at saturation; (**b**) with H in the opposite direction, before inverting the magnetization; (**c**) the FM layer has reversed; (**d**) with H increasing immediately before the FM layer turns to the original direction

Since the AFM atoms exert a torque pulling the FM moments to their original direction, this effect is described as a unidirectional anisotropy, with anisotropy energy $\propto \sin\theta$, which amounts to an angular dependence different from that of the usual (uniaxial) anisotropy, which is proportional to $\sin^2\theta$.

The graph of the anisotropy energy measured by torque magnetometry exhibits the $\sin\theta$ component combined with the usual $\sin^2\theta$ term, and therefore the curve has an absolute minimum, instead of two identical minima observed in the uniaxial case, as in Fig. 3.22 (p. 83). This unidirectional behavior is shown in Fig. 4.18, where the anisotropy energy curves are plotted against θ, the angle between the magnetic field applied during the measurement and the direction of the magnetic field applied in the cooling process.
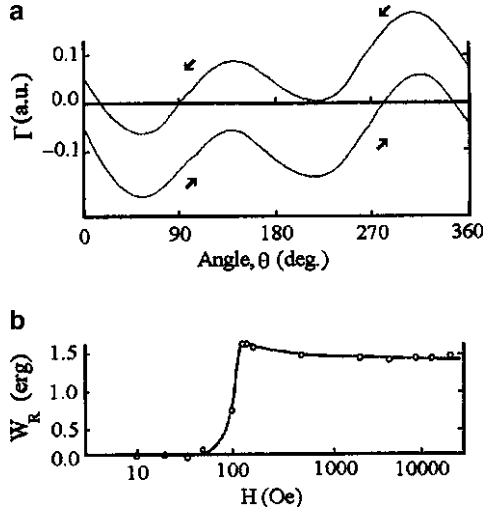
Fig. 4.18. (**a**) Torque magnetization *curves* showing an absolute minimum in the anisotropy energy Γ and (**b**) rotational hysteresis, or the area between the two curves, for a CoO sample at 77 K, as a function of the applied magnetic field ([28], based on [36]). (With permission from Elsevier Science and Technology)
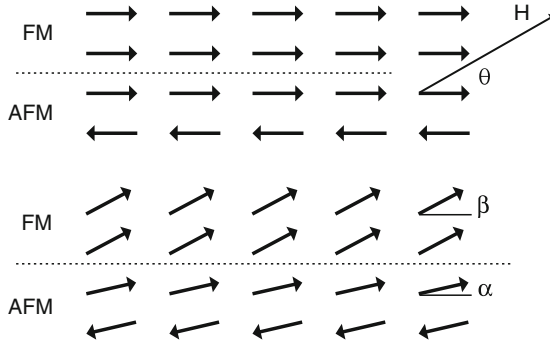
Fig. 4.19. Angles between the magnetic moments and the anisotropy axes (θ), and between the axes and the magnetic field H at the FM/AFM interface (α for the AFM axis and β for the FM axis), used in the definition of the bilayer energy (4.9)

The unidirectional anisotropy is at the basis of the phenomenon of exchange bias. In this simple description, the energy per unit area for a bilayer consisting of one FM layer and one AFM layer of thicknesses, respectively t_{FM} and t_{AFM}, is [23]:

$$E = -\mu_0 H M_{FM} t_{FM} \, \cos(\theta - \beta) + K_{AFM} t_{AFM} \, \sin^2 \alpha - J_{int} \, \cos(\beta - \alpha). \qquad (4.9)$$

In this expression, J_{int} is the effective interface coupling constant, α, β, and θ are, respectively, the angles between the AFM magnetization (M_{AF}) and the AFM anisotropy axis, the FM magnetization and the FM anisotropy axis, and the angle between the applied field and the FM anisotropy axis (see Fig. 4.19). It is assumed

here that the AFM and FM anisotropy axes are collinear, and that the rotation of the moments is coherent.

Minimizing the energy with respect to the angles α and β, the shift of the hysteresis loop is obtained [23]:

$$H_{\mathrm{E}} = \frac{J_{\mathrm{int}}}{M_{\mathrm{FM}} t_{\mathrm{FM}}}. \tag{4.10}$$

The displacement of the hysteresis loop is therefore proportional to the intensity of the effective coupling between the two layers. This result has been generalized to include the Zeeman interaction of the magnetization of the antiferromagnetic layer; this generalization leads to a qualitative agreement for the observed dependence of H_{E} with the thickness of this layer [3].

A requirement for the effect to occur is a condition about the relative importance of the antiferromagnetic anisotropy compared to the interface coupling: the relation should be $K_{\mathrm{AFM}} t_{\mathrm{AFM}} \geq J_{\mathrm{int}}$. If this condition is not satisfied, with the application of the magnetic field H, the AFM magnetization follows the turning motion of the FM spins and the effect disappears.

Another important characteristic of the phenomenon of exchange bias is the accompanying increase in the coercive field observed in the samples. This effect can be understood in a simple way in the case of a FM/AFM interface. The coercivity of the FM layer is increased, since, as its magnetization turns, it has to overcome the AFM anisotropy. If the latter anisotropy is very large, the coupling to the FM moments is less effective, and the FM magnetization turns more easily, therefore not increasing the coercivity. A correlation between the coercivity and the exchange field has been experimentally observed; this is illustrated in Fig. 4.20 with the graph of H_c vs. H_{E} for MnF_2/Fe bilayers .

Another phenomenon observed in systems that present exchange bias is the training effect, the fact that H_{E} depends on the number of measurements performed, decreasing as this number increases. This seems to be produced by changes in the
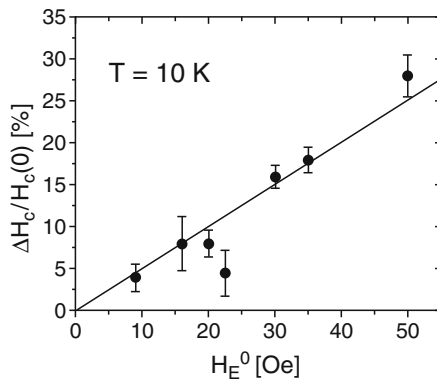
Fig. 4.20. Percentage variation of the coercivity vs. exchange bias field H_{E} for MnF_2/Fe bilayers, showing the correlation between H_c and H_{E}. H_{E} was changed by varying the roughness of the interface [20]. (Reprinted from [20]. Copyright (2000) by the American Physical Society)

AFM domains each time the FM magnetization is turned under the influence of the magnetic field.

A memory effect is also observed, consisting in the fact that the sample retains the information of the temperatures of the field cooling cycle.

There is a maximum temperature, above which the exchange bias does not occur; it is usually called blocking temperature, and may be different from T_N.

Reviews of the theoretical models used to describe the exchange bias phenomenon are given in [17] and [33] (see also [34]); these include the model of coherent rotation, sketched here [23], the model of canted spins [18], the rugosity model [21], and the AFM domain wall model [22].

The exchange bias phenomenon has been studied in a wide variety of physical systems (particles, thin films) in different experimental conditions, varying the rugosity of the interface, crystallinity and size of the grains at the interface, the thickness of the ferromagnetic layer, the existence of compensated and uncompensated AFM interfaces, and so on.

The main practical applications of exchange bias stem from the possibility of observation of giant magnetoresistance (GMR) or tunnel magnetoresistance (TMR) at lower magnetic fields than those required with ordinary multilayer systems. GMR and TMR arise from the difference in electron transport through two FM layers as they are changed from parallel to antiparallel by an applied field, in a device called spin valve (see Chap. 5). In this case the exchange bias is used to pin one of the FM layers; the other layer can be made to invert its magnetization with a smaller magnetic field. Another multilayer arrangement is known as a pseudo spin valve, in the case where one of the ferromagnetic layers is not pinned, but prevented from turning its magnetization simply by its geometry, for example, because it is thicker.

Exchange bias can also be used to stabilize the magnetization in recording heads based on the anisotropic magnetoresistance (AMR). The effect can also be used to fix the chirality (or handedness) in arrays of magnetic nanorings, in view of applications in magnetic data storage (Sect. 6.3, on p. 156).

4.5 Interlayer Exchange Coupling

Two ferromagnetic layers that are part of the same physical system show in general an effective magnetic coupling. Néel predicted that a rough interface between two magnetic layers would lead to uncompensated magnetic poles ("orange peel effect") that would couple these layers through dipolar fields (e.g., [12]).

For two ferromagnetic layers (of magnetic moments μ_1 and μ_2) separated by a nonmagnetic (paramagnetic) thin metallic layer, the energy arising from this coupling is:

$$E = -J_1 \, \mu_1 \cdot \mu_2 \, \cos\theta. \tag{4.11}$$

where θ is the angle between the two magnetizations.

This coupling is called bilinear coupling and the interlayer coupling constant J_1 is given by the difference between the energy per unit area of the antiparallel and parallel arrangements of the magnetic moments of the layers of area A:

$$J_1 = \frac{1}{2A}(E_{\uparrow\downarrow} - E_{\uparrow\uparrow}). \tag{4.12}$$

Another term of the form $-J_2\,\mu_1 \cdot \mu_2 \cos^2\theta$ can also be important, describing an interaction known as biquadratic coupling. This term is usually attributed to extrinsic effects, such as interface roughness [35].

The intensity of the magnetic coupling is given by the coupling constants J_1 and J_2. The constant J_1 generally varies in an oscillatory fashion with the thickness of the spacer layer, as shown in the CoCu multilayers in Fig. 4.21. This effect is reminiscent of the Ruderman–Kittel–Kasuya–Yosida (RKKY) interaction observed in the coupling between two magnetic impurities in a metallic matrix. The interlayer coupling parameter J_1 is usually of the order of $10^{-3}\,\mathrm{J\,m^{-2}}$, and the oscillation period of the order of a few atomic monolayers; some values of these quantities for multilayers of different materials are given in Table 4.3.

The oscillatory coupling arises since in the case of magnetic layers, the interference between incoming electrons and electrons scattered at the interfaces gives rise to oscillations in the probability densities for each electron [35]. All the oscillations cancel out, except those of the electrons at the Fermi level, since there is at this energy a cut-off between filled and unfilled states. The second layer samples these spin oscillations, and the intensity of the coupling to its moment also oscillates.

The cohesive energy per unit area is the integral of the energies of one-dimensional quantum wells, taken on the Brillouin Zone (BZ) of the interface is given by

$$\lim_{t \to \infty} \frac{\Delta E}{A} \approx \frac{\hbar v_F}{2\pi D} \int_{BZ} \frac{d^2 K}{(2\pi)^2} Re\left[e^{i2\pi k_{F_z}(K)t} R_R(K) R_L(K)\right] \tag{4.13}$$
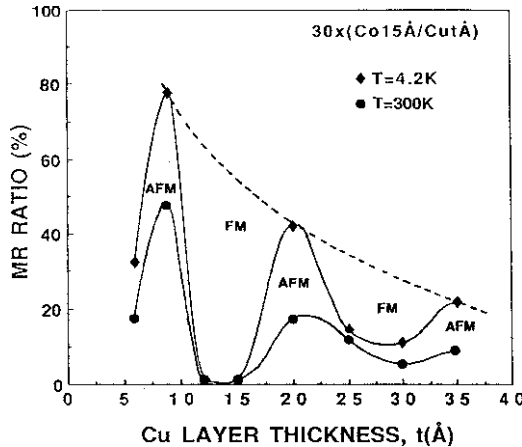
Fig. 4.21. Oscillations in the coupling of CoCu multilayers, measured by the variation of the magnetoresistance as a function of the thickness of the Cu layers. The *diamonds* and *circles* represent measurements at 4.2 and 300 K, respectively. The *dashed line* joins the points corresponding to sample with antiferromagnetic coupling [26]. (With permission from Elsevier Science and Technology)

Table 4.3. Values of interlayer exchange coupling strengths and oscillation periods (in atomic layers and nanometers) for different multilayers [12]

Sample	Maximum strength in mJ m^{-2} at (thickness) in nm	Period in ML and (nm)
Co/Cu/Co (100)	0.4 (1.2)	2.6 (0.47), 8 (1.45)
Co/Cu/Co (110)	0.7 (0.85)	9.8 (1.25)
Co/Cu/Co (111)	1.1 (0.85)	5.5 (1.15)
Fe/Au/Fe (100)	0.85 (0.82)	2.5 (0.51), 8.6 (1.75)
Fe/Cr/Fe (100)	>1.5 (1.3)	2.1 (0.3), 12 (1.73)
Fe/Mn/Fe (100)	0.14 (1.32)	2 (0.33)
Co/Ru (0001)	6 (0.6)	5.1 (1.1)
Co/Rh/Co (111)	34 (0.48)	2.7 (0.6)
Co/Os (111-text'd)	0.55 (0.9)	7 (1.5)
Co/Ir (111)	2.05 (0.5)	4.5 (1.0)

The coupling between the two FM layers depends on the electronic structure of the material of the nonmagnetic spacer. The coupling constant J_1 also depends on the thickness t of the spacer in an inverse quadratic form: $J_1 \propto 1/t^2$.

The oscillation periods are related to the critical spanning vectors, vectors in reciprocal space that connect two parallel sheets of the Fermi surface. Normally, the vectors considered are those of the Fermi surface of the bulk material.

The simplest descriptions of the oscillatory coupling are given by the RKKY model, adequate in the impurity case to rare-earth systems, and the free-electron model, used in simple descriptions of transition metals. Other descriptions are embodied in the quantum confinement model and the interface model. A comparison of the predictions of these different theoretical approaches is given by [35]. In the different theories, for large spacer thickness t, the coupling is given by a sum of terms of the form

$$J_1(t) = \sum_\alpha \frac{J^\alpha}{t^2} \sin\left(\frac{2\pi}{L^\alpha} t + \phi^\alpha \right). \tag{4.14}$$

The variable α labels each critical point, with period $L^\alpha = 2\pi/q_\perp^\alpha$, where $q_\perp^\alpha$ are the spanning vectors, J^α are the coupling strengths and ϕ^α are the phases.

The oscillatory coupling between two ferromagnets is illustrated in an elegant way in an experiment, where they are separated by a nonmagnetic wedge (Fig. 4.22). The direction of magnetization of the top film – up or down – appears as black or white stripes in the image obtained by scanning electron microscopy with spin polarization (SEMPA), a technique in which the polarization of secondary electrons is measured, allowing the determination of the direction of magnetization. In the figure, a Cr wedge is placed between a Fe whisker and a thin Fe film, and the images were obtained at 30°C and 350°C [38].
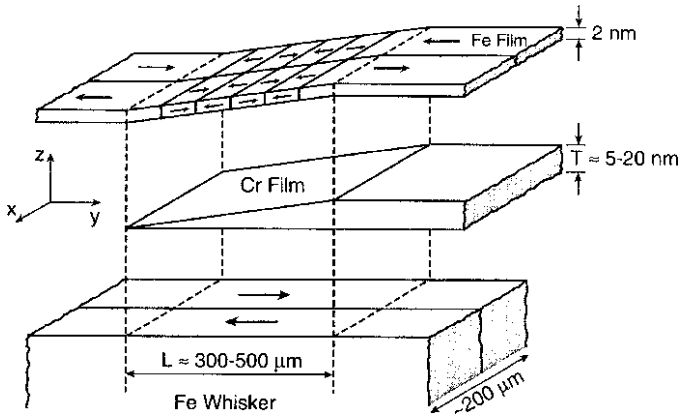
Fig. 4.22. Experiment to illustrate the oscillatory coupling of two FM layers through a non-magnetic wedge. A Cr wedge is placed between a thin Fe film and a Fe whisker with a two-domain structure. The result is that the Fe film is magnetized in segments of opposite magnetization [38]. (Reprinted from [38]. Copyright (1991) from the American Physical Society)

Further Reading

D.E. Burgler, S.O. Demokritov, P. Grünberg, M.T. Johnson, in *Interlayer Exchange Coupling in Layered Magnetic Structures*, ed. by K.J.H. Buschow. Handbook of Magnetic Materials, vol. 13 (Elsevier, Amsterdam, 2001)

G. Cao, *Nanostructures & Nanomaterials* (Imperial College Press, London, 2004)

U. Gradmann, in *Magnetism in Ultrathin Transition Metal Films*, ed. by K.H.J. Buschow. Handbook of Magnetic Materials (North Holland, Amsterdam, 1993), pp. 1–96

P. Grünberg, J. Magn. Magn. Mater. **226**, 1688–1693 (2001)

B. Heinrich, J.F. Cochran, in *Magnetic Ultrathin Films*, ed. by H. Kronmüller, S. Parkin. Handbook of Magnetism and Advanced Magnetic Materials, vol. 4 (Wiley, Chichester, 2007), pp. 2285–2305

J.C. Lodder, in *Patterned Nanomagnetic Films*, ed. by D. Sellmyer, R. Skomski. Advanced Magnetic Nanostructures (Springer, New York, 2005), pp. 295–324

J. Nogués, J. Sort, V. Langlais, V. Skumryev, S. Suriñach, J.S. Muñoz, M.D. Baró, Phys. Repts. **422**, 65–117 (2005)

R.C. O'Handley, *Modern Magnetic Materials* (Wiley, New York, 2000), Chap. 16

J. Slonczewski, in *Theory of Spin-Polarized Current and Spin-Transfer Torque in Magnetic Multilayers*, ed. by H. Kronmüller, S. Parkin. Handbook of Magnetism and Advanced Magnetic Materials, vol. 5 (Wiley, Chichester, 2007), pp. 2648–2667

M.D. Stiles, in *Interlayer Exchange Coupling*, ed. by B. Heinrich, J.A.C. Bland. Ultrathin Magnetic Structures III (Springer, Berlin, 2004)

C.A.F. Vaz, J.A.C. Bland, G. Lauhoff, Rep. Prog. Phys. **71**, 056501–056578 (2008)

M. Wuttig, X. Liu, *Ultrathin Metal Films* (Springer, Berlin, 2004)

References

1. D.A. Allwood, G. Xiong, C.C. Faulkner, D. Atkinson, D. Petit, R.P. Cowburn, Science **309**, 1688–1692 (2005)
2. C.H. Back, R. Allenspach, W. Weber, S.S.P. Parkin, D. Weller, E.L. Garwin, H.C. Siegmann, Science **285**, 864–867 (1999)
3. C. Binek, A. Hochstrat, W. Kleemann, J. Magn. Magn. Mater. **234**, 353–358 (2001)
4. G. Cao, *Nanostructures and Nanomaterials* (Imperial College Press, London, 2004)
5. R.P. Cowburn, Science **311**, 183–184 (2006)
6. R.P. Cowburn, J. Ferré, S.J. Gray, J.A.C. Bland, Phys. Rev. B **58**, 507 (1998)
7. R.P. Cowburn, M.E. Welland, Science **287**, 1466–1468 (2000)
8. H.L. Davis, J.B. Hannon, K.B. Ray, E.W. Plummer, Phys. Rev. Lett. **68**, 2632–2635 (1992)
9. B.N. Engel, C.D. England, R.A. Van Leeuwen, M.H. Wiedmann, C.M. Falco, Phys. Rev. Lett. **67**, 1910–1913 (1991)
10. J. Fassbender, D. Ravelosona, Y. Samson, J. Phys. D: Appl. Phys. **37**, R179–R196 (2004)
11. U. Gradmann, in *Magnetism in Ultrathin Transition Metal Films*, ed. by K.H.J. Buschow. Handbook of Magnetic Materials, vol 7 (North Holland, Amsterdam, 1993), pp. 1–96
12. P. Grünberg, J. Magn. Magn. Mater. **226**, 1688–1693 (2001)
13. F.J. Himpsel, J.E. Ortega, G.J. Mankey, R.F. Willis, Adv. Phys. **47**, 511–597 (1998)
14. D. Hrabovsky, D. Ciprian, J. Jaworowicz, M. Gmitra, D. Horvarth, I. Vavra, A.R. Fert, J. Pistora, Trans. Magn. Soc. Jpn. **2**, 240–243 (2002)
15. A. Imre, G. Csaba, L. Ji, A. Orlov, G.H. Bernstein, W. Porod, Science **311**, 205–208 (2006)
16. R. Kikuchi, J. Appl. Phys. **27**, 1352–1357 (1956)
17. M. Kiwi, J. Magn. Magn. Mater. **234**, 584–595 (2001)
18. N.C. Koon, Phys. Rev. Lett. **78**, 4865–4868 (1997)
19. H. Kronmüller, S. Parkin (eds.), *Handbook of Magnetism and Advanced Magnetic Materials* (Wiley, Chichester, 2007)
20. C. Leighton, J. Nogués, B.J. Jönsson-Åkerman, I.K. Schuller, Phys. Rev. Lett. **84**, 3466–3469 (2000)
21. A.P. Malozemoff, Phys. Rev. B **35**, 3679–3682 (1987)
22. D. Mauri, H.C. Siegmann, P.S. Bagus, E. Kay, J. Appl. Phys. **62**, 3047–3049 (1987)
23. W.H. Meiklejohn, J. Appl. Phys. **33**, 1328–1335 (1962)
24. W.H. Meiklejohn, C.P. Bean, Phys. Rev. **102**, 1413–1414 (1956)
25. S. Middelhoek, J. Appl. Phys. **34**, 1054–1059 (1963)
26. D.H. Mosca, F. Petroff, A. Fert, P.A. Schroeder Jr., W.P. Pratt, R. Laloee, J. Magn. Magn. Mater. **94**, L1–L5 (1991)
27. L. Néel, J. Phys. Rad. **15**, 225–239 (1954)
28. J. Nogués, I.K. Schuller, J. Magn. Magn. Mater. **192**, 203–232 (1999)
29. R.C. O'Handley, *Modern Magnetic Materials* (Wiley, New York, 2000)
30. S.N. Piramanayagam, J. Appl. Phys. **102**, 011301 (2007)
31. M.J. Prandolini, Rep. Prog. Phys. **69**, 1235–1324 (2006)
32. I. Ruiz-Feal, T.A. Moore, L. Lopez-Diaz, J.A.C. Bland, Phys. Rev. B **65**, 054409 (2002)
33. R.L. Stamps, J. Phys. D: Appl. Phys. **33**(23), R247–R268 (2000)
34. R.L. Stamps, J. Phys. D: Appl. Phys. **34**(3), 444 (2001)
35. M.D. Stiles, J. Magn. Magn. Mater. **200**, 322–337 (1999)
36. M. Takahashi, A. Yanai, S. Taguchi, T. Suzuki, Jpn. J. Appl. Phys. **19**, 1093–1106 (1980)
37. J. Tersoff, L. Falikov, Phys. Rev. B **26**, 6186–6200 (1982)
38. J. Unguris, R.J. Celotta, D.T. Pierce, Phys. Rev. Lett. **67**, 140–143 (1991)

5

Introduction to Magnetotransport

Summary. In this chapter, a brief account of some phenomena resulting from the interplay of the magnetization of a sample and the spin-polarized currents will be given, including the giant magnetoresistance and tunnel magnetoresistance effects. Simple models for the description of these effects are presented. These effects depend on the relation between the flow of electrons with a given spin through a sample, and the sample magnetization M, the physical basis of spin electronics, or Spintronics. Other consequence of the interaction with spin-polarized electron currents is the spin-induced, or spin-transfer torque.

5.1 Introduction

Magnetoresistance is the phenomenon of change in the resistance of a sample submitted to a magnetic field. Its quantitative measure MR is given as a function of R_H and R_0, the resistances of the sample with and without applied magnetic field:

$$MR = \frac{R_{\mathrm{H}} - R_0}{R_{\mathrm{H}}}. \tag{5.1}$$

A sample through which an electric current flows, submitted to an applied magnetic field, may change its electrical resistance through magnetoresistance effects that originate from different physical phenomena:

1. *Anisotropic magnetoresistance*: Arises from the interaction of the electron spin with the orbital moment of the matrix atom (it depends on the angle between the magnetization and the direction of the electric current)

2. *Lorentz magnetoresistance* arises from the curvature of the electron orbits in the applied field and consequent increase in the length of the trajectories

3. *Giant magnetoresistance* results from the difference in spin scattering in the regions with different directions of magnetization and in the interfaces (in multilayers and granular systems)

4. *Tunnel magnetoresistance* results from the difference in tunneling probability of electrons with spin up and spin down

5. *Colossal magnetoresistance* arises from conductor–insulator transition induced by applied magnetic field (e.g., in perovskites)

6. *Domain wall magnetoresistance* arises due to the magnetic field dependence of the conduction electron spin scattering at the domain walls

7. *Ballistic magnetoresistance* is an effect observed in nanocontacts, due to spin-dependent scattering at a domain wall in a nanocontact

8. *Tunneling anisotropic magnetoresistance* arises due to spin-orbit induced anisotropy in the density of states

These mechanisms and the magnitudes of the different types of magnetoresistance are given in Table 5.1.

An electron that propagates through a medium in the diffusive transport regime undergoes a process of random walk. This regime is characterized by the condition that the distances travelled by the electron are much smaller than the dimensions of the conductor; the regime where the relation between these dimensions is reversed corresponds to the ballistic regime.

The electron in the diffusive regime, after travelling on the average a distance λ_{mfp}, the mean free path, suffers a collision. Let us consider that the electron undergoes N collisions until it inverts its spin from spin up to down, or vice-versa. At this point, the electron is found at a distance l_{sd} from the starting point, given by

$$l_{\text{sd}} = \sqrt{N}\,\lambda_{\text{mfp}}. \tag{5.2}$$

This is the electron spin diffusion length, the length scale of the exponential decay of the electron current magnetization. The total length of the path of the electron is then

$$N\lambda_{\text{mfp}} = v_{\text{F}}\tau, \tag{5.3}$$

where v_{F} is the Fermi velocity of the electrons, or velocity of the electrons that are at the Fermi level, and τ is the spin relaxation time.

Combining the earlier two equations, the expression of the spin diffusion length is obtained as:

$$l_{\text{sd}} = \sqrt{\lambda_{\text{mfp}}v_{\text{F}}\tau}. \tag{5.4}$$

Table 5.1. Types of magnetoresistance, mechanisms and magnitudes (Based on [7])

Type of magnetoresistance	Origin	ΔR (%) at RT
Anisotropic MR[a] (AMR)	Spin–orbit interaction	5
Lorentz MR[b] (LMR)	Curved paths in the Lorentz curve	$\propto B^2$
Giant MR (GMR)	Spin-dependent transport	50
Colossal MR (CMR)	Band-splitting due to ordering onset	5
Ballistic MR (BMR)	Spin-dependent scattering at DW	$\sim 10^3$
Tunnel MR (TMR)	Spin-dependent transport across tunnel barrier	$\sim 10^2$
Tunnel anisotropic MR (TAMR)	Anisotropic density of states	~ 10
Domain-wall MR (DWMR)	Spin-dependent scattering at DW	~ 1

[a]Sometimes called extraordinary magnetoresistance (EMR)
[b]Sometimes called ordinary magnetoresistance (OMR), or MR

Table 5.2. Spin diffusion lengths l_{sd} for some materials, at different temperatures [4]

	Temperature (K)	l_{sd} (nm)
Fe	4.2	8.5 ± 1.5
Co	4.2	≥ 40
Ni	4.2	21 ± 2
Py	4.2	5.5 ± 1
Py	293	3
$Co_{91}Fe_9$	4.2	12 ± 1
Cu	293	500–700

If one injects a spin polarized current from a magnetic metal into a normal metal, for example, there will be injected a net magnetization. The spin diffusion length is the characteristic length for the exponential decay of the imbalance in the number of conduction electrons with spin up and spin down, and consequently, of the conduction electron magnetization.

The length of the electron trajectory while this magnetization decays is a measure of the spin diffusion length l_{sd}. Table 5.2 contains some values of the length l_{sd}, for different materials. These values vary from a few nanometers to some tens of nanometers in magnetic metals; in nonmagnetic metals they reach several hundred nanometers. The spin diffusion lengths exhibit also a temperature dependence, decreasing with increasing temperature.

"Spin up," is defined as the spin orientation of the majority spins; note that the spin magnetic moment and the spin angular momentum of a free electron point in opposite directions ((2.10), p. 25). Thus a magnetic field pointing down will produce a magnetization in the down direction; the majority spins will have spin up (and moment pointing down).

A magnetic field H_0 applied to an electron gas modifies the population of electrons with spin up and spin down, as the original band splits into two sub-bands, one with spin up, the other spin down, as introduced in Chap. 2. The two sub-bands are displaced by

$$\mu_0 \mu_B H_0, \tag{5.5}$$

and there appears a magnetization due to the electrons, proportional to the difference of electron population in the two sub-bands, and it is given by $\mu_s = \mu_B(n_\uparrow - n_\downarrow)$. In a transition metal ferromagnet, the conduction electron band is spontaneously split through the action of the Coulomb interaction between the electrons.

The computed densities of states for Fe, Co, and Ni illustrate the splitting of the bands and the difference in population of the two sub-bands (Fig. 5.1); the density of states curve of Cu is also given, for comparison. The curves show for Fe, Co, and Ni, besides the difference in energy between the majority spin sub-band ($\uparrow$) and minority spin sub-band ($\downarrow$), the difference in the densities of states at the Fermi level $D(E_F)_\uparrow$ and $D(E_F)_\downarrow$ for the two sub-bands.
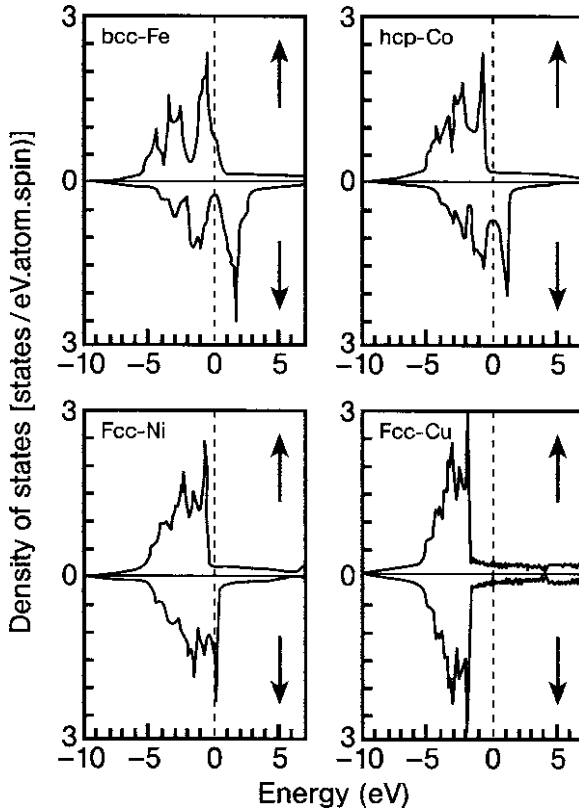
Fig. 5.1. Electron densities of states for Fe, Co, Ni, and Cu. Note that for Fe, Co, and Ni, at the Fermi level ($E = 0$) the numbers of electrons of majority and minority spins, $D(E_F)_\uparrow$ and $D(E_F)_\downarrow$, are different [32]. (Reproduced with permission [32])

This difference in population of spin up and spin down electrons is referred to as an equilibrium polarization. A novel effect is the generation of non-equilibrium polarization, or pumping, arising from an external agent that may be an electric current, electromagnetic radiation, or some resonance phenomenon.

Electrical spin injection is the effect produced by an electric current that creates such non-equilibrium polarization in a material. In its simplest form, an electric field pushes polarized electrons from a magnetic material into a nonmagnetic material, where in consequence there appears a non-equilibrium spin polarization, and a non-equilibrium magnetization δ_M. Another process that creates polarization is the action of a spin filter, a tunnel barrier (see Sect. 5.3) whose height is dependent on the electron spin [15]. The spin polarization will extend into the nonmagnetic volume for a distance comparable to the spin diffusion length l_{sd}, a parameter usually larger in the nonmagnetic material than in the magnetic material.
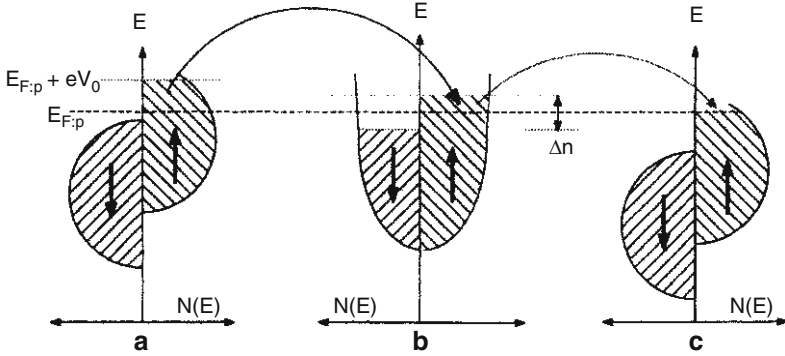
Fig. 5.2. Spin injection of a ferromagnetic metal (FM) into a nonmagnetic metal (NM) and a second ferromagnet. (**a**) density of states of the ferromagnet with the applied voltage V; (**b**) density of states of the paramagnet of thickness smaller than l_{sd}, showing a non-equilibrium magnetization δM; (**c**) density of states of the second ferromagnet. (Reprinted figure from [12]. Copyright (1988) by the American Physical Society)

An illustration of spin polarization is given in Fig. 5.2, for a ferromagnet that has only electrons with one spin direction at the Fermi level; this is known as a strong ferromagnet. This ferromagnet (FM) (a) is in contact with a paramagnet, or nonmagnetic material (NM) (b) of thickness smaller than the spin diffusion length l_{sd}, which is in contact with a second ferromagnet (c). As a voltage is applied to the FM/NM system, the electrons of the ferromagnet gain an energy eV and these excess electrons are transferred to the paramagnet. This produces an imbalance in the two sub-bands of the paramagnet, leading to the appearance in it of an excess magnetization δM.

In two classic works, published in 1936, Nevil Mott [16, 17] argued that at low temperatures, the electrons with spins ↑ and ↓ in a ferromagnet do not mix, since there is no electron scattering with magnons. One may thus consider that an electron current in the material flows through two independent conduction channels, one with spin up, one with spin down.

In the model proposed by Mott [18], the conductivity is due to the s electrons, and the resistivity arises from the $s - d$ transitions. The rate of these transitions depends on the density of states of the electrons at the Fermi level, on the number of electrons per unit volume and on their effective mass. For each spin direction σ ($\sigma =$↑ or ↓) the resistivity is given by

$$\rho_\sigma = \frac{m_\sigma}{n_\sigma e^2 \tau_\sigma}, \qquad (5.6)$$

where the relaxation time τ_σ is related to the density of states of the σ electrons at the Fermi level:

$$\tau_\sigma \propto \frac{1}{D_\sigma(E_F)}. \qquad (5.7)$$

From the difference in resistivity of spin up and spin down electrons, one may define spin asymmetry parameters, or coefficients, for a ferromagnet (F), with the relations:

$$\alpha_F = \frac{\rho_F^{\downarrow}}{\rho_F^{\uparrow}}, \tag{5.8}$$

and

$$\beta_F = \frac{\rho_F^{\downarrow} - \rho_F^{\uparrow}}{\rho_F^{\downarrow} + \rho_F^{\uparrow}}. \tag{5.9}$$

Therefore,

$$\alpha_F = \frac{1 + \beta_F}{1 - \beta_F}. \tag{5.10}$$

If the resistivities for the two spin directions are the same, $\alpha_F = 1$ and $\beta_F = 0$.

There are both intrinsic and extrinsic causes for the difference between the resistivities $\rho_F^{\downarrow}$ and $\rho_F^{\uparrow}$. The intrinsic factors are the difference in density of states of up and down electrons and difference in effective mass, for example; extrinsic factors relate to the number of impurities present in the material and the strength of their scattering potential.

The values of α_F vary for different magnetic systems; for example, in a Ni matrix, impurities of Fe, Co, Mn, Au, and Cu have $\alpha_F \gg 1$ and impurities of Cr and V have $\alpha_F < 1$ [6].

The total current density j is the sum of the current densities of the two channels, with spin up and spin down:

$$j = j_{\uparrow} + j_{\downarrow}. \tag{5.11}$$

The spin current density j_s is

$$j_s = j_{\uparrow} - j_{\downarrow}. \tag{5.12}$$

One may define the electron current polarization P_j as the ratio of the spin current density to the total current density

$$P_j = \frac{j_{\uparrow} - j_{\downarrow}}{j_{\uparrow} + j_{\downarrow}}. \tag{5.13}$$

The out of equilibrium spin density δ_s is

$$\delta_s = \delta n_{\uparrow} - \delta n_{\downarrow}, \tag{5.14}$$

where n is the electron density.

The chemical or electrochemical potential μ is the variation in thermodynamic potential of the system when an additional particle is introduced, for constant volume and entropy. For particles that obey Fermi statistics, as the electrons, μ is given by

$$\mu = E_F \left[1 - \frac{\pi^2}{12} \left(\frac{k_B T}{E_F} \right)^2 \right]. \tag{5.15}$$

At $T = 0$ K, the chemical potential μ is identical to the Fermi energy E_F. In a conductor the chemical potential is constant; if a voltage is applied, μ varies along the conductor, according to Ohm's Law. For a current along the x axis, one has:

$$\frac{\partial \mu}{\partial x} = -\frac{e}{\sigma} j, \tag{5.16}$$

where e is the modulus of the charge of the electron, σ is the conductivity, and j is the current density.

At an interface between two materials, for example, two different metals, the chemical potentials adjust one to the other, in such a way that there is no discontinuity. This situation is changed when a potential difference is applied.

One may treat the electrons with different spin directions as different particles, each one with its value of the chemical potential. At low temperatures, the probability of spin flip, the change of electron spin direction, is small, and therefore the number of electrons with a given spin direction may be considered constant. When the electrons with different spin have different chemical potentials, there is a nonzero out of equilibrium chemical potential μ_s given by:

$$\mu_s = \mu_\uparrow - \mu_\downarrow. \tag{5.17}$$

This potential is a measure of an important effect that arises when electric currents flow through magnetically ordered materials, referred to as spin accumulation. Spin accumulation is the change in the density of electrons of majority spin in both sides of an interface, for example, between a ferromagnetic metal and a nonmagnetic metal. This change is observed in a region of width of the order of the spin diffusion length l_{sd} in each material. At the interface, the chemical potential averaged for the two spin directions μ_0 undergoes a discontinuity given by $\Delta\mu = \mu_0^F - \mu_0^N$, in the case of an F/N interface. This effect is illustrated for a ferromagnet/nonmagnet interface in Fig. 5.3.
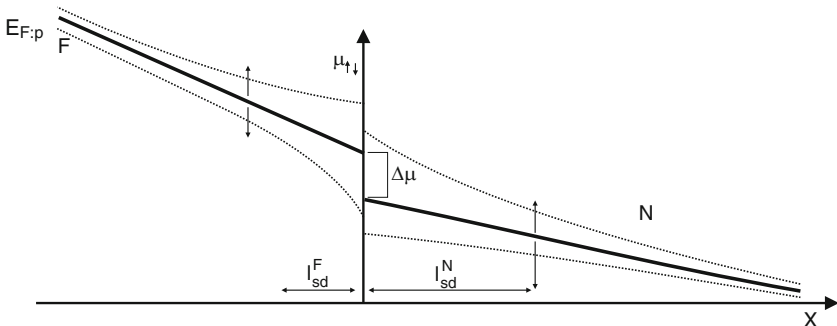
Fig. 5.3. Spin accumulation effect in a ferrromagnetic/nonmagnetic interface. The graph shows the chemical potentials of spin up and spin down electrons flowing from a ferromagnet (*F*, *left*) to a non-magnet (*N*, *right*). The *continuous line* is the average chemical potential, exhibiting a discontinuity $\Delta\mu$ at the interface, that quantifies the spin accumulation

This figure shows spin accumulation on either side of an F/N interface, that is, the chemical potentials $\mu^\uparrow$ and $\mu^\downarrow$ are different (dotted lines), in a region of width comparable to the spin diffusion length l_{sd} of each material. Also shown is the discontinuity $\Delta\mu$, the spin averaged chemical potential.

The spin accumulation is proportional, for example, to the magnetization that appears in a nonmagnetic material, when a polarized electron current crosses the interface, coming from a magnetic material. The spin accumulation is related to the densities of states of electrons of spin up and spin down at the Fermi level $D_\uparrow$ and $D_\downarrow$ of the ordered material through the relation

$$\mu_s = \frac{1}{2e}\frac{D_\uparrow + D_\downarrow}{D_\uparrow D_\downarrow}\delta_s. \tag{5.18}$$

Therefore, the spin accumulation depends on the densities of states of the electrons with spin up and spin down at the Fermi level, and is proportional to the out of equilibrium spin density δ_s.

5.2 Spin Dependent Scattering and Giant Magnetoresistance

The giant magnetoresistance (GMR) is possibly the most important of the magnetoresistances, in view of the interest in its physical basis and on its potential for applications. In an experiment with multilayers, the resistance of the ferromagnetic layers depends on the relative directions of the magnetization and electron spin [2]. This discovery is regarded as an important breakthrough that opened way to the development of spin electronics, or Spintronics. It is illustrated in Fig. 5.4, where the difference in scattering of electrons with up and down spins in the ferromagnetic layers with magnetization up and down is schematically represented.

The simplest quantitative description of the GMR effect is afforded by the model of resistance; the electrical resistance of a multilayer structure traversed by a current of electrons with spin up and spin down is equivalent to a resistance of a circuit with two parallel branches of resistors. When the magnetizations of the ferromagnetic layers are parallel, the equivalent circuit has resistors with small resistance in series in one branch, and large resistors in the other. When the magnetizations of the layers alternate their directions, the parallel circuits contain both large and small resistors. The resistor schemes corresponding to magnetic layers in antiferromagnetic and ferromagnetic arrangements are represented in the lower part of Fig. 5.4; the resistances for the two arrangements of the multilayer are R_P (parallel magnetic layers) and R_{AP} (antiparallel layers).

The GMR effect can be studied in two geometries: (1) with a current applied in the plane of the multilayer – current in plane (CIP) or (2) with a current applied perpendicularly to the plane (CPP). In the CIP geometry, the average path of the electrons is parallel to the interfaces, but the actual trajectories in fact sample the whole multilayer, crossing the boundaries between magnetic and nonmagnetic layers. As the experiments are typically performed with thin films, the CIP arrangement
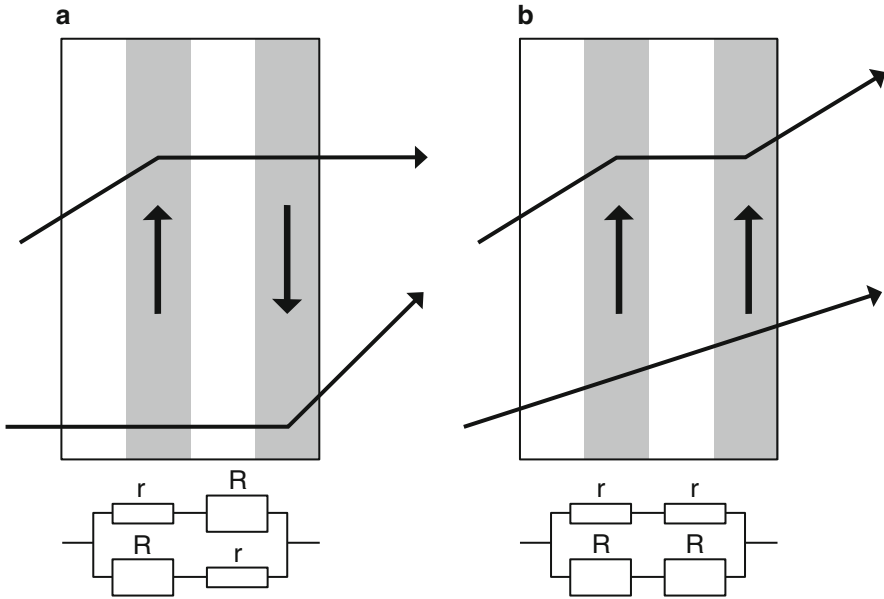
Fig. 5.4. *Top*: The spin dependent electron scattering in a multilayer formed of magnetic and nonmagnetic layers, arranged (**a**) antiferromagnetically and (**b**) ferromagnetically, essence of the effect. *Bottom*: corresponding resistor schemes
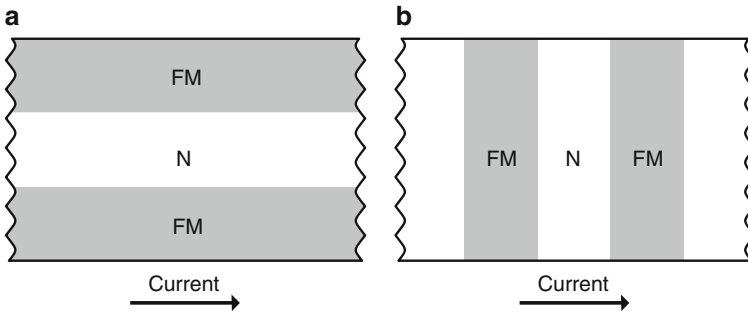
Fig. 5.5. Different geometries of magnetotransport experiments, exemplified with a multilayer with a ferromagnet (FM), a nonmagnetic material (N) and a ferromagnet (FM): (**a**) current in plane (CIP) and (**b**) current perpendicular to the plane (CPP)

is often preferred, since the CPP geometry leads to an electrical resistance that is too low. These two experimental arrangements are illustrated in Fig. 5.5.

An example of measurements of the magnetoresistance and magnetization is given in Fig. 5.6; the figure shows the magnetoresistance of 60X[Co(6nm)Ag(6nm)] multilayers vs. applied magnetic field in the CPP and CIP geometries. The graphs show *MR* vs. *H* in both cases; the magnetic hysteresis curve is also shown.
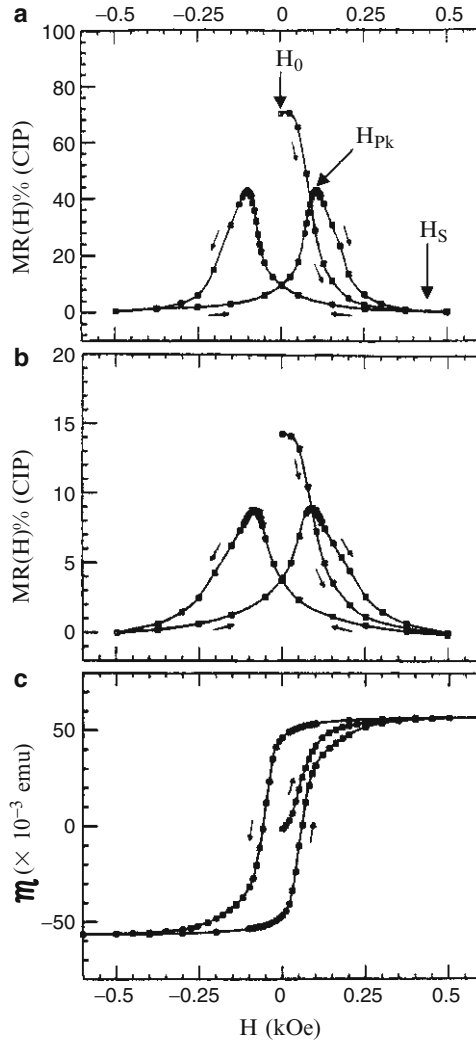
Fig. 5.6. Magnetoresistance and magnetization as function of H for 60X[Co(6nm)Ag(6nm)] multilayer (**a**) in the CPP and (**b**) in CIP geometries; (**c**) shows the hysteresis curve. The field for maximum MR in the as-prepared sample is denoted H_0, the saturation field is H_s, and H_{pk} is the local maximum after attaining saturation [3]. (With permission from Elsevier Science and Technology)

Table 5.3, taken from reference [8], gives some values of GMR measured with multilayers of different materials; the values range from about $1 - 200\%$.

One can illustrate an application of the resistance network model to a multilayer formed of two ferromagnetic layers separated by a nonmagnetic spacer. Its conductance, or inverse of the resistance, can be written in terms of the contributions to the

Table 5.3. Values of GMR measured in different multilayers [8]

Material	Temperature	GMR	Reference
Co(1.2 nm)/Ir(1.6 nm)	RT	0.33%	[34]
Fe(2.5 nm)/Mo(1.2 nm)	4.2 K	~1.8%	[5]
Fe(0.96 nm)/Au(3.3 nm)	RT	2%	[27]
Co(1.5 nm)/Cr(0.4 nm)	RT	2.5%	[23]
Co(3.0 nm)/Al(2.3 nm)	RT	2.8%	[11]
Ni/Cu	4.2 K	9.3%	[25]
$Ni_{80}Fe_{20}$(1.25 nm)/Au(1.1 nm)	RT	12%	[22]
$Ni_{80}Fe_{20}$(1.25 nm)/Ag(1.1 nm)	RT	17%	[24]
$Ni_{80}Fe_{20}$(1 nm)/Cu(1 nm)	RT	18%	[19]
Co(0.6 nm)/Ag(2.5 nm)	RT	22%	[1]
Ni(0.8 nm)/Ag(1.1 nm)	4.2 K	36%	[24]
Co(0.75 nm)/Cu(0.93 nm)	4.5 K	80%	[21]
Fe(0.45 nm)/Cr(1.2 nm)	4.2 K	220%	[26]

electrical resistance for a current of electrons with spin up and a current with spin down. For example, one contribution is $R_{\uparrow\downarrow}$, the resistance to electrons of spin up (the first subscript) crossing a layer with magnetic moment down (the second subscript). The contributions of the nonmagnetic layer $R_\uparrow$ and $R_\downarrow$ contain only the spin direction of the conduction electrons.

The giant magnetoresistance is given quantitatively as:

$$GMR = \frac{\Delta R}{R_P} = \frac{R_{AP} - R_P}{R_P}. \tag{5.19}$$

This equation is consistent with the definition of giant magnetoresistance given in (5.1); the two ferromagnetic layers in the above example have their moments arranged one opposite to the other, in an antiferromagnetic coupling (antiparallel, subscript AP), for $H = 0$. With applied magnetic field ($H \neq 0$) the arrangement is ferromagnetic, or parallel (subscript P).

Considering the current perpendicular to the plane, or CPP geometry, the resistances R_P and R_{AP} are sums of resistances in parallel of electrons with spin up and spin down. Therefore:

$$\frac{1}{R_P} = \left(\frac{1}{R_{\uparrow\uparrow} + R_\uparrow + R_{\uparrow\uparrow}} + \frac{1}{R_{\uparrow\downarrow} + R_\downarrow + R_{\uparrow\downarrow}} \right), \tag{5.20}$$

and

$$\frac{1}{R_{AP}} = \left(\frac{1}{R_{\uparrow\uparrow} + R_\uparrow + R_{\uparrow\downarrow}} + \frac{1}{R_{\uparrow\downarrow} + R_\downarrow + R_{\downarrow\downarrow}} \right). \tag{5.21}$$

Assuming that for the nonmagnetic layers the resistivity is independent of the electron spin (up or down):

$$R_\uparrow = R_\downarrow. \tag{5.22}$$

Equations (5.20) and (5.21) can be simplified if one writes the resistance of the multilayers in the case where electron moment and layer magnetization are parallel or antiparallel as $R^\uparrow$ and $R^\downarrow$, respectively:

$$R^\uparrow = R_{\uparrow\uparrow} + R_\uparrow + R_{\uparrow\uparrow}, \tag{5.23}$$

and

$$R^\downarrow = R_{\uparrow\downarrow} + R_\downarrow + R_{\uparrow\downarrow}. \tag{5.24}$$

With these definitions, (5.20) and (5.21) become:

$$\frac{1}{R_P} = \left(\frac{1}{R^\uparrow} + \frac{1}{R^\downarrow} \right), \tag{5.25}$$

and

$$\frac{1}{R_{AP}} = \left(\frac{4}{R^\uparrow + R^\downarrow} \right). \tag{5.26}$$

The giant magnetoresistance is therefore:

$$GMR = \frac{R_{AP} - R_P}{R_P} = \frac{(R^\uparrow - R^\downarrow)^2}{4R^\uparrow R^\downarrow}. \tag{5.27}$$

From this expression one sees that the giant magnetoresistance does not change if $(R^\uparrow - R^\downarrow)$ is either positive or negative.

The proper calculation of the resistivity of a multilayer formed of nonmagnetic and ferromagnetic layers requires the inclusion of contributions both from the interior of the layers and from the interfaces. The simplest description of the total resistivity is the two-current series resistor model (2CSR), valid for layer thicknesses smaller than the corresponding spin diffusion lengths. In this approximation, layer and interface contributions to the magnetoresistance add up in series.

The resistivities of a ferromagnetic layer for parallel and antiparallel alignment of electron and layer magnetization are written in terms of the bulk resistivity ρ_F. The notation is $\rho_F^\uparrow$ and $\rho_F^\downarrow$ for electron moment and layer moment parallel and antiparallel, respectively:

$$\rho_F^\uparrow = \frac{2\rho_F}{1 + \beta_F}; \qquad \rho_F^\downarrow = \frac{2\rho_F}{1 - \beta_F}. \tag{5.28}$$

The contribution to the resistivity of the interfaces $R_{F/N}$ between F (ferromagnet) and N (nonmagnetic) layers, using an analogous notation, is:

$$R_{F/N}^\uparrow = \frac{2R_{F/N}}{1 + \gamma}; \qquad R_{F/N}^\downarrow = \frac{2R_{F/N}}{1 - \gamma}. \tag{5.29}$$

where a new asymmetry parameter γ, related to the interface, has been introduced.

The spin asymmetry parameters, or coefficients, dependent on the alignment of conduction electron moment at the layers and at the interface are:

$$\alpha_F = \frac{\rho_F^\downarrow}{\rho_F^\uparrow} = \frac{1 + \beta_F}{1 - \beta_F}. \tag{5.30}$$

and

$$\alpha_{F/N} = \frac{R_{F/N}^{\downarrow}}{R_{F/N}^{\uparrow}} = \frac{1+\gamma}{1-\gamma}. \tag{5.31}$$

The specific resistance AR is the product area $\times$ resistance = resistivity $\times$ thickness (or length):

$$AR = \rho \times t. \tag{5.32}$$

The length of the electron path that crosses perpendicularly a multilayer (CPP geometry) is its total thickness; for a system of N equal bilayers of thicknesses t_N and t_F, for the nonmagnetic and the ferromagnetic layers, respectively, it is $t = N(t_N + t_F)$. The quantity AR, the product of the area times the resistance of a multilayer is a sum of the resistance terms at the interfaces and at the different layers. For a magnetic field H_0 that does not saturate the magnetizations, i.e., that produces a configuration of antiparallel (AP) magnetizations, one has:

$$AR_{AP}(T) = N(\rho_N t_N + \rho_F^* t_F + 2AR_{F/N}^*). \tag{5.33}$$

As an approximation, one uses N instead of $N - 1$ or $N + 1$.

The terms with asterisks are the renormalized resistances:

$$\rho_F^* = \frac{\rho_F}{1 - \beta_F^2}; \qquad R_{F/N}^* = \frac{R_{F/N}}{1 - \gamma^2}. \tag{5.34}$$

The spin asymmetry parameters that characterize the interfaces, such as γ, depend on their physical rugosity and their "chemical rugosity" (a measure of the degree of alloying at the interface). See Table 5.4 for some values of the parameters for CoCu multilayers.

For a field that saturates the magnetization $H = H_{sat}$, the magnetizations of the ferromagnetic layers are parallel, the specific resistance is $AR_P(T)$ (P for parallel):

$$AR_P(T) = AR_{AP}(T) - N^2 \frac{(\beta_F \rho_F^* t_F + 2\gamma AR_{F/N}^*)^2}{AR_{AP}(T)}. \tag{5.35}$$

Re-writing this result, one has

$$A\sqrt{R_{AP}(T)[R_{AP}(T) - R_P(T)]} = N(\beta_F \rho_F^* t_F + 2\gamma AR_{F/N}^*). \tag{5.36}$$

Table 5.4. Parameters for Co/Cu multilayers [3]

Parameter	Unit	Value
ρ_{Cu}	nΩ m	6 ± 1
ρ_{Co}^*	nΩ m	75 ± 5
β_F	–	0.46 ± 0.05
γ	–	0.77 ± 0.04
$AR_{Co/Cu}^*$	fΩ m^2	0.51 ± 0.02
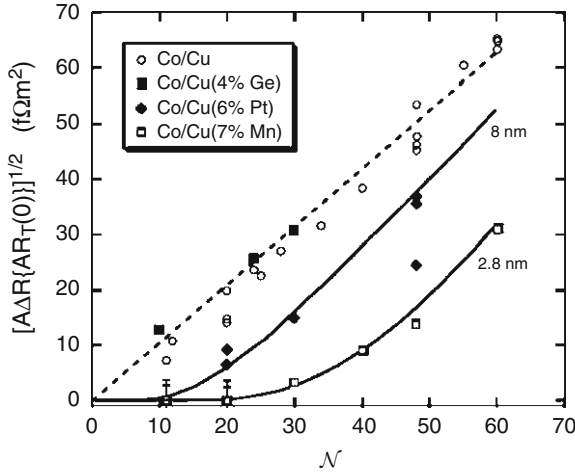
Fig. 5.7. Graph of $A\sqrt{R_{AP}(T)\Delta R}$ vs. number of bilayers of Co and Cu-based alloys. The pure Co/Cu system and the Co/Cu (4%Ge) systems are fitted to a straight line through the origin, given by the 2-resistor model (2CRS) (5.36). The multilayers with Pt and Mn have to be fitted with the Valet–Fert theory. The numbers on the right are the spin diffusion lengths l_{sd} derived from the computer fits. (Reproduced with permission from [4])

Making a plot of the expression on the left-hand side of (5.36) as a function of N (number of bilayers), one can distinguish the different contributions to the magnetoresistance, i.e., the contributions from the volume and from the interfaces. For example, by varying the thickness t_F the volume term varies, and by varying N, the interface contribution varies [9]. This type of plot is shown in Fig. 5.7, where one can see the dependence of $AR_P(T)$ with N in the 2CRS model and in the Valet–Fert model (see below).

An application of the above result (5.36) to an exchange-biased spin valve, consisting of a multilayer of structure [AF/F/N/F], gives for $A\Delta R$, where $A\Delta R = R_{AP} - R_P$:

$$A\Delta R = \frac{4(\beta_F \rho_F^* t_F + \gamma AR_{F/N}^*)^2}{2\rho_F^* t_F + \rho_N t_N + 2AR_{F/N}^* + AR_{AF/F} + \rho_{AF} t_{A/F}}. \tag{5.37}$$

The denominator of $A\Delta R$ corresponds to the specific resistance of the antiparallel configuration AR_{AP}.

In multilayers formed with two different ferromagnetic materials, one can combine one layer with $\alpha_F < 1$ to another with $\alpha_F > 1$, and obtain a system that exhibits an "inverse" GMR, a condition characterized by $R_P > R_{AP}$. Figure 5.8 shows the difference between the "normal" GMR and the inverse GMR.

An example of a system that presents the inverse GMR is the NiCr/Cu/Co/Cu multilayer structure.

Therefore, the normal and inverse giant magnetoresistances are characterized by: (1) Normal GMR: 1 FM metal, $\beta_F > 0$; (2) Inverse GMR: 2 FM metals, $\beta 1 > 0$, $\beta 2 < 0$.

a   **"Normal" GMR**

Single F-metal: $\dfrac{\rho^{\downarrow}}{\rho^{\uparrow}} > 1 \ (\beta > 0)$

$$R_{AP} > R_P$$

b   **Inverse GMR**

Two F-metals: F1 & F2

$\dfrac{\rho^{\downarrow}_{F1}}{\rho^{\uparrow}_{F1}} > 1 \ (\beta1 > 0);$ $\dfrac{\rho^{\downarrow}_{F2}}{\rho^{\uparrow}_{F2}} < 1 \ (\beta2 < 0);$

$$R_{AP} < R_P$$
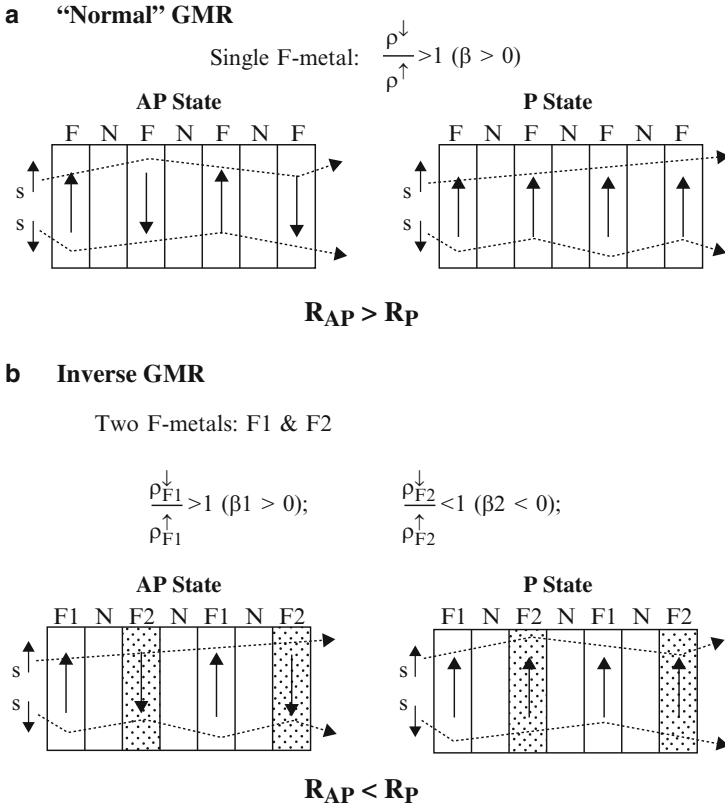
Fig. 5.8. (**a**) "Normal" and (**b**) "inverse" GMR. In the latter there are two ferromagnetic metals with different ratios of α parameters and different β_F parameters [3]. (With permission from Elsevier Science and Technology)

5.2.1 Valet–Fert Model for GMR

The simple two-current series-resistor (2CSR) model is effective in describing the behavior of the magnetoresistance in many simple multilayers, but it breaks down for systems formed of layers that have thicknesses comparable to the spin diffusion lengths. In this case the α and β parameters defined above are dependent on the thicknesses t_F, t_N, and on the number of repetitions N. The deviations from the 2CSR model are consequently notable in the multilayers formed of thicker films, as shown in the plots of magnetoresistance vs. N of Fig. 5.7.

The Valet–Fert model [31] attempts to describe the magnetoresistance of multi-layers that have components with thicknesses that are not much smaller than the spin diffusion length l_{sd}. The results in this description are in general more complicated, and in most cases a numerical solution is required.

One simple application of the Valet–Fert model is that to an exchange-biased spin valve, with composition [AF/F/N/F], where the result depends not only on the

thickness of the nonmagnetic layers, but also on the spin diffusion length of the ferromagnet [3]:

$$A\Delta R = \frac{4(\beta_F \rho_F^* l_{sd}^F + \gamma A R_{F/N}^*)^2}{2\rho_F^* l_{sd}^F + 2A R_{F/N}^* + \rho_N t_N}. \tag{5.38}$$

Comparing the above result to the description of the same multilayer within the 2CSR model (5.37) one notes that the denominator of $A\Delta R$ given in the Valet–Fert model is the same as in the previous case, but now the quantity t_F has been substituted by the thickness of the "active" region of the F-layer, that is, the spin diffusion length l_{sd}^F in the ferromagnet.

5.3 Tunnel Magnetoresistance (TMR)

The tunnel effect is a quantum-mechanical effect that consists in the transmission of a particle through a potential barrier. In a tunnel junction, two electrical conductors are connected through an insulating thin film, and electrons cross the barrier represented by the film; this thin film, for example, made of Al_2O_3, usually has a thickness in the range of nanometers.

Tunnel junctions, under an applied magnetic field, exhibit a magnetoresistance effect, known as tunnel magnetoresistance (TMR). This is observed in magnetic tunnel junctions (MTJ), junctions formed of two ferromagnetic layers separated by a thin insulating film. The effect arises from the dependence of the probability of tunneling on the relation between the direction of the spin of the conduction electrons and the direction of magnetization of the ferromagnetic contacts. An external magnetic field affects the MTJ resistance through its action on the direction of magnetization of the ferromagnets; the resistance for an antiparallel arrangement of magnetizations is different from that measured with a parallel alignment. See, for example, the curve of resistance versus intensity of the magnetic field for a $CoFe/Al_2O_3/Co$ junction (Fig. 5.9).

The TMR, differently from the giant magnetoresistance effect (GMR), does not depend on the difference in resistivity for the electrons with up and down spins inside the ferromagnetic conductors. To a first approximation, the effect correlates only with the differences in electronic structure (densities of states) on either side of the insulating barrier. Therefore, the conductance of a tunnel junction does not depend on the electron spin diffusion length of the constitutive materials.

The magnitude of the tunnel magnetoresistance TMR of a system consisting of a ferromagnet, an insulator, and again a ferromagnet (F/I/F) may be defined as:

$$TMR = \frac{G_P - G_{AP}}{G_{AP}} = \frac{\Delta R}{R} = \frac{R_{AP} - R_P}{R_P}, \tag{5.39}$$

where R_P and R_{AP} are the resistances, and G_P and G_{AP} are the conductances, in the parallel and antiparallel configurations. This magnetoresistance effect may amount to a large effect at room temperature, a fact that has stimulated the study of the applications of MTJ's as field sensors, read heads and other electronic components.
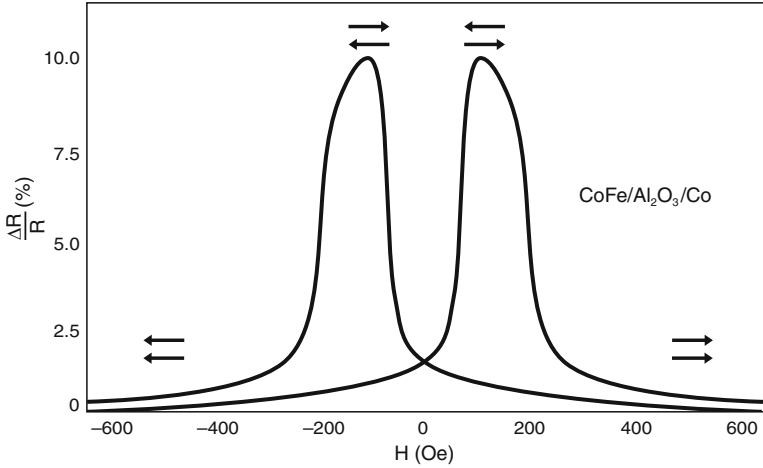
Fig. 5.9. Tunnel magnetoresistance (TMR) vs. magnetic field for a CoFe/Al$_2$O$_3$/Co junction. The *arrows* show the arrangement of the magnetizations of the two ferromagnetic layers. (Adapted from [14])

Values of TMR for some magnetic tunnel junctions, obtained at different temperatures, are given in Table 5.5; they range from a few percent to hundreds of percent. The general trend of increasing TMR with decreasing temperature can be noted in this table.

A model has been proposed by Jullière to describe TMR [13], based on two assumptions: the projections of the spin of the electrons are conserved across the barrier, and second, the conductance is proportional to the effective tunneling density of states (DOS) for the FM electrodes. The latter condition corresponds to the hypothesis that the majority spin electrons tunnel to the majority states of the second electrode if the alignment of the magnetic moments of the layers is parallel, and to the minority states if the alignment is antiparallel; this is shown schematically in Fig. 5.10.

The conductance can then be written as a function of $D(E_F)_i$ $(i = 1, 2)$, the densities of states of the two ferromagnetic electrodes.

The total conductance is the sum of the conductances for spin up and spin down electrons. For the configuration of parallel magnetizations, the conductance for each electron spin projection is proportional to the product of the corresponding densities of states; the total conductance is the sum of the conductances for spin up and spin down. In the parallel arrangement, this conduction can be written:

$$G_P \propto D(E_F)_1^{\uparrow} D(E_F)_2^{\uparrow} + D(E_F)_1^{\downarrow} D(E_F)_2^{\downarrow}. \tag{5.40}$$

For antiparallel arrangement, the conductance is, analogously,

$$G_{AP} \propto D(E_F)_1^{\uparrow} D(E_F)_2^{\downarrow} + D(E_F)_1^{\downarrow} D(E_F)_2^{\uparrow}. \tag{5.41}$$

Table 5.5. Magnetoresistance of some tunnel junctions. Note the difference in the values for different temperatures [10]

Structure of the junction	TMR (%)	Temperature
Co–Ge (10 nm)–Co	16	4.2 K
Fe–Al$_2$O$_3$–Fe	18	300 K
	30	4.2 K
CoFe–Al$_2$O$_3$–Co or NiFe	11.8	295 K
	24	4.2 K
CoFe–ZnS$_2$-CoFe	5	270 K
	10	6 K
CoFeB–Al$_2$O$_3$–CoFeB	70	300 K
CoFeB–MgO-CoFeB	472	300 K
	804	5 K
CoFe–MgO–CoFe	220	300 K
	300	4.2 K
Fe–MgO–Fe	180	300 K
Co$_2$Cr$_{0.6}$Fe$_{0.4}$Al–MgO–CoFe	37	300 K
Co$_2$Cr$_{0.6}$Fe$_{0.4}$Al–Al$_2$O$_3$–CoFe	16	300 K
Co$_2$Cr$_{0.6}$Fe$_{0.4}$Al–MgO–CoFe	90	300 K
	240	4.2 K
Co$_2$MnSi–Al$_2$O$_3$–Co$_2$MnSi	67	300 K
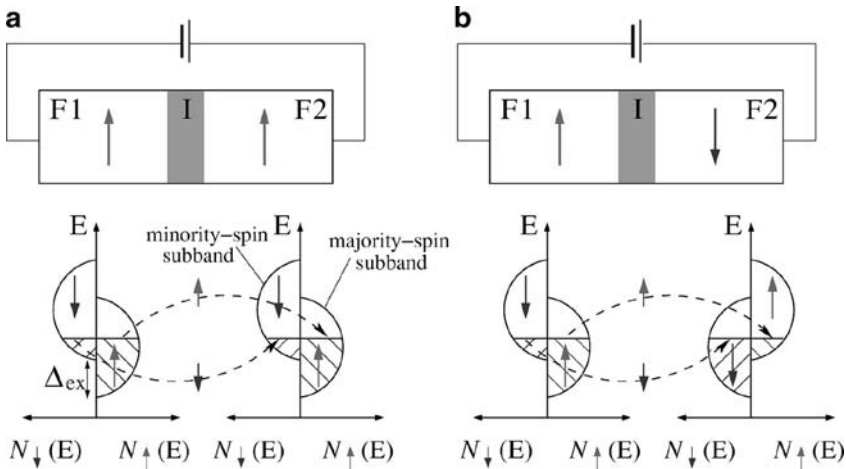
Fig. 5.10. Electron tunneling across a ferromagnet/insulator/ferromagnet junction. In (**a**) the orientation of the magnetizations is parallel and (**b**) antiparallel, showing in both cases the electron density of the split *d* states. *Dashed lines* show spin conserved tunneling. (Reprinted from [35]. Copyright (2004) by the American Physical Society)

It has been shown that the densities of states relevant to the tunneling current are the densities of parabolic bands, or free-electron-like bands [29]. One generally refers to these densities of states as tunneling densities of states.

The polarization in a ferromagnet i is defined as the relative imbalance in the majority and minority spin electron densities of states at the Fermi level:

$$P = \frac{D(E_F)^\uparrow - D(E_F)^\downarrow}{D(E_F)^\uparrow + D(E_F)^\downarrow}. \tag{5.42}$$

Using the expressions for TMR (5.40) and (5.41), and the definition of the polarization (5.42), the Jullière's formula is obtained for the tunnel magnetoresistance, relating it to the polarizations P_1 and P_2 of the two ferromagnets:

$$TMR = \frac{2P_1P_2}{1 - P_1P_2}. \tag{5.43}$$

Jullière's model predicts for $Ni/Al_2O_3/Ni$ and $Co/Al_2O_3/Co$ values of TMR of 25% and 42%, in reasonable agreement with the experiments [30].

A tunnel junction of structure ferromagnet–insulator–ferromagnet is analogous to a trilayer presenting GMR in the perpendicular current geometry (CPP).

In materials known as half-metals, such as the compounds CrO_2 and NiMnSb, the minority spin sub-band is empty, and therefore, the electrons at the Fermi level are exclusively of majority spin. Consequently, there is in this case 100% polarization, i.e., in the first ferromagnet one has

$$P_1 = \frac{D(E_F)^\uparrow}{D(E_F)^\uparrow} = 1. \tag{5.44}$$

The density of states of the CrO_2 half-metal is shown in Fig. 5.11, where the minority sub-band (on the right) is seen empty.

From (5.40) and (5.41) there will be current across the junction only in the case of parallel magnetizations, otherwise the conductance G will be zero.

Although Jullière had assumed, as a first approximation, that tunnel magnetoresistance did not depend on the shape of the density of states curves of its ferromagnetic and insulating components, relating only to the densities of states at the Fermi level of the ferromagnets, many aspects of the effect could not be described within this model. A more complete treatment is required taking into account the dependence of the effect on the electronic structure of the ferromagnets and of the insulating barrier. The Slonczewski model for the tunnel magnetoresistance uses two identical ferromagnetic layers with exchange-split parabolic bands, separated by a rectangular potential barrier [28]. This leads, for a thick barrier, to a conductance that is a linear function of the cosine of the angle between the magnetizations:

$$G(\theta) = G_0(1 + P^2 \cos\theta), \tag{5.45}$$

where P is the effective spin polarization of the tunneling electrons.
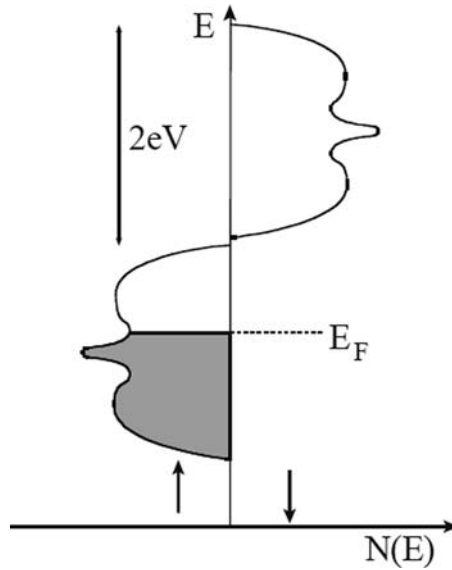
Fig. 5.11. Electronic structure of the half-metal CrO_2, exhibiting an empty minority (spin down) sub-band. (From [33]. Reprinted with permission from AAAS [33])

In this model, the electron wavefunction extends into the insulating barrier, where it is attenuated, with an imaginary wave vector κ as the damping factor, given by:

$$\hbar\kappa = \sqrt{2m(V_b - E_F)}, \tag{5.46}$$

where V_b is the barrier height, m is the electron mass and E_F is the Fermi energy.

The polarization is given by:

$$P = \left[\frac{k_\uparrow - k_\downarrow}{k_\uparrow + k_\downarrow}\right]\left[\frac{\kappa^2 - k_\uparrow k_\downarrow}{\kappa^2 + k_\uparrow k_\downarrow}\right]. \tag{5.47}$$

If V_b, the height of the barrier, tends to infinity, so does the factor κ, then the second fraction tends to 1, and the result, since $D(E_F) \propto k_F$, is identical to Jullière's expression (5.43).

Finally, one could add that ballistic magnetoresistance (BMR) is similar to TMR in its dependence on the polarization of the conduction electrons:

$$BMR = \frac{R_{AP} - R_P}{R_{AP}} = \frac{2P^2}{1 + P^2}F(\delta_0, \lambda_F), \tag{5.48}$$

where $P = P_1 = P_2$ is the same polarization defined in (5.42), δ_0 is the domain wall width and λ_F is the Fermi wavelength. $F(\delta_0, \lambda_F)$ is a function that describes the domain wall scattering.

The similarities between TMR and BMR may make it difficult to distinguish true TMR from conductance through pinholes in the insulating layer. A proof of

true TMR is given by the temperature dependence of the conductance $G(T)$: TMR decreases with increasing temperature, an effect that arises from the reduction of the electron polarization; the polarization is found to follow a Bloch $T^{3/2}$ law. The tunneling magnetoresistance phenomenon shows a magnetic field dependence, and is also modified by variations in voltage (bias).

The practical realization of a MTJ usually employs a hard magnetic layer and a soft magnetic layer. As the magnetic field is applied, it turns the magnetization of the soft layer. When the magnetization of the soft ferromagnet turns, the conductance G varies through its dependence on the angle θ (5.45).

In most cases the magnitude of the TMR is reduced with increasing bias voltage; this effect appears to be related to the creation of magnons at the ferromagnet/insulator interface.

Another type of tunneling magnetoresistance is associated to the anisotropy in the electron density of states, arising from spin–orbit interactions. This anisotropic tunneling magnetoresistance (TAMR) has been observed in structures containing one ferromagnetic semiconductor, a barrier and a nonmagnetic metal, or using instead of a semiconductor, a Co/Pt multilayer (e.g., [20]).

An important effect that arises from the interaction of spin-polarized electrons and the magnetization of nanoobjects is the spin-transfer torque, that allows switching the magnetization through the action of the polarized electric current. This was discussed in Chap. 3, on p. 96.

Further Reading

J. Bass, W.P. Pratt Jr., J. Phys.: Condens. Matter **19**, 183201–183241 (2007)

K. Hathaway, E. Dan Dahlberg, Am. J. Phys. **75**, 871–880 (2007)

J. Slonczewski, in *Theory of Spin-Polarized Current and Spin-Transfer Torque in Magnetic Multilayers*, ed. by H. Kronmüller, S. Parkin. Handbook of Magnetism and Advanced Magnetic Materials, vol 5 (Wiley, Chichester, 2007), pp. 2648–2667

E.Y. Tsymbal, N. Mryasov, P.R. LeClair, J. Phys.: Condens. Matter **15**, R109–R142 (2003)

S.A. Wolf, A.Y. Chtchekalnova, D.M. Treger, IBM J. Res. Dev. **50**, 101–110 (2006)

I. Zutic, J. Fabian, S.D. Sarma, Rev. Mod. Phys. **76**, 323–410 (2004)

References

1. S. Araki, J. Appl. Phys. **73**, 3910–3916 (1993)
2. M. Baibich, J.M. Broto, A. Fert, V.D. Nguyen, F. Petroff, P. Etienne, G. Creuzet, A. Friederich, J. Chazelas, Phys. Rev. Lett. **61**, 2472–2475 (1988)
3. J. Bass, W.P. Pratt Jr., J. Magn. Magn. Mater. **200**, 274–289 (1999)
4. J. Bass, W.P. Pratt Jr., J. Phys.: Condens. Matter **19**, 183201–183241 (2007)
5. M.E. Brubaker, J.E. Mattson, C.H. Sowers, S.D. Bader, Appl. Phys. Lett. **58**, 2306–2308 (1991)
6. I.A. Campbell, A. Fert, in *Transport Properties of Ferromagnets*, ed. by E.P. Wohlfarth. Handbook of Magnetic Materials, vol 3 (North-Holland, Amsterdam, 1982), pp. 747–804

7. C.L. Dennis, R.P. Borges, L.D. Buda, U. Ebels, J.F. Gregg, M. Hehn, E. Jouguelet, K. Ounadjela, I. Petej, I.L. Prejbeanu, M.J. Thornton, J. Phys. Condens. Matter **14**, R1175–R1262 (2002)
8. M.R.J. Gibbs, E.W. Hill, P. Wright, in *Magnetic Microelectromechanical Systems:MagMEMS*, ed. by K.H.J. Buschow. Handbook of Magnetic Materials (Elsevier, Amsterdam, 2008), pp. 457–526
9. M.A.M. Gijs, in *Experiments on the Perpendicular Giant Magnetoresistance in Magnetic Multilayers*, ed. by U. Hartmann. Magnetic Multilayers and Giant Magnetoresistance (Springer, Berlin, 2000), pp. 129–177
10. P. Grünberg, D.E. Burgler, H. Dassow, A.D. Rata, C.M. Schneider, Acta Mater. **55**, 1171–1182 (2007)
11. Q.Y. Jin, M. Lu, Q.S. Bie, Y.B. Xu, H.R. Zhai, Y.H. Shen, J. Magn. Magn. Mater. **140–144**, 565–566 (1995)
12. M. Johnson, R.H. Silsbee, Phys. Rev. B **37**, 5312–5325 (1988)
13. M. Jullière, Phys. Lett. A **54**, 225–226 (1975)
14. J.S. Moodera, L.R. Kinder, T.M. Wong, R. Meservey, Phys. Rev. Lett. **74**, 3273–3276 (1995)
15. J.S. Moodera, T.S. Santos, T. Nagahama, J. Phys.: Condens. Matter **19**(16), 165202 (2007)
16. N.F. Mott, Proc. Roy. Soc. Lond. Ser. A **153**, 699–717 (1936)
17. N.F. Mott, Proc. Roy. Soc. Lond. Ser. A **156**, 368–382 (1936)
18. N.F. Mott, Adv. Phys. **13**, 325–422 (1964)
19. R. Nakatani, T. Dei, Y. Sugita, J. Appl. Phys. **73**, 6375–6377 (1993)
20. B.G. Park, J. Wunderlich, D.A. Williams, S.J. Joo, K.Y. Jung, K.H. Shin, K. Olejnik, A.B. Shick, T. Jungwirth, Phys. Rev. Lett. **100**, 087204–087207 (2008)
21. S.S.P. Parkin, R. Bhadra, K.P. Roche, Phys. Rev. Lett. **66**, 2152–2155 (1991)
22. S.S.P. Parkin, R.F.C. Farrow, R.F. Marks, A. Cebollada, G.R. Harp, R.J. Savoy, Phys. Rev. Lett. **72**, 3718–3721 (1994)
23. S.S.P. Parkin, N. More, K.P. Roche, Phys. Rev. Lett. **64**, 2304–2307 (1990)
24. B. Rodmacq, G. Palumbo, P. Gerard, J. Magn. Magn. Mater. **118**, L11–L16 (1993)
25. T. Matsudai, H. Sato, W. Abdul-Razzaq, C. Fierz, P.A. Schroeder, J. Phys. Condens. Matter **6**, 6151–6162 (1994)
26. R. Schad, C.D. Potter, P. Belien, G. Verbanck, J. Dekoster, G. Langouche, V.V. Moshchalkov, Y. Bruynseraede, J. Magn. Magn. Mater. **148**, 331–332 (1995)
27. K. Shintaku, Y. Daitoh, T. Shinjo, Phys. Rev. B **47**, 14584–14587 (1993)
28. J.C. Slonczewski, Phys. Rev. B **39**, 6995–7002 (1989)
29. M.B. Stearns, J. Magn. Magn. Mater. **5**, 167–171 (1977)
30. E.Y. Tsymbal, N. Mryasov, P.R. LeClair, J. Phys. Condens. Matter **15**, R109–R142 (2003)
31. T. Valet, A. Fert, Phys. Rev. B **48**, 7099–7113 (1993)
32. E.L. Wolf, *Nanophysics and Nanotechnology* (Wiley, Weinheim, 2006)
33. S.A. Wolf, D.D. Awschalom, R.A. Buhrman, J.M. Daughton, S. von Molnar, M.L. Roukes, A.Y. Chtchelkanova, D.M. Treger, Science **294**, 1488–1495 (2001)
34. H. Yanagihara, K. Pettit, M.B. Salamon, S.S.P. Parkin, E. Kita, J. Appl. Phys. **81**, 5197–5199 (1997)
35. I. Zutic, J. Fabian, S.D. Sarma, Rev. Mod. Phys. **76**, 323–410 (2004)

6

Magnetism of Nanodisks, Nanorings, and Nanowires

Summary. This chapter contains a brief survey of the remarkable magnetic properties of low-dimensional magnetic objects such as nanodisks, nanorings, and nanowires. These nanoscopic systems have been intensely studied in the last years, not only because of these properties, but also for their enormous potential for high-density information storage. Nanodisks and nanorings are promising as elements of bit-patterned magnetic recording systems, and nanowires, among other applications, can store and process information through the motion of magnetic domain walls.

6.1 Introduction

Besides the nanoscopic and mesoscopic systems that may be classed as almost bidimensional, such as thin films, or quasi-zero-dimensional, as nanoparticles other structures built on the same scale had their magnetic properties investigated. We deal here with some of these low-dimensional systems: nanodisks or nanodots, nanorings, and nanowires. Some of these systems can be prepared with the same techniques used to make thin films: the samples of nanodisks and nanorings are usually thin, shaped from a thin film of magnetic material deposited on a nonmagnetic substrate. Nanowires can be made in the same way, but most of the nanowires are prepared from templates with narrow channels or pores. One common characteristic of these samples is that in many cases they are prepared as regular arrays, a form that favors the handling of the samples and measurement of the magnetic properties, such as magnetization, etc.

In some aspects the magnetism of these objects is comparable to the magnetism of nanoparticles, and therefore, much of what is applicable to nanoparticles is also valid for nanodisks, nanorings, and nanowires. On the other hand, the fact that the nanoscopic disks and rings of interest are approximately bidimensional, justifies why some results valid for extended thin films are also relevant for their study.

6.2 Nanodisks

Arrays of near circular magnetic islands of nanoscopic or mesoscopic dimension deposited on nonmagnetic substrates present interesting physical properties and have been extensively studied. These systems are also relevant as models for the development of patterned (or bit-patterned) magnetic recording media, magnetic media where each individual bit has the pre-determined position as an element of the array. Media with this structure are candidates for higher density magnetic recording (see Chap. 7).

The magnetic elements in such arrays can be nanodots or nanopillars with circular, elliptical, or other cross-sections (e.g., [8]). These magnetic arrays have also been made of nanorings, or sub-micron rings, that will be considered in Sect. 6.3.

We remarked in Sect. 3.1 that in the lowest energy state, spherical particles of soft magnetic material (e.g., permalloy), have for some range of diameters a vortex spin structure; this is shown in Fig. 3.5, p. 62 and Fig. 3.8, p. 65. The same has been found experimentally to be true of magnetic circular nanodots, or nanodisks (Fig. 6.1). For example, for permalloy disks 15 nm thick, these vortices are observed above a critical diameter of about 100 nm [8]. Micromagnetic simulations lead to a critical diameter of 10 l_{ex} for permalloy disks of thickness 5 l_{ex}, where l_{ex} is the exchange length [31]. A theoretical derivation arrives, for thin disks, at the following expression for the minimum disk diameter for the observation of a vortex structure as the lowest energy state [23]:

$$D_{cr}^{vo} = 7.4 \, l_{ex}. \tag{6.1}$$

For permalloy, for example, $l_{ex} \sim 5$ nm; thus, for a disk made of permalloy, this critical diameter D_{cr}^{vo} is about 40 nm.

In thin magnetic disks, or circular dots of thickness of the order of the exchange length l_{ex} that exhibit a vortex spin structure, the magnetization is mostly confined to the plane of the disk. Near the center of the disk, where the vortex center is located,
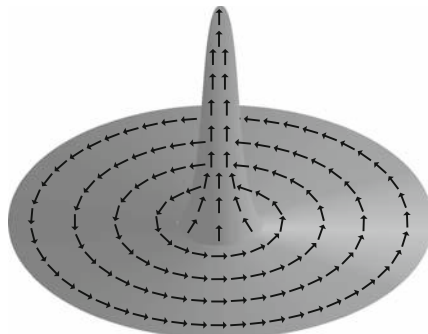
Fig. 6.1. Vortex arrangement of magnetic moments in a circular nanodot of soft magnetic material; the height at each point represents the z component of the magnetization. Note how the tips of the moments point out of the plane near the center – this is the vortex core, a region that has a net magnetization perpendicular to the plane of the disk

however, the equilibrium arrangement for the magnetic moments is such that the tips of the magnetic moment vectors move out of the plane, and consequently there is a perpendicular component of the magnetization, that reaches its maximum amplitude at the center of the disk. This is illustrated in Fig. 6.1.

The existence of this z component is due to the fact that the cost, in terms of exchange energy, of keeping the magnetic moments turning in a small circle in the plane near the center of the disk is locally very high, and the only form of lowering this energy is to tend towards parallelism of the atomic moments, pointing them out of the disk plane in the vortex core.

This perpendicular magnetization of the vortex core is verified experimentally through images of nanodisk arrays obtained using magnetic force microscopy (MFM), that shows dark or light dots at the center of the disks, arising from the uncompensated magnetic poles, indicating up or down vortex core magnetization. First principles calculations performed for Fe nanodisks also show that the electronic structure of the atoms at the center of the vortex core is modified, and an orbital moment perpendicular to the plane appears [28].

Vortices observed in soft magnetic nanodisks correspond to the limiting arrangement of the domain structures found in square nanodots when four Landau states, i.e., four triangular domains separated by 90° domain walls, are formed. A perfect vortex is the spin structure obtained as the number of such domains increases indefinitely, the angles between the magnetization of neighbor domains tend to zero.

The vortex core has in general a radius R_c of the order of the exchange length; the computed radius is close to l_{ex} in the limit of a negligibly thin disk (see [17]). Its shape, or vortex profile, i.e., the form of the radial distribution of perpendicular magnetization $M_z(r)$, is axially symmetric, with a dependence with r given, in the case of positive core magnetization, by [16]:

$$M_z(r) = M_0(ce^{-r^2/l_{ex}} + (1-c)e^{-r^2/4l_{ex}^2}) .\qquad(6.2)$$

Here c depends on the thickness of the nanodot, with the value $c = 0.52$ in the limit of very thin dot. In this limit, the core radius is given by $R_c = \pi l_{ex}/(\sqrt{2+6c})$ [16].

Micromagnetic simulations derive a radial dependence of the z component of the magnetization M_z very close to the above function; $M_z(r)$ is positive in the core, with a small negative component just outside the core. Other forms for the vortex magnetization profile were given by other authors [1, 16].

The z component of the magnetization of the vortex core can point up or down; from this characteristic, one defines the vortex polarity p, a parameter with, respectively, values $+1$ or -1:

Polarity $p = +1$ $\qquad$ $M_z > 0$ (up)
Polarity $p = -1$ $\qquad$ $M_z < 0$ (down)

The sense of rotation of the vortices can be either clockwise (CW) or counterclockwise (CCW). This defines the circulation c, or vorticity of the vortex, quantitatively measured by the integral of the angle along the magnetization, divided by 2π. Thus, $c = -1$ for a clockwise rotating vortex, and $c = +1$ for a counterclockwise vortex.

When one takes into account the fact that nanodisks in the vortex state also have a core with perpendicular magnetic moment which can point up or down (polarities $+1$ and -1), the nanodisks behave as chiral objects. We use the word in the sense as used more than a century ago by Lord Kelvin, i.e., "if its image in a plane mirror, ideally realized, cannot be brought to coincide with itself" [2], like the human hand, *kheir*, in Greek.[1]

There are, consequently, four possible combinations of vortex sense of rotation or circulation c (CW and CCW), and the vortex core polarity p (up or down):

$p = +1$ (up)	$c = -1$ (CW)	$cp = -1$
$p = +1$ (up)	$c = +1$ (CCW)	$cp = +1$
$p = -1$ (down)	$c = -1$ (CW)	$cp = +1$
$p = -1$ (down)	$c = +1$ (CCW)	$cp = -1$

In the four combinations given above, the product cp may take two values, ± 1, that define the handedness, or chirality of the vortex.

The experimental determination of polarity can be made with the MFM technique; the tip of the microscope samples the stray field and from it determines the sign of M_z at the core. The chirality can be determined with the Photoemission Electron Microscopy technique (PEEM). In this technique, X-rays illuminate the sample, and the emitted photoelectrons are focused to obtain an image of the object; it allows the determination of the distribution of magnetization directions. The chirality can also be determined from the motion of the vortex core induced by an in-plane pulse of magnetic field, as will be described below.
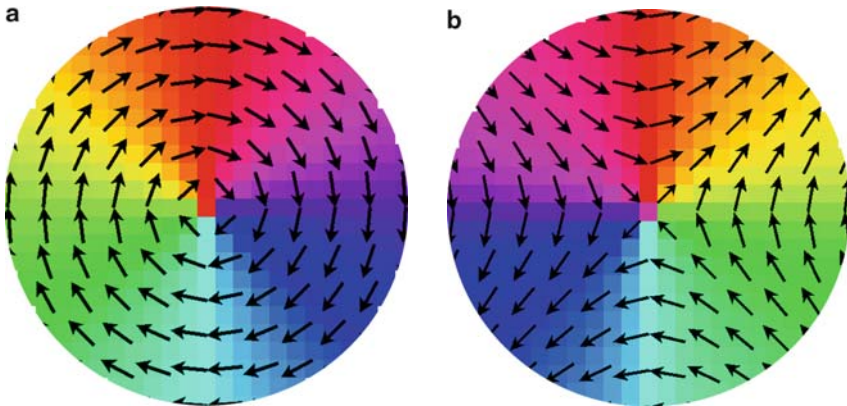
Fig. 6.2. Vortex (**a**) and antivortex (**b**) spin structures in magnetic nanodisks; the *color code* represents the angles of the local magnetic moments

---

[1] There is no agreement between different authors on this nomenclature: some use chirality for the circulation defined here, and use vorticity as a synonym of winding number.

A nanodisk can also magnetize itself in the form of an antivortex (Fig. 6.2b). This spin structure is equivalent to the superposition of two perpendicular 180° domain walls. The antivortex does not correspond to an energy minimum for a nanodisk. An antivortex also has perpendicular magnetization components at its center, according to MFM measurements in permalloy astroid-shaped thin films and micromagnetic simulations [34].

A vortex has a winding number $n = +1$, that does not depend on its chirality C; an antivortex has winding number $n = -1$. The winding number of a vector field $\mathbf{V}(P)$ is calculated by counting, along a counterclockwise rotation, the number of revolutions of $\mathbf{V}(P)$; if the revolutions are clockwise this number is negative, if counterclockwise, positive (e.g., [26]).

A static magnetic field H applied in the plane of a nanodisk will displace the core from its center, along a radial trajectory perpendicular to H. As the intensity of the magnetic field is increased, the core will eventually be forced out of the disk, or, in other words, the vortex will be destroyed. Increasing the intensity of the field, a single-domain configuration will be reached.

The observed behavior of the vortex core is different if a short in-plane magnetic field pulse is applied. Immediately after the application of a field pulse, the core begins to move in the direction of the field, in the case of right-handed chirality ($cp = +1$), or in the opposite sense, for left-hand chirality ($cp = -1$), as measured by time-resolved X-ray imaging [9]; this effect can be understood from the torque produced on the magnetic moments in the vortex. After cessation of the magnetic field pulse, the vortex core precesses around its equilibrium position, in a near spiral trajectory. The core in this gyrotropic motion is under the influence of the magnetostatic field that appears with its displacement. The rotating direction of the vortex core is also defined by the chirality of the vortex.

Micromagnetic simulations show that the anti-vortices also perform spiral-like trajectories after being submitted to in-plane magnetic field pulses [46].

A static magnetic field applied perpendicularly to the plane of the nanodisk can invert the polarity of a vortex core. This field must have an intensity above a certain critical value H_{cr}^{vo}, and direction opposed to the vortex core magnetization. This magnetization reversal can also be produced through the application of an in-plane rotating magnetic field of much smaller intensity than this critical field H_{cr}^{vo}. The process of inversion of the polarity of the vortex core goes through an intermediate phase, in which an antivortex is created and, in its turn, annihilates the initial vortex [45].

Another form of reverting the vortex polarity is achieved through the application of a spin-polarized ac electric current [47], through a mechanism called spin-switching [4,36], discussed in Sect. 3.5.3, p. 96. The ac current induces a precession of the vortex core, or gyrotropic motion, and a magnetic field results, proportional to the velocity of the motion of the core. This current has to have a frequency close to the resonance frequency of the magnetic core, usually of a few hundred megahertz.

When the vortex core velocity reaches a critical value, of a few hundred meters per second in the experiment with 500 nm permalloy disks, this out-of-plane magnetic field has an intensity of about 0.2 T, which is sufficient to invert the core
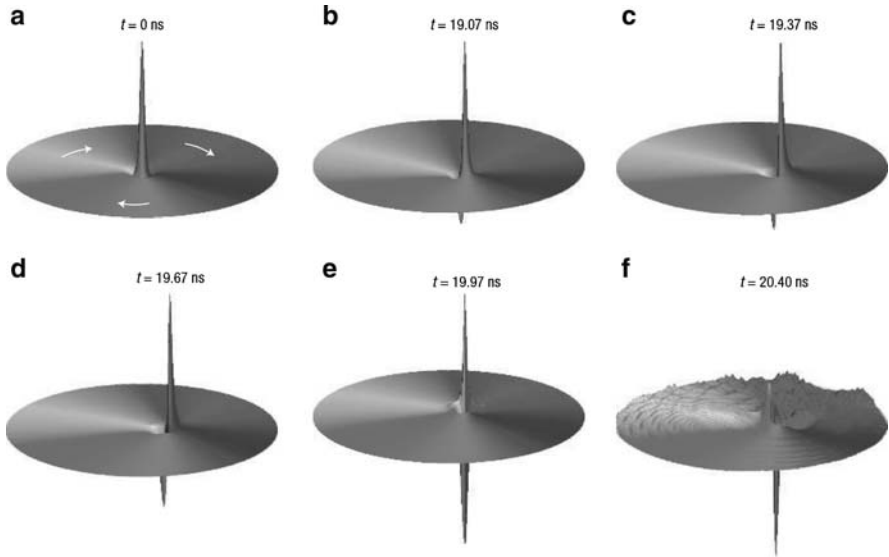
Fig. 6.3. Sequence of computed magnetization of a soft magnetic disk at different times show-
ing the current-induced inversion of polarity of a vortex core in a permalloy 500 nm disk. The
vertical axis represents the z magnetization: in (**a**) the vortex core is at rest, in the following
images (**b–f**) the core moves under the influence of an ac current, and eventually changes polar-
ity completely [47]. Reprinted by permission from Macmillan Publishers Ltd. [47], copyright
(2007)

magnetization [47]. The several stages of this inversion of polarity are shown in
Fig. 6.3.

This critical velocity v_c is similar to the critical velocity of one-dimensional
domain wall motion (Walker velocity, Sect. 2.4.2, p. 50) that corresponds to the
Walker breakdown [32]. This velocity is approximately given (expressing in SI
units) by

$$v_c \approx (\frac{\gamma_G}{4\pi}) M_s R_c \approx (\frac{\gamma_G}{\sqrt{4\pi}}) M_s l_{ex} \tag{6.3}$$

where R_c is the vortex core radius and l_{ex} is the exchange length, γ_G is the gyromag-
netic factor; it is estimated as $v_c = 350\,\mathrm{m\,s^{-1}}$ for a permalloy nanodot [14].

Let us a consider a soft magnetic disk that has a diameter sufficiently large that
its zero-field spin configuration is a vortex state. Its hysteresis curve, drawn under
a magnetic field applied parallel to the plane of the disk, has zero magnetization
for $H = 0$, increases the magnetization as the vortex core is displaced and finally
expelled from the disk, reaching saturation corresponding to a single-domain spin
configuration. As the magnetic field intensity H is reduced from saturation, a sharp
drop in magnetization is observed at the point in the hysteresis curve that corresponds
to the reappearance of the vortex, and in continuation, depending on the dimensions
of the disk, the curve may go through the point ($H = 0, M = 0$), therefore exhibiting
no coercivity, as shown in Fig. 6.4.

a

b
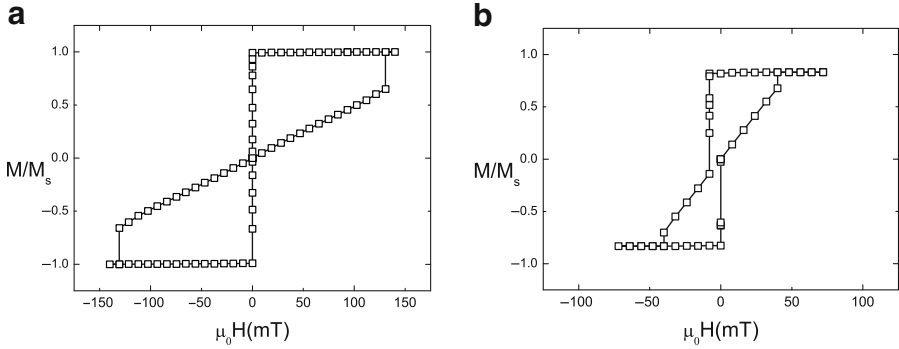
Fig. 6.4. Hysteresis curves for permalloy nanodisks, under an in-plane applied magnetic field, obtained by micromagnetic simulation. *Left*: nanodisk of 120 nm diameter, with single-domain spin configuration, and *right*, nanodisk of 500 nm diameter, with vortex ground state

The symmetry properties of vortices and antivortices can be expressed through (1) the polarity p, that can take values of $+1$ or -1, (2) winding number, $n = +1$ for vortices and $n = -1$ for antivortices, and (3) the skyrmion number, q given by

$$q = \frac{np}{2} \ . \tag{6.4}$$

When a pair vortex–antivortex meets, they are annihilated. Since $n = +1$ for a vortex and $n = -1$ for an antivortex, it follows that $q_v = +p_v$ for a vortex and $q_{av} = -p_{av}$ for an antivortex. Therefore, a pair vortex–antivortex with parallel polarities has zero total skyrmion number q. In this case the annihilation leads to a gradual decrease of the total energy of the spin arrangement. On the other hand, if the polarities are opposite, the total skyrmion number is $|q| = 1$, and the annihilation of the pair produces a burst of spin waves [41].

Elliptic nanodots have a shape anisotropy contribution to the anisotropy, and consequently, for smaller dimensions, tend to form single domains with magnetization parallel to their longer axis. This lower symmetry leads to a magnetic behavior that is more complex than that observed with the nanodisks. Some of the possible spin configurations observed in micromagnetic simulations for soft elliptic nanodots are shown in Figs. 6.5 and 6.6: these figures show a single-domain in-plane magnetization, a single-domain with magnetization perpendicular to the dot plane, and configurations with one and two vortices.

Larger elliptical nanodots tend to form more than one vortex, with two senses of rotation (CW and CCW); the polarities of these vortices may be the same, or opposite. For example, with two vortices, the product of the polarities $p_1 p_2$ takes value of ± 1.

A static in-plane magnetic field leads to a new equilibrium position of the vortex that is different from the position for $H = 0$. A field parallel to the long axis of the ellipse produces a displacement of the vortices to the opposite sides of this axis; a perpendicular field displaces them along the same axis. This behavior does
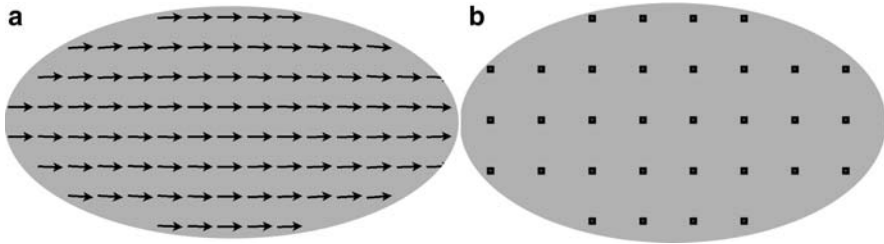
Fig. 6.5. Single-domain spin configurations of soft elliptic nanodots obtained by micromagnetic simulation: (**a**) single-domain with in-plane magnetization, (**b**) single-domain with magnetization perpendicular to the plane of the nanodot
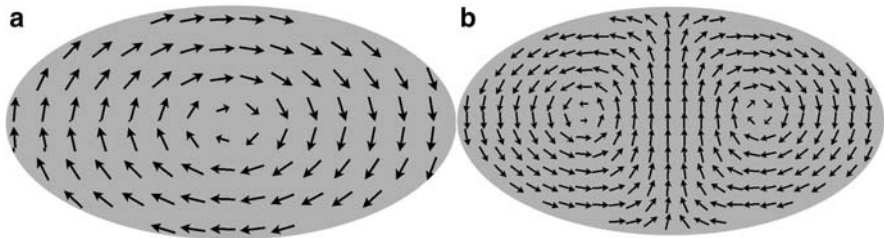
Fig. 6.6. Two vortex spin configurations of soft elliptic nanodots obtained by micromagnetic simulation: (**a**) single vortex and (**b**) double vortex

not depend on their polarities; however, the dynamic behavior observed during the excitation with oscillating magnetic fields, on the other hand, is dependent on the vortex polarities [5].

6.3 Nanorings

Macroscopic magnetic rings known as magnetic core memories were developed in the 1950s, and were used in computers for some 20 years. The rings were typically of 1 mm diameter, the size gradually decreasing with the development of this technology. Each ring was used to store a single bit, and the switching between the two magnetic states was induced by the field produced by wires that run through a matrix of cores.

In recent years, magnetic rings of micrometric or sub-micrometric size, with thicknesses much smaller than their diameters have attracted much attention of workers in magnetism. They are other types of bidimensional structure that have interesting magnetic properties; they are usually deposited as an array on a nonmagnetic substrate. For a review on magnetic nanorings, see [43].

Their study also has relevance to the development of technologies of high-density magnetic recording (see Chap. 7, on magnetic recording). Nanorings present some advantages in comparison with the nanodisks for application to magnetic recording, allowing higher density storage, arising from their flux closure structure and more

stability in the switching conditions [50]. Rings may also be used as microsensors, to detect magnetic nanoparticles [27].

Both disks and rings, in the vortex state, if used to store magnetic recording bits, have the advantage that in this state the interactions between neighbor elements are minimized, due to the smaller stray magnetic fields.

Nanorings have many properties in common with the disks due to their similar morphology; for example, for thicknesses comparable to the exchange length, the magnetic moments are contained in the plane, they also present magnetic vortices in their minimum energy configuration for a range of diameters. A significant difference, though, in this geometry the exchange energy term associated to the vortex core structure is absent.

One can schematically classify the magnetic moment configurations observed in narrow nanorings, i.e., nanorings that have the inner diameter much smaller than their outer dimensions into three types. These are shown in Fig. 6.7: in the first case the directions of local magnetization may turn around the central opening, in which case the magnetization is tangential and in the same sense around the perimeter of the nanoring, forming a vortex. A second common magnetic configuration is an arrangement of spins in which the ring is divided into two magnetic domains, with magnetizations oriented tangentially in two different directions, clockwise and counterclockwise, a structure that is usually referred to as an onion state; these two configurations are inferred from the shape of the hysteresis curve for a Co ring in Fig. 6.8. A third common structure is an asymmetric onion state, containing two regions of opposite direction of rotation and different lengths, and is referred to as a twisted state. This is a metastable magnetic structure, with two close $180°$ domain walls, or $360°$ wall, and was observed in nanorings with smaller radii [6].

Nanorings with vortex or circular magnetization ground state can be prepared with smaller diameters than nanodisks with the same spin structure, typically with a minimum diameter of 10 nm for a NiFeCo ring [50]. This nanoring critical diameter for the vortex configuration D_{cr}^{ring} has a value given, in general, by the relation [23]:

$$D_{cr}^{ring} = 2\sqrt{3}\, l_{ex}, \tag{6.5}$$

where l_{ex} is the exchange length.

For a permalloy ring, this corresponds to a critical diameter $\sim$17 nm, much smaller than the equivalent critical diameter for a permalloy nanodisk, of the order of 100 nm.
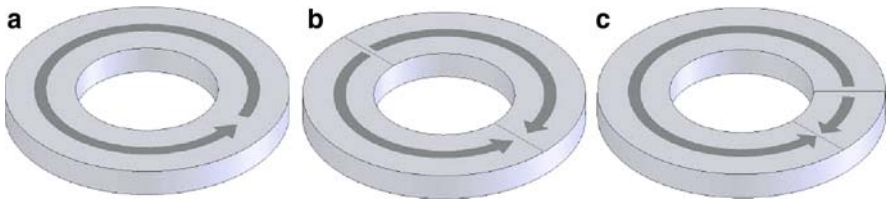
Fig. 6.7. Narrow magnetic ring exhibiting (**a**) vortex state, (**b**) onion state, and (**c**) twisted state
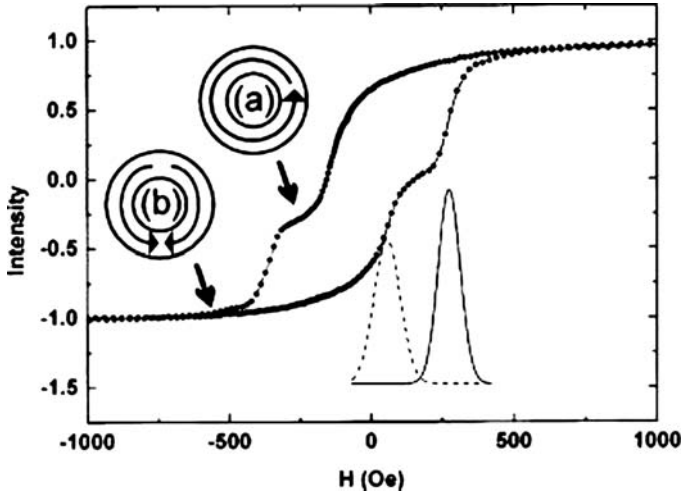
Fig. 6.8. Hysteresis curve of narrow Co nanoring exhibiting (**a**) vortex and (**b**) "onion" states. (Reprinted with permission from [49]. Copyright (2003), American Institute of Physics)

The walls separating the domains in the onion state or in the vortex state may be much more complex than the transverse domain walls shown in Fig. 6.7. Vortex wall is a type of wall that has radial magnetization which may be formed, giving rise to substantial magnetic charges at the edge of the rings.

In the broader rings, that is, in those that have an internal diameter much smaller than the external diameter, minor or inner vortices are observed. The coexistence of minor vortices with vortices that occupy the whole perimeter of these rings may occur. In the narrower rings this usually does not happen.

The magnetization state of a nanoring is modified with the application of an external magnetic field. For example, a magnetic field applied to a thin magnetic nanoring in the vortex state will magnetize the ring, with the appearance of two domains, in the form of the onion state. For some rings, as the applied field is removed, the domain walls are depinned, and the ring reverts to the vortex state. The hysteresis curve measured for magnetic rings show, in thin rings, two possible routes from the saturated configuration to zero magnetization at the coercive field [8]. In both cases the saturated nanoring is in the onion state. A magnetic field applied opposite to the onion magnetization, leads in the first case to (1) a rotation of the onion structure, with a nonzero coercivity. The other possible evolution under applied field is (2) the annihilation of one of the branches of the onion, turning the structure into a vortex state; in this case the coercivity is zero. If the negative applied magnetic field continues to increase its intensity, the onion state is re-established at a higher (negative) value of H. These two possible evolutions of the magnetization under applied field may occur simultaneously in an array of nanorings, due to differences among individual elements, a more complex resultant hysteresis curve rises.

A magnetic field applied to a nanoring opposite to its magnetization in the onion state may displace the domain walls in such a way that they almost coalesce on the opposite side of the ring, which remains in this configuration at remanence, in a spin structure called the twisted state [6], shown in Fig. 6.7. The hysteresis curve obtained through the application of a spin-polarized current to this type of ring is essentially a bi-state system, and therefore, promising for applications in magnetic storage [8].

Stacks of nanorings in the twisted state may constitute cells, in applications as magnetic memory elements [50]. These elements may be switched through the passage of spin-polarized current (for a discussion on magnetic recording, see Chap. 7). A stack of nanorings can have its magnetization state changed from onion to vortex through the application of either external magnetic fields or electric currents in the CPP geometry [48].

In the broader rings, when there may be a superposition of the different magnetic states, the hysteresis curves are more complex. Figure 6.9 shows the hysteresis curves of cobalt rings, for different temperatures. The more complex structure found in the curve measured at 300 K is explained (see schemes *a*, *b*, *c*, and *d*, shown at the top left of the figure) by the fact that the rings evolve from an onion magnetization to
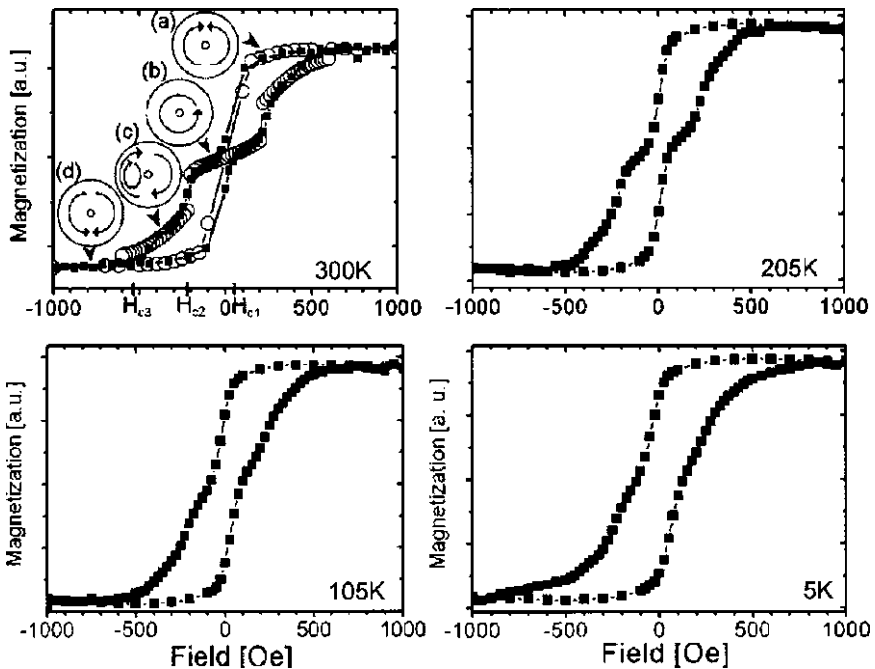
Fig. 6.9. Magnetization curves of sub-micron Co rings, showing, in the curve at 300 K, three states (**a**) "onion" state, (**b**) vortex state, (**c**) an intermediate state, combination of vortex and "onion", and (**d**) "onion" state in the opposite direction. (Reprinted with permission from [22]. Copyright (2004), American Institute of Physics)

another, through intermediate configurations that include a single vortex, and onion associated to a minor or internal vortex [22].

Magnetic rings of Co/IrMn of elliptical shape can be obtained with controlled circulation (or direction of rotation) through the use of the exchange bias phenomenon [18]. The ability of changing the circulation of the nanorings is necessary for the use of this parameter in data storage.

Constrictions or notches in the nanorings may pin the magnetic domain walls. Constrictions appear to a transverse domain wall as an attractive potential, and as a repulsive potential to vortex walls (e.g., [20]). The narrower the constriction, the higher the magnetic field (the depinning field H_{dp}) that is necessary to move the domain wall. A depinning field of about 300 Oe was obtained for a constriction of some tens of nanometers in 200 nm wide permalloy ring [21].

The interactions between the elements of an array of magnetic rings were studied in the case of permalloy and Co rings [24]. The results show that this interaction changes the nucleation of domain walls in the neighbor nanorings. For small separation, the transverse domain walls are favored, whereas, for large separation vortex walls predominate.

6.4 Nanowires

Magnetic nanoscopic quasi-unidimensional systems have been the object of many studies. Those that have a high aspect ratio (ratio of length to diameter) are known as nanowires, in other cases, nanopillars. They may be prepared either by deposition of magnetic materials on stepped crystal surfaces, or by lithography of a magnetic film, or by electrochemical deposition. In the electrochemical deposition method the magnetic material is deposited inside the pores of a template or matrix, usually of alumina (Fig. 6.10). The alumina template is formed by anodization of an aluminium surface, and the pore length and diameter can be controlled in the electrodeposition process. Typical dimensions for the pores are 10–200 nm in diameter and lengths of some microns (see a review on nanowires in [44]).

Due to shape anisotropy, the form of the nanowires favors the alignment of the magnetization along their lengths. However, depending on the intensity of the crystalline anisotropy of the constitutive material, the resulting anisotropy may point towards another direction, for example, perpendicularly to the axis. It was shown that in the case of cobalt nanowires the preparation conditions through the electrochemical technique could favor either final anisotropy direction [10]. Apparently, the microcrystals that coalesce to form the nanowire can keep the hexagonal symmetry axes perpendicular to the longitudinal direction, in such a way that the crystalline anisotropy ends up favoring perpendicular alignment, prevailing over the shape anisotropy. Cobalt nanowires, or stripes, of rectangular cross section and width of several nanometers, prepared through the deposition of the metal via molecular beam onto MgO also present in general anisotropy perpendicular to the axis [11].

In Fig. 6.11, one sees two images of a nanowire with the direction of the crystalline anisotropy along the axis, obtained after exposure to a saturation magnetic
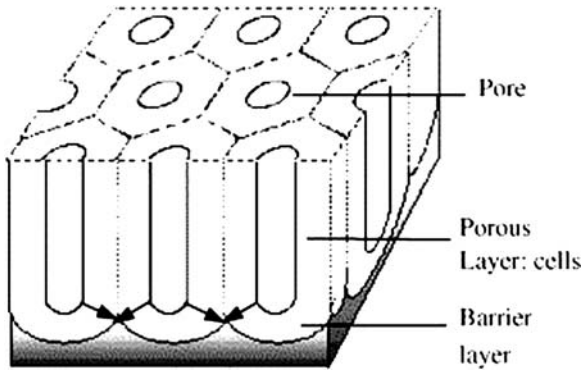
Fig. 6.10. Alumina (Al$_2$O$_3$) porous matrix employed for the electrodeposition of nanowires [29]. (With permission from Elsevier Science and Technology)
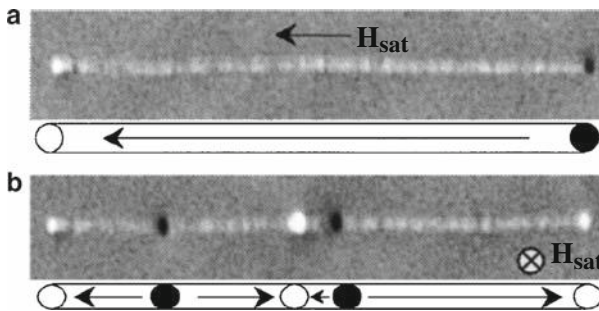
Fig. 6.11. MFM images of a 35 nm diameter Co wire for $H = 0$, after saturation in (**a**) magnetic field parallel to the wire and (**b**) magnetic field perpendicular to the wire [12]. The cartoons below the images show the structure of magnetic domains, Reprinted figure from [12]. (Copyright (2000) by the American Physical Society)

field pointing (1) along the axis and (2) perpendicular to the axis. In the images, obtained with MFM the regions in black and white correspond to "magnetic charges" of the poles of the domains. In the first case, after removal of the external field, the nanowire takes up a single-domain structure. In the second case, several domains are formed, being noticeable neighbor domains with opposite magnetizations. The magnetic domain walls are situated in planes perpendicular to the axes of the wires.

Analogously to what is observed in magnetic particles, nanowires exhibit a magnetic behavior that is dependent on their dimensions. This is exemplified by the dependence of the magnetic ordering temperature (T_C) of nickel nanowires with their diameter (Fig. 6.12 [37]). The dependence of the Curie temperature with diameter of the nanowires obeys a relation of the form of (1.29) [37]:

$$\frac{(T_C(\infty) - T_C(d))}{T_C(\infty)} = \pm \left(\frac{\xi}{d}\right)^{\lambda}. \tag{6.6}$$
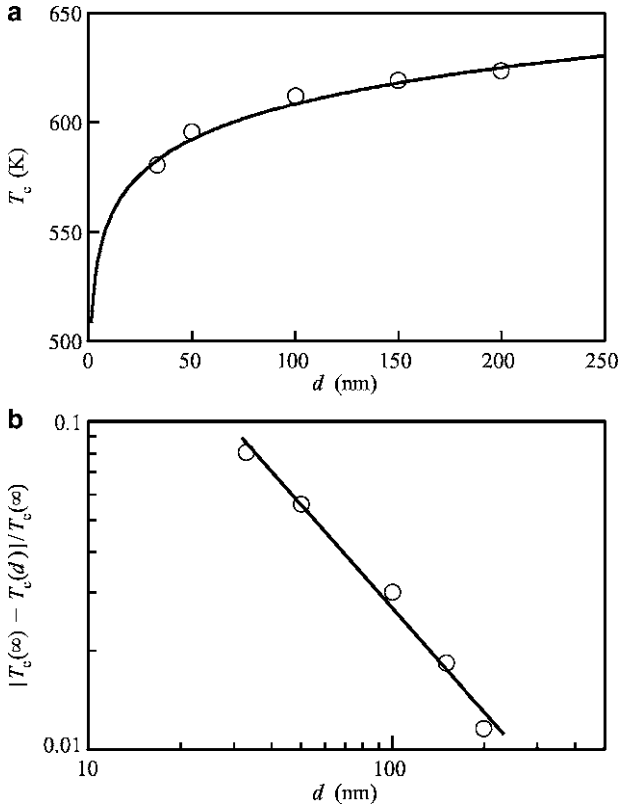
Fig. 6.12. Dependence of the Curie temperature (T_C) of nickel nanowires with the diameter. $T_C(d)$ is the T_C of a wire of length d and $T_C(\infty)$ is the T_C of a macroscopic sample of Ni. (**a**) $T_C(d)$ vs. d and (**b**) $(T_C(d) - T_C(\infty))/T_C(\infty)$ vs. d [37]. (Reprinted from [37] with permission from IBM Technical Journals)

where $T_C(\infty)$ is the Curie temperature of the nanowire material in bulk form, and $T_C(d)$ is the same quantity, for the nanowire of diameter d. In this equation, ξ is the correlation length and λ is the shift exponent. The data for the Ni nanowires of Fig. 6.12 are fitted with $\xi = 2.2$ nm and $\lambda = 0.94$.

Nanowires that have a volume below a certain critical value present superparamagnetic behavior (see Superparamagnetism, Sect. 3.3). In nanoobjects, depending on the ratio of the height of the energy barrier for reversal of the magnetization E_B, to the thermal energy $k_B T$, this behavior is observed. For values of $E_B/k_B T > 40$, the magnetization of the wires is stable, with relaxation times above 10 years.

The barrier height is related to the anisotropy and the applied field H and was given by (3.47) (p. 82), valid for homogeneous magnetization reversal. For reversal by curling, this expression is written in terms of the effective anisotropy K_{eff}, and the switching field H_{sw}; the exponent is in this case $3/2$ [19]:

$$E_B = K_{\text{eff}} V \left(1 - \frac{H}{H_{\text{sw}}} \right)^{3/2}. \tag{6.7}$$

For nanowires of a given length, there is a critical diameter for superparamagnetic behavior. In Fig. 6.13 are shown the values of the ratio E_B/k_BT, for wires of Ni as a function of the radius, for some nanowire lengths, using (6.7), without applied field ($H = 0$) [37]. The curves of the figure were computed assuming that the only contribution to the anisotropy of the wires is the shape anisotropy.

The curves of Fig. 6.13 show, for example, that for a nanowire of Ni 100 nm long, the ratio E_B/k_BT varies from ~10, for a radius of 1 nm, to 500, for $r \approx 7$ nm. The nanowires of smaller radius are superparamagnetic and those with r above a few nanometers are ferromagnetic.

The hysteresis loops obtained with magnetic nanowires indicate that the easy magnetization axis may or may not coincide with the longitudinal axis of the wires. Fe nanowires, typically with diameters from 10 to 100 nm and lengths from 0.1 to 1 μm, have the easy axis of magnetization along the wire length [33]. The observed coercivity is of about 2,300 Oe for measurements along the nanowire axis. The Ni nanowires also present easy magnetization along the longitudinal axis, with coercivity varying from 500 to 1,000 Oe [33]. Some magnetic properties of 3d metal nanowires are shown in Table 6.1.
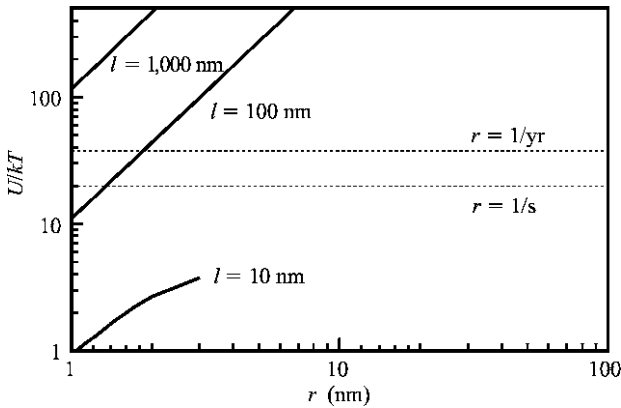
Fig. 6.13. Graph of the ratio E_B/k_BT for Ni nanowires as a function of the radius, for different lengths. The *two horizontal lines* correspond to relaxation times of 1 s and 1 year [37]. (Reprinted from [37] with permission from IBM Technical Journals)

Table 6.1. Magnetic properties of 3d metal nanowires [33]

Material	Fe	Co	Ni	Unit
M_s	1,707	1,400	485	10^3 A m^{-1}
δ_0	13	4	26	nm
H_A	795	597	239	10^3 A m^{-1}
$H_c(\text{RT})$	239	207	75.6	10^3 A m^{-1}
H_c/H_A	0.30	0.35	0.32	–
M_r/M_s	0.93	0.91	0.90	–
$V^*(H_c, RT)$	1.5	2.1	6.0	10^{-24} m^3

The given values of H_c are the maximum values obtained
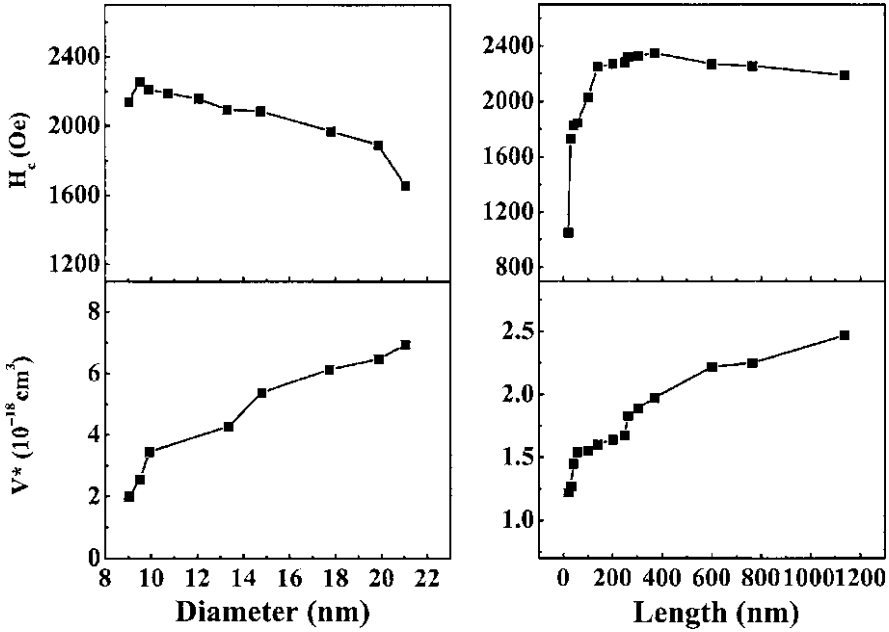
Fig. 6.14. Coercive field H_C and activation volume V^* of cobalt nanowires as a function of the length and diameter. (Reproduced with permission from [33])

The coercivity of the nanowires also varies with their dimensions, as it is shown in Fig. 6.14 for Co nanowires: H_c decreases from about 2.2 kOe for $d = 10$ nm to about 1.6 kOe for $d = 21$ nm (length $= 0.5 - 1\,\mu$m). For a diameter of 10 nm, H_c increases with length, from 1 kOe, reaching a plateau of about 2.3 kOe for 1 µm.

In Fig. 6.14 one also sees the dependence of the activation volume (or nucleation volume) V^* with the diameter of the nanowire. This volume appears in the expression of the magnetic viscosity ((3.29), p. 73). V^* is given by [35]:

$$V^* = \frac{m}{2} \left(\frac{25 k_B T}{KV} \right)^{1-1/m} V. \tag{6.8}$$

where V can be taken as the geometric volume and m is an exponent that depends on the energy landscape.

Heterogeneous nanowires have also been studied, particularly those with a multilayer structure, for example, with layers of Co and Cu. One example of such wires is shown in Fig. 6.15. In this type of layered structure containing a magnetic and a nonmagnetic material, by varying the thickness of the magnetic sector, shape anisotropies perpendicular to the axis of the wire can be obtained, and also blocking temperatures T_B smaller than that of a homogeneous magnetic wire. In Fig. 6.16 one can see the changes in the shape of the hysteresis curves of multilayer NiCu nanowires, as the aspect ratio (length/diameter) of the Ni segments is varied from
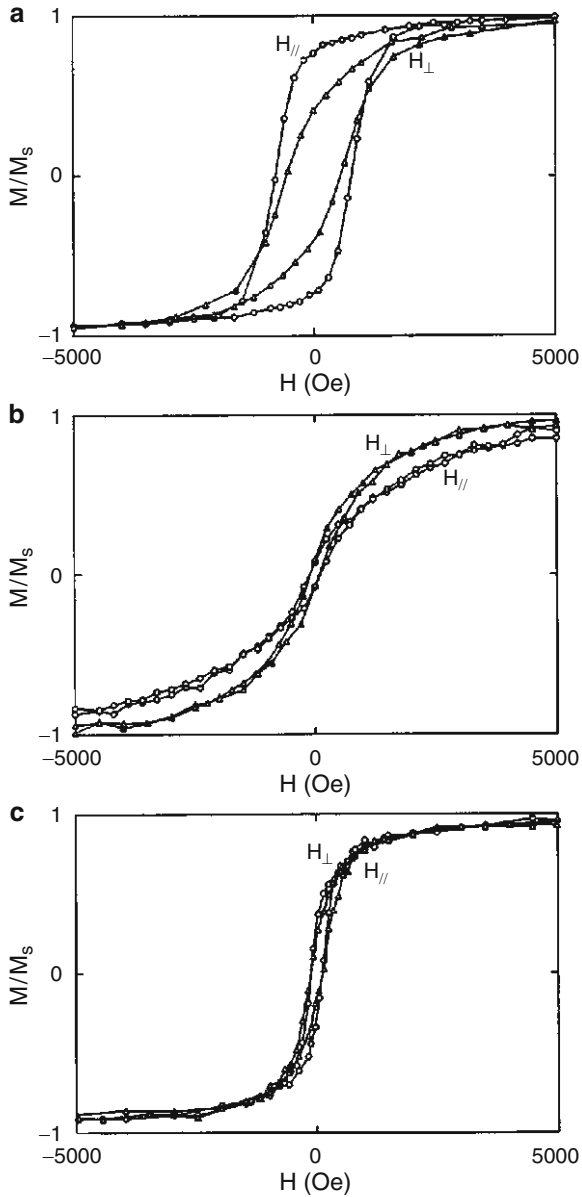
Fig. 6.15. Hysteresis curves of NiCu multilayer nanowires with Ni segments of different aspect ratios (length/diameter): (**a**) rod-shaped Ni segments with $d = 50$ nm and aspect ratio 2.5; (**b**) disk-shaped Ni with $d = 50$ nm and aspect ratio 0.1, and (**c**) Ni segments with intermediate shape, $d = 100$ nm and aspect ratio 1.0. (Reprinted with permission from [7]. Copyright (2003), American Institute of Physics)
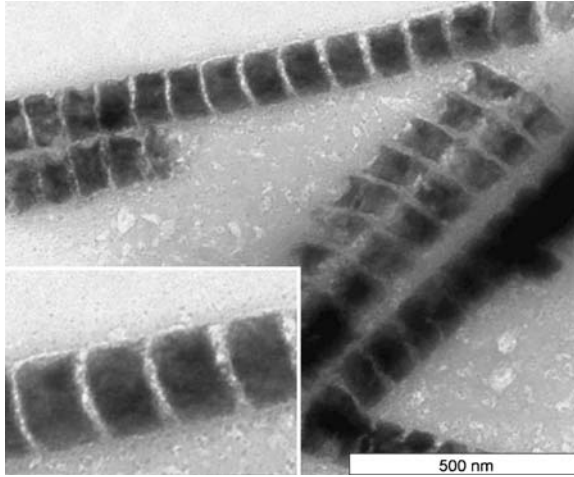
Fig. 6.16. Transmission electron microscopy (TEM) image of cobalt/copper multilayer nanowires prepared by electrochemistry [25]

disk-shaped to rods of aspect ratio 2.5. The hysteresis curves for thin Ni segments reveal a shape anisotropy perpendicular to the axis of the nanowire.

The giant magnetoresistance (GMR) effect was also studied in heterogenous nanowires (see Chap. 5). Nanowires with a multilayer structure, of (Co10 nm/Cu10 nm)×500 electrodeposited from a single bath, were measured in the CPP geometry and found to present a magnetoresistance of 15% [30].

The reversal of the magnetization of magnetic nanowires has also been the subject of many studies. This reversal in thin nanowires usually does not occur through homogenous rotation, but by curling. The nucleation field for an ellipsoidal sample was given by the expression of (3.68) (p. 91):

$$H_{\mathrm{N}} = \frac{2K_1}{\mu_0 M_{\mathrm{s}}} - N M_{\mathrm{s}} + \frac{cA}{\mu_0 M_{\mathrm{s}}} \frac{1}{R^2}, \tag{6.9}$$

where R is the smaller dimension of the spheroid and c is a numerical factor that depends on the aspect ratio. For a cylinder of infinite length we have obtained in Chap. 3 the critical diameter above which the magnetization reversal is made via the curling mode ((3.70), p. 92):

$$D = 5.20 \, l_{\mathrm{ex}}, \tag{6.10}$$

where l_{ex} is the exchange length.

The dependence of the nucleation field with the angle ψ between the anisotropy axis and the applied magnetic field, observed experimentally in nanowires also agrees more with the inhomogeneous magnetization reversal process (curling). This can be established by comparing the experimental dependence of the coercivity H_{c} with the angle ψ with the expression for homogeneous reversal ((3.55), p. 84) and that for the curling mode ((3.73), p. 93).

   In nanowires two main types of magnetic domain walls have been found,
depending on the dimensions of the sample: a transverse wall and a vortex wall.
For wires with rectangular cross-section, of thickness t and width w, the transverse
domain walls constitute the lowest energy configuration below the boundary given
by (e.g., [40]):

$$t \cdot w = C l_{\text{ex}}^2, \tag{6.11}$$

where C is a constant that depends on the material, being equal to 128 for permalloy,
and l_{ex} is the exchange length.

   With an applied magnetic field, the result from micromagnetic simulations for
Co nanowires indicates that these two types of walls move with different velocities,
as shown in Fig. 6.17; also, for nanowires with diameter above 40 nm, only vortex
walls appear [13]. The simulations show that, under an applied magnetic field, vortex
domain walls move faster than transverse walls. For example, with an applied field H
of 500 kA m^{-1}, transverse domain walls travel in a 20 nm wire at a velocity of about
500 m s^{-1}; the velocity of a vortex wall in the same wire is some 150 m s^{-1} higher.

   The domain wall velocity increases with larger wire diameter and smaller damp-
ing constant. The domain wall motion is dependent on the intensity of the applied
magnetic field H. This velocity depends initially in a linear fashion on the intensity of
H, up to a critical field H_{p}, called the Walker field (see the discussion of domain wall
motion in Sect. 2.4.2, p. 50). Beyond this value of H, there is a change in regime, and
at higher values of the field, there are oscillations in the motion of the domain wall,
and from then onwards it is the average velocity that is linearly dependent on H.
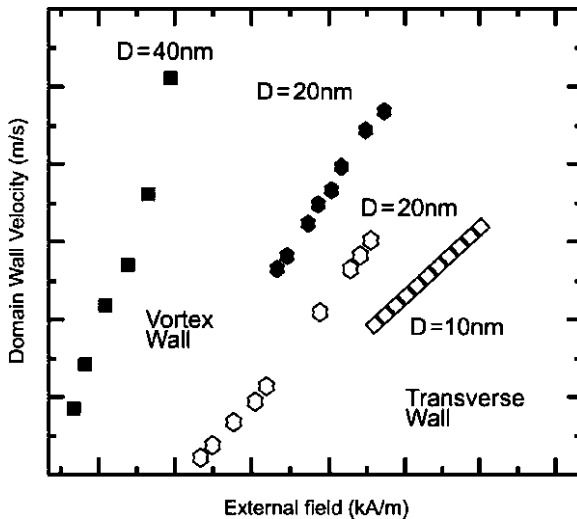
Fig. 6.17. Velocity of two types of domain walls in Co nanowires, transverse (*white symbols*)
and vortex walls (*black symbols*), as a function of applied magnetic field, obtained from mi-
cromagnetic simulation (adapted from [13]). Note that, for the same intensity of external field,
vortex walls move faster than transverse walls

A polarized spin current can also give rise to the displacement of walls, in the phenomenon known as current-induced domain wall motion (CIDM) (for a review of CIDM in magnetic nanostructures, see [40]). When a spin-polarized electric current flows through a nanowire, the velocity of the domain wall can either be increased or decreased, depending on the direction of the current [15]. The effect of the current also varies, depending on the intensity of the field H. Transverse and vortex domain walls move with the same velocity, when current driven [40].

If a nanowire has several 180° domain walls, the application of a magnetic field will move tail-to-tail walls and head-to-head walls in the opposite directions, since the field will always tend to increase the domain parallel to it. An important difference of the current-induced motion is that in this case all the domain walls will move in the same direction.

There are two mechanisms of interaction of the conduction electrons with the domain wall [38]. The first one, producing an effect proportional to the charge current, and important only in narrow domain walls, is the linear momentum transfer arising from the reflection at the wall. The other mechanism arises from the torque exerted by the conduction electron spins on the spins of the atoms in the domain wall. In thick walls it is reached the adiabatic limit, since the conduction electron spins may follow adiabatically the domain wall magnetic moments, i.e., the electron spins become aligned with the magnetization direction.

One may account for the effect of the electric current simply by introducing in the expressions of the rate of change of the coordinate of the domain wall ($\dot{q}$) and rate of change of the angle ϕ ($\dot{\phi}$) in the linear case ((2.111) and (2.112) from Sect. 2.4.2, p. 52), respectively, the terms u and $(\beta/\delta)u$ [39]. This results in the following equations:

$$\dot{\phi} = \gamma_G H - \frac{\alpha_G}{\Delta_H}\dot{q} + \frac{\beta}{\Delta}u, \tag{6.12}$$

and

$$\dot{q} = \frac{1}{2}\gamma_G \Delta_H \mu_0 M_s \sin 2\phi + \alpha_G \Delta_H \dot{\phi} + u . \tag{6.13}$$

The quantity u, present in the two terms that describe the effect of the current, has dimension of velocity, depends on the conduction electron polarization p and the current density $\mathbf{j}$:

$$u = -\frac{g\mu_B p}{2eM_s}j. \tag{6.14}$$

The quantities that appear in u are: g is the electron g-factor and e is the electronic charge. The parameter β measures how non-adiabatic the effect of the current on the domain wall moments is. In the expression of $\dot{q}$, u may be multiplied by a factor $\eta \sim 1$ which depends on the material. The analysis of magnetic field and current-induced motion of domain walls in 20 nm × 600 nm $Ni_{20}Fe_{80}$ nanowires lead to the relation [3]:

$$\alpha/\beta \approx 1. \tag{6.15}$$

In the limit of $\dot{\phi} = 0$, which is valid below the Walker breakdown, one obtains for the domain wall velocity:

$$v = \dot{q} = \frac{\gamma_G \Delta}{\alpha_G} H + \frac{\beta}{\alpha_G} u. \tag{6.16}$$

Above the Walker limit, the domain wall velocity becomes [15]:

$$v = \frac{\gamma_G \Delta}{\alpha_G} \left(H - \frac{\sqrt{4[H + u(\beta - \alpha)/\gamma_G \Delta]^2 - (\alpha_G H)^2}}{2\alpha_G(1 + \alpha_G^2)} \right) + \frac{\beta}{\alpha_G} u. \tag{6.17}$$

Equation (6.16) is the same equation presented on Sect. 2.4.2 ((2.113), p. 52) describing the velocity of a domain wall in the motion induced by an applied magnetic field, now modified by the presence of the extra term due to the electronic current $(\beta/\alpha)u$.

In the limit $\dot{\phi} \gg 1$, neglecting some smaller terms, one obtains for the domain wall velocity

$$v = \dot{q} = \alpha_G \gamma_G \Delta H + u. \tag{6.18}$$

It should be noted that in this case the domain wall velocity is still proportional to the domain width parameter Δ, as in the previous case, but it is also directly proportional to the damping constant α_G.

Figure 6.18 shows the dependence of the transverse domain wall velocity in a $120 \times 5 \, \text{nm}^2$ nanowire computed using the LLG equation with the electronic current contribution vs. u, that is proportional to the polarized current density, for different values of the parameter β [39]. One can see that for $\beta = 0$ there is a critical value of u, and therefore a critical current density J_c below which, there is no steady domain wall motion (there is some transient motion after the application of the current). For non-zero β, and a perfect nanowire, as in this case, there is domain wall motion for any value of the current density.
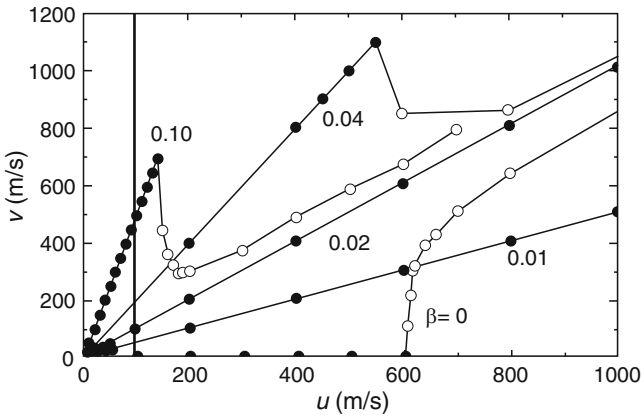
Fig. 6.18. Micromagnetic computation of transverse domain wall velocity vs. spin-polarized current contribution, for different values of the non-adiabaticity parameter β [39]

Further Reading

C.L. Chien, F.Q. Zhu, J.-G. Zhu, Phys. Today **60**, 40–45 (2007)

A. Fert, L. Piraux, J. Magn. Magn. Mater. **200**, 338–358 (1999)

M. Kläui, in *Magnetic Rings: A Playground to Study Geometrically Confined Domain Walls*, ed. by B. Azzerboni, G. Asti, L. Pareti, M. Ghidini. Magnetic Nanostructures in Modern Technology (Springer, Dordrecht, 2008), pp. 85–104

C.A. Ross, F.J. Castaño, D. Morecroft, W. Jung, H.I. Smith, T.A. Moore, T.J. Hayward, J.A.C. Bland, T.J. Bromwich, A.K. Petford-Long, J. Appl. Phys. **99**, 08S501–08S506 (2006)

D.J. Sellmyer, M. Zheng, R. Skomski, J. Phys. Condens. Matter. **13**, R433–R460 (2001)

L. Sun, Y. Hao, C.L. Chien, P.C. Searson, IBM J. Res. Dev. **49**, 79–102 (2005)

L. Thomas, S. Parkin, in *Current Induced Domain-Wall Motion in Magnetic Nanostructures*, ed. by H. Kronmüller, S. Parkin. Handbook of Magnetism and Advanced Magnetic Materials, vol 2 (Wiley, Chichester, 2007), pp. 942–982

C.A.F. Vaz, T.J. Hayward, J. Llandro, F. Schackert, D. Morecroft, J.A.C. Bland, M. Kläui, M. Laufenberg, D. Backes, U. Rüdiger, F.J. Castaño, C.A. Ross, L.J. Heyderman, F. Nolting, A. Locatelli, G. Faini, S. Cherifi, W. Wernsdorfer, J. Phys. Condens. Matter. **19**, 255207–255214 (2007)

M. Vazquez, in *Advanced Magnetic Nanowires*, ed. by H. Kronmüller, S. Parkin. Handbook of Magnetism and Advanced Magnetic Materials, vol 4 (Wiley, Chichester, 2007), pp. 2193–2226

T.L. Wade, J.E. Wegrowe, Eur. J. Appl. Phys. **29**, 3–22 (2005)

References

1. A.S. Arrott, in *Introduction to Micromagnetics*, ed. by B. Heinrich, J.A.C. Bland. Ultra-thin Magnetic Structures IV (Springer, Berlin, 2005), pp. 101–148

2. L.D. Barron, in *Chirality at the Sub-Molecular Level: True and False Chirality*, ed. by W.J. Lough, I.W. Wainer. Chirality in Natural and Applied Science (Blackwell, Victoria, 2002), pp. 53–86

3. G.S.D. Beach, C. Knutson, M. Tsoi, J.L. Erskine, J. Magn. Magn. Mater. **310**, 2038–2040 (2007)

4. L. Berger, Phys. Rev. B **54**, 9353–9358 (1996)

5. K.S. Buchanan, P.E. Roy, M. Grimsditch, F.Y. Fradin, K.Y. Guslienko, S.D. Bader, V. Novosad, Nat. Phys. **1**, 172–176 (2005)

6. F.J. Castaño, C.A. Ross, A. Eilez, W. Jung, C. Frandsen, Phys. Rev. B **69**, 144421 (2004)

7. M. Chen, P.C. Searson, C.L. Chien, J. Appl. Phys. **93**, 8253–8255 (2003)

8. C.L. Chien, F.Q. Zhu, J.-G. Zhu, Phys. Today **60**, 40–45 (2007)

9. S.-B. Choe, Y. Acremann, A. Scholl, A. Bauer, A. Doran, J. Stohr, H.A. Padmore, Science **304**, 420–422 (2004)

10. M. Darques, A. Encinas, L. Vila, L. Piraux, J. Phys. D: Appl. Phys. **37**, 1411–1416 (2004)

11. C.L. Dennis, R.P. Borges, L.D. Buda, U. Ebels, J.F. Gregg, M. Hehn, E. Jouguelet, K. Ounadjela, I. Petej, I.L. Prejbeanu, M.J. Thornton, J. Phys. Condens. Matter **14**, R1175–R1262 (2002)

12. U. Ebels, A. Radulescu, Y. Henry, L. Piraux, K. Ounadjela, Phys. Rev. Lett. **84**, 983–986 (2000)

13. H. Forster, T. Schrefl, W. Scholz, D. Suess, V. Tsiantos, J. Fidler, J. Magn. Magn. Mater. **249**, 181–186 (2002)

14. K.Y. Guslienko, K.-S. Lee, S.-K. Kim, Phys. Rev. Lett. **100**, 027203–027204 (2008)
15. M. Hayashi, L. Thomas, Y.B. Bazaliy, C. Rettner, R. Moriya, X. Jiang, S.S.P. Parkin, Phys. Rev. Lett. **96**, 197207 (2006)
16. R. Höllinger, A. Killinger, U. Krey, J. Magn. Magn. Mater. **261**, 178–189 (2003)
17. A. Hubert, R. Schäfer, *Magnetic Domains. The Analysis of Magnetic Microstructures* (Springer, Berlin, 1999)
18. W. Jung, F.J. Castaño, C.A. Ross, Phys. Rev. Lett. **97**, 247209 (2006)
19. A.F. Khapikov, J. Appl. Phys. **89**, 7454–7456 (2001)
20. M. Kläui, in *Magnetic Rings: A Playground to Study Geometrically Confined Domain Walls*, ed. by B. Azzerboni, G. Asti, L. Pareti, M. Ghidini. Magnetic Nanostructures in Modern Technology (Springer, Dordrecht, 2008), pp. 85–104
21. M. Kläui, H. Ehrke, U. Rüdiger, T. Kasama, R.E. Dunin-Borkowski, D. Backesb, L.J. Heyderman, C.A.F. Vaz, J.A.C. Bland, G. Faini, E. Cambril, W. Wernsdorfer, Appl. Phys. Lett. **87**, 102509 (2005)
22. M. Kläui, C.A.F. Vaz, J.A.C. Bland, E.H.C.P. Sinnecker, A.P. Guimarães, W. Wernsdorfer, G. Faini, E. Cambril, L.J. Heyderman, C. David, Appl. Phys. Lett. **84**, 951–953 (2004)
23. V.P. Kravchuk, D.D. Sheka, Y.B. Gaididei, J. Magn. Magn. Mater. **310**, 116–125 (2007)
24. M. Laufenberg, D. Bedau, H. Ehrke, M. Kläui, U. Rudiger, D. Backes, L.J. Heyderman, F. Nolting, C.A.F. Vaz, J.A.C. Bland, T. Kasama, R.E. Dunin-Borkowski, S. Cherifi, A. Locatelli, S. Heun, Appl. Phys. Lett. **88**, 212510–212513 (2006)
25. J.D.L.T. Medina, M. Darques, T. Blon, L. Piraux, A. Encinas, Phys. Rev. B **77**, 014417–014419 (2008)
26. N.D. Mermin, Rev. Mod. Phys. **51**, 591–648 (1979)
27. M.M. Miller, G.A. Prinz, S.-F. Cheng, S. Bounnak, Appl. Phys. Lett. **81**, 2211–2213 (2002)
28. K. Nakamura, T. Ito, A.J. Freeman, Phys. Rev. B **68**, 180404–180408 (2003)
29. S. Ono, M. Saito, H. Asoh, Electrochim. Acta **51**, 827–833 (2005)
30. L. Piraux, J.M. George, J.F. Despres, C. Leroy, E. Ferain, R. Legras, K. Ounadjela, A. Fert, Appl. Phys. Lett. **65**, 2484–2486 (1994)
31. W. Scholz, K.Y. Guslienko, V. Novosad, D. Suess, T. Schrefl, R.W. Chantrell, J. Fidler. J. Magn. Magn. Mater. 155–163 (2003)
32. N.L. Schryer, L.R. Walker, J. Appl. Phys. **45**, 5406–5420 (1974)
33. D.J. Sellmyer, M. Zheng, R. Skomski, J. Phys. Condens. Matter **13**, R433–R460 (2001)
34. K. Shigeto, T. Okuno, K. Mibu, T. Shinjo, T. Ono, Appl. Phys. Lett. **80**, 4190–4192 (2002)
35. R. Skomski, J. Zhou, in *Nanomagnetic Models*, ed. by D. Sellmyer, R. Skomski. Advanced Magnetic Nanostructures (Springer, New York, 2006), pp. 41–90
36. J.C. Slonczewski, J. Magn. Magn. Mater. **159**, L1–L7 (1996)
37. L. Sun, Y. Hao, C.L. Chien, P.C. Searson, IBM J. Res. Dev. **49**, 79–102 (2005)
38. G. Tatara, H. Kohno, Phys. Rev. Lett. **92**, 086601–086604 (2004)
39. A. Thiaville, Y. Nakatani, J. Miltat, Y. Suzukim, Europhys. Lett. **69**, 990–996 (2005)
40. L. Thomas, S. Parkin, in *Current Induced Domain-Wall Motion in Magnetic Nanostructures*, ed. by H. Kronmüller, S. Parkin. Handbook of Magnetism and Advanced Magnetic Materials (Wiley, Chichester, 2007), pp. 942–982
41. O.A. Tretiakov, O. Tchernyshyov, Phys. Rev. B **75**, 012408–012409 (2007)
42. N.A. Usov, S.E. Peschany, Phys. Met. Metall. **12**, 13–24 (1994)
43. C.A.F. Vaz, T.J. Hayward, J. Llandro, F. Schackert, D. Morecroft, J.A.C. Bland, M. Kläui, M. Laufenberg, D. Backes, U. Rüdiger, F.J. Castaño, C.A. Ross, L.J. Heyderman, F. Nolting, A. Locatelli, G. Faini, S. Cherifi, W. Wernsdorfer, J. Phys. Condens. Matter. **19**, 255207–255214 (2007)

44. M. Vázquez, in *Advanced Magnetic Nanowires*, ed. by H. Kronmüller, S. Parkin. Handbook of Magnetism and Advanced Magnetic Materials, vol 4 (Wiley, Chichester, 2007), pp. 2193–2226
45. B. Van Waeyenberge, A. Puzic1, H. Stoll, K.W. Chou, T. Tyliszczak, R. Hertel, M. Fähnle, H. Brückl, K. Rott, G. Reiss, I. Neudecker, D. Weiss, C.H. Back, G. Schütz1, Nature **444**, 461–464 (2006)
46. H. Wang, C.E. Campbell, Phys. Rev. B **76**, 220407 (2007)
47. K. Yamada, S. Kasai, Y. Nakatani, K. Kobayashi, H. Ono, A. Thiaville, T. Ono, Nat. Mater. **6**, 269–273 (2007)
48. T. Yang, M. Hara, A. Hirohata, T. Kimura, Y. Otani, Appl. Phys. Lett. **90**, 022504 (2007)
49. Y.G. Yoo, M. Kläui, C.A.F. Vaz, L.J. Heyderman, J.A.C. Bland, Appl. Phys. Lett. **82**, 2470–2472 (2003)
50. J.-G. Zhu, Y. Zheng, G.A. Prinz, J. Appl. Phys. **87**, 6668–6673 (2000)

7

Magnetic Recording

Summary. Magnetic storage is the most important technology for data recording, and has evolved very rapidly in the last half century. Although it has reached a high level of refinement, it is based on relatively simple principles. The limitations eventually imposed on its continued evolution have stimulated the development of other solutions, magnetic or not, for the storage of data, in the face of the information explosion. Some of the magnetic solutions include the encoding of information onto a string of magnetic domains in magnetic nanowires, or in the magnetization states of magnetic nanodisks and nanorings.

7.1 Introduction

Magnetic storage technology is incorporated into hard disk drives (HDD's), magnetic tapes and magnetic stripes, as in credit cards, badges, and tags. Many applications use analog recording, a technique whereby the intensity of a signal is encoded in the magnitude of the magnetization of the magnetic medium. We will deal mostly with digital recording, the encoding system in which the information is recorded as a succession of binary digits (bits), which is the form used to store data in hard disks and computer random magnetic memories.

Magnetic recording technology, embodied in the ubiquitous hard disk drive, has, together with the integrated circuit, revolutionized data handling and storage, thus opening the Information Age. Magnetic recording has covered a long route since its invention at the end of the nineteenth century. The rate of evolution of this technology has accelerated in the last decades, as can best be measured by the vertiginous increase in areal density of stored information in the magnetic disks in this period, of the order of 10^7 times in the last 50 years. In parallel with this increase in density, the cost per bit of recorded data also fell dramatically in the period, by about the same factor (this evolution is shown in Fig. 1.2, on p. 3). For a recent review of the evolution and present reality of magnetic data storage, see [14].

The basis of magnetic data storage is that, on an essentially two-dimensional geometry, small volumes of magnetic material are magnetized, and a sequence of these

magnetically ordered regions corresponds to binary digits, represented by "0" or "1." The variation of the state of magnetization of these volumes can be identified by a transducer, and therefore the recorded bits can be read. The technical realization of this relatively simple idea went through continuous improvement and optimization, leading to the solution of complex problems, that ultimately made possible the great advances in magnetic recording. This has meant development in the magnetic recording material itself, its intrinsic and extrinsic properties, the better understanding or the magnetization process, the refinement of the servo control of the recording and reading device, the study of tribology of the head-medium system, and so on.

7.2 Principles of Magnetic Recording

The magnetic material now used in hard disk magnetic recording is in the form of a polycrystalline thin film, usually made of a CoCr alloy. The magnetization can either be contained in the plane of the film or be perpendicular to it; this defines two different recording technologies, longitudinal and perpendicular recording, shown schematically in Fig. 7.1. The film is composed of grains that have a diameter of under 10 nm, and their anisotropy axes are randomly oriented in the longitudinal recording media, or oriented within a few degrees of the normal to the plane, in magnetic media for perpendicular recording. The dominant technology from the discovery of the technique to the present days has been longitudinal recording, although, the trend is towards the growth of perpendicular recording HDD's [13].

In a hard disk, the information is recorded on the magnetic medium through a recording head, essentially a coil wound on a soft magnetic core that produces at its gap a magnetic field, inducing a magnetization on the medium. The medium is magnetized into two opposite directions, according to the direction of the current in the write head. Two segments magnetized in sequence constitute a bit cell; the cells
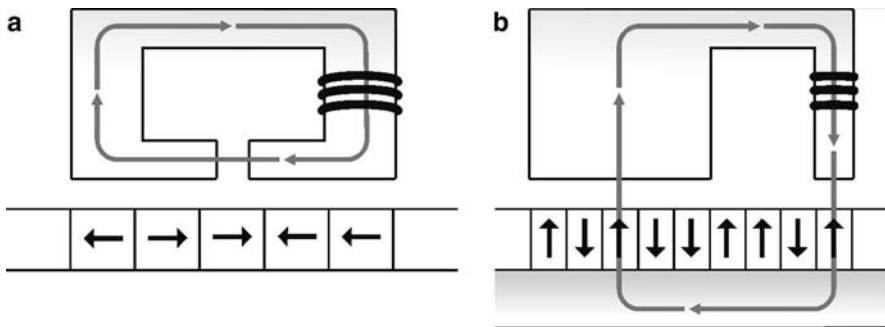
Fig. 7.1. Longitudinal (**a**) and perpendicular (**b**) write heads showing the two types of magnetic recording technologies. Note that the magnetic circuit in the case of perpendicular magnetization is closed through a layer below the magnetic medium, the soft magnetic underlayer (SUL)

that have a change in the direction of magnetization encode a "1," those that do not, correspond to a "0."

The recorded data are read from the medium by a read head that usually detects the magnetization of the medium through a change in the resistivity of a sensor. In the longitudinal magnetic recording system, the sensor detects the stray field at the transition between two magnetized regions of the medium. In the perpendicular recording, since these regions are magnetized in the vertical direction, the sensor is sensitive to their individual magnetizations.

An important difference between the two magnetic recording technologies is the fact that in longitudinal recording, the magnetic circuit of the head-medium system is closed with some flux through the magnetic medium, whereas in the case of perpendicular recording, the geometry is such that there is the need of an extra layer of magnetic material to allow closing this circuit, the soft magnetic underlayer (SUL), as shown in Fig. 7.1b. The magnetic underlayer is usually made of a high permeability material such as FeCoB, CoTaZr, or, less often, CoZrNb; simple or laminated SUL's may be employed [13].

The read and write heads are mobile, and the platter with the magnetic medium rotates rapidly beneath them. This allows the use of most of the surface of the disk for recording and reading the recorded information. The area used for recording consists of concentric tracks divided into sectors. The relative motion also implies that once the head is positioned on the right sector, each bit is read in a very short time, of the order of a fraction of a nanosecond, for a disk rotating at 10,000 rpm. The temporal pattern of currents at the write head is translated into a spatial magnetization pattern on the magnetic medium.

The data areal density on the disk is defined by the width of the recorded track (W), the distance between recorded transitions (B) and the separation between neighbor tracks (H). The linear density is the reciprocal of B and the track density is the reciprocal of ($W + H$); their product is the areal density. Present-day areal densities are approaching 1 Tbit in^{-2} (1 terabit=10^{12} bits); in metric units, this corresponds to ≈ 0.155 Tbit cm^{-2}.

The write head consists essentially of a soft magnetic core wound with a coil through which a current flows, producing a time-varying magnetic field at the gap. This field is proportional to the current and also to an efficiency factor, to be defined below. The line integral of the magnetic field H in a magnetic circuit is equal to the current that flows around this circuit; if there is a coil with N turns through which a current I circulates, then

$$NI = \int H \cdot d\mathbf{l}, \tag{7.1}$$

where $d\mathbf{l}$ is the element of length of the magnetic circuit, shown in Fig. 7.1.

If this magnetic circuit is a core with a gap, as in the write head, the drop in potential across this gap is given by

$$V_a - V_b = NI - \int_{core} H \cdot d\mathbf{l}. \tag{7.2}$$

The efficiency η measures the ratio of this potential drop to the magnetomotive force provided by the current, given by $V = NI$. This ratio, from the integral that appears in (7.1), is equal to

$$\eta = \frac{g H_g}{\ell_c H_c + g H_g},$$ (7.3)

where g is the gap width, H_g and H_c are the magnetic fields in the gap and inside the core, and ℓ_c is the length of the core.

The magnetic field inside the gap of the write head, of width g is known as the deep gap field, is therefore given by [1]:

$$H_0 = \frac{NI}{g} \eta.$$ (7.4)

The magnetic field produced by the write head varies spatially as a function of the distance from the gap. The expression for this dependence, in the case of a gap of width g and infinite length, was derived by Karlqvist [7] and is written, as a function of the deep gap field H_0:

$$H_x = \frac{1}{\pi} H_0 \left[\arctan\left(\frac{(g/2)+x}{y} \right) + \arctan\left(\frac{(g/2)-x}{y} \right) \right].$$ (7.5)

This is the component of the magnetic field H along the direction of the normal to the face of the pole pieces, the direction of the displacement of the write head (the x direction). The y axis is the axis perpendicular to the magnetic medium.

In Fig 7.2 are shown the surfaces of equal magnetic field, of decreasing intensity as their radius increases. As can be seen in the figure, the intensity of the magnetic field is not constant inside the magnetic medium. For example, on the surface of the circle that satisfies $H = H_c$, the magnetization is zero (from the definition of H_c),
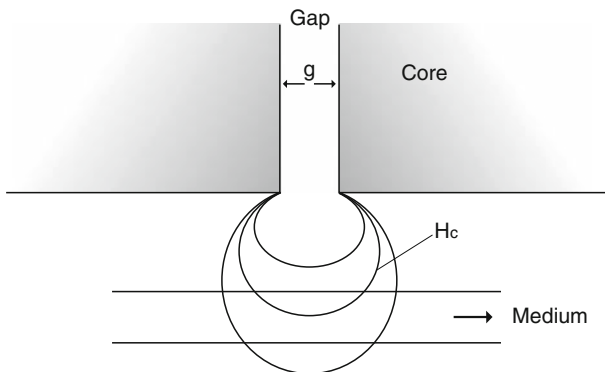
Fig. 7.2. Gap of write head, of width g, and lines of equal intensity of transverse magnetic field H_x, in longitudinal magnetic recording. The line of field for $H = H_c$ (the coercive field) is shown
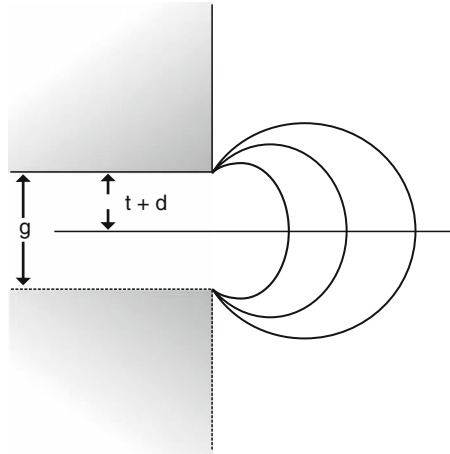
Fig. 7.3. Perpendicular head showing its mirror image formed below the soft underlayer (SUL). Since this underlayer is at a distance $t + d$ from the real head, the gap has an effective width $g = 2(t + d)$

and half the magnetic moments have inverted. For smaller radii, the proportion of inverted moments is higher, and the opposite applies for larger radii.

The magnetic field on a perpendicular medium can be computed using the same Karlqvist head, but turning it sideways, as shown in Fig. 7.3. Since in this case the magnetic medium has underneath a high permeability layer (SUL) of thickness t, at a distance d from the head, a mirror image of the head is formed at the same distance $(d + t)$ below the upper surface of this layer. The gap in this case is the distance between the head and this image, and therefore $g = 2(d + t)$. The magnetic field in the gap is approximately the deep gap field H_0, and the dependence with distance of the y component is given, from (7.5):

$$H_y = \frac{1}{\pi} H_0 \left[\arctan\left(\frac{d + (t/2)}{x} \right) + \arctan\left(\frac{d + (3t/2)}{x} \right) \right]. \tag{7.6}$$

Originally, the write head and the read heads both operated based on the same principle. But long time ago the read head started to follow a different design. Nowadays, it makes use of a magnetoresistance effect to convert the information obtained from the stray field of the recorded medium into electrical signals. The effect that is used to provide a large signal is the giant magnetoresistance (GMR) effect, which converts the magnetic information into variations of the resistivity ρ (see Chap. 5, where magnetic transport properties are discussed). Another effect that is used for the same purpose is the tunnel magnetoresistance (TMR) effect, also discussed in Chap. 5.

The GMR read heads use spin valves as sensing elements. These are compact thin film structures formed essentially of two magnetic layers, one of which rotates its magnetization through the influence of the magnetization of the recorded medium,

the other remaining fixed, or pinned. The usual geometry is current in plane (CIP), and the magnetic layers may be prepared from CoFe or NiFe (see e.g., [5]). The magnetic layer that is pinned derives this condition from the interface with an antiferromagnetic layer, through the phenomenon of exchange bias, as discussed in Sect. 4.4, beginning on p. 117. The sensing element of the read head should have low coercivity and high permeability to respond to small stray magnetic fields from the medium.

In order to guarantee long term stability of the magnetic recorded information, the grains that constitute the polycrystalline magnetic medium must have such dimensions that thermal fluctuations do not affect the magnetization, in other words, the magnetization relaxation time at room temperature must be long, situating them far away from the superparamagnetic regime (see Chap. 3, for the properties of magnetic nanoparticles).

Since the inverse of the relaxation time depends exponentially on the height of the anisotropy energy barrier for magnetization reversal (KV), the barrier must be much higher than the thermal energy at room temperature; this usually implies $KV \geq 40k_{B}T$. This condition is equivalent, for values of the anisotropy in current use, to a requirement of grain size larger than about 5 nm. A stability or integrity of the recorded information for a period of 10 years is normally assumed.

The necessity of stable ferromagnetic behavior and the continued quest for increasing recording densities have led to the use of magnetic media with higher and higher anisotropies, a trend that is limited by the corresponding need of increased field produced by the write head. The set of three conflicting goals of magnetic recording technology, i.e., (1) improving signal to noise ratio (can be achieved with smaller grains), (2) guaranteeing thermal stability (requires larger grains and higher anisotropy), and (3) preserving write-ability (given by smaller anisotropy) is known as the magnetic recording trilemma.

The HDD remains a vital component in the digital computer. Notwithstanding its remarkable success, it has limitations inherent to a technology that relies on the mechanical motion of platter and arm for its operation. This implies that further increases in performance may be limited by some mechanical obstacles; e.g., the linear velocity at the rim of a 3.5 inch disk turning at some 60,000 rotations per minute approaches the velocity of sound [14].

Three main pathways are being investigated to allow increases in the density of magnetic storage using most of the advances accumulated in the development of magnetic hard disks. These are the use of patterned media, heat-assisted magnetic recording (HAMR), and microwave-assisted magnetic recording (MAMR). The first development involves a change in the magnetic structure of the magnetic hard disk, with the magnetic bits recorded in pre-determined, and magnetically non-interacting, dots on the surface of the disk. Heat-assisted recording, on the other hand, makes use of laser to raise the temperature of the magnetic medium, therefore lowering the effective anisotropy field. This implies that with magnetic fields in use with the present write heads, magnetic media of higher coercivity could be used, allowing higher magnetic recording densities. The last of these proposed new recording techniques uses the fact that a magnetic particle subject to a microwave field will switch its

magnetization at a smaller applied magnetic field (e.g., [17]). This is another form of recording that makes viable media with higher coercivity. These new technologies, however, involve several technical problems, still not completely solved.

HDD's are relatively slow, with access times orders of magnitude slower than random access memories (RAM's). Which technologies will supersede the hard magnetic disk and the semiconductor random access memory is still an open question. Many physical processes have been explored for their potential as candidates to base future magnetic recording technologies. We will briefly consider some of them in Sect. 7.3, discussing recent suggestions of non-conventional systems to store magnetic data.

7.3 Novel Magnetic Recording Systems

Many new approaches to data storage have been attempted and practically realized at the demonstration level. These include nonmagnetic storage, for example, using probe-based techniques, that rely on cantilevers developed for atomic force microscopy (e.g., [10]), three-dimensional optical storage using photochromic crystals (e.g., [8]), phase-change random access memory (PCRAM) [12] and so on. An overview of new solid-state storage technologies is presented in [3]. In the field of magnetic storage, an important effort is directed to devices that have no moving parts, as it is the case of magnetic hard disks, and at the same time are economical and non-volatile. This may eventually provide the market with magnetic recording technologies that will substitute both the random access memories (RAM's) and the HDD's.

7.3.1 Nanodisk and Nanoring Memories

Magnetic rings and disks, or dots, of nanoscopic or mesoscopic dimensions, have physical properties that can be used to encode digital information. For example, nanodots of magnetically soft material with diameters around 100 nm typically show a vortex spin configuration at their ground states, that have potential for data storage. Nanodisks and nanorings have the advantage that, since they are structures that present flux closure, they have intrinsically low stray fields. This is important for practical applications, since nanostructures formed with these elements can be arranged into more compact arrays, in view of the reduced near-neighbor interactions.

The vortex structures that are spontaneously formed in magnetic disks of nanoscopic or sub-micron dimensions can be used for magnetic storage, specifically as vortex-based magnetic random access memories (VRAM's). This application is based on the possibility of using the direction of rotation of the vortices, or circulation (clockwise or anti-clockwise), or the direction of the magnetization of the vortex core, up or down, that is, with polarity p equal to $+1$ or -1, respectively (Sect. 6.2, p. 150). Vortices therefore may present themselves in four different states, and in principle could store two bits of information. Vortices are fairly stable, and can remain indefinitely in the same configuration without the need of application of current or external magnetic field.

Some proposals for writing and reading data from arrays of nanodisks have been presented, but the practical use of these arrays will require further investigation. We will consider two proposed forms of realizing VRAM devices.

One suggestion uses the polarity p of the vortex, i.e., the direction of the magnetization of the core, to store magnetic information. The data is written by forcing the polarity through the application of either an in-plane rotating magnetic field or an in-plane spin-polarized current [9]. This scheme uses the fact that the amplitude of the rotation of the vortex core, induced by a rotating magnetic field $H(t)$ or current $i(t)$, is dependent on the direction of rotation of this field and is independent of the direction of circulation of the vortex (clockwise or counterclockwise). For example, in the case of vortex with a polarity $p = +1$ ($M_z > 0$), a counterclockwise rotating field induces a gyrotropic motion of the vortex with larger amplitude than a rotating CW field. One may therefore choose an amplitude of H that switches the vortex polarity for one rotating direction, but not for the other. This selectivity may then be used to write the desired data unit, and from the response of the vortex, the rotating field reads its configuration. Since this is a resonant effect, the magnetic fields or spin-polarized ac currents must have a frequency close to the vortex eigenfrequency, of a few hundred megahertz. This idea has been demonstrated in computer simulations with permalloy disks of 600 nm diameter and 20 nm thickness [9].

Another possible use of vortices in nanodisks for data storage is based on employing the combined polarity (p) and sense of rotation, or circulation, of the vortex (c), i.e., the pair that constitutes its chirality, determined univocally by the product cp, (see Sect. 6.2, p. 152), to store magnetic data. This can be achieved in a scheme where permalloy thin film elements are actuated by spin-polarized current pulses and applied fields [2]. Depending on the relative directions of field and current, the amplitude of the gyrotropic vortex motion is either enhanced or attenuated.

To read the chirality, the signal induced in a pick-up coil by the precession of the vortex is measured, or alternatively, the resistivity of the element is determined. The chirality is detected through the amplitude of the rotation of the vortex when excited by a small spin-polarized current and a magnetic field.

Magnetic nanorings also offer many promises as components of magnetic memory devices. As we have seen in Chap. 6, they have several possible spin configurations, with properties that can be made to correspond to different data states; these properties are the sense of rotation of the vortex, i.e., their circulation, and the direction of magnetization in the onion state, or in the asymmetric, or twisted state (Sect. 6.3, p. 156).

A simple arrangement of nanorings that may be used for data storage is a three-layered structure formed of two superposed magnetic nanorings separated by a nonmagnetic layer, constituting a spin valve, as illustrated schematically in Fig. 7.4; actual cells used in applications may have a much more complex structure.

This structure of nanorings can have its magnetic state probed by an electric current flowing along the length of the stack, in the perpendicular (CPP) geometry. Using the GMR effect, the variation of the resistance allows the identification of parallel or antiparallel magnetic moments in the ferromagnetic rings, therefore reading the recorded information. If, instead of a nonmagnetic conducting layer, the interme-
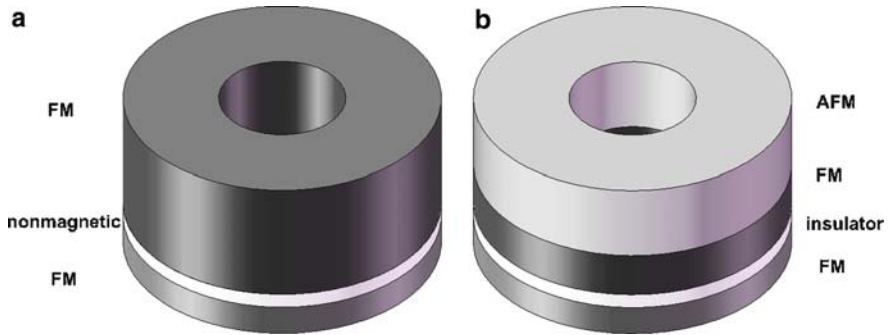
Fig. 7.4. Magnetic nanoring magnetoresistance memory cells using (**a**) pseudo spin valve with FM/Cu/soft FM structure, based on the GMR phenomenon, and (**b**) spin valve structure with AFM/FM/insulator/soft FM rings, based on TMR

diate layer is an insulating thin film, this arrangement constitutes a magnetic tunnel junction (MTJ) and may use the tunnel magnetoresistance effect (TMR) for readout (for TMR, see Sect. 5.3, p. 142). Simulations have shown that memory cells based on this idea, with stacks of FM/Cu/soft FM nanorings forming short pillars produced by lithography, are viable as the basis of a high-density magnetic recording system, with an estimated maximum recording areal density of $400\,\mathrm{Gb\,in^{-2}}$ [16].

Writing on these ring structures is effected through switching between the different vortex states. This was experimentally demonstrated using the spin-transfer torque and the Oersted field, the latter being the dominant contribution, with a stack of Co nanorings with dimensions in the range of hundreds of nanometers [15]. In other studies using tunnel magnetoresistance of rings of diameters between 80 nm and 4 μm, structured as a stack of AFM/FM/insulator/FM and FM/insulator/soft FM layers, the magnetization reversal was dominated by spin polarized switching, but the Oersted magnetic field also played a role [6].

Another example of annular memory elements, this time switching magnetic rings between two twisted states through the action of the Oersted field, was demonstrated by micromagnetic simulation using a stack of rings forming a magnetic tunnel junction (MTJ) [18].

These developments are immediately relevant to applications in magnetic (or magnetoresistive) random access memories (MRAM's), devices that present many advantages relative to other types of memories, since they are non-volatile, radiation resistant, and present no fatigue. Stacks of magnetic rings are evolving in terms of storing density, although are not yet comparable to other MRAM designs, as seen in Fig. 7.5, where the evolution of the storage capacity per chip of magnetic random memories is exhibited [6].

7.3.2 Domain Wall Memories

The studies of the interaction of spin-polarized currents with magnetic domain walls and with the magnetization of nanoobjects opened many possibilities of using
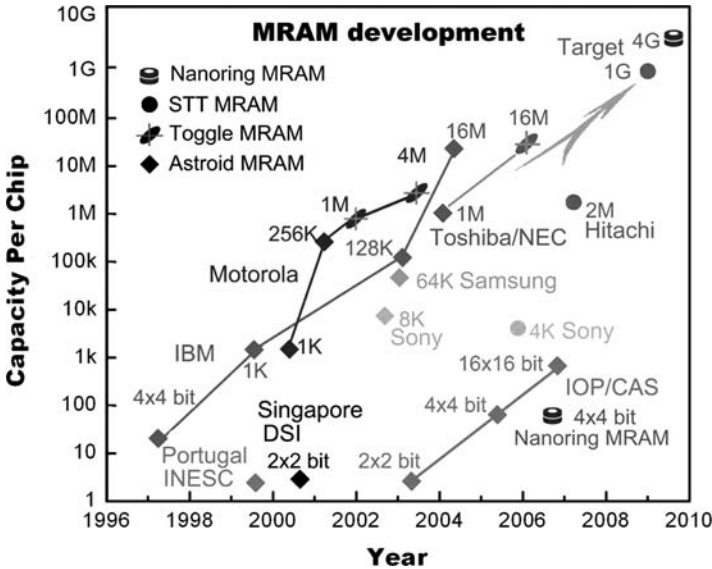
Fig. 7.5. Evolution of the storage capacity of magnetic random access memories (MRAM). The graph shows the capacity per chip for different MRAM designs, as a function of the year of development. (Reprinted with permission from [6]. Copyright (2008), American Institute of Physics)

these effects for magnetic storage of digital information. On the one hand, spin-polarized currents can switch the magnetization of magnetic elements, an idea that has been applied to the development of magnetic random access memories. Also, these currents are able to interact with and displace the domain walls in the same direction, independently of the orientation of the domains, (see Sect. 6.4, p. 160, on the properties of nanowires). This, of course, is unlike the effect of the application of a magnetic field, that has as consequence the expansion of the domains that are magnetized in the same direction of $H(t)$.

The interaction of the current with the domain walls is used to create a shift register, moving bits recorded as a sequence of DW's in nanowires. These nanowires can form arrays arranged on a plane or on a three-dimensional structure, and can be connected in series; Figure 7.6 shows the device in planar geometry. These domain wall memories or racetrack memories are described in [11].

Writing the data is accomplished by the magnetic field produced by the motion of domains in a perpendicular wire. The encoded pattern in the racetracks is read by a read head formed of a magnetic tunnel junction (MTJ) in contact with it.

The nanowires are prepared in such a way as to guarantee that all the domains have the same length and are formed in pre-defined places, for example, by the inclusion of pinning centers. The domains are shifted through the application of polarized current in the form of short pulses. The amplitude of the pulsed voltage can
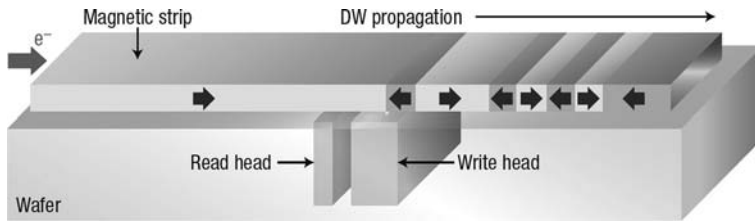
Fig. 7.6. Domain wall memory with read and write heads. On a magnetic stripe, an electric current displaces the domains, which are then given the desired orientation (i.e., the data is recorded) as they move past the write head [4]. (Reprinted by permission from Macmillan Publishers Ltd. [4], copyright (2007))

be optimized if the signal is in resonance, with a period equal to half the period of oscillation of the domain walls.

In the design investigated at IBM, each track stores up to 100 domains, and the experiments with permalloy nanowires show that a velocity of the order of $100\,\mathrm{m\,s^{-1}}$ is attained by the domain walls, making the operating speed of the device comparable to that of other memories. The access time is of the order of tens of nanoseconds, which compares very favorably with the HDD access time of some 5 ms.

The possibility of assembling three-dimensionally the nanowire memories is very appealing, since this may allow a much higher storage density than in two-dimensional devices, as the magnetic hard disk or semiconductor memories.

Further Reading

H.N. Bertram, *Theory of Magnetic Recording* (Cambridge University Press, 1994)

W.H. Doyle, in *Magnetic Recording Devices: Future Technologies*, ed. by K.H.J. Buschow. Concise Encyclopedia of Magnetic and Superconducting Materials, 2nd edn. (Elsevier, Amsterdam, 2005), pp. 539–548

P.P. Freitas, H. Ferreira, S. Cardoso, S. van Dijken, J. Gregg, in *Nanostructures for Spin Electronics*, ed. by D. Sellmyer, R. Skomski. Advanced Magnetic Nanostructures (Springer, New York, 2006), pp. 403–460

Y. Li, A.K. Menon, in *Magnetic Recording Technologies: Overview*, ed. by K.H.J. Buschow. Concise Encyclopedia of Magnetic and Superconducting Materials, 2nd edn. (Elsevier, Amsterdam, 2005), pp. 627–634

H. J. Richter, J. Phys. D: Appl. Phys. **40**, R149–R177 (2007)

J. Shi, in *Magnetization Reversal in Patterned Magnetic Nanostructures*, ed. by B. Heinrich, A.C. Bland. Ultrathin Magnetic Structures, vol 4 (Springer, Berlin, 2004), pp. 307–331

T. Thomson, L. Abelman, H. Groenland, in *Magnetic Storage: Past, Present and Future*, ed. by B. Azzerboni, G. Asti, L. Pareti, M. Ghidini. Magnetic Nanostructures in Modern Technology (Springer, Dordrecht, 2008), pp. 237–306

References

1. H.N. Bertram, *Theory of Magnetic Recording* (Cambridge University Press, Cambridge, 1994)
2. S. Bohlens, B. Krüger, A. Drews, M. Bolte, G. Meier, D. Pfannkuche, Appl. Phys. Lett. **93**, 142508 (2008)
3. G.W. Burr, B.N. Kurdi, J.C. Scott, C.H. Lam, K. Gopalakrishnan, R.S. Shenoy, IBM J. Res. Dev. **52**, 449–464 (2008)
4. C. Chappert, A. Fert, F. Nguyen Van Dau, Nat. Mater. **6**, 813–823 (2007)
5. P.P. Freitas, H. Ferreira, S. Cardoso, S. van Dijken, J. Gregg, in *Nanostructures for Spin Electronics*, ed. by D. Sellmyer, R. Skomski. Advanced Magnetic Nanostructures (Springer, New York, 2006), pp. 403–460
6. X.F. Han, Z.C. Wen, H.X. Wei, J. Appl. Phys. **103**, 07E933–07E939 (2008)
7. O. Karlqvist, Trans. Roy. Inst. Technol. Stockholm. **86**, 3–27 (1954)
8. S. Kawata, Y. Kawata, Chem. Rev. **100**, 1777–1788 (2000)
9. S.K. Kim, K.S. Lee, Y.S. Yu, Y.S. Choi, Appl. Phys. Lett. **92**, 022509 (2008)
10. A. Knoll, P. Bachtold, J. Bonan, G. Cherubini, M. Despont, U. Drechsler, U. Durig, B. Gotsmann, W. Haberle, C. Hagleitner, D. Jubin, M.A. Lantz, A. Pantazi, H. Pozidis, H. Rothuizen, A. Sebastian, R. Stutz, P. Vettiger, D. Wiesmann, E.S. Eleftheriou, Microelectron. Eng. **83**, 1692–1697 (2006)
11. S.S.P. Parkin, M. Hayashi, L. Thomas, Science **320**, 190–194 (2008)
12. S. Raoux, G.W. Burr, M.J. Breitwisch, C.T. Rettner, Y.-C. Chen, R.M. Shelby, M. Salinga, D. Krebs, S.-H. Chen, H.-L. Lung, C.H. Lam, IBM J. Res. Dev. **52**, 465–479 (2008)
13. H.J. Richter, J. Phys. D: Appl. Phys. **40**, R149–R177 (2007)
14. T. Thomson, L. Abelman, H. Groenland, in *Magnetic Storage: Past, Present and Future*, ed. by B. Azzerboni, G. Asti, L. Pareti, M. Ghidini. Magnetic Nanostructures in Modern Technology (Springer, Dordrecht, 2008), pp. 237–306
15. T. Yang, A. Hirohata, L. Vila, T. Kimura, Y. Otani, Phys. Rev. B **76**, 172401–172404 (2007)
16. J.-G. Zhu, Y. Zheng, G.A. Prinz, J. Appl. Phys. **87**, 6668–6673 (2000)
17. J.-G. Zhu, X. Zhu, Y. Tang, IEEE Trans. Magn. **44**, 125–131 (2008)
18. X. Zhu, J.-G. Zhu, IEEE Trans. Magn. **39**, 2854–2856 (2003)

A

Units in Magnetism

The International System of Units (Système International d'Unités) (SI) contains two types of units: base units and derived units. The seven base units are: meter, kilogram, second, ampere, kelvin, mole, and candela.

Some units relevant to magnetism have special names in the SI. They are the following, together with their expression in terms of other SI units:

Table A.1. Table of magnetic units in the SI

Unit	Symbol	Equivalence	Quantity
weber	Wb	V s	Unit of magnetic flux
henry	H	Wb A^{-1}	Unit of inductance
tesla	T	Wb m^{-2}	Unit of magnetic flux density

The unit of magnetic field strength **H** has no special name; **H** is measured in amperes per meter (A m^{-1}).

The magnetic induction or magnetic flux density **B** (or simply B-field) has the tesla (T) as the unit and is related to the magnetic field intensity **H** through the magnetic constant or vacuum magnetic permeability μ_0, that has a value of $4\pi \times 10^{-7}$ H m^{-1} in the SI.

The relations between **B** and **H** in the two systems of units are:

$$\mathbf{B} = \mu_0(\mathbf{H} + \mathbf{M}) \qquad \text{(SI)}$$

$$\mathbf{B} = \mathbf{H} + 4\pi\mathbf{M} \qquad \text{(CGS)}$$

(A.1)

In the last equation (in the centimeter-gram-second system (CGS)) **B** is measured in gauss (G) and the unit of **H** is the oersted (Oe). In the CGS system the constant 4π appears explicitly in the expression of **B**.

The magnetization **M** of a sample, defined as the total magnetic moment divided by the volume, is measured in A m^{-1}. A close concept is that of polarization **J** $= \mu_0$**M**, measured in teslas (T).

The literature of magnetism contains results both in SI and CGS units. Some useful relations for conversion of CGS into the SI are:

$$1\,\mathrm{G} = \quad 10^{-4}\,\mathrm{T}$$

$$1\,\mathrm{Oe} = \quad \tfrac{10^3}{4\pi}\,\mathrm{A\,m^{-1}} \quad \approx 80\,\mathrm{A\,m^{-1}} \tag{A.2}$$

$$1\,\mathrm{emu\,g^{-1}} = 1\,\mathrm{J\,T^{-1}kg^{-1}}$$

Note that "emu" is not the name of a unit, it designates 1 erg gauss^{-1}.

The relative magnetic permeability μ_r of a material is dimensionless, and is defined as the ratio of the permeability of the material μ to the magnetic constant (or free-space permeability) μ_0:

$$\mu_r = \frac{\mu}{\mu_0}. \tag{A.3}$$

The relative permeability of a material μ_r is measured by the same number in the SI and in the CGS. Its relation to the susceptibility $\chi = M/H$, however, is different in the two systems:

$$\mu_r = 1 + \chi \qquad (\mathrm{SI})$$
$$\mu_r = 1 + 4\pi\chi \qquad (\mathrm{CGS}) \tag{A.4}$$

The expressions differ because the values of the susceptibilities are different in the two systems:

$$\chi_{\mathrm{SI}} = 4\pi\,\chi_{\mathrm{CGS}}. \tag{A.5}$$

Further Reading

R.A. Carman, *Numbers and Units for Physics* (Wiley, New York, 1969)

J. de Boer, Metrologia **31**, 405 (1995)

P.J. Mohr, B.N. Taylor, D.B. Newell, Rev. Mod. Phys. **80**, 633–730 (2008)

NIST Special Publication 811, 2008 edition, *Guide for the Use of the International System of Units (SI)*, ed. by Ambler Thompson Technology Services, B.N. Taylor, http://physics/nist/gov

Magnetic quantities and units. To obtain the values of the quantities in SI units, the corresponding CGS values should be multiplied by the conversion factors

Quantity	Symbol	CGS	SI	Conversion factor
Magnetic induction	**B**	G	T	10^{-4}
Magnetic field intensity	**H**	Oe	$A\,m^{-1}$	$10^3/4\pi$
Magnetization	**M**	$erg\,G^{-1}\,cm^{-3}$ or $emu\,cm^{-3}$	$A\,m^{-1}$	10^3
Magnetic polarization	**J**	–	T	–
Magnetic moment	m	$erg\,G^{-1}\,(\equiv emu)$	$J\,T^{-1}\,(\equiv A\,m^2)$	10^{-3}
Specific magnetization	σ	$emu\,g^{-1}$	$A\,m^2\,kg^{-1}\,(J\,T^{-1}\,kg^{-1})$	1
Magnetic flux	ϕ	Mx (Maxwell)	Wb (Weber)	10^{-8}
Magnetic energy density	E	$erg\,cm^{-3}$	$J\,m^{-3}$	10^{-1}
Demagnetizing factor	N_d	–	–	$1/4\pi$
Susceptibility (volume)	χ	–	–	4π
Mass susceptibility	χ_g	$erg\,G^{-1}\,g^{-1}\,Oe^{-1}$ or $emu\,g^{-1}\,Oe^{-1}$	$m^3\,kg^{-1}$	$4\pi \times 10^{-3}$
Molar susceptibility	χ_{mol}	$emu\,mol^{-1}\,Oe^{-1}$	$m^3\,mol^{-1}$	$4\pi \times 10^{-6}\ m^3\,mol^{-1}$
Magnetic permeability	μ	$G\,Oe^{-1}$	$H\,m^{-1}$	$4\pi \times 10^{-7}$
Relative permeability	μ_r	–	–	1
Magnetic constant (vacuum permeability)	μ_0	$G\,Oe^{-1}$	$H\,m^{-1}$	$4\pi \times 10^{-7}$
Anisotropy constant	K	$erg\,cm^{-3}$	$J\,m^{-3}$	10^{-1}
Exchange stiffness constant	A	$erg\,cm^{-1}$	$J\,m^{-1}$	10^5
Specific domain wall energy	γ	$erg\,cm^{-2}$	$J\,m^{-2}$	10^{-3}
Gyromagnetic ratio	γ	$s^{-1}\,Oe^{-1}$	$m\,A^{-1}\,s^{-1}$	$4\pi\,10^{-3}$

B

Physical Constants

Quantity	Symbol	Value	CGS	SI
Speed of light in vacuum	c	2.997925	10^{10} cm s^{-1}	10^{8} m s^{-1}
Elementary charge	e	1.60218	4.80654×10^{-10} statC	10^{-19}C
Planck constant	h	6.62607	10^{-27} erg s	10^{-34} J s
	$\hbar = h/2\pi$	1.054572	10^{-27} erg s	10^{-34} J s
Avogadro's constant	N_A	6.02214×10^{23} mol^{-1}		
Atomic mass constant	m_u	1.66054	10^{-24} g	10^{-27} kg
Electron mass	m_e	9.10939	10^{-28} g	10^{-31} kg
Proton mass	m_p	1.67262	10^{-24} g	10^{-27} kg
Ratio of proton and electron masses	m_p/m_e	1836.153		
Electron gyromagnetic ratio	γ_e	1.760859770	10^{7} s^{-1} G^{-1}	10^{11} s^{-1} T^{-1}
Gilbert gyromagnetic ratio	$\mu_0\gamma_e$	2.2127606		10^{5} m A^{-1}s^{-1}
Electron Compton wavelength	λ_c	2.42631	10^{-10} cm	10^{-12} m
Bohr radius	a_0	0.529177	10^{-8} cm	10^{-10} m
Bohr magneton	μ_B	9.2740154	10^{-21} erg G^{-1}	10^{-24} JT^{-1}
Nuclear magneton	μ_N	5.0507866	10^{-24} erg G^{-1}	10^{-27} JT^{-1}
Electronvolt	eV	1.60218	10^{-12} erg	10^{-19} J
Boltzmann constant	k	1.380658	10^{-16} erg K^{-1}	10^{-23} JK^{-1}
Reciprocal of fine structure constant	$1/\alpha$	137.036		
Rydberg constant	$R_\infty hc$	2.179874	10^{-11} erg	10^{-18} J
Molar gas constant	R	8.31451	10^{7} erg mol^{-1} K^{-1}	J mol^{-1} K^{-1}
Vacuum permittivity	ε_0	–	1	$10^{7}/4\pi c^2$
Magnetic constant (vacuum permeability)	μ_0		1	$4\pi \times 10^{-7}$ Hm^{-1}

Materials

Symbols

References

Preface

1. A.P. Guimarães, *From Lodestone to Supermagnets: Understanding Magnetic Phenomena* (Wiley, Berlin, 2005)
2. J.A.C. Bland, B. Heinrich (eds.), *Ultrathin Magnetic Structures*, vols I–IV (Springer, Berlin, 2005)

Chapter 1

1. S. Odenbach, in *Ferrofluids*, ed. by K.H.J. Buschow. Handbook of Magnetic Materials, vol 16 (Elsevier, Amsterdam, 2006), pp. 127–208
2. C. Alexiou, R. Jurgons, in *Magnetic Drug Targeting*, ed. by W. Andrä, H. Nowak. Magnetism in Medicine: A Handbook, 2nd edn. (Wiley, Weinheim, 2007), pp. 596–605
3. R. Hergt, W. Andrä, in *Magnetic Hyperthermia and Thermoablation*, ed. by W. Andrä, H. Nowak. Magnetism in Medicine: A Handbook, 2nd edn. (Wiley, Weinheim, 2007), pp. 550–570
4. M.E. Evans, F. Heller, *Environmental Magnetism* (Academic Press, San Diego, 2003)
5. R. Wiltschko, W. Wiltschko, *Magnetic Orientation in Animals* (Springer, Berlin, 1995)
6. G. Fleissner, B. Stahl, P. Thalau, G. Falkenberg, G. Fleissner, Naturwissenschaften **94**, 631–642 (2007)
7. D. Weller, T. McDaniel, in *Media for Extremely High Density Recording*, ed. by D. Sellmyer, R. Skomski. Advanced Magnetic Nanostructures (Springer, New York, 2006), pp. 295–324
8. R.F. Freitas, W.W. Wilcke, IBM J. Res. Dev. **52**, 439–447 (2008)
9. P.P. Freitas, H. Ferreira, S. Cardoso, S. van Dijken, J. Gregg, in *Nanostructures for Spin Electronics*, ed. by D. Sellmyer, R. Skomski. Advanced Magnetic Nanostructures (Springer, New York, 2006), pp. 403–460
10. J. Jorzick, C. Kramer, S.O. Demokritov, B. Hillebrands, B. Bartenlian, C. Chappert, D. Decanini, F. Rousseaux, E. Cambril, E. Sondergard, M. Bailleul, C. Fermon, A.N. Slavin, J. Appl. Phys. **89**, 7091–7095 (2001)
11. V.E. Borisenko, S. Ossicini, *What is What in the Nanoworld* (Wiley, Weinheim, 2004)
12. S. Ohnishi, A.J. Freeman, M. Weinert, Phys. Rev. B **28**, 6741–6748 (1983)

13. R. Wu, A.J. Freeman, Phys. Rev. Lett. **69**, 2867–2870 (1992)
14. C.A.F. Vaz, J.A.C. Bland, G. Lauhoff, Rep. Prog. Phys. **71**, 056501–056578 (2008)
15. S.N. Song, J. Ketterson, in *Ultrathin Films and Superlattices*, ed. by R.W. Cahn, P. Haasen, E.J. Kramer. Electronic and Magnetic Properties of Metals and Ceramics, vol 3A (Wiley, New York, 1991)
16. O. Fruchart, A. Thiaville, Compt. Rend. Phys. **6**, 921–933 (2005)
17. M.J. Prandolini, Rep. Prog. Phys. **69**, 1235–1324 (2006)
18. K.H.J. Buschow (ed.), *Concise Encyclopedia of Magnetic and Superconducting Materials*, 2nd edn. (Elsevier, Amsterdam, 2005)
19. I. Mertig, in *Thin Film Magnetism: Band Calculations*, ed. by K.H.J. Buschow. Concise Encyclopedia of Magnetic and Superconducting Materials, 2nd edn. (Elsevier, Amsterdam, 2005)
20. M. Hosokawa, K. Nogi, M. Naito, T. Yokoyama, *Nanoparticle Technology Handbook* (Elsevier, Amsterdam, 2007)
21. M. Le Bellac, *Quantum and Statistical Field Theory* (Oxford University Press, Oxford, 1991)
22. Y. Li, K. Baberschke, Phys. Rev. Lett. **68**, 1208–1211 (1992)
23. F. Huang, M.T. Kief, G.J. Mankey, R.F. Willis, Phys. Rev. B **49**, 3962–3971 (1994)
24. K. Chen, A.M. Ferrenberg, D.P. Landau, Phys. Rev. B **48**, 3249–3256 (1993)
25. L. He, C. Chen, N. Wang, W. Zhou, L. Guo, J. Appl. Phys. **102**, 103911–103914 (2007)
26. S.D. Bader, Rev. Mod. Phys. **78**, 1–15 (2006)
27. X. Batlle, A. Labarta, J. Phys. D: Appl. Phys. **35**, R15–R42 (2002)
28. J.A.C. Bland, B. Heinrich, *Ultrathin Magnetic Structures* (Springer, Berlin, 2005)
29. J.F. Bobo, L. Gabillet, M. Bibes, J. Phys. Condens. Matter. **16**, S471–S496 (2004)
30. C. Chappert, A. Barthelémy, in *Nanomagnetism and Spin Electronics*, ed. by C. Dupas, P. Houdy, M. Lahmany. Nanoscience (Springer, Berlin, 2007), pp. 503–582
31. C.L. Dennis, R.P. Borges, L.D. Buda, U. Ebels, J.F. Gregg, M. Hehn, E. Jouguelet, K. Ounadjela, I. Petej, I.L. Prejbeanu, M.J. Thornton, J. Phys. Condens. Matter. **14**, R1175–R1262 (2002)
32. A. Enders, P. Gambardella, K. Kern, in *Magnetism of Low-Dimensional Metallic Structures*, ed. by H. Kronmüller, S. Parkin. Handbook of Magnetism and Advanced Magnetic Materials, vol 1 (Wiley, Chichester, 2007), pp. 577–639
33. M.R. Fitzsimmons, S.D. Bader, J.A. Borchers, G.P. Felcher, J.K. Furdyna, A. Hoffmann, J.B. Kortright, I.K. Schuller, T.C. Schulthess, S.K. Sinha, M.F. Toney, D. Weller, S. Wolf, J. Magn. Magn. Mat. **271**, 103–146 (2004)
34. C.P. Poole Jr., F.J. Owens, *Introduction to Nanotechnology* (Wiley, Hoboken, 2003)
35. R. Skomski, J. Phys. Condens. Matter. **15**, R841–R896 (2003)

Chapter 2

1. H. Kronmüller, in *General Micromagnetic Theory*, ed. by H. Kronmüller, S. Parkin. Handbook of Magnetism and Advanced Magnetic Materials, vol 2 (Wiley, Chichester, 2007), pp. 703–741
2. Landolt-Börnstein, *Tables of Magnetic Properties of 3d Elements*, New Series, vol 3 (Springer, Berlin, 1986)
3. K.H.J. Buschow, F.R. de Boer, *Physics of Magnetism and Magnetic Materials* (Kluwer, New York, 2003)
4. C. Kittel, Rev. Mod. Phys. **21**, 541–583 (1949)

5. J.A. Osborn, Phys. Rev. **67**, 351–357 (1945)
6. A. Hubert, R. Schäfer, *Magnetic Domains. The Analysis of Magnetic Microstructures* (Springer, Berlin, 1999)
7. L. Néel, J. Phys. Rad. **15**, 225–239 (1954)
8. A.P. Guimarães, *Magnetism and Magnetic Resonance in Solids* (Wiley, New York, 1998)
9. L.D. Landau, E. Lifshitz, Phys. Z. Sowjetunion **8**, 153–169 (1935)
10. W.F. Brown, Phys. Rev. **58**, 736–743 (1940)
11. W.F. Brown, Phys. Rev. **60**, 139–147 (1941)
12. W.F. Brown Jr., *Magnetostatic Principles in Ferromagnetism* (North-Holland, Amsterdam, 1962)
13. A. Aharoni, *Introduction to the Theory of Ferromagnetism*, 2 edn. (Oxford University Press, Oxford, 2000)
14. C.A.F. Vaz, J.A.C. Bland, G. Lauhoff, Rep. Prog. Phys. **71**, 056501–056578 (2008)
15. P.J. Mohr, B.N. Taylor, D.B. Newell, Rev. Mod. Phys. **80**, 633–730 (2008)
16. O. Fruchart, A. Thiaville, Compt. Rend. Phys. **6**, 921–933 (2005)
17. A.P. Malozemoff, J.C. Slonczewski, *Magnetic Domain Walls in Bubble Materials* (Academic Press, New York, 1979)
18. H. Kronmüller, M. Fähnle, *Micromagnetism and the Microstructure of Ferromagnetic Solids* (Cambridge University Press, Cambridge, 2003)
19. D. Goll, A.E. Berkowitz, H.N. Bertram, Phys. Rev. B **70**, 184432 (2004)
20. G.S.D. Beach, C. Nistor, C. Knutson, M. Tsoi, J.L. Erskine, Nat. Mater. **4**, 741–744 (2005)
21. Y. Nakatani, A. Thiaville, J. Miltat, Nat. Mater. **2**, 521–523 (2003)
22. E. Lewis, D. Petit, A.V. Jausovec, H.T. Zeng, D.E. Read, L.A. O'Brien, J. Sampaio, R.P. Cowburn (2009 to be published)
23. G. Herzer, J. Magn. Magn. Mater. **294**, 99–106 (2005)
24. Y. Yoshizawa, S. Oguma, K. Yamauchi, J. Appl. Phys. **64**, 6044–6046 (1988)
25. G. Bertotti, *Hysteresis in Magnetism* (Academic Press, San Diego, 1998)
26. R.C. O'Handley, *Modern Magnetic Materials* (Wiley, New York, 2000)
27. R. Skomski, J.M.D. Coey, *Permanent Magnetism* (Institute of Physics Publishing, Bristol, 1999)
28. R. Skomski, J. Zhou, in *Nanomagnetic Models*, ed. by D. Sellmyer, R. Skomski. Advanced Magnetic Nanostructures (Springer, New York, 2006), pp. 41–90

Chapter 3

1. N. Pinna, S. Grancharov, P. Beato, P. Bonville, M. Antonietti, M. Niederberger, Chem. Mater. **17**, 3044–3049 (2005)
2. O. Iglesias, A. Labarta, Phys. Rev. B **63**, 184416 (2001)
3. C.L. Dennis, R.P. Borges, L.D. Buda, U. Ebels, J.F. Gregg, M. Hehn, E. Jouguelet, K. Ounadjela, I. Petej, I.L. Prejbeanu, M.J. Thornton, J. Phys. Condens. Matter **14**, R1175–R1262 (2002)
4. F.E. Luborsky, J. Appl. Phys. **32**, 171S–183S (1961)
5. A. Aharoni, *Introduction to the Theory of Ferromagnetism*, 2nd edn. (Oxford University Press, Oxford, 2000)
6. G. Bertotti, *Hysteresis in Magnetism* (Academic Press, San Diego, 1998)
7. W.F. Brown Jr., J. Appl. Phys. **39**, 993–994 (1968)
8. W.F. Brown Jr., Ann. N.Y. Acad. Sci. **147**, 463–488 (1969)

9. A. Kákay, L.K. Varga, J. Appl. Phys. **97**, 083901–083904 (2005)

10. J.L. Dormann, D. Fiorani, E. Tronc, Adv. Chem. Phys. **98**, 283–494 (1997)

11. G.F. Goya, T.S. Berquó, F.C. Fonseca, M.P. Moralesm, J. Appl. Phys. **94**, 3520–3528 (2003)

12. A. Labarta, O. Iglesias, L. Balcells, F. Badia, Phys. Rev. B **48**, 10240–10246 (1993)

13. W. Wernsdorfer, E.B. Orozco, B. Barbara, K. Hasselbach, A. Benoit, D. Mailly, B. Doudin, J. Meier, J.E. Wegrowe, J.P. Ansermet, N. Demoncy, H. Pascard, N. Demoncy, A. Loiseau, L. François, N. Duxin, M.P. Pileni, J. Appl. Phys. **81**, 5543–5545 (1997)

14. D. Givord, M.F. Rossignol, in *Coercivity*, ed. by J.M.D. Coey. Rare-Earth Iron Permanent Magnets (Clarendon Press, Oxford, 1996)

15. N.T. Gorham, R.C. Woodward, T.G.St. Pierre, B.D. Terris, S. Sun, J. Magn. Magn. Mater. **295**, 174–176 (2005)

16. A.P. Guimarães, *Magnetism and Magnetic Resonance in Solids* (Wiley, New York, 1998)

17. J.K. Vassiliou, V. Mehrotra, M.W. Russell, E.P. Giannelis, R.D. McMichael, R.D. Shull, R.F. Ziolo, J. Appl. Phys. **73**, 5109–5116 (1993)

18. X. Batlle, A. Labarta, J. Phys. D: Appl. Phys. **35**, R15–R42 (2002)

19. F. Bødker, S. Mørup, S. Linderoth, Phys. Rev. Lett. **72**, 282–285 (1994)

20. B.R. Pujada, E.H.C.P. Sinnecker, A.M. Rossi, C.A. Ramos, A.P. Guimarães, Phys. Rev. B **67**, 024402–024406 (2003)

21. S.A. Majetich, Y. Jin, Science **284**, 470–473 (1999)

22. R.H. Kodama, A.E. Berkowitz, Phys. Rev. B **59**, 6321–6336 (1999)

23. J. Nogués, J. Sort, V. Langlais, V. Skumryev, S. Suriñach, J.S. Muñoz, M.D. Baró, Phys. Repts. **422**, 65–117 (2005)

24. S. Gangopadhyay, G.C. Hadjipanayis, B. Dale, C.M. Sorensen, K.J. Klabunde, V. Papaefthymiou, A. Kostikas, Phys. Rev. B **45**, 9778–9787 (1992)

25. O. Iglesias, A. Labarta, X. Batlle, J. Phys.: Condens. Matter **19**, 406232–406237 (2007)

26. E.C. Stoner, E.P. Wohlfarth, Phil. Trans. Roy. Soc. A **240**, 599–642 (1948). Reprinted in IEEE Trans. Magn. **27**, 3475–3518 (1991)

27. I.S. Jacobs, C.P. Bean, in *Fine Particles, Thin Films and Exchange Anisotropy (Effects of Finite Dimensions and Interfaces on the Basic Properties of Ferromagnets)*, ed. by G.T. Rado, H. Suhl. Magnetism, vol III (Academic Press, New York, 1963), p. 271–350

28. E. Kondorsky, J. Phys. Moscow **2**, 161 (1940)

29. H. Kronmüller, K.-D. Durst, G. Martinek, J. Magn. Magn. Mater. **69**, 149–157 (1987)

30. C. Thirion, W. Wernsdorfer, M. Jamet, V. Dupuis, P. Mélinon, A. Pérez, D. Mailly, J. Magn. Magn. Mater. **242–245**, 993–995 (2002)

31. Z.Z. Sun, X.R. Wang, Phys. Rev. Lett. **97**, 077205-1–077205-4 (2006)

32. C. Tannous, J. Gieraltowski, Eur. J. Phys. **29**, 475–487 (2008)

33. R. Skomski, J. Zhou, in *Nanomagnetic Models*, ed. by D. Sellmyer, R. Skomski. Advanced Magnetic Nanostructures (Springer, New York, 2006), pp. 41–90

34. R.W. Chantrell, K. O'Grady, in *The Magnetic Properties of Fine Particles*, ed. by R. Gerber, C.C. Wright, G. Asti. Applied Magnetism (Kluwer, Dordrecht, 1994), pp. 113–164

35. A. Thiaville, Phys. Rev. B **61**, 12221–12232 (2000)

36. R. Skomski, J.M.D. Coey, *Permanent Magnetism* (Institute of Physics Publishing, Bristol, 1999)

37. E.H. Frei, S. Shtrikman, D. Treves, Phys. Rev. **106**, 446–455 (1957)

38. A. Aharoni, J. Appl. Phys. **82**, 1281–1287 (1997)

39. R. Kikuchi, J. Appl. Phys. **27**, 1352–1357 (1956)

40. J.G. Zhu, in *Magnetization Reversal Dynamics*, ed. by K.H.J. Buschow. Concise Encyclopedia of Magnetic and Superconducting Materials, 2nd edn. (Elsevier, Amsterdam, 2005), pp. 754–760
41. M. Bauer, J. Fassbender, B. Hillebrands, R.L. Stamps, Phys. Rev. B **61**, 3410–3416 (2000)
42. Q.F. Xiao, B.C. Choi, J. Rudge, Y.K. Hong, G. Donohoe, J. Appl. Phys. **101**, 24306 (2007)
43. J.-G. Zhu, X. Zhu, Y. Tang, IEEE Trans. Magn. **44**, 125–131 (2008)
44. J.C. Slonczewski, J. Magn. Magn. Mater. **159**, L1–L7 (1996)
45. L. Berger, Phys. Rev. B **54**, 9353–9358 (1996)
46. X.R. Wang, Z.Z. Sun, Phys. Rev. Lett. **98**, 077201–077204 (2007)
47. Z. Li, S. Zhang, Phys. Rev. B **68**, 024404–024410 (2003)
48. W. Weber, S. Riesen, H.C. Siegmann, Science **291**, 1015–1018 (2001)
49. S. Thamm, J. Hesse, J. Magn. Magn. Mater. **154**, 254–262 (1996)
50. S. Thamm, J. Hesse, J. Magn. Magn. Mater. **184**, 245–255 (1998)
51. Z.V. Golubenko, A.Z. Kamzin, L.P. Ol'khovik, M.M. Khvorov, Z.I. Sizova, V.P. Shabatin, Phys. Solid. State **44**, 1698–1702 (2002)
52. E.P. Wohlfarth, J. Appl. Phys. **29**, 595–596 (1958)
53. O. Henkel, Phys. Stat. Solidi. **7**, 919–929 (1964)
54. P.E. Kelly, K. O'Grady, P.I. Mayo, R.W. Chantrell, IEEE Trans. Magn. **25**, 3881–3883 (1989)
55. J. García-Otero, M. Porto, J. Rivas, J. Appl. Phys. **87**, 7376–7381 (2000)
56. P. Allia, M. Coisson, P. Tiberto, F. Vinai, M. Knobel, M.A. Novak, W.C. Nunes, Phys. Rev. B **64**, 14420 (2001)
57. S. Shtrikman, E.P. Wohlfarth, Phys. Lett. A **85**, 467 (1981)
58. J.L. Dormann, R. Cherkaoui, L. Spinu, M. Nogués, L. Lucari, F. D'Orazio, D. Fiorani, A. Garcia, E. Tronc, J.P. Olivet, J. Magn. Magn. Mater. **187**, L139–L144 (1998)
59. M. El-Hilo, R.W. Chantrell, K. O'Grady, J. Appl. Phys. **84**, 5114–5122 (1998)
60. D. Kechrakos, K.N. Trohidou, J. Magn. Magn. Mater. **177**, 943–944 (1998)
61. B.D. Cullity, *Introduction to Magnetic Materials* (Addison-Wesley, Reading, 1972)
62. A.B. Denison, L.J. Hope-Weeks, R.W. Meulenberg, in *Quantum Dots*, ed. by M. di Ventra, S. Evoy, J.R. Heflein. Introduction to Nanoscale Science and Technology (Springer, New York, 2004), p. 183
63. D. Fiorani (ed.), *Surface Effects in Magnetic Nanoparticles* (Springer, New York, 2005)
64. S. Mørup, M.F. Hansen, in *Superparamagnetic Particles*, ed. by H. Kronmüller, S. Parkin. Handbook of Magnetism and Advanced Magnetic Materials, vol 4 (Wiley, Chichester, 2007), pp. 2159–2176
65. J. Stöhr, H.C. Siegmann, *Magnetism From Fundamentals to Nanoscale Dynamics* (Springer, Berlin, 2006)
66. W. Wernsdorfer, in *Molecular Nanomagnets*, ed. by D. Sellmyer, R. Skomski. Advanced Magnetic Nanostructures (Springer, New York, 2005), pp. 147–181
67. E.P. Wohlfarth, in *Fine Particle Magnetism*, ed. by L. Falicov, J. Moran-Lopez. Magnetic Properties of Low-Dimensional Systems (Springer, Berlin, 1986)

Chapter 4

1. S.N. Piramanayagam, J. Appl. Phys. **102**, 011301 (2007)
2. G. Cao, *Nanostructures and Nanomaterials* (Imperial College Press, London, 2004)

3. H. Kronmüller, S. Parkin (eds.), *Handbook of Magnetism and Advanced Magnetic Materials* (Wiley, Chichester, 2007)

4. F.J. Himpsel, J.E. Ortega, G.J. Mankey, R.F. Willis, Adv. Phys. **47**, 511–597 (1998)

5. H.L. Davis, J.B. Hannon, K.B. Ray, E.W. Plummer, Phys. Rev. Lett. **68**, 2632–2635 (1992)

6. R.C. O'Handley, *Modern Magnetic Materials* (Wiley, New York, 2000)

7. J. Tersoff, L. Falikov, Phys. Rev. B **26**, 6186–6200 (1982)

8. U. Gradmann, in *Magnetism in Ultrathin Transition Metal Films*, ed. by K.H.J. Buschow. Handbook of Magnetic Materials, vol 7 (North Holland, Amsterdam, 1993), pp. 1–96

9. J. Fassbender, D. Ravelosona, Y. Samson, J. Phys. D: Appl. Phys. **37**, R179–R196 (2004)

10. R.P. Cowburn, M.E. Welland, Science **287**, 1466–1468 (2000)

11. D. Hrabovsky, D. Ciprian, J. Jaworowicz, M. Gmitra, D. Horvarth, I. Vavra, A.R. Fert, J. Pistora, Trans. Magn. Soc. Jpn. **2**, 240–243 (2002)

12. D.A. Allwood, G. Xiong, C.C. Faulkner, D. Atkinson, D. Petit, R.P. Cowburn, Science **309**, 1688–1692 (2005)

13. A. Imre, G. Csaba, L. Ji, A. Orlov, G.H. Bernstein, W. Porod, Science **311**, 205–208 (2006)

14. R.P. Cowburn, Science **311**, 183–184 (2006)

15. L. Néel, J. Phys. Rad. **15**, 225–239 (1954)

16. B.N. Engel, C.D. England, R.A. Van Leeuwen, M.H. Wiedmann, C.M. Falco, Phys. Rev. Lett. **67**, 1910–1913 (1991)

17. P. Grünberg, J. Magn. Magn. Mater. **226**, 1688–1693 (2001)

18. S. Middelhoek, J. Appl. Phys. **34**, 1054–1059 (1963)

19. I. Ruiz-Feal, T.A. Moore, L. Lopez-Diaz, J.A.C. Bland, Phys. Rev. B **65**, 054409 (2002)

20. R.P. Cowburn, J. Ferré, S.J. Gray, J.A.C. Bland, Phys. Rev. B **58**, 507 (1998)

21. R. Kikuchi, J. Appl. Phys. **27**, 1352–1357 (1956)

22. C.H. Back, R. Allenspach, W. Weber, S.S.P. Parkin, D. Weller, E.L. Garwin, H.C. Siegmann, Science **285**, 864–867 (1999)

23. J. Nogués, I.K. Schuller, J. Magn. Magn. Mater. **192**, 203–232 (1999)

24. W.H. Meiklejohn, C.P. Bean, Phys. Rev. **102**, 1413–1414 (1956)

25. M.J. Prandolini, Rep. Prog. Phys. **69**, 1235–1324 (2006)

26. W.H. Meiklejohn, J. Appl. Phys. **33**, 1328–1335 (1962)

27. M. Takahashi, A. Yanai, S. Taguchi, T. Suzuki, Jpn. J. Appl. Phys. **19**, 1093–1106 (1980)

28. C. Binek, A. Hochstrat, W. Kleemann, J. Magn. Magn. Mater. **234**, 353–358 (2001)

29. M. Kiwi, J. Magn. Magn. Mater. **234**, 584–595 (2001)

30. R.L. Stamps, J. Phys. D: Appl. Phys. **33**(23), R247–R268 (2000)

31. R.L. Stamps, J. Phys. D: Appl. Phys. **34**(3), 444 (2001)

32. N.C. Koon, Phys. Rev. Lett. **78**, 4865–4868 (1997)

33. A.P. Malozemoff, Phys. Rev. B **35**, 3679–3682 (1987)

34. D. Mauri, H.C. Siegmann, P.S. Bagus, E. Kay, J. Appl. Phys. **62**, 3047–3049 (1987)

35. C. Leighton, J. Nogués, B.J. Jönsson-Åkerman, I.K. Schuller, Phys. Rev. Lett. **84**, 3466–3469 (2000)

36. M.D. Stiles, J. Magn. Magn. Mater. **200**, 322–337 (1999)

37. D.H. Mosca, F. Petroff, A. Fert, P.A. Schroeder Jr., W.P. Pratt, R. Laloee, J. Magn. Magn. Mater. **94**, L1–L5 (1991)

38. J. Unguris, R.J. Celotta, D.T. Pierce, Phys. Rev. Lett. **67**, 140–143 (1991)

39. D.E. Burgler, S.O. Demokritov, P. Grünberg, M.T. Johnson, in *Interlayer Exchange Coupling in Layered Magnetic Structures*, ed. by K.J.H. Buschow. Handbook of Magnetic Materials, vol 13 (Elsevier, Amsterdam, 2001), p. 1

40. B. Heinrich, J.F. Cochran, in *Magnetic Ultrathin Films*, ed. by H. Kronmüller, S. Parkin. Handbook of Magnetism and Advanced Magnetic Materials, vol 4 (Wiley, Chichester, 2007), pp. 2285–2305
41. A. Imre, G. Csaba, L. Ji, A. Orlov, G.H. Bernstein, W. Porod, Science **311**, 205–208 (2006)
42. J.C. Lodder, in *Patterned Nanomagnetic Films*, ed. by D. Sellmyer, R. Skomski. Advanced Magnetic Nanostructures (Springer, New York, 2005), pp. 295–324
43. J. Nogués, J. Sort, V. Langlais, V. Skumryev, S. Suriñach, J.S. Muñoz, M.D. Baró, Phys. Repts. **422**, 65–117 (2005)
44. J. Slonczewski, in *Theory of Spin-Polarized Current and Spin-Transfer Torque in Magnetic Multilayers*, ed. by H. Kronmüller, S. Parkin. Handbook of Magnetism and Advanced Magnetic Materials, vol 5 (Wiley, Chichester, 2007), pp. 2648–2667
45. M.D. Stiles, in *Interlayer Exchange Coupling*, ed. by B. Heinrich, J.A.C. Bland. Ultrathin Magnetic Structures III (Springer, Berlin, 2004), pp. 99–137
46. C.A.F. Vaz, J.A.C. Bland, G. Lauhoff, Rep. Prog. Phys. **71**, 056501–056578 (2008)
47. M. Wuttig, X. Liu, *Ultrathin Metal Films* (Springer, Berlin, 2004)

Chapter 5

1. C.L. Dennis, R.P. Borges, L.D. Buda, U. Ebels, J.F. Gregg, M. Hehn, E. Jouguelet, K. Ounadjela, I. Petej, I.L. Prejbeanu, M.J. Thornton, J. Phys. Condens. Matter **14**, R1175–R1262 (2002)
2. J. Bass, W.P. Pratt Jr., J. Phys.: Condens. Matter **19**, 183201–183241 (2007)
3. E.L. Wolf, *Nanophysics and Nanotechnology* (Wiley, Weinheim, 2006)
4. J.S. Moodera, T.S. Santos, T. Nagahama, J. Phys.: Condens. Matter **19**(16), 165202 (2007)
5. M. Johnson, R.H. Silsbee, Phys. Rev. B **37**, 5312–5325 (1988)
6. N.F. Mott, Proc. Roy. Soc. Lond. Ser. A **153**, 699–717 (1936)
7. N.F. Mott, Proc. Roy. Soc. Lond. Ser. A **156**, 368–382 (1936)
8. N.F. Mott, Adv. Phys. **13**, 325–422 (1964)
9. I.A. Campbell, A. Fert, in *Transport Properties of Ferromagnets*, ed. by E.P. Wohlfarth. Handbook of Magnetic Materials, vol 3 (North-Holland, Amsterdam, 1982), pp. 747–804
10. M. Baibich, J.M. Broto, A. Fert, V.D. Nguyen, F. Petroff, P. Etienne, G. Creuzet, A. Friederich, J. Chazelas, Phys. Rev. Lett. **61**, 2472–2475 (1988)
11. J. Bass, W.P. Pratt Jr., J. Magn. Magn. Mater. **200**, 274–289 (1999)
12. M.R.J. Gibbs, E.W. Hill, P. Wright, in *Magnetic Microelectromechanical Systems:MagMEMS*, ed. by K.H.J. Buschow. Handbook of Magnetic Materials (Elsevier, Amsterdam, 2008), pp. 457–526
13. H. Yanagihara, K. Pettit, M.B. Salamon, S.S.P. Parkin, E. Kita, J. Appl. Phys. **81**, 5197–5199 (1997)
14. M.E. Brubaker, J.E. Mattson, C.H. Sowers, S.D. Bader, Appl. Phys. Lett. **58**, 2306–2308 (1991)
15. K. Shintaku, Y. Daitoh, T. Shinjo, Phys. Rev. B **47**, 14584–14587 (1993)
16. S.S.P. Parkin, N. More, K.P. Roche, Phys. Rev. Lett. **64**, 2304–2307 (1990)
17. Q.Y. Jin, M. Lu, Q.S. Bie, Y.B. Xu, H.R. Zhai, Y.H. Shen, J. Magn. Magn. Mater. **140–144**, 565–566 (1995)
18. T. Matsudai, H. Sato, W. Abdul-Razzaq, C. Fierz, P.A. Schroeder, J. Phys. Condens. Matter **6**, 6151–6162 (1994)

19. S.S.P. Parkin, R.F.C. Farrow, R.F. Marks, A. Cebollada, G.R. Harp, R.J. Savoy, Phys. Rev. Lett. **72**, 3718–3721 (1994)
20. B. Rodmacq, G. Palumbo, P. Gerard, J. Magn. Magn. Mater. **118**, L11–L16 (1993)
21. R. Nakatani, T. Dei, Y. Sugita, J. Appl. Phys. **73**, 6375–6377 (1993)
22. S. Araki, J. Appl. Phys. **73**, 3910–3916 (1993)
23. S.S.P. Parkin, R. Bhadra, K.P. Roche, Phys. Rev. Lett. **66**, 2152–2155 (1991)
24. R. Schad, C.D. Potter, P. Belien, G. Verbanck, J. Dekoster, G. Langouche, V.V. Moshchalkov, Y. Bruynseraede, J. Magn. Magn. Mater. **148**, 331–332 (1995)
25. M.A.M. Gijs, in *Experiments on the Perpendicular Giant Magnetoresistance in Magnetic Multilayers*, ed. by U. Hartmann. Magnetic Multilayers and Giant Magnetoresistance (Springer, Berlin, 2000), pp. 129–177
26. T. Valet, A. Fert, Phys. Rev. B **48**, 7099–7113 (1993)
27. J.S. Moodera, L.R. Kinder, T.M. Wong, R. Meservey, Phys. Rev. Lett. **74**, 3273–3276 (1995)
28. I. Zutic, J. Fabian, S.D. Sarma, Rev. Mod. Phys. **76**, 323–410 (2004)
29. M. Jullière, Phys. Lett. A **54**, 225–226 (1975)
30. P. Grünberg, D.E. Burgler, H. Dassow, A.D. Rata, C.M. Schneider, Acta Mater. **55**, 1171–1182 (2007)
31. M.B. Stearns, J. Magn. Magn. Mater. **5**, 167–171 (1977)
32. E.Y. Tsymbal, N. Mryasov, P.R. LeClair, J. Phys. Condens. Matter **15**, R109–R142 (2003)
33. S.A. Wolf, D.D. Awschalom, R.A. Buhrman, J.M. Daughton, S. von Molnar, M.L. Roukes, A.Y. Chtchelkanova, D.M. Treger, Science **294**, 1488–1495 (2001)
34. J.C. Slonczewski, Phys. Rev. B **39**, 6995–7002 (1989)
35. B.G. Park, J. Wunderlich, D.A. Williams, S.J. Joo, K.Y. Jung, K.H. Shin, K. Olejnik, A.B. Shick, T. Jungwirth, Phys. Rev. Lett. **100**, 087204–087207 (2008)
36. K. Hathaway, E. Dan Dahlberg, Am. J. Phys. **75**, 871–880 (2007)
37. J. Slonczewski, in *Theory of Spin-Polarized Current and Spin-Transfer Torque in Magnetic Multilayers*, ed. by H. Kronmüller, S. Parkin. Handbook of Magnetism and Advanced Magnetic Materials, vol 5 (Wiley, Chichester, 2007), pp. 2648–2667
38. S.A. Wolf, A.Y. Chtchekalnova, D.M. Treger, IBM J. Res. Dev. **50**, 101–110 (2006)

Chapter 6

1. C.L. Chien, F.Q. Zhu, J.-G. Zhu, Phys. Today **60**, 40–45 (2007)
2. W. Scholz, K.Y. Guslienko, V. Novosad, D. Suess, T. Schrefl, R.W. Chantrell, J. Fidler. J. Magn. Magn. Mater. 155–163 (2003)
3. V.P. Kravchuk, D.D. Sheka, Y.B. Gaididei, J. Magn. Magn. Mater. **310**, 116–125 (2007)
4. K. Nakamura, T. Ito, A.J. Freeman, Phys. Rev. B **68**, 180404–180408 (2003)
5. A. Hubert, R. Schäfer, *Magnetic Domains. The Analysis of Magnetic Microstructures* (Springer, Berlin, 1999)
6. N.A. Usov, S.E. Peschany, Phys. Met. Metall. **12**, 13–24 (1994)
7. R. Höllinger, A. Killinger, U. Krey, J. Magn. Magn. Mater. **261**, 178–189 (2003)
8. A.S. Arrott, in *Introduction to Micromagnetics*, ed. by B. Heinrich, J.A.C. Bland. Ultrathin Magnetic Structures IV (Springer, Berlin, 2005), pp. 101–148
9. L.D. Barron, in *Chirality at the Sub-Molecular Level: True and False Chirality*, ed. by W.J. Lough, I.W. Wainer. Chirality in Natural and Applied Science (Blackwell, Victoria, 2002), pp. 53–86

10. K. Shigeto, T. Okuno, K. Mibu, T. Shinjo, T. Ono, Appl. Phys. Lett. **80**, 4190–4192 (2002)
11. N.D. Mermin, Rev. Mod. Phys. **51**, 591–648 (1979)
12. S.-B. Choe, Y. Acremann, A. Scholl, A. Bauer, A. Doran, J. Stohr, H.A. Padmore, Science **304**, 420–422 (2004)
13. H. Wang, C.E. Campbell, Phys. Rev. B **76**, 220407 (2007)
14. B. Van Waeyenberge, A. Puzic1, H. Stoll, K.W. Chou, T. Tyliszczak, R. Hertel, M. Fähnle, H. Brückl, K. Rott, G. Reiss, I. Neudecker, D. Weiss, C.H. Back, G. Schütz1, Nature **444**, 461–464 (2006)
15. K. Yamada, S. Kasai, Y. Nakatani, K. Kobayashi, H. Ono, A. Thiaville, T. Ono, Nat. Mater. **6**, 269–273 (2007)
16. L. Berger, Phys. Rev. B **54**, 9353–9358 (1996)
17. J.C. Slonczewski, J. Magn. Magn. Mater. **159**, L1–L7 (1996)
18. N.L. Schryer, L.R. Walker, J. Appl. Phys. **45**, 5406–5420 (1974)
19. K.Y. Guslienko, K.-S. Lee, S.-K. Kim, Phys. Rev. Lett. **100**, 027203–027204 (2008)
20. O.A. Tretiakov, O. Tchernyshyov, Phys. Rev. B **75**, 012408–012409 (2007)
21. K.S. Buchanan, P.E. Roy, M. Grimsditch, F.Y. Fradin, K.Y. Guslienko, S.D. Bader, V. Novosad, Nat. Phys. **1**, 172–176 (2005)
22. C.A.F. Vaz, T.J. Hayward, J. Llandro, F. Schackert, D. Morecroft, J.A.C. Bland, M. Kläui, M. Laufenberg, D. Backes, U. Rüdiger, F.J. Castaño, C.A. Ross, L.J. Heyderman, F. Nolting, A. Locatelli, G. Faini, S. Cherifi, W. Wernsdorfer, J. Phys. Condens. Matter **19**, 255207–255214 (2007)
23. J.-G. Zhu, Y. Zheng, G.A. Prinz, J. Appl. Phys. **87**, 6668–6673 (2000)
24. M.M. Miller, G.A. Prinz, S.-F. Cheng, S. Bounnak, Appl. Phys. Lett. **81**, 2211–2213 (2002)
25. F.J. Castaño, C.A. Ross, A. Eilez, W. Jung, C. Frandsen, Phys. Rev. B **69**, 144421 (2004)
26. Y.G. Yoo, M. Kläui, C.A.F. Vaz, L.J. Heyderman, J.A.C. Bland, Appl. Phys. Lett. **82**, 2470–2472 (2003)
27. M. Kläui, C.A.F. Vaz, J.A.C. Bland, E.H.C.P. Sinnecker, A.P. Guimarães, W. Wernsdorfer, G. Faini, E. Cambril, L.J. Heyderman, C. David, Appl. Phys. Lett. **84**, 951–953 (2004)
28. T. Yang, M. Hara, A. Hirohata, T. Kimura, Y. Otani, Appl. Phys. Lett. **90**, 022504 (2007)
29. W. Jung, F.J. Castaño, C.A. Ross, Phys. Rev. Lett. **97**, 247209 (2006)
30. M. Kläui, in *Magnetic Rings: A Playground to Study Geometrically Confined Domain Walls*, ed. by B. Azzerboni, G. Asti, L. Pareti, M. Ghidini. Magnetic Nanostructures in Modern Technology (Springer, Dordrecht, 2008), pp. 85–104
31. M. Kläui, H. Ehrke, U. Rüdiger, T. Kasama, R.E. Dunin-Borkowski, D. Backesb, L.J. Heyderman, C.A.F. Vaz, J.A.C. Bland, G. Faini, E. Cambril, W. Wernsdorfer, Appl. Phys. Lett. **87**, 102509 (2005)
32. M. Laufenberg, D. Bedau, H. Ehrke, M. Kläui, U. Rudiger, D. Backes, L.J. Heyderman, F. Nolting, C.A.F. Vaz, J.A.C. Bland, T. Kasama, R.E. Dunin-Borkowski, S. Cherifi, A. Locatelli, S. Heun, Appl. Phys. Lett. **88**, 212510–212513 (2006)
33. M. Vázquez, in *Advanced Magnetic Nanowires*, ed. by H. Kronmüller, S. Parkin. Handbook of Magnetism and Advanced Magnetic Materials, vol 4 (Wiley, Chichester, 2007), pp. 2193–2226
34. S. Ono, M. Saito, H. Asoh, Electrochim. Acta **51**, 827–833 (2005)
35. M. Darques, A. Encinas, L. Vila, L. Piraux, J. Phys. D: Appl. Phys. **37**, 1411–1416 (2004)
36. C.L. Dennis, R.P. Borges, L.D. Buda, U. Ebels, J.F. Gregg, M. Hehn, E. Jouguelet, K. Ounadjela, I. Petej, I.L. Prejbeanu, M.J. Thornton, J. Phys. Condens. Matter **14**, R1175–R1262 (2002)

37. D.J. Sellmyer, M. Zheng, R. Skomski, J. Phys. Condens. Matter **13**, R433–R460 (2001)
38. U. Ebels, A. Radulescu, Y. Henry, L. Piraux, K. Ounadjela, Phys. Rev. Lett. **84**, 983–986 (2000)
39. L. Sun, Y. Hao, C.L. Chien, P.C. Searson, IBM J. Res. Dev. **49**, 79–102 (2005)
40. A.F. Khapikov, J. Appl. Phys. **89**, 7454–7456 (2001)
41. M. Chen, P.C. Searson, C.L. Chien, J. Appl. Phys. **93**, 8253–8255 (2003)
42. R. Skomski, J. Zhou, in *Nanomagnetic Models*, ed. by D. Sellmyer, R. Skomski. Advanced Magnetic Nanostructures (Springer, New York, 2006), pp. 41–90
43. J.D.L.T. Medina, M. Darques, T. Blon, L. Piraux, A. Encinas, Phys. Rev. B **77**, 014417–014419 (2008)
44. L. Piraux, J.M. George, J.F. Despres, C. Leroy, E. Ferain, R. Legras, K. Ounadjela, A. Fert, Appl. Phys. Lett. **65**, 2484–2486 (1994)
45. L. Thomas, S. Parkin, in *Current Induced Domain-Wall Motion in Magnetic Nanostructures*, ed. by H. Kronmüller, S. Parkin. Handbook of Magnetism and Advanced Magnetic Materials (Wiley, Chichester, 2007), pp. 942–982
46. H. Forster, T. Schrefl, W. Scholz, D. Suess, V. Tsiantos, J. Fidler, J. Magn. Magn. Mater. **249**, 181–186 (2002)
47. M. Hayashi, L. Thomas, Y.B. Bazaliy, C. Rettner, R. Moriya, X. Jiang, S.S.P. Parkin, Phys. Rev. Lett. **96**, 197207 (2006)
48. G. Tatara, H. Kohno, Phys. Rev. Lett. **92**, 086601–086604 (2004)
49. A. Thiaville, Y. Nakatani, J. Miltat, Y. Suzukim, Europhys. Lett. **69**, 990–996 (2005)
50. G.S.D. Beach, C. Knutson, M. Tsoi, J.L. Erskine, J. Magn. Magn. Mater. **310**, 2038–2040 (2007)
51. A. Fert, L. Piraux, J. Magn. Magn. Mater. **200**, 338–358 (1999)
52. C.A. Ross, F.J. Castaño, D. Morecroft, W. Jung, H.I. Smith, T.A. Moore, T.J. Hayward, J.A.C. Bland, T.J. Bromwich, A.K. Petford-Long, J. Appl. Phys. **99**, 08S501–08S506 (2006)
53. T.L. Wade, J.E. Wegrowe, Eur. J. Appl. Phys. **29**, 3–22 (2005)

Chapter 7

1. T. Thomson, L. Abelman, H. Groenland, in *Magnetic Storage: Past, Present and Future*, ed. by B. Azzerboni, G. Asti, L. Pareti, M. Ghidini. Magnetic Nanostructures in Modern Technology (Springer, Dordrecht, 2008), pp. 237–306
2. H.J. Richter, J. Phys. D: Appl. Phys. **40**, R149–R177 (2007)
3. H.N. Bertram, *Theory of Magnetic Recording* (Cambridge University Press, Cambridge, 1994)
4. O. Karlqvist, Trans. Roy. Inst. Technol. Stockholm. **86**, 3–27 (1954)
5. P.P. Freitas, H. Ferreira, S. Cardoso, S. van Dijken, J. Gregg, in *Nanostructures for Spin Electronics*, ed. by D. Sellmyer, R. Skomski. Advanced Magnetic Nanostructures (Springer, New York, 2006), pp. 403–460
6. J.-G. Zhu, X. Zhu, Y. Tang, IEEE Trans. Magn. **44**, 125–131 (2008)
7. A. Knoll, P. Bachtold, J. Bonan, G. Cherubini, M. Despont, U. Drechsler, U. Durig, B. Gotsmann, W. Haberle, C. Hagleitner, D. Jubin, M.A. Lantz, A. Pantazi, H. Pozidis, H. Rothuizen, A. Sebastian, R. Stutz, P. Vettiger, D. Wiesmann, E.S. Eleftheriou, Microelectron. Eng. **83**, 1692–1697 (2006)
8. S. Kawata, Y. Kawata, Chem. Rev. **100**, 1777–1788 (2000)

9. S. Raoux, G.W. Burr, M.J. Breitwisch, C.T. Rettner, Y.-C. Chen, R.M. Shelby, M. Salinga, D. Krebs, S.-H. Chen, H.-L. Lung, C.H. Lam, IBM J. Res. Dev. **52**, 465–479 (2008)
10. G.W. Burr, B.N. Kurdi, J.C. Scott, C.H. Lam, K. Gopalakrishnan, R.S. Shenoy, IBM J. Res. Dev. **52**, 449–464 (2008)
11. S.K. Kim, K.S. Lee, Y.S. Yu, Y.S. Choi, Appl. Phys. Lett. **92**, 022509 (2008)
12. S. Bohlens, B. Krüger, A. Drews, M. Bolte, G. Meier, D. Pfannkuche, Appl. Phys. Lett. **93**, 142508 (2008)
13. J.-G. Zhu, Y. Zheng, G.A. Prinz, J. Appl. Phys. **87**, 6668–6673 (2000)
14. T. Yang, A. Hirohata, L. Vila, T. Kimura, Y. Otani, Phys. Rev. B **76**, 172401–172404 (2007)
15. X.F. Han, Z.C. Wen, H.X. Wei, J. Appl. Phys. **103**, 07E933–07E939 (2008)
16. X. Zhu, J.-G. Zhu, IEEE Trans. Magn. **39**, 2854–2856 (2003)
17. C. Chappert, A. Fert, F. Nguyen Van Dau, Nat. Mater. **6**, 813–823 (2007)
18. S.S.P. Parkin, M. Hayashi, L. Thomas, Science **320**, 190–194 (2008)
19. W.H. Doyle, in *Magnetic Recording Technologies: Future Technologies*, ed. by K.H.J. Buschow. Concise Encyclopedia of Magnetic and Superconducting Materials, 2nd edn. (Elsevier, Amsterdam, 2005), pp. 539–548
20. Y. Li, A.K. Menon, in *Magnetic Recording Technologies: Overview*, ed. by K.H.J. Buschow. Concise Encyclopedia of Magnetic and Superconducting Materials, 2nd edn. (Elsevier, Amsterdam, 2005), pp. 627–634
21. J. Shi, in *Magnetization Reversal in Patterned Magnetic Nanostructures*, ed. by B. Heinrich, A.C. Bland. Ultrathin Magnetic Structures, vol 4 (Springer, Berlin, 2004), pp. 307–331

Author Index

Index